Structural and Optical Studies of Condensed Gases under Extreme Conditions

Mengnan Wang

Doctor of Philosophy
The University of Edinburgh
June 2023

Abstract

Dense solidified gases are sources of rich physical and chemical phenomena and model objects to be widely used in theoretical calculations. The focus of this thesis has been the structural and optical properties of simple gases and gas mixtures under extreme conditions. Three simple dense gas systems, methane (CH_4), Xe-Ar mixture and nitrogen-trifluoride (NF_3) have been studied and characterized using high pressure and high temperature techniques in combination with Raman spectroscopy and x-ray diffraction in diamond anvil cells (DACs).

CH_4 is one of the major constituents of the Uranus and Neptune interiors, and large amounts of it are also present in the deep Earth. As the simplest hydrocarbon, CH_4 presents a rich variety of crystal structures at low temperature and pressure regime. However, despite being widely studied, phase relations between numerous CH_4 phases are poorly understood even at relatively low pressure. In this thesis, by combining Raman spectroscopy and *in-situ* high-pressure, high-temperature resistive heating techniques, we demonstrate the complexity of the phase diagram of CH_4 up to 45 GPa and 1400 K. Changes in the frequencies and Raman profiles of the ν_1 and ν_3 vibrational modes of CH_4 molecule were used to detect phase transitions and construct boundaries between individual phases in the phase diagram. A triple point between fluid, phases I, and phase A alone the melting curve was found and precisely located in the studied P-T range. The melting curve changes its slope above the triple point. Moreover, previously reported sluggish transitions from phase A to phase B was found to be controlled by kinetics. These results represent a significant revision of the existing phase diagram of CH_4.

The second system under investigation is the binary mixture of xenon and argon. The simple closed-shell electronic configurations make rare gases and their mixtures an ideal system for comparing experiment with theory. Rare gases are archetypal van der Waals systems. Previously, no binary compounds of Xe and Ar were known. We have explored rare gas solids Xe-Ar system up to pressure of 60 GPa with combined Raman spectroscopy, x-ray diffraction and first-principles density functional theory (DFT) calculations. A novel van der Waals compound $XeAr_2$ has been observed at 3.5 GPa. We find that pressure stabilizes the formation of this stoichiometric, solid van der Waals compound of composition $XeAr_2$. Synchrotron x-ray diffraction shows that this compound adopts a $MgZn_2$-type crystal structure, which is in a Laves phase. Our DFT calculation of the formation enthalpy indicates that $XeAr_2$ stays stable to at least 80 GPa.

The last condensed gas solid presented here is nitrogen-trifluoride (NF_3). Since first synthesized by molten salt electrolysis, NF_3 has attracted wide interests, ranging from fundamental study to industrial applications. However, structures and phase relations on NF_3 under high pressure remains unknown. In the contributing work, NF_3 has been studied by synchrotron x-ray diffraction and Raman spectroscopy combined with DFT calculation. At 300 K, NF_3 solidifies at 3.5 GPa into the orthorhombic structure (*Pnma*). Phase diagram of NF_3 has been studied by Raman spectroscopy, two solid phases have been observed between 77 and 300 K up to 120 GPa. Our DFT calculations suggests NF_3 remains stable to at least 150 GPa.

Lay Summary

High pressure has been widely used in many fields to explore properties and revolutions of the Earth and some giant planets and to allow fruitful comparison of experiment with theory. Moreover, high pressure can dramatically enhance the chemical reactivity, forming new compounds and materials which do not exist under ambient conditions.

To generate pressures orders of magnitude higher than ambient pressure, a special device - diamond anvil cell (DAC) is used. Modern DAC is designed based on a very straightforward principle, by applying force on the back of two opposite diamond anvils that are compressing a sample contained in a metal gasket. The portable size of DAC makes it easy to conduct *in-situ* measurements in the laboratory. Due to the transparency property, diamond anvils provide good windows for optical and x-ray measurements.

Materials normally exhibit fascinating phenomena under high pressure. For example, the noble gases are known for their inertness because of the closed-shell electronic configuration. However, their reactivities are found to increases with pressure and some van der Waals compounds are found to be formed in rare gas systems. Modern design of DAC allows not only to reach pressures of hundreds GPa but also simultaneously vary temperatures by combining a cryostat and laser/resistive heating techniques. Phase transitions and phase relations of materials can be studied up to very high P-T conditions in a DAC thus helping us to better describe the internal structure and evolution in the icy giant planets and in the deep Earth.

In this work, by combining x-ray diffraction and Raman spectroscopy characterization methods, we have investigated structures and properties of three simple gas systems: Xe-Ar, methane (CH_4) and nitrogen-trifluoride (NF_3) under high-pressure and high-temperatures.

Declaration

I declare that this thesis was composed by myself, that the work contained herein is my own except where explicitly stated otherwise in the text, and that this work has not been submitted for any other degree or professional qualification except as specified.

.

(*Mengnan Wang, June 2023*)

Acknowledgements

I would like to express my deepest gratitude and appreciation to everyone who has helped me during the past three years. In particular, the following:

I'm extremely grateful to my supervisor Prof. Eugene Gregoryanz for taking me on as a PhD student. For all his inspirations, patient guidance and constant support.

Dr. Miriam Peña-Alvarez for her precious friendship. For all her help with the high temperature experiments. Without her patient training, I would not be able to conduct the work for this thesis.

Dr. Ross Howie for his constant help in the past 7 years, and especially for captivating my interest in high pressure science.

Dr. Mikhail Kuzovnikov for his help with the x-ray analysis, for all his useful opinion and honest criticisms. For his great accompany, for all the happy hikings in Pentland hills.

Mr. Calum Strain, for his help and companionship in the lab and the bemalines. Dr. Israel Osmond and Miss. Hannah Shuttleworth for doing the proofreading for my thesis.

To all the CSEC people for their constant help and support. For the happy beer hours, lunch breaks and all the happy memories.

To the Principal's Career Development Scholarship of the University of Edinburgh for financial support.

谢谢一路走来帮助过我的各位老师和师兄师姐，感谢胡蕙昕小师妹。

感恩父母，公婆，家人和朋友们一直以来的理解和支持。尤其感谢我的妈妈，谢谢你二十几年前坚定勇敢地选择我，感谢你的支持和鼓励，我希望一直成为你的骄傲！谢谢我的朋友李甜禄女士。感谢我的好朋友张馨月博士，这12年来的珍贵友谊，谢谢她每日的分享和对我的关心，陪我走过很多艰难的日子。最后要感谢我先生李洪浩的理解和支持，我很抱歉没能给你很多的陪伴，以后会加倍补偿。

这个水博就先读到这儿啦！

Contents

List of Figures

List of Tables

Chapter 1

Introduction

1.1 Brief Review of High Pressure Science

Nowadays, high pressure science has been widely used in various fields including physics, chemistry, material science, geoscience and biology. Modern high pressure science can be easily dated back to 1905 when Percy W. Bridgman invented a new apparatus, in which a force was applied to the small area between two tungsten-carbide (WC) anvils. This device allowed him to explore the properties of materials under pressure orders of magnitude higher than ambient pressure [6]. He investigated more than 177 substances at high pressure and received the Nobel Prize in 1946 for his vast scientific achievements. The modern diamond anvil cell (DAC) design was inspired by Bridgman, by replacing the two WC anvils with diamonds. Diamond is the hardest material which can withstand more strains to generate higher pressure than WC anvils. Another advantage of diamond is its transparency to most electromagnetic (EM) radiation. Therefore, optical diagnostics such as Raman spectroscopy and synchrotron x-ray diffraction can be employed *in-situ*.

The first DAC was made by Van Valkenburg and Charles Weir in 1958 with two opposite diamond anvils [7]. This design allowed them to see the effect of pressure in a transparent sample chamber under a microscope. With this device, John C. Jamieson could perform x-ray diffraction measurements in 1959 on bismuth [8]. Mao and Bell first attained static pressures exceeding 100 GPa in 1976, using the Mao-Bell diamond anvil cell with bevelled diamonds [9]. Since then, the field of high-pressure science utilising DACs has seen significant growth. Researchers have successfully achieved pressures in the multimegabar range, pushing the boundaries of our understanding of materials under extreme conditions. This progress has been accompanied by the application of a diverse array of advanced analytical techniques, yielding a wealth of valuable insights into the behaviour of materials subjected to these extreme conditions.

In 1972, the pressure scale based on the pressure-induced shift of ruby fluorescence wavelength was developed [10]. Nowadays, this spectroscopic method is widely used to measure pressures up to 50 GPa accurately and rapidly.

Diamond is also the best thermal conductor, which makes it possible to accurately measure temperature of the sample with an external thermocouple. By placing an external resistive heater around the cell and coiling resistance wires around diamond anvils, a temperature above 1000 °C can be easily reached. Higher temperatures can be obtained by the laser heating technique.

In the context of the research contributions, the previously mentioned techniques, namely Raman spectroscopy, X-ray diffraction, resistive heating, and laser heating within DACs, have played pivotal roles as the primary tools for investigating structural alterations and phase transitions in rare gases and the "bad rare gas" - methane (CH_4) as well as nitrogen-trifluoride under extreme conditions.

1.2 Review of Rare Gases and Their Mixtures

The simple closed-shell electronic configurations make rare gases and their mixtures an ideal case to compare experiments and theory. Structures and properties of rare gases and rare gas mixtures are of great importance for chemistry, physics, and planetary science as they have been considered to help in the understanding of van der Waals (vdW) interactions. Moreover, heavier rare gases (Kr, Xe) are important for chemical synthesis. The following section reviews the available literature on the structures and properties of rare gas solids (RGSs) at high pressure. Rare gas binary mixtures of van der Waals compounds both experimental and theoretical, will also be discussed.

Rare gases, also known as noble gases, are sometimes referred to as inert gases. Rare gas Helium(He), Neon(Ne), Argon(Ar), Krypton(Kr), and Xenon(Xe) make

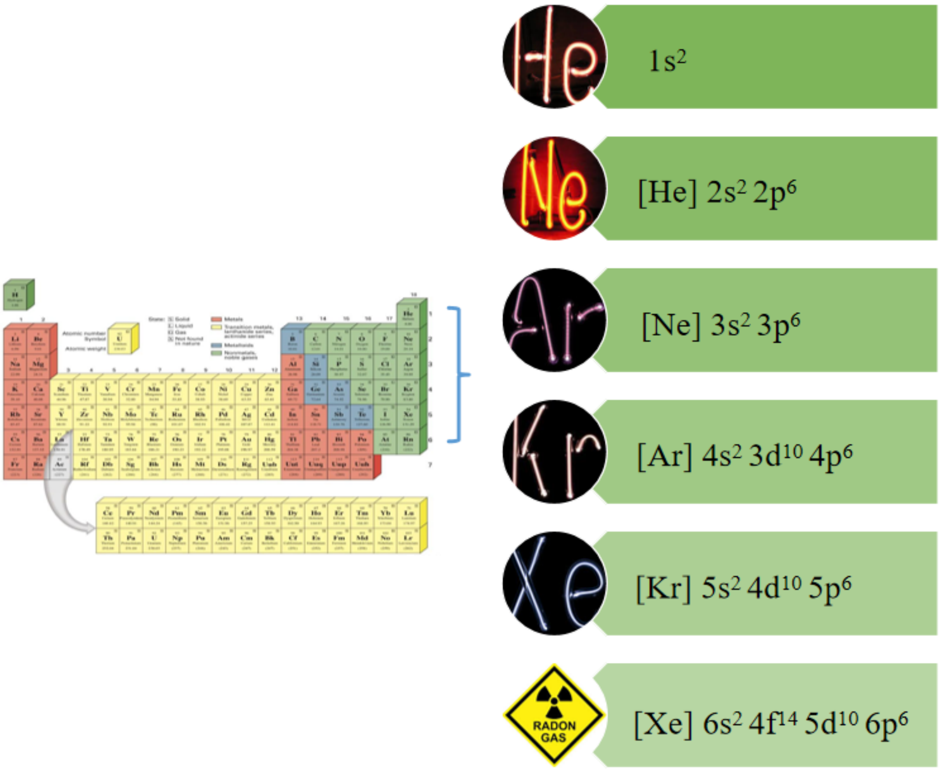

Figure 1.1 *Rare gases and their closed-shell electronic configurations.*

up the group 18 elements with similar closed-shell electronic configurations and properties. In 1784, English chemist and physicist Henry Cavendish, after chemically removing O_2 and N_2 from air in the laboratory, discovered that air contains less than 1/250 of an unknown gas [11]. Inspired by Henery Cavendish, Rayleigh and Ramsay removed O_2 by reacting with Cu and N_2 in a reaction with Mg. They found a chemically unreactive monatomic gas weight 40 and named Argon in 1895 [12]. Subsequent discoveries unfolded at a rapid pace. William identified helium (He) in 1895 while studying the spectrum of argon (Ar) [13]. Then, in 1898, Ramsay and his colleagues made significant contributions by discovering three more elements: Ne, Kr, and Xe through fractional distillation of liquid air [14]. These discoveries firmly established the concept of a periodic table that included the inert gases in Group 18. Figure 1.1 illustrates the position of rare gases in the periodic table along with their respective electronic configurations.

With the discovery of more and more elements and compounds, scientists noticed that during the formation of a chemical bond, atoms combine together by gaining, losing or sharing electrons in such a way that each atom has eight electrons in its valence shell which was known as “octet rule” [15]. Rare gases have been considered as archetypical candidates to understand octet rules in chemistry as their outer shells are full and have no intention to gain or lose electrons. For a long time, it was believed that the rare gases were chemically unreactive and unable to form chemical bonds with other elements under ambient conditions. However, since the 1960’s, stable halide and oxide xenon compounds XeF_4 [16], XeF_6 [17] and XeO_4 [18] have been synthesised through powerful oxidising agents, opening up new pathways of chemical synthesis.

High pressure can dramatically enhance the chemical reactivity, thus helping to form compounds which do not exist at ambient conditions. The noble gases are the most inert group of the periodic table. However, their reactivity is found to increase with pressure. The following section is focused on the properties and behaviour of rare gases, including He, Ne, Ar, Kr and Xe, under high pressure.

1.2.1 Rare Gases Structures and Properties under High Pressure

A). Helium

Helium, the lightest and most abundant rare gas in the universe, was first observed in the solar spectrum in 1868 [19]. It constitutes approximately 24 % of the total elemental mass in the universe, surpassing the combined mass of all heavier elements by over twelve-fold. Helium is believed to present in metallic state in some giant planets such as Jupiter and Saturn with abundance which is similar to the Earth in both the Sun and in Jupiter [20]. These properties are of significant importance when modeling giant planets, where helium serves as a primary constituent [21, 22]. As the lightest rare gas, the relative stability of the *fcc* and *hcp* phases of solid helium have been studied both theoretically and experimentally. Helium was observed to crystallize at 11.5 GPa under room temperature [23]. Unlike the rest of the elements in group 18, helium crystallized in hexagonal-closed-pack (*hcp*) structure instead of face-center-cubic(*fcc*). Through single x-ray diffraction, Mao *et al.* observed only *hcp* phase from 1.6 GPa up to 23 GPa and 300 K [24]. Only limited optical studies have been conducted on pure helium due to the low-Z number and relatively small volume under high pressure. Equation of state and melting curve of helium were detail studied through x-ray diffraction up to 58 GPa over the temperature range

46 - 400 K by P. Loubeyre *et al.* [25]. Helium was also investigated by many other techniques, such as Raman scattering, Brillouin scattering, shock-compression to determine the phase diagram, thermodynamic properties, and elasticity under high pressure [23, 26, 27].

B). Neon

Neon was discovered by Ramsay and his colleagues in 1898 through fractional distillation of liquid air [14]. Neon solidifies at 4.7 GPa and remains a *fcc* structure (space group *Fm3m*) at room temperature [28–30]. Synchrotron x-ray diffraction confirmed that solid neon remains the same *fcc* structure up to 110 GPa at room temperature [31]. Molecular dynamics calculation have predicted a possible *fcc*-*bcc* phase transition in rare gas systems under high pressure and temperatures [32]. However, powder x-ray diffraction study observed that neon maintains the same *fcc* structure up to at least 240 GPa [33]. The sound velocities, elastic modulus, bulk modulus of liquid and solid neon has been well explored by Brillouin spectroscopy, with more details available in [30]. Neon has been widely used in high pressure field as pressure transmitting medium in diamond anvil cell [34]. The equation of state (EoS) of neon has been well calibrated under high pressure and high temperatures thus can be reliably used as x-ray pressure gauge for high P-T diamond anvil cell studies [34].

C). Argon

Argon is the third component of dry air in its volume. Solid argon has been intensively studied in recent years. Argon solidified in a *fcc* structure (space group *Fm3m*) at 1.3 GPa under room temperature [28, 35]. Various fundamental properties, such as the acoustic velocities, elastic constants, bulk modulus and density under high pressure can be found in [36]. X-ray diffraction studies have revealed that solid argon undergoes a phase transition from *fcc* to *hcp* at 47 GPa, with the two phases coexisting over a broad range up to 114 GPa [37]. First principles DFT calculation predicted the phase transition to be completed above 230 GPa [38]. Raman spectroscopy study was conducted on argon up to 56 GPa at room temperature [39]. No Raman-active mode can be observed for solid *fcc* Ar above 21 GPa, but in *hcp* phase the transverse E_{2g} phonon mode appears as a Raman-active band. Rare gas, particularly argon, have been widely used to allow meaningful comparisons between theoritical predictions and experimental results. However, in a comprehensive comparison study based on argon, models employing two-body interatomic potentials were found to better describe the properties of argon compared to DFT calculations. [39].

D). Krypton

Krypton crystallizes in a *fcc* structure at 0.83 GPa under room temperature [40]. Below 3.2 GPa under room temperature, only the *fcc* phase is observed. Further increasing pressure induces the transition from *fcc*-*hcp* and the two phases coexist up to 50 GPa [41]. The result shows a very good agreement with previous study on argon, which indicates a common behavior of heavier rare gas solids [37]. Detailed physical properties, such as elastic constants, bulk modulus and density under high pressure can be found in [42]. Optical studies were conducted on krypton at room temperature up to 75 GPa, revealing a *fcc*-to-*hcp* phase transition occurring around 20 GPa [43]. The E_{2g} Raman-active phonon mode of solid krypton was observed at wavenumber of 90 cm^{-1} and increased to 145 cm^{-1} at 74.5 GPa [43]. The increase in Raman intensity suggests the formation of the *hcp* phase of krypton within the two-phase *fcc*-*hcp* mixture [43].

E). Xenon

Xenon is of particular interest experimentally and theoretically as it has been predicted to have the lowest metallization pressure among rare gases [44, 45]. As a heavy rare gas, xenon has been intensively studied, resulting in the formation of numerous xenon compounds under high pressure. Xenon crystallizes in a *fcc* structure at 0.42 GPa at room temperature [46]. Laser heating Raman spectroscopy experiments showed that the direct *fcc*-*hcp* transformation occurs at 21 GPa and is kinetically sluggish [47]. High-pressure x-ray diffraction studies at room temperature have demonstrated that xenon transforms at 14 GPa from the fcc structure to an intermediate close-packed phase, Xe-II. The *fcc*-to-*hcp* phase transition is completed at 75 GPa, and the *hcp* phase remains stable up to 137 GPa [48]. However, the diffraction pattern and crystal structure of the *hcp* phase was not well resolved and the claimed intermediate phase remains unknown. Recently, through x-ray diffraction the *fcc*-*hcp* transformation takes place between 3 and 70 GPa without any intermediate phase and the possible underlying mechanism is that the stacking disorder in the fcc lattice at low pressure, which grows into hcp domains with increasing pressure [49]. Optical studies, such as Brillouin and Raman spectroscopy, have been conducted on Xe at room temperature.

Xe is relatively reactivate compared with other group 18 elements. A hydrogen-rich $Xe(H_2)_8$ compound was observed in Xe and H_2 mixture at 4.8 GPa in a diamond anvil cell with a structure of tripled hydrogen lattice covered by layers of dimer xenon [50]. Two Xe oxides Xe_2O_5 and Xe_3O_2 were found to form under oxygen atmosphere under 100 GPa which provides a possible explanation for the geochemical missing Xe problem [18]. Xe could also form nitride with N_2 under extreme conditions: above 4.9 GPa, a stable van der Waals compound $Xe(N_2)_2$ ($MgZn_2$-type Laves phase) was observed which further transformed into a tetragonal structure at higher pressure[51].

Previous studies show the crystallisation pressure for rare gases (He, Ne, Ar, Kr, Xe), with a decreasing trend, at 11.5 GPa, 4.7 GPa, 1.3 GPa, 0.83 GPa and 0.42 GPa, respectively. The aforementioned pressure induced *fcc-hcp* phase transition in most rare gases generally exhibits a decreasing trend as the atomic number (Z number) increases. This suggests that high Z number rare gases, such as argon and xenon, have the potential to form new compounds even at relatively low pressures

1.2.2 Van der Waals compounds and Laves Phase

As a consequence of their simplicity and inert chemical behaviour, RGSs are not known to react with one another, but can form van der Waals compounds under extreme pressure conditions. With the application of pressure, a variety of rare-gas van der Waals compounds have been produced, such as $Ar(H_2)_2$ [52], $Kr(H_2)_4$[53], $Xe(H_2)_7$ [50] and $Xe(N_2)_2$ [54]. As such, the RGSs can be considered archetypical cases to understand the van der Waals interaction [55].

Weakly bonded van der Waals compounds under high pressures via van der Waals attraction were first reported in 1992 by W. L. Vos in the helium-nitrogen system [56]. In their study, by using Raman spectroscopy and X-ray diffraction, they observed the first high pressure van der Waals compounds, $He(N_2)_{11}$. In fact, the formation of closed-shell van der Waals compounds are not unique in high pressure science. After a study on the helium-nitrogen system, more and more weakly bonded van der Waals compounds have been discovered in high pressure science.

In the binary systems, the mixtures whose ratios of atomic radii r_A/r_B are close to 1.2:1 (this value could vary from 1.05 to 1.7 under extreme conditions) are usually considered to be the substitutional AB_2 compounds, referred to as the Laves phases [57–59]. For geometric reasons, Laves phase compounds have closed-packed structures with maximum packing fraction. Three different poly-types of the Laves phase structure are generally observed: cubic $MgCu_2$-type, the hexagonal $MgZn_2$-type, and the hexagonal $MgNi_2$-type. Although a great variety of Laves phase compounds have been synthesised, it is impossible to predict which type of Laves phase one compound belongs to. It is well known that the geometric and electronic factors such as the atomic size ratio, electronegativity and valence electron numbers can affect the structure type of a Laves phase [59].

1.2.3 RG - RG Binary Mixtures

Pressure-induced reactions typically result in the formation of new compounds that do not naturally exist under ambient pressure conditions. Many of these compounds exist in molecular states, and the interactions between these molecules are of the van der Waals type. Consequently, these compounds are commonly referred to as van der Waals (vdW) compounds. Systems with closed electron shells, such as hydrogen, nitrogen, and mixtures of rare gases, have the ability to form stoichiometric compounds when subjected to high pressures. The van der Waals compounds have unique properties and thus play an important role in understanding the structure and properties of interiors of planets and their satellites.

Due to their simplicity and inert chemical behaviour caused by closed-shell electronic configurations, RGSs are not known to react with one another. However, the formation of novel van der Waals compounds $NeHe_2$ [60], $ArHe_2$ [61] and $ArNe_2$ [62] under pressure make RG-RG reactions possible. $NeHe_2$ was the first compound reported in the RG–RG binary system by Loubeyre *et al.* in 1993. With a radii ratio of 1.19 of its constituent atoms at 15 GPa, this compound has a $MgZn_2$-type Laves phase structure (space group $P6_3/mmc$), with helium and neon occupying the $2a + 6h$ and $4f$ sites, respectively [60]. $NeHe_2$ remains stable up to 90 GPa, and its bulk modulus is bigger than He while smaller than Ne. Another stoichiometric compound, $ArNe_2$, adopts the same structure with $r_{Ar}/r_{Ne} = 1.228$ at 6 GPa. The bulk modulus of $ArNe_2$ also lies in between its constituent elements and remains stable up to 65 GPa [62]. However, a recent first-principles study predicted that the comparatively heavier Xe–Ar binary noble gas system would behave differently, instead forming a $MgCu_2$-type Laves phase structure at pressures above 1.1 GPa [63].

1.3 Review of the CH_4 Phase Diagram

Methane (CH_4), the simplest hydrocarbon, has long been considered as " bad rare gas " as it can be treated as an orientational disordered neutral molecule like the rare gas argon. CH_4 also has a closed electron shell and an almost spherically symmetric molecular structure (*i.e.*, the dipole moment equals zero). Despite the diverse crystal structures observed under extreme conditions, methane (CH_4) remains a relatively straightforward compound. Similar to the rare gases (RGS), CH_4 also crystallises in the *fcc* structure, characterised by van der Waals interactions between its constituent molecules.

CH_4 is one of the major constituents of Uranus and Neptune interiors, and large amounts of it are also present in the deep Earth [64–66]. Figure 1.2 shows the schematic view of Uranus and Neptunes' interior structure. Density profiles suggest that, between a rocky core and a hydrogen-helium outer layer, there is an intermediate mantle of "hot ices" (ranging from 20 GPa and 2000 K to 600 GPa and 8000 K), which consists of 56 % water, 36 % methane, and 8 % ammonia. It has even been proposed that hot compression of CH_4 could lead to the synthesis of longer oligomers, perhaps even complex prebiotic molecules; or to decompose into hydrogen and diamond [3, 67, 68]. Study of the properties of CH_4 is of critical importance for an improved understanding of the physics and chemistry of planetary interiors and the origin of their magnetic field distribution.

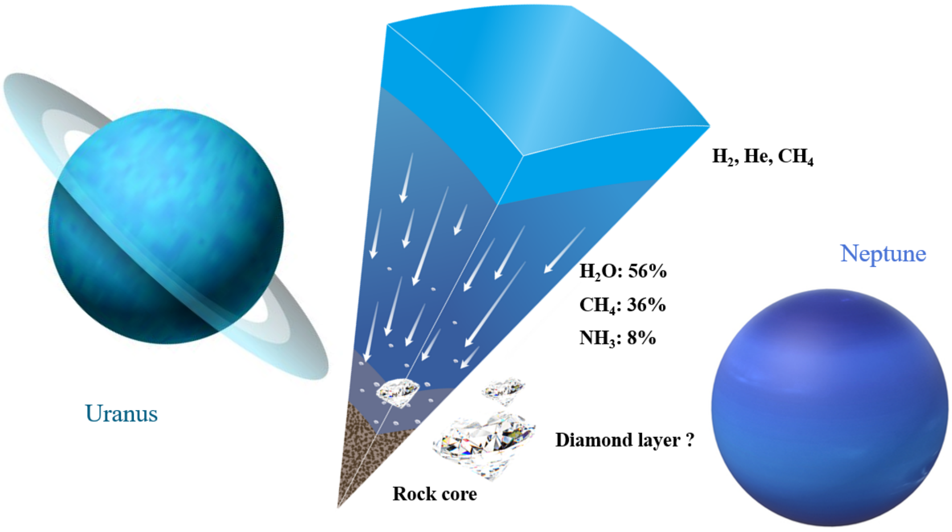

Figure 1.2 *Schematic view of Uranus and Neptune interior structure.*

1.3.1 Physical and Chemical properties of CH_4

CH_4 consists of one carbon atom and four hydrogen atoms. The carbon atom in the center forms four sigma bonds with four hydrogen atoms, resulting in a stable symmetrical tetrahedral arrangement. The four identical C–H bonds are relatively strong. However, unlike H_2O, NH_3 and HF, there is no hydrogen bond in CH_4. Just like RGS, CH_4 also crystallizes in *fcc* structure with van der Waals interaction between molecules. Figure 1.3 depicts the skeletal formula of CH_4. Each C-H bond has a length of 109 pm and an angle of 109.5 °. Table 1.1 shows some basic chemical and physical properties of CH_4 at ambient conditions.

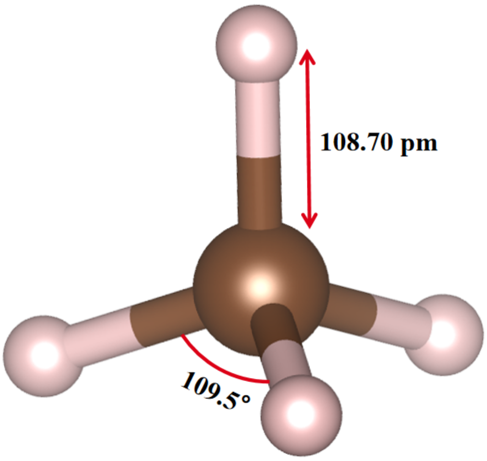

Figure 1.3 *Skeletal formula of CH_4; pink atoms stand for H atoms while brown one represents C atom.*

It is well known that molecular CH_4 has four characteristic fundamental internal vibrational modes under ambient conditions: a symmetric $\nu_1(A_1)$ at around 2913 cm^{-1}, a doubly degenerate $\nu_2(E)$ at around 1582.7 cm^{-1} and two triply degenerate $\nu_3(F_2)$ and $\nu_4(F_2)$ at 3063 cm^{-1} and 1367.4 cm^{-1} respectively. These four modes are Raman active, while ν_1 and ν_3 are IR active. Both Raman modes and IR modes of CH_4 have proven effective as probes for phase transitions due to their sensitivity to pressure variations [69–71]. In the subsequent research, Raman spectra were meticulously collected and employed as the primary method for characterising different phases and detecting phase transitions under extreme conditions.

As the simplest hydrocarbon, CH_4 presents a wide variety of crystal structures due to differences in the orientational ordering of molecules. In the low temperature

Table 1.1 *Physical and Chemical properties of CH_4*

	$\mathrm{CH_4}$	References
Molecular Weight ($g.mol^{-1}$)	16.043	[72]
Physical Description	Colorless, odorless natural gas	[72]
Density ($kg.m^{-3}$)	0.657	[73]
Boiling point (K)	111.6	[74]
Melting point (K)	90.694	[74]
Dipole moment (D)	0	[72]
Heat capacity ($J.mol^{-1}.K^{-1}$)	35.7	[74]
Gibbs free energy ($kJ.mol^{-1}$)	-50.5	[74]

and moderate pressure regime, $\mathrm{CH_4}$ has six cryogenic solids, *i.e.,* phases I, II, III, IV, V, and VI, which only exist below 150 K and 25 GPa. Previous x-ray diffraction (XRD), infrared, and Raman spectroscopic studies up to 86 GPa at 300 K have revealed that at room temperature, $\mathrm{CH_4}$ crystallized in plastic phase I with *fcc* structure at 1.5 GPa [75]. This structure transforms at 5.4 GPa to a complex rhombohedral structure phase A with 21 atoms in the unit cell [76]. Further increase in pressure leads to a phase transition to phase B with α-Mn arrangement cubic structure [77]. The phase transition from phase A to phase B is sluggish and could be easily missed if fast compressed at around 8 GPa [78]. Once phase A to phase B transition has been missed, phase A remains stable in further compression [79]. Phase B has been reported to transform to a high pressure phase at around 25 GPa, which structure can be viewed as rhombohedrally distorted phase B [4]. Recent time-resolved Raman measurements conducted by Hirai *et al.* have unveiled an intermediate, metastable phase known as pre-B, emerging at pressures exceeding 12 GPa. This pre-B phase exhibits a structure close to that of phase B, yet with molecular rotations similar to those of phase A [78]. Notably, both Phase B, pre-B, and phase HP share a simple cubic symmetry and display similar lattice parameters with respect to pressure, making their differentiation solely achievable through X-ray diffraction analysis.

1.3.2 The Known Phase Diagram of $\mathrm{CH_4}$

At temperatures below 300 K and 30 GPa, a region out of the scope of this work is the existence of phase I to phase VI, found via Fourier transform infrared spectroscopy measurements combined with x-ray diffraction [70]. Phase diagram of $\mathrm{CH_4}$ under low temperature and moderate pressure are given by Bini *et al.*

[69, 70]. In contrast with the abundance of experimental and theoretical work at low temperatures and pressures, phase relations in the C–H system under high temperatures are poorly understood even at relatively low pressures.

CH_4 melting curve measurements were reliably reported up to 4.8 GPa [1] and 6.8 GPa [2]. Remarkably, only two experimental studies have been performed to explore the melting behaviour of CH_4 at elevated pressures and temperatures using laser heating experiments. These studies suggest that CH_4 undergoes congruent melting under such conditions. The melting line would go from 700 K at 20 GPa to below 1000 K at 80 GPa [3]. Their results imply that the melting line of CH_4 up to 80 GPa would be below or similar to the melting of hydrogen whose maximum is around 900 K at around 75 GPa [5, 80]. However, the uncertainties in their laser heating temperature measurements are larger than 200 K, especially significant at low pressure where the melting temperature is also low. Instead of the melting curve, they predicted a rough band of melting (Figure 1.5 light green area).

On the other hand, theoretical works predict the melting line of CH_4 to be considerably steeper and higher in temperature than the laser heating experiments reported, going from approximately 1000 K at 10 GPa to 1250 K at 80 GPa[81, 82].

Experimentally probing the melting conditions of CH_4 is essential not only because of the planetary impact of CH_4 and their reactivity but also because these conditions are representative of those of the Earth's lower mantle.

Moreover, it has been reported that at temperatures of 1200 K, melted CH_4 would undergo a carbon-hydrogen reaction, suggesting the formation of longer oligomers and hydrogen release [3, 67, 68, 83, 84]. However, no such reactivity was observed in shock compression experiments despite reaching pressures and temperatures orders of magnitude higher [85, 86]. Contrary to the shock-wave experiments, computer simulation does not predict the dissociation of CH_4 into hydrogen and carbon/diamond but a mixture of hydrocarbons instead at pressures below 300 GPa and 4000 K [67, 87–90]. Hydrocarbon reactions would be of great relevance to the internal structure and evolution of icy giant planets since these heavy molecules would fall through the mantle, leading to stratified planetary cores. In shock experiments at uncertain P-T conditions, polystyrene has been shown to further react to form carbon, leading to exotic predictions of the "diamond rain" with tonnes of diamonds falling from the Jovian atmosphere [91]. Table 1.2 has summarised previous both experimental and theoretical work on CH_4 after its melting. It is almost certain that polymerisation of CH_4 and diamond formation would occur under extreme conditions.

1.3.3 Summary

This section has summarised the fundamental physical and chemical properties of CH_4 and some phase transitions under different conditions. A brief overview of the established phase diagram of CH_4, encompassing both low and high-temperature regimes, is also provided herein. It becomes evident that the most enigmatic segment within CH_4's phase diagram may hold the most valuable insights. Consequently, delving into this region assumes fundamental importance, as it promises to provide answers to pivotal questions such as:

(1). What is the nature of the sluggish transition from phase A to phase B?

(2). How will the melting line continue at higher pressures and temperatures?

(3). How many triple points exist along the melting curve? What is the nature of the CH_4 triple point(s)?

(4). What will happen after the melting of CH_4? Polymerise into heavier hydrocarbons or disassociate into diamond and molecular hydrogen? What is the mechanism of polymerisation/dissociation?

(5). How does the evolution of CH_4 under extreme conditions depend on temperature and pressure?

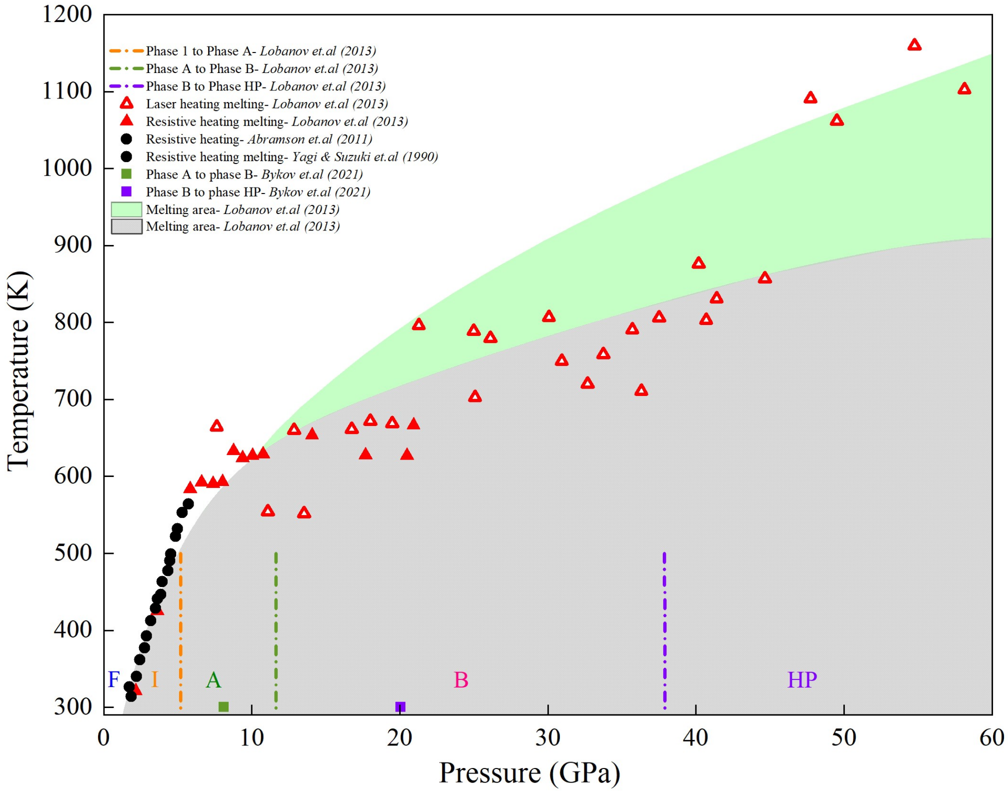

Figure 1.4 *The known high pressure and high temperature phase diagram of CH_4. Black circles represent CH_4 melting after Yagi and Abramson [1, 2] by resistive heating. Red triangles and open red triangles represent CH_4 melting after Lobanov et al. [3] via resistive heating and laser heating respectively. Olive and purple squares are phase A and phase B observed under room temperature by Bykov et al. [4]. Different dashed lines represents phase boundaries: orange dashed line is boundary of phase I and phase A, olive dashed line is boundary of phase A to phase B and purple dashed line shows boundary of phase B and phase HP. Grey area shows solid CH_4 region while light green area represents CH_4 melting according to laser heating experiments [3].*

Table 1.2 *CH_4 after melting, polymerization or dissociation?*

Methods	Products at high temperature and pressures	P/T dependence	Ref.
Shock-wave Experiment	Diamond + molecular H_2 at 3000 K, 20 - 40 GPa	T	[91]
First Principles MD Simulation	$<$ 100 GPa, mixture of hydrocarbon; $>$ 300 GPa, diamond + H_2	P	[90]
Laser Heating/Raman/XRD	Hydrocarbon + diamond at 10-50 GPa, 2000-3000 K		[68]
Electrical Conductivity	$<$ 30 GPa, molecular CH_4; $>$ 43 GPa, C-polymers + H_2	P	[85]
Laser Heating/Raman	Diamond + molecular H_2 at 2300 K, 13 GPa		[84]
Laser Heating/Raman/XRD	$<$ 1100 K, Polymerized hydrocarbons; $>$ 3000 K, Diamond + H_2	T	[67]
Laser Heating/Raman	1000 - 1500 K, $>$ 2 GPa Saturated hydrocarbon + graphite + H_2	P	[87]
ab-initio Calculation	$<$ 95 GPa, C_2H_6 + C_4H_{10} ; $>$ 287 GPa, Diamond + H_2	P	[88]
Laser Heating/Raman	$<$ 1200 K, Carbon + H_2 ; $>$ 1500 K, alkanes + unsaturated hydrocarbons	T	[3]
Dynamic Shock Experiment	Diamond + molecular H_2 at 150 GPa, 5000 K	T/P	[86]

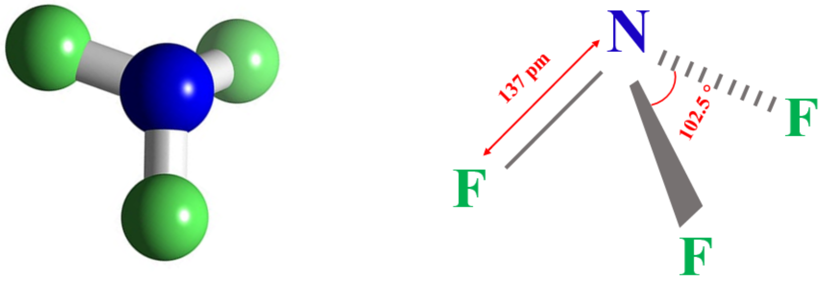

Figure 1.5 *NF_3 molecular geometry under ambient conditions.*

1.4 Review of Nitrogen-Fluoride System

Since first synthesised by molten salt electrolysis in 1928, nitrogen-trifluoride (NF_3) has attracted wide interest, ranging from fundamental study to industrial applications. As a significant fluorine compound, NF_3 has found versatile applications, serving as nuclear fuel [92], a component in powerful chemical lasers [93], and a cathode reactant in high-capacity Li-gas batteries [94]. Its short atmospheric lifetime and exceptional efficiency in decomposition render it a widely utilised etching material and serves as a cleaning gas within the electronics industry [95]. Moreover, as a powerful oxidiser and fluorinating agent, NF_3 is an important compound in many chemical synthesis processes[96]. On the other hand, NF_3 is an atmospherically persistent potent greenhouse gas (GHG) with an atmospheric abundance of 0.454 *ppt* in 2008 [97, 98]. A better understanding of NF_3 will have implications for addressing the global warming issues.

As an archetypal nitrogen-halogen bond system, the structure and properties of nitrogen-fluorine compounds are of fundamental interest. Unlike its analogous binary nitrogen-halogen species, nitrogen-fluorine compounds are usually thermodynamically stable [99]. Especially NF_3 is one of the most stable compound at ambient pressure [100, 101]. At ambient conditions, NF_3 adopts a trigonal pyramidal structure analogous to that of NH_3 and PH_3 (Figure 1.5). NH_3 and PH_3 have been reported to be chemically dissociates to their elemental atoms under high temperatures [102–104]. However, the large electronegativity of fluorine atoms and the lack of hydrogen bond in NF_3 makes these compounds differ significantly. For example, the dipole moment of NF_3 (0.234 D) is over six times smaller than that of NH_3 and oriented in the opposite directio n[105]. Moreover, hydrogen-bonds have a great influence on the interactions of NH_3, while repulsive lone pair-long pair reactions were proposed to play an important role in the interactions of NF_3 [102].

Two different structures of NF_3 have been reported at low temperatures, an α-NF_3 phase with orthorhombic structure (space group $Pnma$) at 6 K and a plastic β-NF_3 with tetragonal structure (space group $P4_2/mnm$) at 66 K[106, 107]. In contrast with the only solid phase under low temperature, three solid-solid phase transitions have been reported up to 55 GPa by Raman spectroscopy in diamond anvil cell [102]. However, the crystal structures of these three high pressure phases of NF_3 remain unknown. Moreover, no experiment has been performed on the correlation between low and room temperature phases, due to the lack of information on the crystal structures in a wide portion of the phase diagram in the intermediate range of temperature.

1.5 Thesis Outline

The objectives of the contributing work can be divided into three parts: (1) investigation of rare gases and their mixtures to study the van der Waal interaction under high pressure. (2) revision of the high P-T phase diagram of CH_4 and extending our current understanding of its melting curve. (3) exploring the structure and stability of nitrogen-trifluoride under extreme conditions.

This thesis consists of six chapters. The **introductory chapter** has furnished a concise review of high pressure science and offered an overview of rare gas solids, the notable‘ bad rare gas ’ - CH_4, and the nitrogen trifluoride systems under high-pressure conditions. The following chapters are composed as follows:

Chapter 2 concerns a brief background theory on Raman spectroscopy and X-ray diffraction used in this work. 2.1 gives a general background theory of Raman spectroscopy in both classical and quantum mechanical views. Section 2.2 describes high pressure Raman setups used in this work. Section 2.3 provides principles of diffraction and crystallography. In section 2.4, high pressure synchrotron x-ray diffraction is discussed.

Chapter 3 shows high pressure and high temperature techniques used for the contributing work including diamond anvil cell preparation, and different loading methods, pressure calibrants, resistive heating and laser heating techniques.

Section 3.1 discusses the diamond anvil cell, providing underlying principles of diamond anvil cell preparation for high pressure experiments, including diamond, cell and gasket selection, cryogenic and gas loading methods for different gas and gas mixtures a variation of pressures. Section 3.2 concerns the resistive heating and laser heating techniques used in the contributing work. 3.3 introduces pressure markers, such as ruby fluorescence, diamond edge scale, the CH_4 vibron gauge to determine pressure in this work. Section 3.4 shows experimental details in the aforementioned three systems.

Chapter 4 presents results on the phase diagram of CH_4. Section 4.1 is about the rich phases of CH_4 under high pressures, initially presenting the fluid phase and moving through to the high pressure phase at room temperature. Section 4.2 examines the phase diagram under 10 GPa and further explores the phase diagram up to 60 GPa and 1200 K. Section 4.3 investigates phase A of CH_4 up to 178 GPa under both room temperature and elevated temperatures to study the sluggish phase transition from phase A to phase B.

Chapter 5 investigates rare gases and their binary mixtures. 5.1 is about the novel van der Waals compound $XeAr_2$ synthesized in the Xe-Ar system and its structure as determined by synchrotron x-ray diffraction. 5.2 presents Raman spectroscopy studies on the Xe-Ar system. Section 5.3 shows our first principles DFT calculation on the Xe-Ar binary system.

Chapter 6 presents the main results of nitrogen-trifluoride (NF_3) under extreme conditions. Section 6.1 gives synchrotron x-ray diffraction results on NF_3 under high pressure. Section 6.2 presents Raman spectroscopy studies on the N-F system. In particular, we explored the phase diagram of NF_3 under low temperature and high pressure. Section 5.3 shows our first principles DFT calculation on the NF_3 system.

Conclusion Chapter summarises and draws together the main conclusions from the contributing studies on the three systems and presents ideas for future work.

Chapter 2

Background Theory

This chapter contains a brief background theory on Raman spectroscopy and X-ray diffraction used in this work. Section 2.1 gives a general background theory of Raman spectroscopy from both classical and quantum mechanical standpoints. Section 2.2 delves into the high-pressure Raman setups employed throughout this study. Section 2.3 elaborates on the fundamental principles of diffraction and crystallography. Lastly, Section 2.4 introduces the primary tool employed for determining crystal structures within DACs under high-pressure conditions, namely synchrotron x-ray diffraction.

2.1 Raman Spectroscopy

2.1.1 Introduction

Optical spectroscopy has been widely used to characterise atoms and molecules and to study chemical or physical properties qualitatively or quantitatively since the early 20th century.

A brief review of some relevant light-matter interactions with energy and wavelength range are presented in Figure 2.1 from microwaves up to x-ray spectroscopy. Based on the interactions of radiation and matter, optical spectroscopy can be classified into emission, absorption and Raman scattering.

Excited atoms and molecules can decay to lower energy levels by emitting

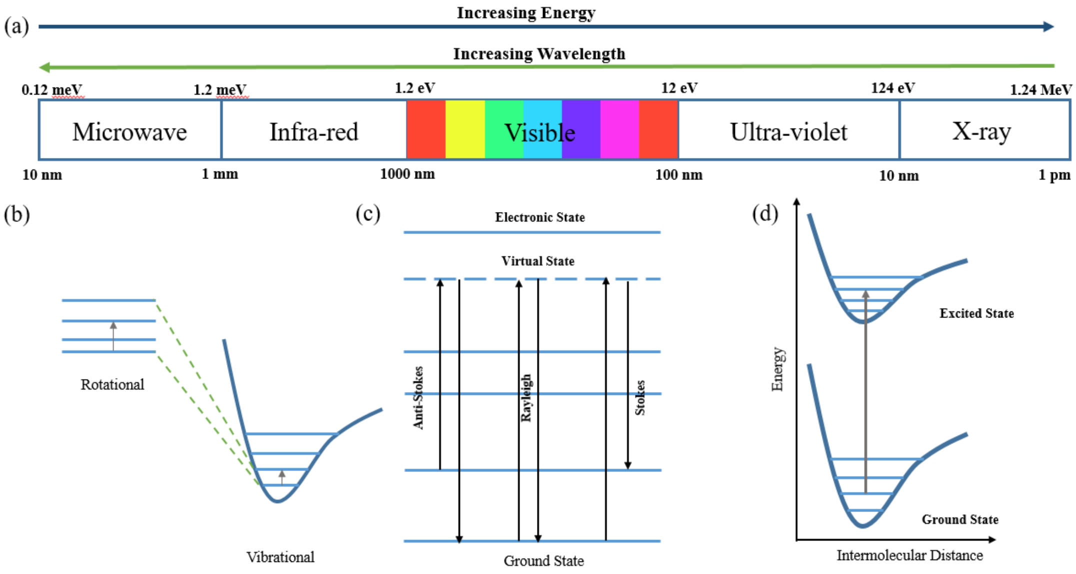

Figure 2.1 *(a) Electromagnetic spectrum with energy ranges from low energy to high energy. (b) Low energy vibrational and rotational transition (c) Energy diagram detailing transitions for Rayleigh, Stokes and anti-Stokes scattering. These virtual transitions are higher in energy than vibrational transitions, but lower energy than electronic transitions (d) High energy electronic transitions.*

radiation. By measuring photons with distinct energy levels, it becomes possible to determine the concentration of analyte atoms or molecules. One illustrative technique is atomic emission spectroscopy (AES), which utilises the heat of a flame to disrupt intra-molecular bonds, resulting in the generation of free atoms. Each element emits characteristic light with a certain wavelength, which is dispersed by a grating and detected in the spectrometer. In the spectrum, the wavelength of the atomic spectral line gives the identity of the element, while the intensity is proportional to the number of atoms of the element.

Absorption spectroscopy has been widely used in analytical chemistry to determine the presence of a certain substance in a material and to test the amount of the substance present quantitatively. When a continuous radiation light passes through a material, those energies which lie close to certain transitions will be absorbed as they excite those transitions. The highest energies lie in the UV-Visible range and are electronic transitions. Molecular vibrations have lower energies and are responsible for infra-red absorption, while rotations have the lowest energies and can be excited by microwave region radiation (See Figure 2.1).

In 1923, Smekal predicted that a system of quantised energy states would inelastically scatter incident radiation with shifted frequency, known as the Raman effect [108]. Raman scattering was proved experimentally by two individual groups in 1928; Landsberg and Mandelstam discovered Raman scattering in crystals (quartz and calcite), while C.V. Raman and K.S. Krishnan observed the Raman effect in liquids and gases[109, 110]. Crude instrumentation was used by Sir Raman to observe Raman scattering in 1928: sunlight as light source, telescope as collector and eyes as detector[111]. With the development of modern, powerful laser and sensitive charge-coupled devices (CCD), high-resolution Raman spectroscopy has been widely used in chemistry, materials, Earth and planetary science.

Raman Spectroscopy was used as the main diagnostic in this work as it can provide a great wealth of *in-situ*, easily analysable information. A broad spectrum of excitations can be simultaneously investigated at various energy levels, facilitating the measurement of a material's elastic, vibrational, electronic, and magnetic characteristics. Furthermore, the Raman spectra of phonons exhibit exceptional selectivity, making them sensitive indicators of a material's composition, state, and phase transitions. These properties are particularly responsive to alterations in pressure and temperature.

2.1.2 Theory of Raman Scattering

In Figure 2.1(c), When a beam of monochromatic radiation with frequency ν_0 illuminates transparent gas, liquid or solid, 99.999999% of the scatterings are elastic (Rayleigh Scattering, ν_0) while a small part of them (less than 0.000001%) are scattered which change both direction and frequency (Stokes and Anti-Stokes scattering, ν_M). After inelastic scattering, the energies of the emitted photons are of either lower or higher energy than the incident photon and the molecular is in vibrational and rotational states. Raman excitations at frequencies lower than the Rayleigh band are referred to as Stokes lines (ν_0-ν_M), and the symmetrical higher frequency excitations are anti-Stokes lines (ν_0+ν_M). Raman spectrum plots intensity as a function of frequency in units of reciprocal centimetres, relative to the energy of the incident radiation (rel cm^{-1}). By analysing the characteristic vibrational and rotational information, the molecules in the system can be determined. Raman effect can be explained by classical theory and quantum mechanics.

Classical Theory

Classical theory can also be used to explain Raman scattering. At ambient conditions, the electrons are equally distributed in homo-nuclear diatomic molecule without permanent dipole or dipole change, which make them IR-inactive. However, when an electric field is applied to the molecule, the dipole moment, u_{ind} is proportional to the applied electric field strength, E and the polarisability of the molecule α:

$$u_{ind} = E\alpha \tag{2.1}$$

The proportionality constant which relate to the properties of molecules and the scattering medium can be affected by external electric field. In any non-spherical molecule the polarisability is described by a tensor as it depends on the atomic coordinates, but in this case is considered as a scalar. The polarisability of a molecule therefore depends on the electronic distribution. The intensity of the dipole moment itself is affected by the electric field strength. Consider the strength of electric field as E, so the incident electromagnetic wave is:

$$E_t = E_0 \cos(2\pi\nu_o t) \tag{2.2}$$

where E_0 is the vibrational amplitude and ν_0 is the frequency of laser. By substituting equation 2.2 to equation 2.1, one can get the equation for induced dipole moment:

$$u_{ind}(t) = \alpha E_o \cos(2\pi\nu_o t) \tag{2.3}$$

Where α is the proportionality constant and called polarisability. If a molecular is vibrating with frequency of ν_M,the nuclear displacement q can be written:

$$q = q_0 \cos(2\pi\nu_M t) \tag{2.4}$$

where q_0 is the vibrational amplitude. For a small vibration of molecule, polarisability α has a linear function of q:

$$\alpha = \alpha_0 + (\frac{\partial\alpha}{\partial q})_0 q_0 + \ldots \tag{2.5}$$

Where α_0 is the polarizability at equilibrium position and $\dfrac{\partial\alpha}{\partial q}$ is the change of α to the change of q. By combining equation 2.3, 2.4, 2.5 and trigonometry:

$$u_{ind}(t) = \alpha_o E_o \cos(2\pi\nu_o t) + \frac{1}{2}(\frac{\partial\alpha}{\partial q})q_0 E_o[\cos 2\pi(\nu_o + \nu_M)t + \cos 2\pi(\nu_o - \nu_M)t] \tag{2.6}$$

In equation 2.6 the first term contains Rayleigh scattering contribution, v_o. The second term comes from Raman Stokes scattering, $v_o - v_M$ and Raman anti-Stokes scattering $v_o + v_M$. If $(\dfrac{\partial\alpha}{\partial q})_0$ is zero, the vibration is Raman-inactive. To be Raman-active, the rate change of polaribility with the vibration must not be zero.

Figure 2.1(c) illustrates energy diagram in terms of simple diatomic energy level. Under ambient conditions, the population of molecules in the ground state is much larger than that in the excited vibrational state. Consequently, Stokes lines are stronger than the anti-Stokes lines.

Quantum Theory

Classical theory is a good example of light-matter reaction by relating molecule polaribility with electric field. However, some characteristics such as intensities of scattered photons and the origin of the selection rules can not be explained by classical theory[112]. In this case, quantum theory can be used to explain the nature of Raman effect.

Figure 2.1(c) is the energy-level diagram of Rayleigh, Raman stokes and anti-stokes scattering. The energy of virtual states are higher than vibrational transitions, but lower than electronic transitions. When photon at ground state get excited to a higher energy level or an unstable virtual state, it can return to lower energy level states in one of the three possible ways:

1) Rayleigh scattering: the excited photon returns to its original state with same energy, ν_o.

2) Stokes scattering: the excited photon returns to a higher energy level with lower energy, $\nu_o - \nu_M$. The Raman spectrum lines at lower frequencies.

3) Anti-stokes scattering: the excited photon returns to a higher energy level with higher energy, $\nu_o + \nu_M$. The Raman spectrum lines at greater frequencies.

Apart from the origin of selection rules, quantum mechanics can also explain the differences between the intensity of stokes and anti-stokes. It is well known that in Raman spectra at room temperature, the intensities of anti-stokes are much lower than that of stokes. By introducing Boltzmann distribution of vibrational populations, the intensity ratio of Raman anti-Stokes to Stokes radiation[113]:

$$\frac{I_{aS_t}}{I_{S_t}} = \frac{(\nu_o + \nu_M)^4}{(\nu_o - \nu_M)^4} e^{\frac{-h\nu_M}{k_B T}} \tag{2.7}$$

where ν_0 and ν_M are the frequencies of the incident radiation and the molecular vibration respectively, k_B is the Boltzmann constant, h is the Planck constant, T is the absolute temperature of the molecular. By rearranging temperature, one can get:

$$T = \frac{\frac{h\nu_M}{k_B}}{ln(\frac{I_{aS_t}}{I_{S_t}}) + ln(\frac{I_{aS_t}}{I_{S_t}})_0 + \frac{h\nu_M}{k_B}} \tag{2.8}$$

From equation 2.7 and 2.8 we can find that the intensity of the Raman anti-Stokes increases with increasing temperature, therefor anti-Stokes to Stokes ratio can be used as temperature marker in high temperature experiments. For example, Raman spectra of liquid hydrogen and deuterium have been collected in diamond anvil cell as a function of temperature at 3 GPa covering the range from 80 to 1000 K[114].

2.2 High Pressure Raman Setup

Section 2.1 provides background theories of Raman spectroscopy. This chapter gives details on the micro-focused Raman setup used in this work. The components of the experimental setup will be described following the path of the laser from its source to the detector.

In the contributing work, we used gas lasers (Argon, 514 nm and Krypton, 647 nm) and solid-state (532 nm) lasers to excite the samples. Figure 2.2 shows the diagram of the micro-focused high pressure Raman setup used in this work. The laser first passes through the holographic band pass filter (BPF) to reject the undesired wavelengths from the excitation lines. The BPF reflects the laser beam by 90 ° with only about 2 % of intensity loss. Two high reflective silver mirrors were used in the contributing Raman setups. The first mirror was used to redirect the incident beam and the second one was used to elevate the height of the beam.

To increase its diameter, the filtered beam undergoes expansion through an expander/collimator assembly comprising expanding and converging lenses. This setup employs a negative focal length objective lens in conjunction with a positive focal length image lens. The absence of an internal focal point renders this Galilean beam expander particularly well-suited for high-power laser applications.

A filter wheel (revolver-type attenuator) reduces the laser beam when necessary, for example, when we are measuring the pressure using ruby fluorescence pressure scale.

Two mirrors (M_1 and M_2) in a "Z" configuration direct the beam to a holographic notch filter (NF_1). This notch filter has two functions: for the incoming beam, it works as a mirror to redirect the beam into the Mitutoyo objective; for the light scattered by the sample, it works as a rejection filter to suppress elastically scattered components. The Mitutoyo objective works in a back-scattering mode - it focuses the incoming laser beam on the sample and collects the scattered light with sample information. There are a variety of objectives with various magnifications, ranging from x10 to x50. In the contributing work, we used two interchangeable objectives with different magnifications: x20 was used for high temperature experiments at pressures below 70 GPa while x50 was used for multimegabar pressure at room temperature.

The two beam-splitter cubes installed between the notch filter and the Mitutoyo objective are used when aligning the sample before spectra acquisition. During data collection, BS1 and BS2 are removed, and both front and back lights are switched off to minimize elastic scattering. This design enables visible observation of the sample, facilitating the detection of phase transitions, melting, and the assessment of the sample's mechanical stability under load.

The backscattered light passes through the NF_1 notch filter again, and the image of the sample is projected onto the object diaphragm (pinhole), which works as a spatial filter to reject stray scattering. The image of the pinhole is focused onto the entrance slit of the spectrometer. There is a series of additional notch filters (NF_2 and NF_3) between the pinhole and the spectrometer which further suppress the elastic component.

The signal is then focused into the spectrometer and finally imaged by a Princeton Instrument's array CCD. Coherent Innova 70-C Ar^+ and Innova

300-C Kr$^+$ ion lasers were used with Princeton Instruments Acton SpectraPro 2500i spectrometers in tandem with Princeton Instruments 7500-0003 CCDs, outputting to computers using LightField software. Coherent 532 nm Verdi solid-state lasers were used with Princeton Instruments Iso-Plane SCT-320 spectrometers in tandem with Princeton Instruments PyLoN CCDs, connected to computers running Princeton Instruments Light-Field. For this work, the green (514 nm, Argon) laser was used for all the high temperature experiments as the CCD drops in quantum efficiency at longer wavelengths. However, a red laser (647 nm, Krypton) was used for multimegabar experiments to avoid the enhanced fluorescence from the diamond anvils. Data were exported and then analysed by Fityk and Origin 2019 software packages [115].

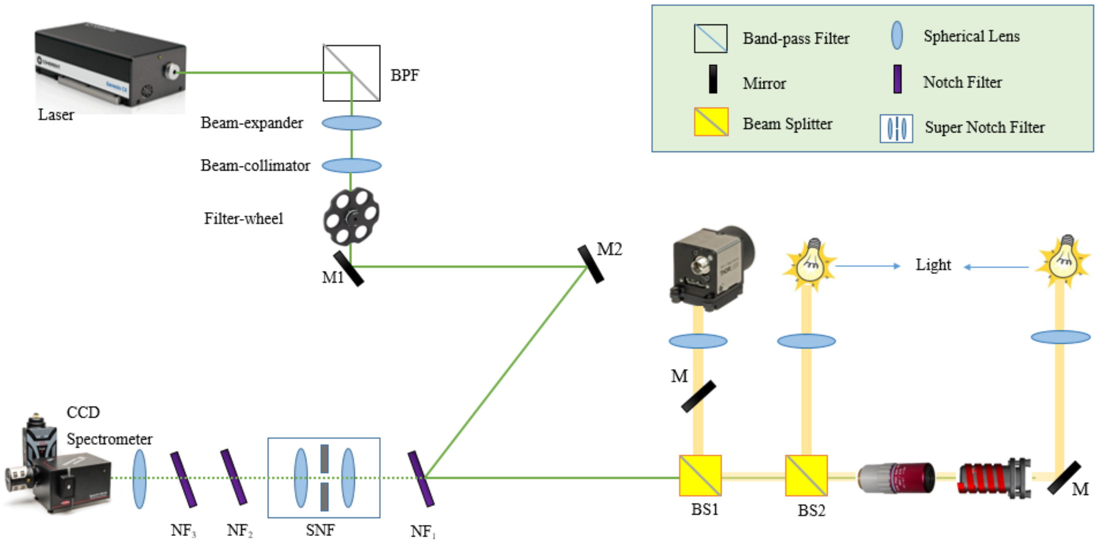

Figure 2.2 *Diagram of the micro-focused high-pressure Raman setup.*

2.3 X-ray Diffraction

As a versatile method for the determination of the crystal structure, X-ray crystallography is widely used in chemistry, physics, biology and engineering. In this work, we employ synchrotron-based X-ray diffraction to explore the high pressure behavior of the Xe-Ar system and nitrogen-trifluoride (NF_3). This section provides a concise introduction to X-ray diffraction (XRD), focusing on its fundamental theory, especially in the context of powder diffraction. Additionally, we explore the implications of utilising synchrotron-based x-ray diffraction in diamond anvil cell.

X-ray diffraction was first discovered by Max von Laue in 1912 when he observed that crystal can work as a three-dimensional grating to diffract x-ray (Nobel Prize in physics in 1914) [116]. It was further developed by W. L. Bragg and his father W. H. Bragg, in 1915 by conducting x-ray diffraction analysis on single crystals (Nobel prize in physics in 1915) [117, 118].

To obtain structural information about a material at the atomic and molecular level, the x-ray radiation wavelength needs to be comparable to the period of the crystal lattice. In present synchrotron powder x-ray diffraction experiments, monochromatic synchrotron radiation with energies between 30 and 45 keV was used.

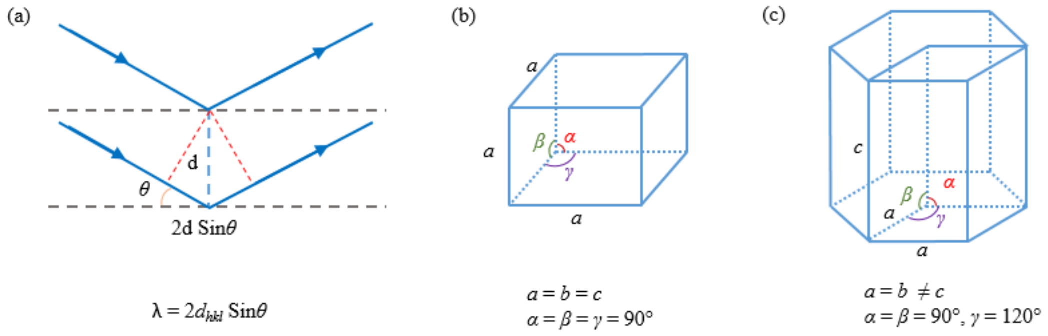

Figure 2.3 *(a). The scattering conditions for x-ray diffraction. (b). diagrams of cubic crystal structure, described by the lengths (a, b, c) and angles (α, β, γ) of the unit cell volumes. (c). diagrams of hexagonal crystal structure, described by the lengths (a, b, c) and angles (α, β, γ) of the unit cell volumes.*

2.3.1 Diffraction Conditions

X-rays interact and can be scattered by solid matter in different ways. In many cases, solid materials exhibit a crystalline atomic arrangement characterised by long-range order and translational symmetry in all three spatial dimensions. These crystals can be described as an array of unit cells that repeat infinitely, each containing symmetrically equivalent atoms or molecules. The entire crystal structure is described by specifying the unit cell, its interior and the symmetry operations of the lattice.

Figure 2.3 (a) depicts the scattering conditions for x-ray diffraction. When a monochromatic radiation x-ray beam is incident at an angle (θ) on a series of planes of ordered arrays of atoms, the waves are scattered from lattice planes separated by the distance d between different layers of atoms. X-ray diffraction can be observed under the Bragg condition [117]:

$$\lambda = 2d_{hkl}\sin\theta \tag{2.9}$$

where λ is the wavelength of the monochromatic beam, d_{hkl} is the interplanar distance corresponding to the reciprocal lattice vector (h,k,l), and θ is the corresponding incident angle. h, k and l are called the Miller indices of a given (hkl) plane.

Figure 2.3 (b) shows the cubic crystal where $a = b = c$ and $\alpha = \beta = \gamma = 90$ °, in which case the inter-planar distance d_{hkl} can be calculated by:

$$\frac{1}{d_{hkl}^2} = \frac{h^2}{a^2} + \frac{k^2}{a^2} + \frac{l^2}{a^2} \tag{2.10}$$

While for hexagonal crystal structure (see Figure 2.3 (c)), the interplanar distance can be described by the following equation:

$$\frac{1}{d_{hkl}^2} = \frac{4}{3a^2}(h^2 + hk + k^2) + \frac{l^2}{c^2} \tag{2.11}$$

Reflected waves meeting the Bragg equation have measurable intensity. In a typical diffraction experiment, the intensity of the scattered radiation is measured as a function of scattering angle 2θ. The peak positions contain the information about the interplanar spacings, and the intensities of the peaks depend on the content of the unit cell. By measuring the reflected intensity as a function of the incidence angle, one can obtain unique information about the orientations and interplanar spacings of atoms.

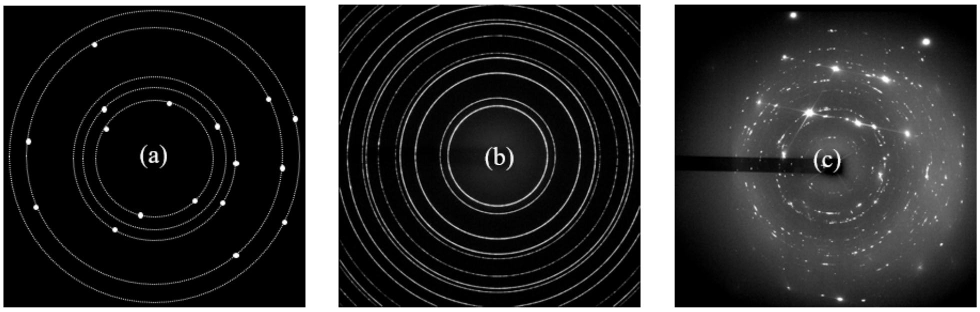

Figure 2.4 *Representative diffraction patterns of different materials: (a) a schematic diagram illustrating a typical single crystal diffraction pattern; (b) the good quality powder diffraction pattern of* CeO_2*; (c) an example diffraction pattern from this work, containing both powder diffraction Debye-Scherrer rings from* $XeAr_2$ *(see Chapter 5) and single-crystal diffraction spots from Xe (spots with lines in the middle) and diamond anvil (spots near the edges).*

2.3.2 Powder Diffraction and Rietveld Refinement

Figure 2.4 (a) is a schematic diagram illustrating a typical single crystal diffraction pattern. Figure 2.4 (b) is a good quality powder from CeO_2 standard under ambient conditions. In this work, the sample was not perfect single crystals (see Figure 2.4(c)). Thus, we did the azimuthal integration of the scattering intensity using the DIOPTAS0.5.5 software and treated the resulting structure factors as powder patterns [119]. Figure 2.5 shows the cake representation and the integrated profile of a standard pattern.

A powder sample can be treated as polycrystalline with randomly oriented crystals. Every plane of the polycrystalline meets the Bragg's Law. Instead of presenting the diffraction spots, the diffraction pattern of a powder sample is formed of different Debye-Scherrer rings. Due to the overlap of the diffraction peak positions with similar d - spacings, some important information, such as peak intensities, might lost/unreliable when the diffraction data is integrated into a 2D image. The aforementioned disadvantage of the powder sample makes it hard to accurately determine the space group and atom positions. Considering this disadvantage, structure refinement (Rietveld/ Le Bail refinement) is required to resolve the intensities for all the powder samples in this work.

To determine the lattice parameters of our materials, we utilised both Rietveld and Le Bail refinement methods, which are implemented in the POWDERCELL 2.4 software [120]. This method involves the calculation of a diffraction pattern based on a specified structural model. Subsequently, the structural parameters are systematically adjusted to minimise the disparity between the calculated and measured patterns.

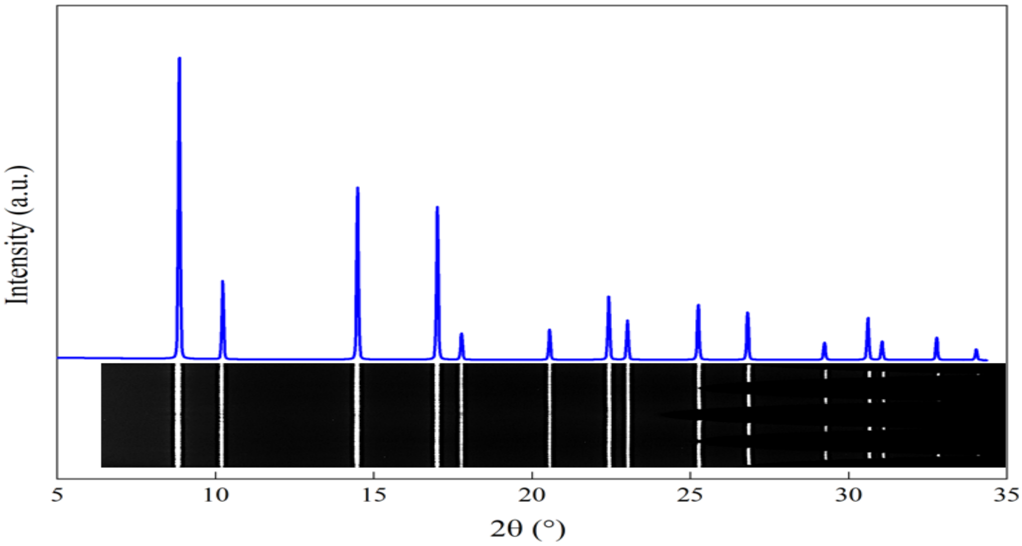

Figure 2.5 *Powder XRD pattern of* CeO_2 *at ambient conditions with its raw cake image* ($\lambda = 0.4828$ Å). *The XRD pattern was recorded at at P02.2 at PETRA-III using Perkin Elmer (XRD1621) detector.*

2.4 Synchrotron X-ray Diffraction

This section gives a brief introduction to the synchrotron radiation source and outlines practical considerations for conducting synchrotron XRD on samples contained in DACs.

As a powerful characterization method, x-ray diffraction has been widely used in obtaining crystal structure, chemical composition, and physical properties of materials. The appropriate selection of cell, diamond and seat type will be described in section 3.1.1. The seat and cell aperture limits the available range of scattering angles and the background of diamond anvil and heavy gasket material

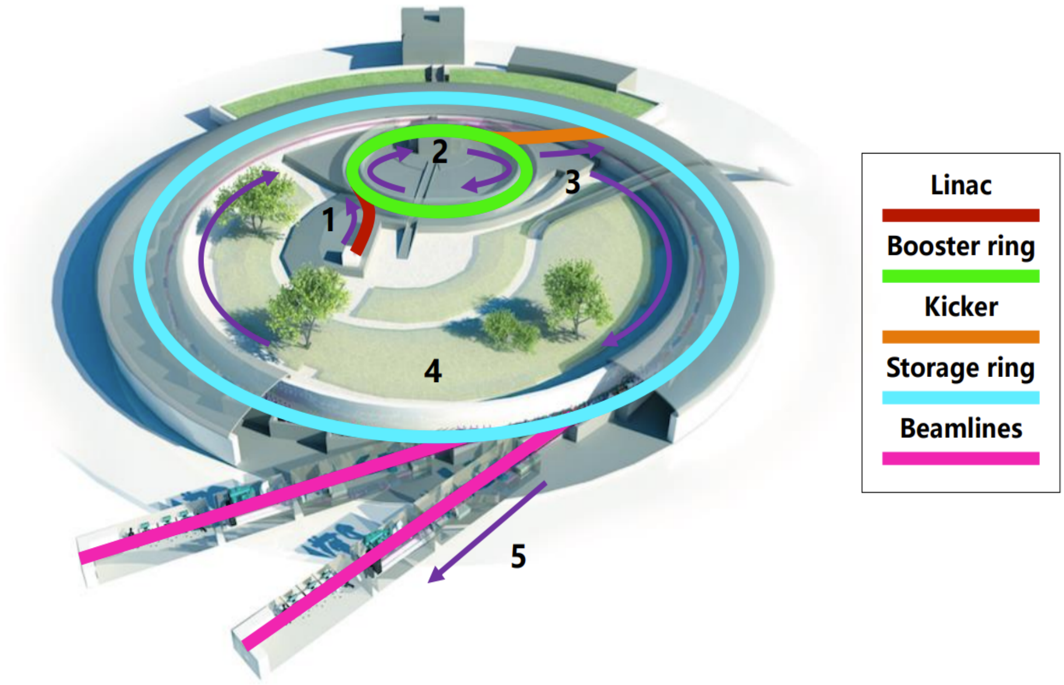

Figure 2.6 *A schematic of typical synchrotron showing layout of Linear accelerator, booster ring, storage ring and beamlines in ESRF.*

(Re, W and Os) makes it hard to measure light elements studied in the work. Taking these factors into consideration, powerful and intense synchrotron x-ray diffraction has been used in this work to provide structural information of the samples in DAC.

The most significant advantage of synchrotron radiation source over a laboratory x-ray radiation is its brilliance. Typically synchrotron source of a third generation such as ESRF has a flux which is about one billion times more brilliant than laboratory x-ray sources. The intense and highly focused radiation provide a window into molecular and atomic world and allow us to detect more structural details of our sample (particularly for light atoms).

The generation of intense x-ray synchrotron radiation is based on the principle that an accelerating charged particle emits electromagnetic radiation. Electrons need to accelerate in several stages to reach energy orders of billion electronvolts - GeV. Figure 2.6 shows the sequential path of electrons from generation (linear accelerator) to the storage ring in the European Synchrotron Radiation Facility. First, electrons are accelerated in a linear accelerator to gain certain energy before being injected into a circular booster ring. The booster ring works as a mini synchrotron source where electrons are further accelerated and attain enough energy (100 MeV to several GeV). This is realized by applying bending magnetic field towards the running directions of high speed electrons. The electrons are ready to inject to the main storage ring via kicker after gaining speed comparable to near relativistic speeds. The electrons circulate in the storage ring and pass through some insertion devices such as wigglers and undulators which bend electrons path and generate x-rays tangentially to the electron beam. X-rays then delivered via the different beamlines to various of experimental stations where different experiments are performed. Another useful feature of synchrotron source is the beam can be combined with other techniques, such as laser heating and resistive heating to conduct specific experiments *in-situ*.

There are over 70 synchrotron facilities worldwide in various stages of development, each with different power and sizes. Different beamlines in the synchrotron radiation sources have various configurations. However, the general procedure for conducting DAC experiments in synchrotron light source is similar: first mount the diamond anvil cell onto a goniometer and then align the sample to the centre of the beam with transmission scans. Before conducting x-ray diffraction measurements, a diffraction pattern of a well-studied compound such as CeO_2 or LaB_6 is usually obtained as calibration file to provide parameters such as the exact photon wavelength, distance between detector and sample, to accurately integrate the experimental data. Figure 2.5 shows the calibration diffraction pattern of a CeO_2 sample.

In this work, powder X-ray diffraction data were collected at the following beamtimes: ID15B at ESRF (France; 0.4101 Å), P2.02 at PETRA III (Germany; 0.4828 Å), GSECARS at Advanced Photon Source (United States; 0.3344 Å), and 10XU at the SPring-8 (Japan; 0.4141 Å)[121], incident beam energies in the range 25–30 keV were used. Pressure was determined from the equation of state of Au [122] and crosschecked with the ruby fluorescence [123]. Calibration of the sample-detector distance, primary processing, integration and background subtraction were performed using the DIOPTAS 0.5.5 software [119]. The Rietveld refinements were done in POWDERCELL 2.4 program [120] and the equations of state data were determined using EosFIT7 [124].

Chapter 3

High Pressure and High Temperature Techniques

In this chapter, high pressure and high temperature techniques used for the contributing work will be described. The first section is the diamond anvil cell, including underlying principles of diamond anvil cell preparation for high pressure experiments, cryogenic and gas loading methods for different gas and gas mixtures. Section 3.2 shows high temperature resistive heating technique. Section 3.3 explains experimental details on high temperature laser heating technique and time-resolved Raman spectroscopy used in this work. Section 3.4 provides various of pressure and temperature markers, such as ruby fluorescence, diamond edge scale and CH_4 vibronal pressure gauge. Section 3.5 discusses the experimental details in three systems of the contributing work.

3.1 Diamond Anvil Cell

A brief review of high pressure science and DAC can be found in section 1.1. Figure 3.1 shows the schematic of DAC. Modern DAC is designed in a very straightforward principle: uniaxial force is applied on the back of two opposite diamond anvils that are compressing a sample contained in a metal gasket.

Since pressure is force per unit area, a pressure comparable to that in the planetary cores can be generated using a modest application of force to a small area.

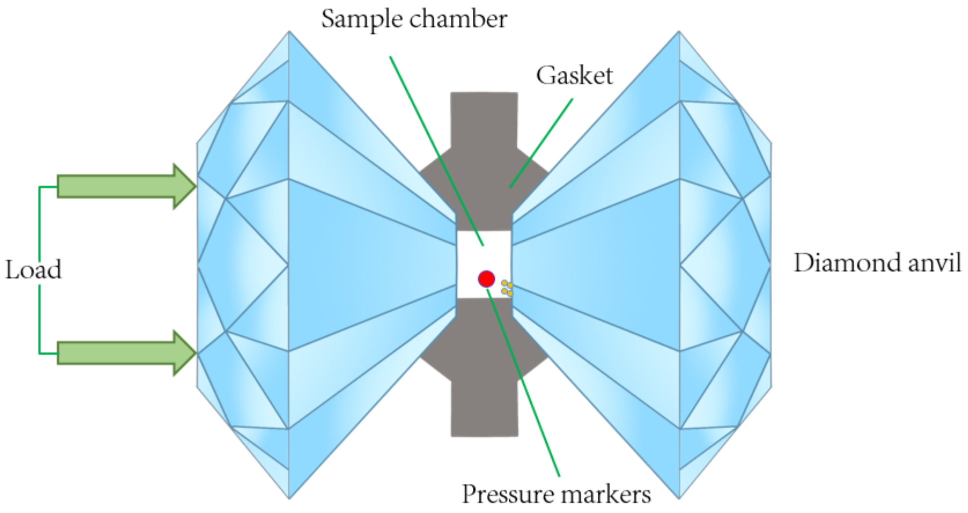

Figure 3.1 *A schematic illustration of the basic operating principle in diamond anvil cell with pressure markers (Au and ruby) in the sample chamber.*

Modern design of DAC allows not only to reach pressures of hundreds of GPa but also simultaneously vary the temperature by using a cryostat and laser/resistive heating techniques. The portable size of DAC makes it easy to conduct *in-situ* measurements in the laboratory. Due to the transparency property, diamond anvils provide good windows for optical and x-ray measurements.

3.1.1 Diamond Anvil Cell Preparation

Cell Selection

There are varieties of DAC designs available for different purposes. In the contributing work, high-temperature Mao–Bell cell and GG-symmetrical cell were used for conducting Raman spectroscopy and XRD experiments respectively (Figure 3.2 (a) and 3.3 (b)).

GG-type symmetrical cells were used for room temperature Raman and XRD measurements. The four guide posts design makes it easy to load cryogenically, and the wide opening benefits X-ray diffraction. The Mao–Bell cell offers distinct advantages over the GG-symmetric cell due to its piston-cylinder design, which ensures a tighter fit and superior alignment, especially at elevated temperatures. For high temperature experiments, our customised Mao-Bell cell was enhanced with external and two internal heaters, along with three thermocouples for precise temperature monitoring.

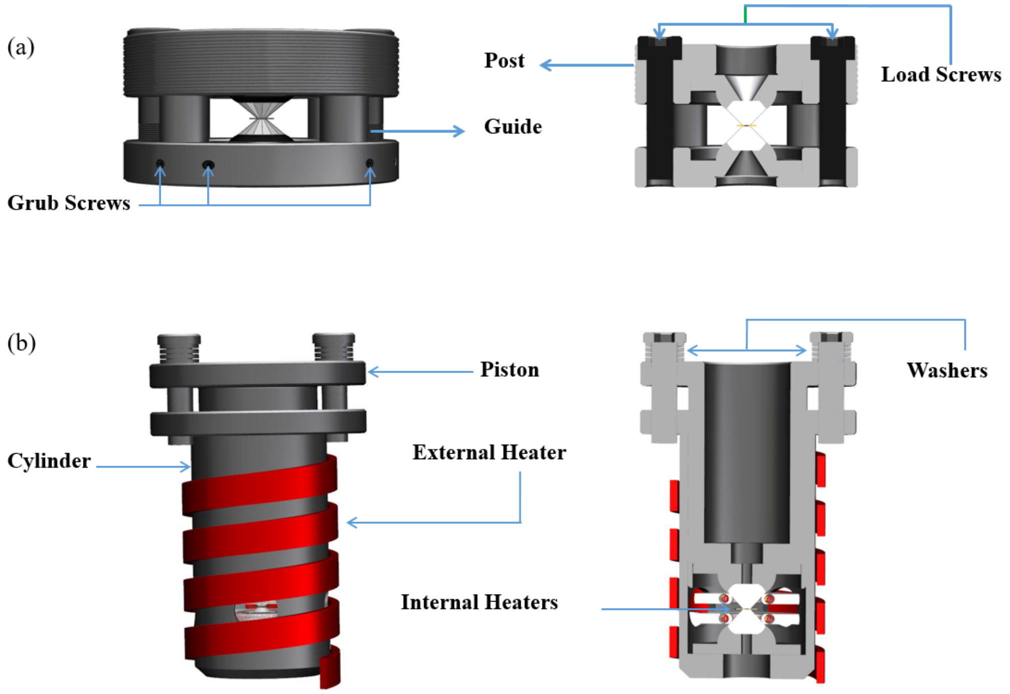

Figure 3.2 *(a) Schematics of GG-symmetric cell design used for room temperature experiments. (b) schematics of Mao-Bell cell design used for high temperature experiments.*

Diamond and Seat Selection

Diamond selection depends on the target pressure. Diamonds with large culet are used for relatively low pressure, while smaller ones are used for higher pressure. Normally with flat-culet 200 μm diamonds, pressures up to 60 GPa are reachable, with a maximum pressure of 100 GPa is possible for 100 μm bevelled culets. Higher pressure can be achieved by double-bevelled diamonds. Various factors should considered when choosing diamonds and seats for particular experiments. For Raman experiments, low-fluorescence diamonds need to be used where possible to minimise the background-to-signal ratio. For X-ray diffraction measurements, a large opening angle from the back side of the diamond (table) through the seat is desired to maximise the scattering angle. Diamonds with a culet size of 200 μm were used for both Raman and XRD experiments, which allowed us to reach pressure up to 50 GPa. Diamonds were glued into *Boehler-Almax* (BA) tungsten-carbide seats using a thermally conducting Stycast epoxy.

When gluing diamonds to the seats, it is important to ensure that the culet of the diamonds is parallel to the seats.

DAC Alignment

The critical stage in DAC preparation is the alignment of the culets. Ensuring the precise alignment of the diamond culets not only prevents mechanical failures of the diamonds but also enables the attainment of higher pressures. Initially, one culet with a diamond is securely affixed to the centre of the piston using four precisely adjusted grub screws, the other seat with a diamond is then fixed slightly to the center of the cylinder. Bring piston and cylinder parts close carefully by using four load-screws and two set-screws. Once two parallel culets get close enough (normally within a few microns), as monitored under a microscope, flap the cell and align four screws of the cylinder part until the two culets overlap completely. The whole alignment process needs to be done under a microscope to make sure diamonds are in a safe distance.

Gasket Selection

Rhenium and tungsten are widely used in high pressure science as gasket materials. The bulk modulus for rhenium and tungsten are 370 GPa and 460 GPa, respectively [125, 126]. Rhenium foil of 200-300 μm thicknessis used as gasket material in the contributing work at room temperature. It is widely recognised that rhenium reacts with hydrogen at pressures exceeding 5 GPa, leading to the formation of rhenium hydrides even at room temperature [125]. In our investigation of CH_4 high P-T phase diagram, we employed osmium as the gasket material at high temperatures to minimise the formation of hydrides. Osmium has a higher bulk modulus compared to rhenium and reacts with hydrogen at much higher pressure (39 GPa), which may reduce sample loss even at elevated pressure and temperatures. A recent high pressure study has further revealed that osmium does not form any polyhydrides until 186 GPa [127].

For gasket preparation, a small rhenium sheet is first pre-indented by the two well-aligned anvils to make a thin indentation. A ruby sphere is placed in the center of the indentation and compressed to around 25 GPa, which gives a thickness of 25 μm - 30 μm for 200 μm culets [128]. The depth of the sample chamber (gasket thickness) is measured using interferometry, normally 1/10 to 1/5 of the diamond culet diameter [128]. When white light passes through the diamond anvils, it generates an interference pattern with maxima occurring wherever an integer number of wavelengths fit within one length of the cavity. The periodicity of the fringe is shown in Figure 3.5 (c) and can be expressed by the following equation:

$$d = (2n\Delta\nu)^{-1} \tag{3.1}$$

Where sample thickness d can be calculated by the refractive index of the cavity (n) and wavenumbers (ν). A culet sized hole was drilled in the center of the indent with a laser-drilling system. A culet-sized hole was drilled in the center of the indentation using a laser-drilling system. The hole was subsequently filled with Osmium powder and re-indented to 25 GPa before drilling a 50 % culet-sized hole as the sample chamber for high temperature experiments.

3.1.2 Gas Loading and Cryogenic Loading

The samples were loaded into the DAC using a high pressure gas loading system combined with cryogenic loading technique. A description on the high pressure gas-loading system design was given by Mills *et al.* [129]. The DAC is placed in a sealed bomb with a well-calibrated gear box. CH_4 (BOC, 99.9 % purity) is compressed to 2000 bar in the vessel by a three-stage compressor. Once pressure reached 0.2 GPa, the DAC is closed through the gear system by the handle outside the bomb. Gas loading method was used for the contributing work on CH_4.

Cryogenic loading was used to load Xe in the contributing work. The entire cryo-loading process for Xe was performed in a sealed glove-bag with nitrogen atmosphere. The cell was well-calibrated and marked before mounting into a v-block in a polystyrene container. One low temperature thermocouple was attached in the cell to monitor the loading temperature throughout the whole loading process. Purging the glove-bag with nitrogen gas three times to ensure a nitrogen atmosphere before filling liquid nitrogen to the level of the seats in the container. The Xe cylinder was connected to a hose and nozzle via a corrosion resistant regulator, and fed through the glove-bag wall. Once the melting point (161.4 K) of Xe reached, the Xe in nozzle is condensed on the culets of cold diamonds. Close the cell with the four calibrated screws to the markers and warm the cell up slowly to room temperature. High purity Argon was subsequently gas loaded into the same sample chamber at 0.2 GPa, partially substituting Xe. Raman spectroscopy was initially used to rule out possible contamination after sample loading and to identify compound formation.

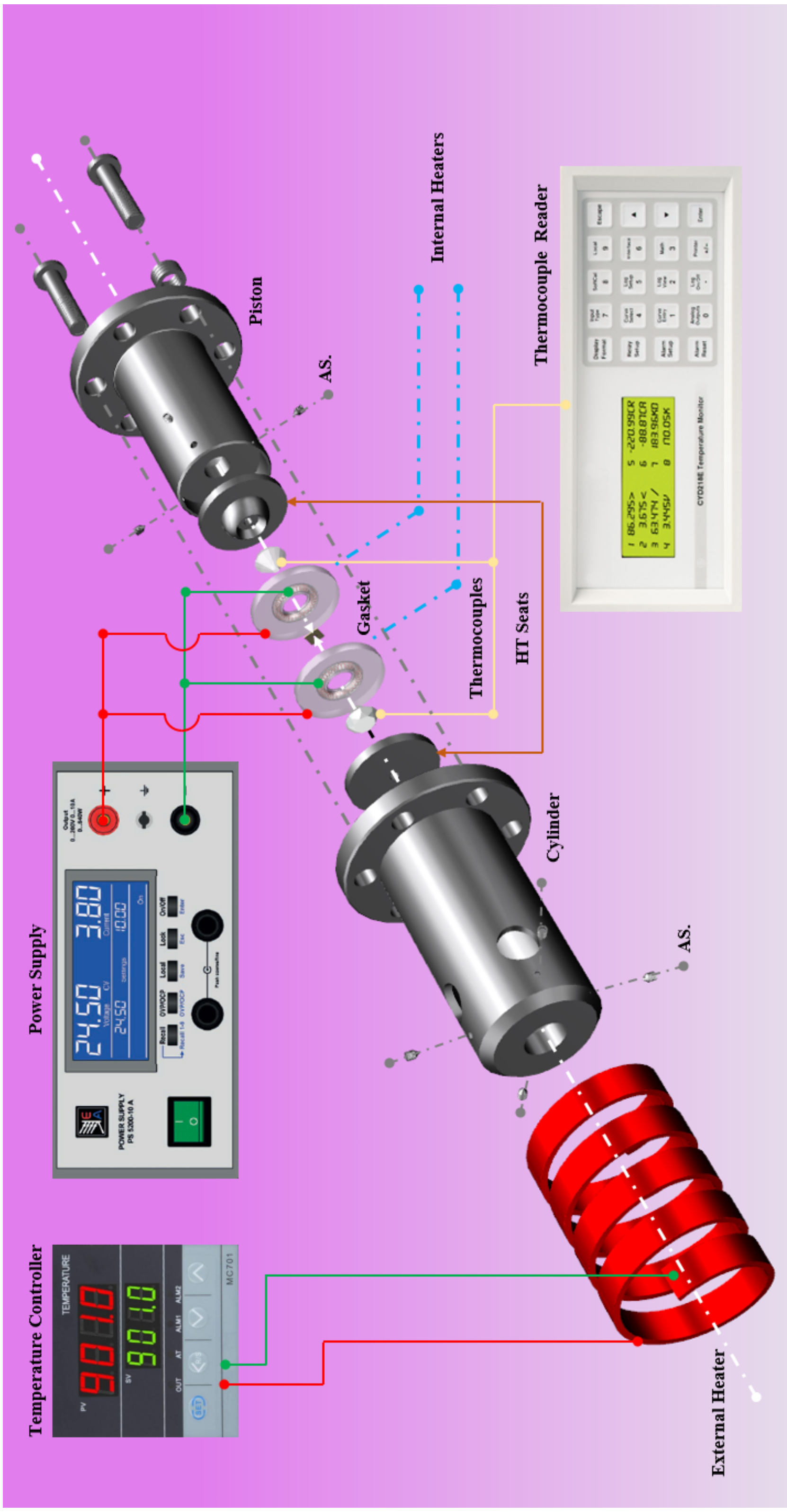

Figure 3.3 *Exploded diagram of a modified Mao-Bell diamond anvil cell (DAC) used in high-temperature high-pressure studies.*

3.2 Resistive Heating and Laser Heating Techniques

3.2.1 Resistive Heating Technique

Well-established laser heating and resistive-heating techniques have been widely used in high pressure science to obtain high temperature in DAC [80, 130, 131]. External-resistive heating was used in the contributing work as an efficient simple technique with a high accuracy within the laboratory.

Figure 3.3 shows the schematic diagram of resistive-heating of high temperature Mao-Bell DAC equipped with a primary and two secondary heaters attached with thermocouples. Primary heater heats up the whole cell body and gives temperature above 500 K (the temperature could be higher when coupled with water cooling system to protect the Mitutoyo objective). Two secondary heaters were attached to two seats in the culet level of the diamonds to provide higher temperatures. Typically, this setup can give us temperature above 1000 K with an accuracy of ± 10 K in DAC.

For high-temperature experiments, diamonds need to be attached to special high-temperature seats designed to accommodate internal heaters. To enhance temperature measurement accuracy, two thermocouples are epoxied to both diamonds (see Figure 3.4 (b) for placement). Figure 3.4 (a) shows the construction of our built in-house internal heater. The heater itself is made of a Pt element, a material chosen for its desirable high-melting temperature (2041.4 K) whilst low oxidation. The heating element is coiled around a 8 mm diameter Al_2O_3 ring and tightly wound around platinum tubes to provide ports for electrical probes so that it can driven by a DC power supply. The heating element is then set in high-temperature cement and a pyrophyllite ring, providing thermal insulation as well as preventing oxidation of the heating element and premature failures. Unlike disposal molybdenum and tungsten heaters, Pt-coiled heater can be reused for high temperature experiments. Two secondary heaters are identical and pre-tested before placing in the cell to provide a rough temperature range for high temperature experiments.

We used either two type-K thermocouples, for experiments up to 800 K or two type-R thermocuples, above 800 K. Good mechanical contact ensures a more accurate temperature measurement, while ensuring optimum proximity to the sample chamber. Heating was done in two stages: the primary heater, external to the cell assembly, heated the entire cell body to 500 K (Fig. 3.4(c)). It was driven by a DC power supply on a feedback loop with a high sampling rate proportional–integral–derivative (PID) controller. Additionally, there were two secondary internal heaters situated around the diamond anvils, which heated to temperatures above 1200 K. These internal heaters were controlled by manually adjusting the voltage supplied to them.

Two thermocouples on the culets and one additional thermocouple in the primary heater allow us to guage thermal gradients, and assess the accuracy of the measurements which was typically found to be of the order of $\sim$ 10 K [132]. Additional thermocouples was inserted into the primary heater, used as a feedback to control the operation temperature of the power supply.

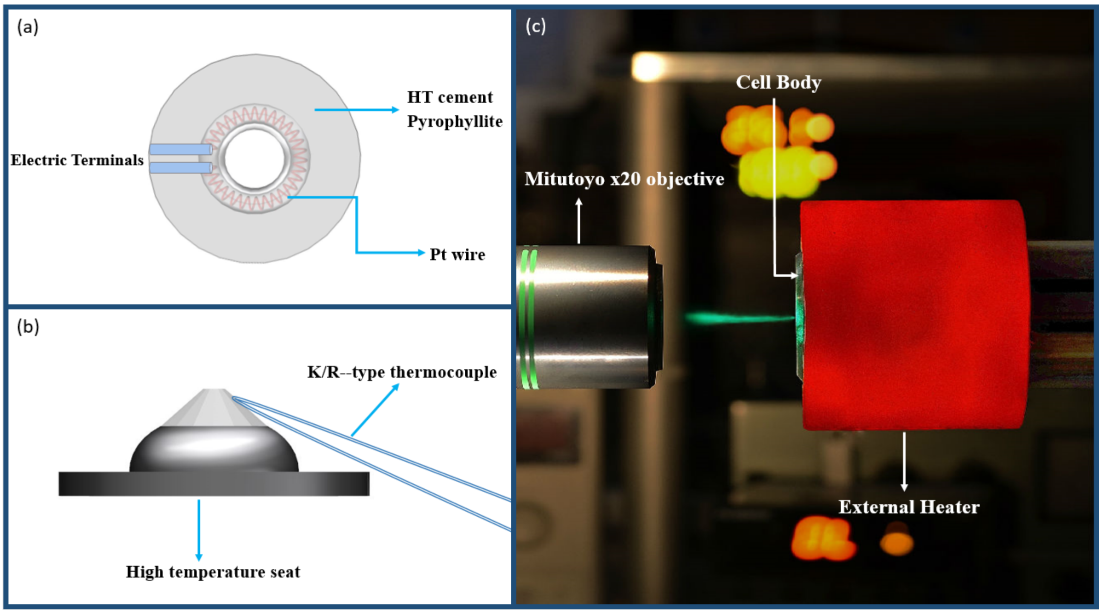

Figure 3.4 *(a) Schematic of the internal heater used in the high temperature* CH_4 *phase diagram experiment. (b) A diagram demonstrating the diamonds and thermocouple positions. (c) A picture of a micro-focussed Raman experiment of* H_2 *at 600 K and 150 GPa [5].*

3.2.2 Laser Heating Experiment and Time-resolved Raman Spectroscopy

Ag foil is used as an absorber (coupler) of infrared radiation from a heating laser. The coupler is isolated from the diamonds by a 0.1–0.2 μm thick insulation layer of Al_2O_3, proven not to react with hot methane.[84] The sample was heated from both sides with 200 W fiber laser operating in continuous wave mode (λ 1.07 μ) focused to the coupler hole region using a Mitotoyo M Plan Apo NIR 10x/0.26 infrared objective on the front and a Mitutoyo objective Plan Apochromat NIR 5x/0.14 on the back. The temperature detection system was an Acton SP-2300i spectrometer (Princeton Instruments) equipped with a 150 mm^{-1} grating and CCD (Princeton Instrument- 7500-0003). Thermal emission spectra were collected with a central wavelength of 700 nm with a collection time between 0.1 ms and 1 s depending on the intensity of the emitted light. The collected emission spectra were fitted using a two parameter gray body Plank distribution, corrected for the transmission function of the optical system [133]. The average temperature is used for each set of measurements. The uncertainties of these temperatures were determined using the standard error of the mean of the fitted temperatures.

In back-scattering configuration and following the same optical path as for the temperature detection system we have a Raman scattering setup equipped with a pulsed laser (532 nm-spectra physics, 35 ns pulse width, 15 kHz repetition rate), used as the Raman probe. A gated intensified CCD detector (Pimax 3, Princeton Instruments, photocathode High Blue QE- HBf- Gen III, photophospor type P43) is coupled to an Acton SP-2500i spectrometer (Princeton Instruments) equipped with a 300 mm^{-1} grating that we used for Raman measurements. The laser pulse triggers the gated CCD *via* a digital oscilloscope (TBS 20000B, Tektronix).The spectra shown here were measured using the intensifier at 100 % and with 40.000 accumulations.

3.3 Pressure Calibrants

Determining pressure in a rapid and precise way is of great importance for high pressure science. This section provides a brief review of pressure scales used in the contributing work, including ruby fluorescence, Raman shifts of diamond scale and CH_4 vibron pressure gauge. All these pressure scales mentioned above were used in the present work for different diagnostic methods, pressure ranges and accuracies. Below 25 GPa, ruby fluorescence was used as pressure marker. Diamond Raman shift pressure scale was used for pressure determination technique employed at pressure higher than 25 GPa and high temperatures.

3.3.1 Ruby Fluorescence

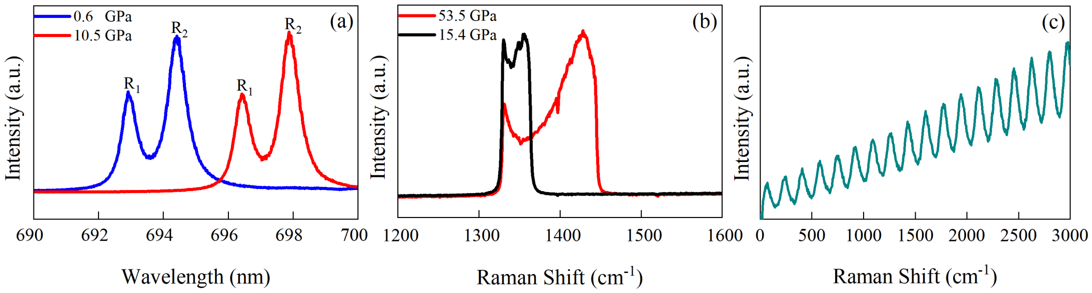

Figure 3.5 *(a) R_1 and R_2 fluorescence lines from ruby at 0.6 GPa and 10.5 respectively. (b) Example Raman diamond edge spectra obtained from the same DAC experiments at 15.4 and 53.5 GPa respectively. (c) Interference pattern obtained from a Re gasket with thickness of 24 μm, used to determine the depth of the sample chamber.*

In 1972, Forman *et al.* developed a rapid and convenient technique to determine pressure in diamond anvil cell by measuring the R-shift of ruby (Al_2O_3 doped with 0.05% of Cr^{3+}) [10]. This method is very straightforward, a ruby sphere or ruby powder is placed in the sample chamber. Ruby will fluoresce upon illumination with powerful laser, producing a doublet of emission lines; R_1 and R_2 which normally observed at 692.7 nm and 694.2 nm, respectively. The distinct R_1 was observed to shift linear to pressure up to 20 GPa [134]. The non-linear calibration was later reported and revised by Mao *et al.* up to 80 GPa [123] with equation below:

$$P = 380.8[(\frac{\delta\lambda_{R1}}{694.2})^5 - 1] \tag{3.2}$$

where P is pressure (GPa), $\delta\lambda_{R_1}$ is the shift of R_1 fluorescence line from 694.2 nm at room temperature.

Figure 3.5 (a) shows the ruby fluorescence as pressure marker for CH_4 at 1 GPa and 20 GPa respectively. Due to the chemical inertness of ruby, ruby scale has been the most common pressure determination method in high pressure science. However, ruby fluorescence pressure scale cannot be used precisely at pressure above 100 GPa as the fluorescence from the diamond anvil get stronger and the emission intensity from ruby R_1 decrease dramatically.

3.3.2 Diamond Edge Scale

Raman shifts of diamond edge scale (DES) has been widely used at high pressure and temperature, especially for pressure above 100 GPa. It is well known that the optical phonon of diamond shifts linearly to higher frequencies with increasing pressure thus making it possible to measure pressure *in-situ* in diamond anvil cell without additional pressure scale. Diamond edge scale works in a straightforward way: when laser was focus on the sample chamber through diamond anvil, sample modes together with two intensive sharp peaks can be observed in Raman spectroscopy. Figure 3.5 (b) shows the diamond edge scale at different pressures. The low frequency edge come from the unstressed table which normally appears at around 1333 cm^{-1} wavenumber under ambient condition while the high frequency edge was found to be associated with the stress of the *(100)* diamond culet face and had a linear dependence with pressure. It was first proposed and calibrated to 40 GPa by Hanfland *et al.* to use optical phonon of diamond as pressure gauge [135]. Under higher pressure, it was found that the frequency no longer follow a linear dependence on pressure while follow the equation below:

$$P = A\frac{\delta_\omega}{\omega_0}[1 + \frac{(B-1)}{2}\frac{\delta_\omega}{\omega_0}] \tag{3.3}$$

Where A and B are the constant with value of 547 and 3.7; ω and ω_0 are the Raman frequencies of unstressed table and stressed culet[136, 137]. In this work, the pressure scale calibrated by Akahama *et al.* up to 310 GPa in 2006 is used to provide consistency, and the stressed edge frequency is chosen such that it minimises the differential $\frac{d_I}{d_w}$ of the signal [137].

Diamond edge pressure scale does not need synchrotron radiation source or introduce any additional pressure marks such as ruby sphere. However, it's important to note that DES may not provide the same level of precision as the ruby pressure scale or measurements using known metals' equations of state at pressures below 25 GPa.

It is important to comment on the inaccuracy of the diamond edge pressure scale due to the weak temperature dependence of the diamond modes at high temperatures (T > 800 K). Diamond Raman spectra were found to be affected by temperature changes under ambient pressure [138]. As the temperature increased, the Raman peak shifted toward a lower frequency, and the full width at half maximum increased. Unfortunately, to date, no temperature corrections have been performed to explore the consequences for DES when used as a pressure gauge under high pressure. In this study on the high-pressure and high-temperature phase diagram of CH_4, we assumed a continued weak temperature dependence under high pressure. Pressure control was achieved using the following approaches: for the isothermal decompression experiments, pressure was determined by comparing the initial frequencies of the stressed diamond edge before and after heating. For the isobaric heating cycles, a stressed diamond edge was used as a reference, allowing us to maintain relatively stable pressure (± 5 GPa). For example, during the heating experiments, when the stressed diamond edge drifted to higher frequencies (suggesting an increase in pressure), the load on the lever arm was reduced, and vice versa if the stressed diamond edge drifted to lower frequencies.

3.3.3 Use of the CH_4 Vibron as Pressure Gauge under Room Temperature

The CH_4 Raman spectrum has a distinct peak at frequencies between 2913.6 cm^{-1} and 3213.8 cm^{-1} in the pressure range of 0.5 - 64 GPa which corresponds to the vibrational motion of the CH_4 molecule and its frequency is particularly sensitive to pressure changes under room temperature. In the contributing work, the CH_4 vibron gauge has been used in addition to the ruby and the diamond anvil pressure scales as an additional pressure marker at room temperature. Cross-referenced with the frequency of the vibrational modes of CH_4 from our previous room temperature experiments to maintain self-consistency. An example of how the frequency of the stressed diamond edge was determined, and the dependence of the vibrational frequency of CH_4 versus the frequency of ruby and the stressed diamond edge is given in Fig 3.6.

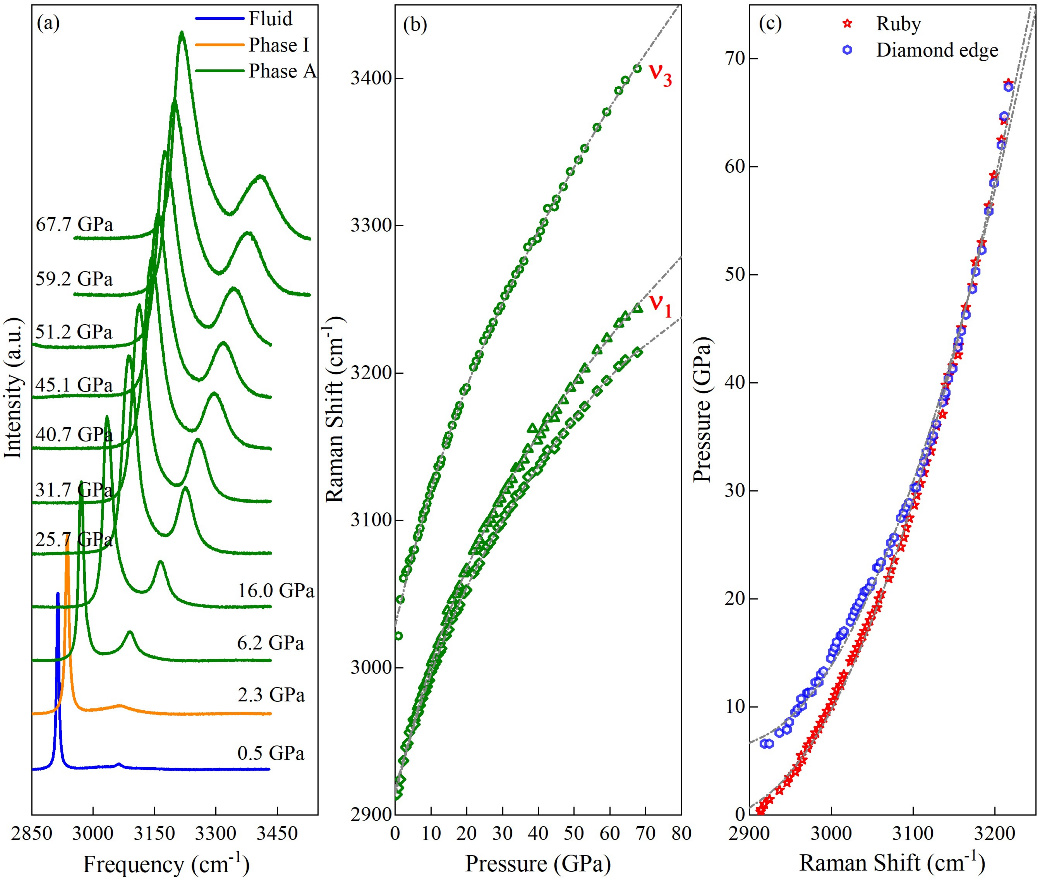

Figure 3.6 *(a). Raman spectrum of CH_4 phase transitions up to 67.7 GPa at room temperature; the blue line is the Raman spectra of methane fluid phase, the orange lines are the Raman spectra of methane phase I, the olive lines are the Raman spectra of methane phase A; (b). Raman frequency as a function of pressure for two ν_1 and one ν_3 C-H stretching modes; (c-d). The ν_3 vibron mode of CH_4 plotted against pressure.*

3.4 Experimental Details

3.4.1 High Pressure and High Temperature Phase Diagram of CH_4

For this study we conducted a total of 60 independent experiments up to pressures of 270 GPa (Appendix table 1.1 for experimental sample list). Pressure was generated in a DAC with culet dimensions of 200 μm for high temperature experiments and culet dimensions of 40 μm and 50 μm for multimegabar high pressure experiments. The rhenium foils (thicknesses of 200 – 250 μm) and osmium powder (BOC, 99.99 %) were used as the gasket materials to form the sample chamber. The research grade CH_4 (BOC, 99.9995%) was loaded into diamond anvil cell at 0.2 GPa under room temperature with the gas loading system.

High-temperature experiments were conducted using Mao–Bell DACs equipped with a primary and two secondary heaters with thermocouples. We used either two type-K thermocouples, for experiments up to 800 K or two type-R thermocuples, above 800 K. In each experiment each thermocouple was partially clamped between the gasket and the diamond anvil. Figure 3.4 is the schematic of thermocouple position between diamond and gasket. Good mechanical contact ensures a more accurate temperature measurement (normally errors within 20 K), while ensuring optimum proximity to the sample chamber.

Heating was done in two stages: (i) the external heater, external to the cell assembly heating to 500 K; and (ii) two secondary internal heaters, situated around the diamond anvils, heating up to 1200 K. The internal heaters made of a Pt-coil heating element was driven by a DC power supply on a feedback loop with a high sampling rate controller. A construction of the internal heaters can be seen in figure 3.4 (a). The heater consists of platinum heating element, a material chosen for its desirable high-melting temperature (2041.4 K) whilst having a workable malleability. The thin Pt wire is coiled around an alumina ring and tightly wound around platinum tubes to provide ports for electrical probes so that it can be driven by an external power supply, seen in figures 3.3. The heating element is then set in high-temperature cement and a pyrophyllite ring, providing thermal insulation as well as slowing down oxidation of the heating element and premature failures. When this internal heater is used in conjunction with the external heater temperatures in excess of 1000 K can be explored. To reach higher temperature as well as prevent internal heater failure, normally two internal heaters were used in most experiments.

High-quality Raman spectra were acquired using the custom-built micro-focused Raman system described earlier in chapter 2, using a 514 nm laser as the excitation line. For pressure measurements, ruby and stressed-diamond-edge frequency were used and, where applicable, cross-referenced with the frequency of the vibrational modes of CH_4 from previous room temperature experiments to maintain self-consistency. An example of how the frequency of the stressed diamond edge was determined, and the dependence of the vibrational frequency of CH_4 versus the frequency of the stressed diamond edge is given in chapter 3.3.3.

3.4.2 Xe−Ar Binary System

High purity Xe (BOC, 99.99%) was initially cryogenically loaded as a solid into diamond anvil cells (DACs) under a nitrogen atmosphere below 161 K. After temperature was quenched loading was confirmed by the change in refractive index between the empty and loaded DAC. High purity Argon (BOC, 99.998%) was subsequently gas loaded into the sample chamber at 0.2 GPa, partially substituting Xe [5, 139]. Due to the inherent complexity of the gas loading procedure, the exact Xe/Ar sample ratio could not be controlled. However, both our Raman and XRD data suggest excess of Xe in Xe-Ar system. Diamonds with 200 μm culet diameter were used to generate pressure in all experiments and rhenium foil was used as the gasket material. Raman spectroscopy was initially used to rule out possible contamination after sample loading and to identify compound formation. Raman measurements were performed using the Raman system described above in chapter 2 with a 514 nm excitation wavelength of Ar^+ ion laser. Powder X-ray diffraction data were collected at P02.2 at PETRA-III (Germany), incident beam energies in the range 25–30 keV were used. Pressure was determined from the equation of state of Au [140] for synchrotron x-ray diffraction measurements and ruby fluorescence for Raman spectroscopy measurements [123]. Calibration of the sample-detector distance, primary processing, azimuthal intergration and background subtraction were performed using the DIOPTAS 0.5.5 software [119]. Indexing was carried out using GSAS-II [141], while the Rietveld refinements were done in POWDERCELL

2.4 [120] and the equations of state data were determined using EosFIT7 [124].

Total energy calculations were carried out within the framework of density functional theory (DFT) in conjunction with the projector-augmented wave (PAW) method and a plane wave basis, as implemented in the VASP code[142]. We used the PBE exchange-correlation functional[143] and standard PAW data sets (cutoff radii: $r_{Xe} = 2.5\ a_B$, $r_{Ar} = 1.9\ a_B$) that include eight electrons in the valence space for each element. The $MgCu_2$, $MgZn_2$, and $MgNi_2$ structure types were fully optimised at a series of pressures up to 80 GPa, until remaining force components were below 2 meV/Å(0.5 meV/Åfor the $MgZn_2$ structure). The plane wave cutoff energy was 400 eV and Brillouin zone sampling was done on regular k-point grids with separations of 0.05 $Å^{-1}$. Phonon dispersions, densities of states (DOS's), and Raman intensities were obtained using the finite displacement method in suitable supercells, combining VASP with the phonopy and Phonopy-Spectroscopy packages[144, 145].

3.4.3 Nitrogen-trifluoride under extreme conditions

We have studied the stability of nitrogen-trifluoride up to pressures of 120 GPa in a diamond anvil cell (DAC). 100 and 200 culet diamonds were used for experiments. Rhenium foil was used as the gasket material for all experiments.

High purity NF_3 (99.99% purity) was initially cryogenically loaded into a DAC under a nitrogen atmosphere at 100 K. Sample loading and Raman spectroscopy measurements were collected in a wide temperature range (77–300 K) up to 151 GPa; room temperature experiments were performed with a 514.5 nm Ar^+ excitation laser, and low temperature experiments were performed using a 532 nm solid-state excitation laser, controlling temperature with a modified continuous-flow cryostat using liquid-N_2 (80 K) or liquid-He ($<$ 80 K) cryogens, coupled with two thermostat heaters and proportional-integral-derivative controllers. Synchrotron XRD data were collected up to 91 GPa from four separate runs at room temperature at the following beamlines and synchrotrons (wavelengths): ID 15B at ESRF (France; 0.4101 Å), P2.02 at PETRA III (Germany; 0.4828 Å), GSECARS at Advanced Photon Source (United States; 0.3344 Å), and 10XU at the SPring-8 (Japan; 0.4141 Å). XRD experiments utilized a combination of ruby fluorescence, the Raman diamond edge, Re and Au pressure markers, calibrated using the Vinet equation of state[137]. Intensity vs 2θ plots were obtained by integrating image plate data in various formats using DIOPTAS[119].

Indexing was carried out in GSAS-II[141], Rietveld refinements were carried out in Jana2006[146].

The first-principles density functional theory calculations were performed using the Wien2k package.[147] All internal atomic coordinates were relaxed until the calculated forces were less than 1 mRy/Bohr (0.03 eV/A^{-1}). The Wu-Cohen generalized gradient approximation (WC-GGA) was applied to the exchange-correlation potential calculation. The muffin tin radii are chosen to be 1.25 a.u. for nitrogen and 1.38 a.u. for fluorine. The plane-wave cut off is defined by $RK_{\text{max}} = 7.0$, where R is the minimum linearized augmented plane wave (LAPW) sphere radius and K_{max} is the maximum plane-wave vector cutoff. Brillouin zone integrations were performed using a $9 \times 8 \times 12$ k-point mesh in the self-consistent field (SCF) calculation. Phonon spectra are calculated using the method of finite displacements implemented in the Phonopy code [144]. We chose a $2 \times 2 \times 2$ supercell with 128 atoms to calculate the phonon dispersion.

Chapter 4

Phase Diagram of Methane

By combining the high-pressure high-temperature techniques with Raman spectroscopy, we have studied the phase diagram of CH_4 up to 45 GPa and 1400 K, illustrating the complexity and (meta)stability of its solid phases [1]. Our results accurately locate the triple point (fluid - phase I - phase A) at 16.7 GPa, 710 K along the melting line. Interestingly, we find that the P-T boundaries of the different phases are path dependent, allowing us to discuss their kinetics, formation and (meta)stability. More importantly, we demonstrate that the melting curve changes its slope above the triple point, and melting occurs at temperatures considerably higher than previously thought.

4.1 Exploring the Known Phase Diagram of Solid CH_4

4.1.1 Rich Phases of CH_4 and Phase Transitions at Room Temperature

CH_4 has four characteristic fundamental internal vibrational modes: a symmetric $\nu_1(A_1)$ at around 2914.2 cm^{-1}, a doubly degenerate $\nu_2(E)$ at around 1526 cm^{-1}

---

[1] Mengnan Wang prepared high temperature DACs, carried out the high temperature resistive heating experiments with the help of Dr. Miriam Peña-Alvarez, carried out the high temperature laser heating experiments with the help of Prof. Eugene Gregoryanz. Synchrotron X-ray diffraction data were collected by Dr. Mikhail Kuzovnikov and data were analysed by Mengnan Wang.

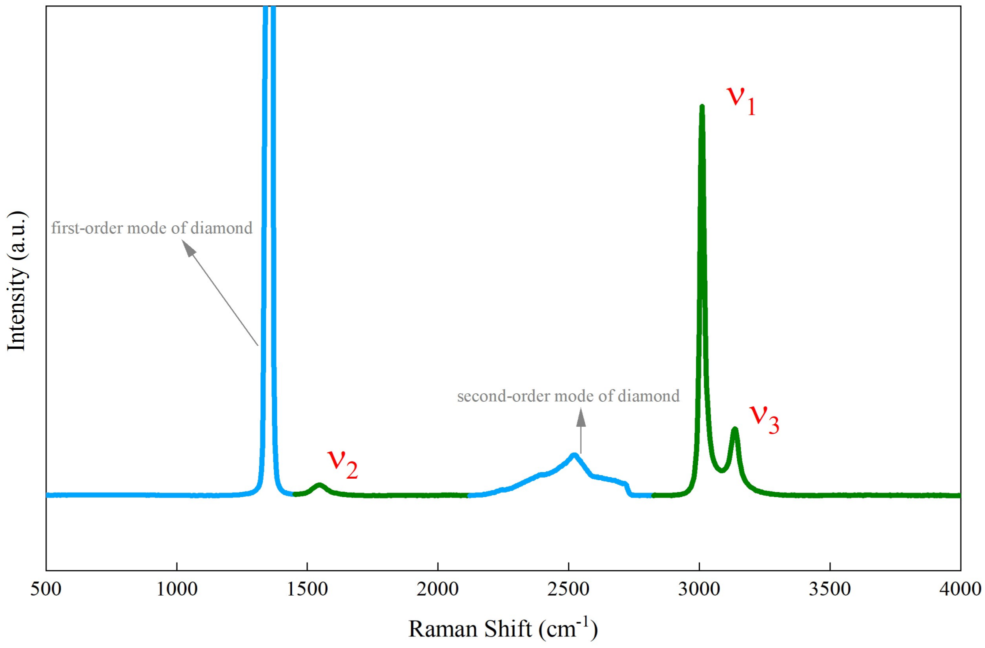

Figure 4.1 *A typical Raman spectrum of* CH_4 *phase A at 11.8 GPa at room temperature with 3 visible vibrational modes.*

and two triply degenerate $\nu_3(F_2)$ and $\nu_4(F_2)$ at 3022 cm^{-1} and 1367.406.2 cm^{-1} respectively [148]. These four modes are all Raman active. However, only ν_1, ν_2 and ν_3 can be observed in DAC experiment, as ν_4 overlaps with first-order Raman peak of diamond anvil (1331 cm^{-1} under ambient pressure). Raman mode of ν_2 does not vary significantly with increasing pressure [69, 71]. Therefore, optical studies of CH_4 are focused on the symmetric stretching mode ν_1 and ν_3, which are particularly sensitive to pressure and temperature changes. A typical Raman spectrum of CH_4 phase A is presented in Figure 4.1. The shifts and full width at half maximum (FWHM) of ν_1 and ν_3 were collected and determined as a function of pressure through the phase transitions in the contributing work. We have measured the vibrational spectrum in the ν_1 and ν_3 regions, from 2800 - 3500 cm^{-1}, as a function of pressure up to 270 GPa at room temperature. Four solid high pressure phases have been identified successfully by Raman spectroscopy at room temperature.

Phase I

After gas loading at 0.2 GPa, the symmetric stretching mode ν_1 of fluid CH_4 was observed at 2912 cm^{-1}. In the fluid phase, only one Raman mode can

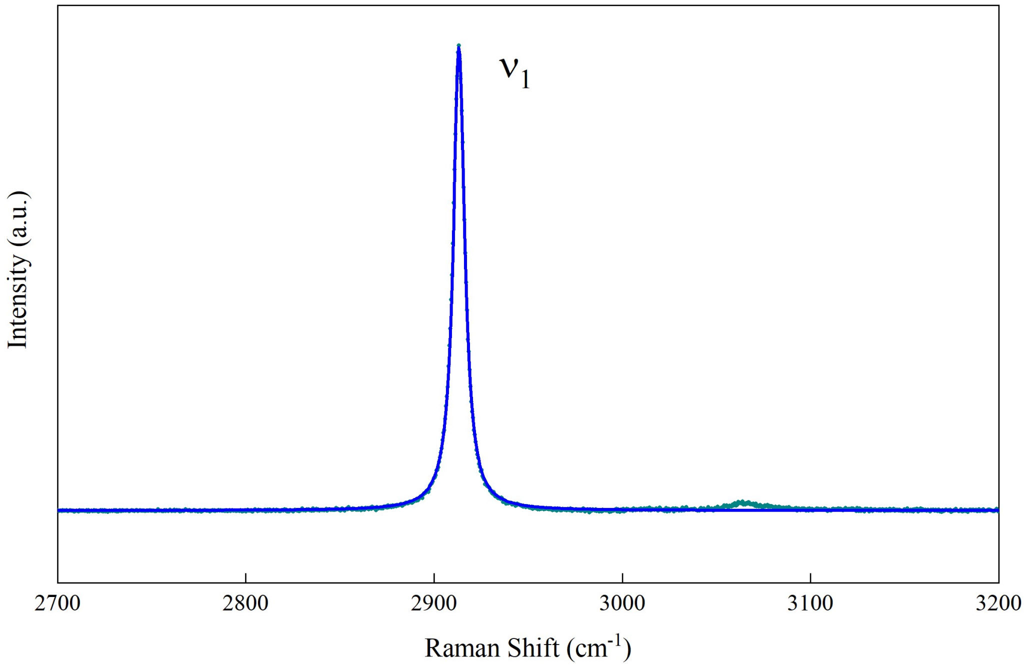

Figure 4.2 *Raman spectrum of CH_4 fluid phase at 0.7 GPa at room temperature; The dots are the experimental data and the solid blue line is the Lorentzian fitting with one ν_1 peak.*

be observed which shows good agreement with previous experiments (Fig 4.2). Raman spectra of this fluid phase are of great important as it provides evidence for melting, thus helping us to locate the melting curve in the contributing work under high temperatures and high pressures. Further compressing liquid CH_4 to 1.6 GPa shows changes in the sample texture, indicating the first phase transition from liquid to phase I.

The structure of phase I has been well studied by single x-ray diffraction both at low temperature and room temperatures [75]. Phase I has a fcc structure (space group *Fm3m*) with cell parameter a = 5.443 Å at 1.6 GPa. There is only one CH_4 molecular in the unit cell which can rotate freely (Fig 4.3 inset). Room temperature phase I of CH_4 shows the same crystal structure and similar properties as low temperature CH_4-phase I, indicating that CH_4 solidifies into a *fcc* structure directly in all the temperature range up to 300 K, as shown in the previous measurements by Bini *et al.* [69].

Figure 4.3 is the Raman spectrum of CH_4-phase I at 4.3 GPa under room temperature. As we can see in the spectrum, CH_4 exhibits a sharp ν_1 stretching

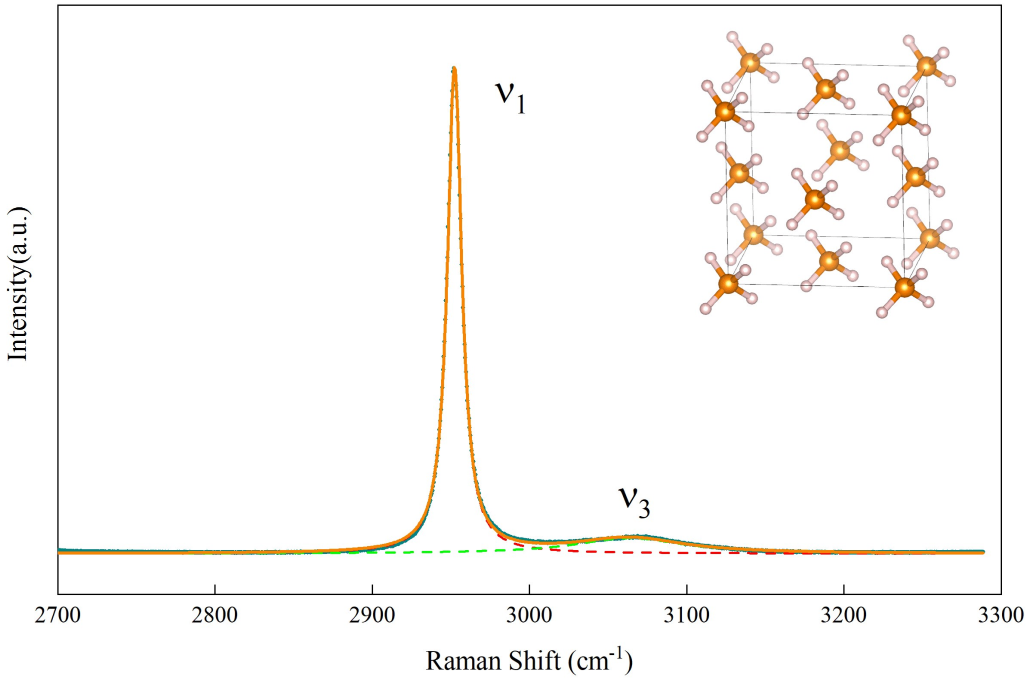

Figure 4.3 *Raman spectrum of CH_4 phase I at 4.3 GPa at room temperature. The dots are the experimental data and the solid lines are the Lorentzian fitting with two peaks; variable color lines show the individual ν_1 and ν_3 components. Inset is the crystal structure of CH_4 phase-I at 1.6 GPa at room temperature. Phase-I has a fcc structure (space group Fm3m) with cell parameter a = 5.443 Å at 1.6 GPa at room temperature.*

mode at 2951 cm^{-1} with a very broad second symmetric component at higher frequency, around 3061 cm^{-1}. We fit two lorentzian components to all spectra of CH_4 phase I up to 5 GPa. Our experimental results of phase I show good agreement with previous Raman spectra of phase I [149].

Phase A

Phase transition from CH_4-phase I to phase A was first observed by R.M. Hazen *et.al.* in 1980 via x-ray diffraction at room temperature [75]. In their work of collecting single crystal phase I of CH_4, they observed the polycrystalline powder at 5.3 GPa which they concluded that the transition from phase I to phase A is reconstructive and the transition is of first order in nature. However, the crystal structure of CH_4-phase A was not solved until 2010 by neutron powder diffraction [76]. This is because studying the crystal structure of CH_4-phase A is highly challenging: on the one hand, growing single crystal of phase A directly not in contact with melting curve was unsuccessful while alternative way by compressing phase I to higher pressure only produced polycrystalline aggregate instead of single crystal of CH_4-phase A. On the other hand, this is also challenging for characterization as it is almost impossible to determine hydrogen positions of such large molecular in synchrotron x-ray diffraction and it is also difficult to collect quality data in a limited volume of neutron cell to solve such complicated structure.

Phase A of CH_4 exhibits a rhombohedral structure (space group R3), featuring 21 fixed orientation molecules within the unit cell [76]. The structure of phase A has lots of similarities with that of phase I but it is highly distorted from the face-centered closed-packed structure in phase I in a number of different ways and to varying degrees (Figure 4.4 inset).

Figure 4.4 shows the Raman spectrum of CH_4-phase A at 5.9 GPa under room temperature. Previous studies indicate that both Raman and infrared (IR) spectra do not exhibit distinct splitting of the ν_1 and ν_3 C-H stretching modes [4, 71]. However, the micro-focused Raman spectroscopy we used in this study allowed us to observe the phase I to phase A transition. We observed a clear splitting of ν_1 on high frequency side at pressure above 5.2 GPa. As seen in Figure 4.4, the primary sharp ν_1 stretching mode at 2965 cm^{-1} shifted with increasing pressure, and a subsidiary peak at around 2982 cm^{-1} overlapped with the main peak. The ν_3 mode at around 3088 cm^{-1} becomes sharper and the intensity increases compared with that of phase I. In the transition of phase I to phase A, there is an obvious change in the width of ν_3, which could be used as another indicator of the phase transition. We fit three Lorentzian components to all spectra of CH_4 phase A up to 8.2 GPa. Our results show very good agreement with previous optical study of CH_4 phase A [148].

Phase B

Phase A remains stable up to 8.6 GPa. Upon further compression, there is another phase transition from phase A to phase B which has been reported by several groups via different characterization methods [69, 71, 78]. However, this phase transition could be easily missed if one compresses CH_4 fast at around 8 GPa from phase A. The mechanism behind this sluggish phase transition remains unclear. There are some assumptions on the sluggish transition: two Raman spectroscopy

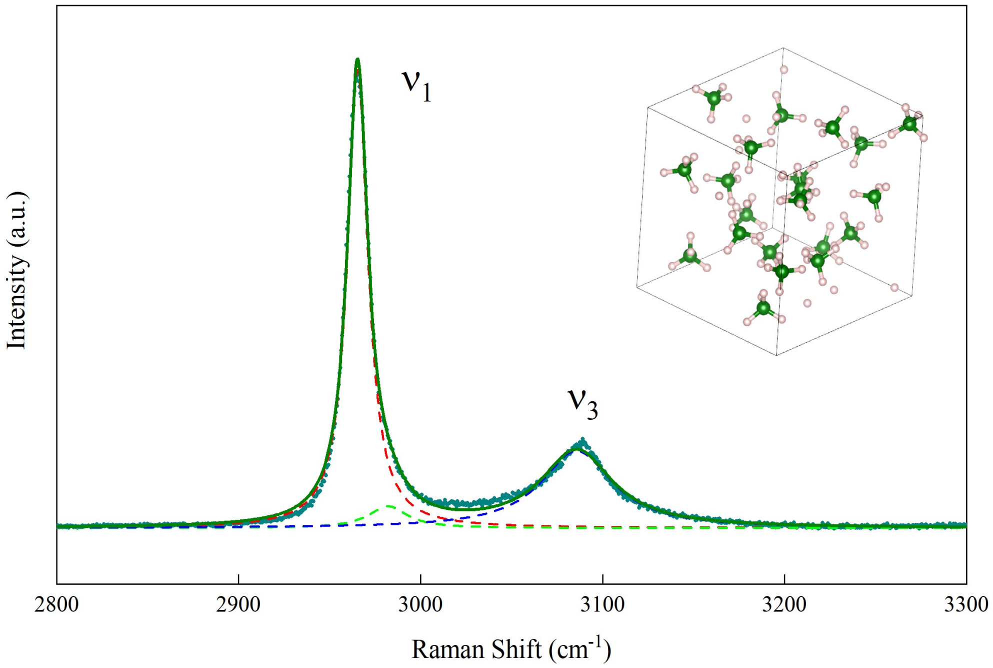

Figure 4.4 *Raman spectrum of CH_4 phase A at 5.9 GPa at room temperature. The dots are the experimental data and the solid lines are the Lorentzian fitting with three peaks; variable color lines show the individual ν_1 and ν_3 components. Inset is the crystal structure of CH_4 phase-A at 11.4 GPa at room temperature. Phase-A has a rhombohedral structure (space group R3) with cell parameter a = 8.326 Å at 11.4 GPa at room temperature, and 21 oriental molecules in the unit cell.*

studies suggest that there is an intermediate cubic pre-phase B (or phase α) in between phase A and phase B, where the Raman active ν_1 and ν_3 C-H stretching modes are not split suggesting that CH_4 molecules are orientationally disordered [71, 78]. Angle dispersive x-ray diffraction together with IR spectroscopy study indicate that the rhombohedral to cubic transition requires a complex reconstruction of molecules and the formation of the intermediate phases reported may be kinetically controlled and depends on waiting for a long time between each pressure increment [70, 150]. However, a full structural study of pre-phase B, phase α of CH_4 have not been performed.

The cubic structure of CH_4 phase B was first proposed by S. Umemoto *et.al.* in 2002 [151]. Full structure study of CH_4 phase B has been reported by combining single and powder synchrotron x-ray diffraction in 2014 [151]. Phase B CH_4 is cubic (space group $I\bar{4}3m$) with cell parameter a = 11.911 Å at 8.3 GPa. Further structural research proves that there is only a little correlation between phase A and phase B. Unlike phase A which has a significant distorted center closed-packed structure of phase I, structure of phase B bears little relationship to a close-packed arrangement. Interestingly, the 58 molecules in the phase B unit cell and the arrangement of carbon atoms were found to be very similar to that of α-manganese at ambient conditions [77] (Figure 4.5 inset). The significant structural differences between rhombohedral phase A and cubic phase B could be the reason of sluggish transition between these two phases.

Figure 4.5 is the Raman spectrum of phase B-CH_4 at 9.5 GPa. This phase is easily identifiable due to its remarkable vibrational structure, containing three vibrational modes and a clear shoulder peak at lower frequencies of ν_1. There is no obvious change on the profile of ν_3 from phase A to phase B. We fit four Lorentzian components to all spectra of CH_4 phase B up to 16.6 GPa. Our results show good agreement with previous optical studies [4, 69, 71, 148].

Phase HP

High pressure phase (phase HP) of CH_4 was first observed by Bini *et al.* using infrared spectroscopy in 1997. In their study, they reported a sudden change in both ν_1 and ν_3 C-H stretching modes for low temperature phase V to phase HP at 12 GPa and room temperature phase B to phase HP at around 25 GPa [70]. It was also referred to as hexagonal phase and was previously believed to be in a hexagonal structure [70]. Phase HP was found to be stable to at least 35 GPa at room temperature. In 2008, Hirai *et al.* reported two more new high pressure phases, phase HP2 and phase HP3 at 35 GPa and 62 GPa respectively by a combination of x-ray diffraction and Raman spectroscopy [78]. However, there were no obvious changes in the structure of these three high pressure phases and the subtle Raman frequency changes were not observed by other research groups. It remains debatable on the accurate phase transition pressure from phase B to phase HP and the numbers of HP phases in CH_4 at room temperature.

The crystal structure of phase HP of CH_4 is now believed to be cubic [78, 150]. X-ray diffraction experiments have been performed on CH_4, where a simple cubic structure was observed at 19 GPa and persisted to 69 GPa. Under higher pressure, no obvious structural change was observed [150] up to 202 GPa. The full structural study of CH_4 was performed by Bykov *et al.* recently by single-crystal synchrotron x-ray diffraction and first principles calculation. Phase HP of

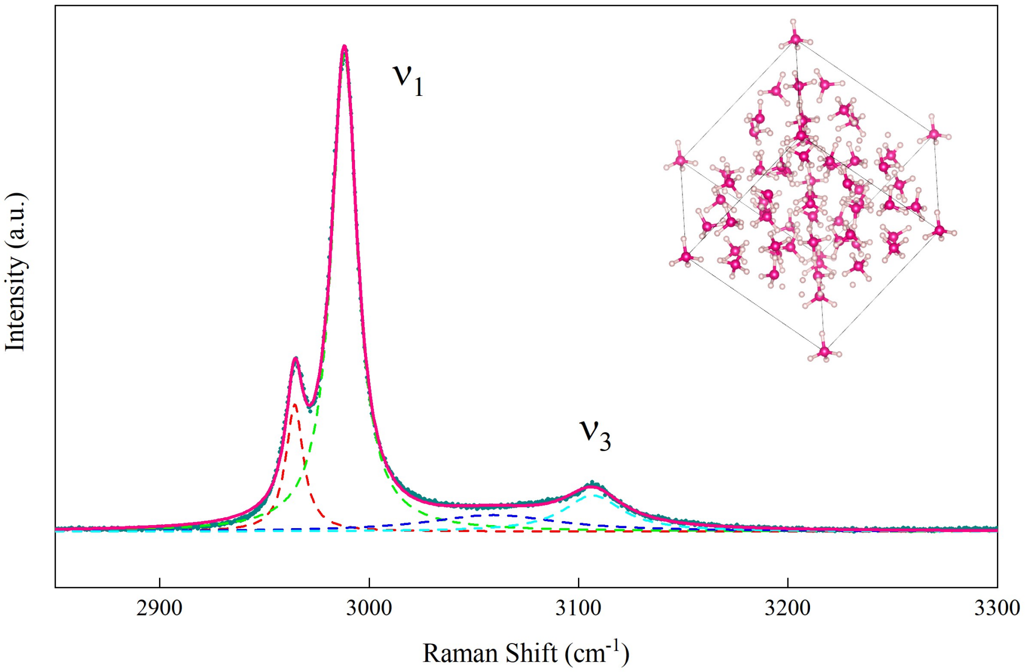

Figure 4.5 *Raman spectrum of CH_4 phase B at 9.5 GPa at room temperature. The dots are the experimental data and the solid lines are the Lorentzian fitting with four peaks; variable color lines show the individual ν_1 and ν_3 components. Inset is the crystal structure of CH_4 phase-B at 8.3 GPa at room temperature. Phase B has a cubic (space group $I\bar{4}3m$) structure with cell parameter a = 11.911 Å at 8.3 GPa. The 58 molecules in the phase B unit cell and the arrangement of carbon atoms were found to be very similar to that of α-manganese at ambient conditions.*

CH_4 was reported to have a complex rhombohedral distortion of cubic structure (space group R3) with 87 molecules in the unit cell (Figure 4.6 inset) [4].

In our study, phase HP was observed from 16.6 GPa, this transition pressure is below the literature transition pressure value of 24 GPa [70, 71, 78]. Figure 4.6 is the corresponding Raman spectra of phase HP-CH_4 at 21.6 GPa. In phase HP, the ν_1 mode further splits into four components and ν_3 further split into three components. The increase in the number of peaks indicates a new phase transition from phase B to phase HP. We fit seven Lorentzian components to all spectra of CH_4 phase HP up to the highest pressure in the study, 270 GPa.

Previous Raman study claimed an intermediate pre-phase B in between phase B and phase HP at around 12 GPa with an additional mode at around 3075 cm^{-1} [71]. However, in our study, we did not observe the intermediate phase between

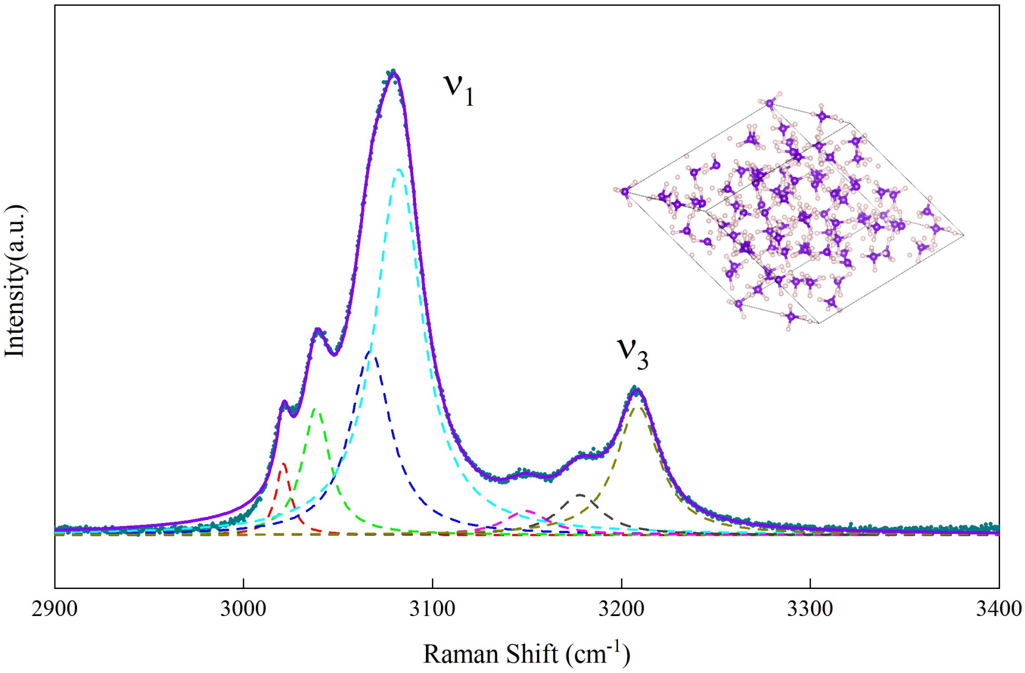

Figure 4.6 *Raman spectrum of* CH_4 *phase HP at 21.6 GPa at room temperature. The dots are the experimental data and the solid lines are the Lorentzian fitting with seven peaks; variable color lines show the individual* ν_1 *and* ν_3 *components. Inset is the crystal structure of* CH_4 *phase-HP at 25 GPa at room temperature. Phase HP of* CH_4 *has a complex rhombohedral distortion of cubic structure (space group R3) with cell parameter* $a = 15.735$ *Å,* $c = 9.660$ *Å at 22.4 GPa and 87 molecules in the unit cell.*

the phase B to phase HP transition, suggesting that the formation of the pre-B phase is controlled by kinetics and depends on the compression rate between each pressure increment. Our results show good agreement with previous x-ray diffraction study [150].

4.1.2 Room Temperature Phase Transitions up to 270 GPa

Phase Transitions to 60 GPa at Room Temperature

Our room temperature experiments mentioned above prove that Raman spectroscopy could be successfully used as characterization tool to identify different solid phases of CH_4. Changes in the frequencies and Raman profiles of the ν_1 and ν_3 vibrational modes of CH_4 molecule were used to detect phase transitions and construct boundaries between individual phases in the phase diagram.

The rhombohedral–cubic (phase A to phase B) transition was found to be extremely sluggish. A long reacting time was given to phase A to fully transform to phase B (normally overnight). Figure 4.7 shows the Raman spectra of CH_4 phase transitions up to 59 GPa upon slow compression at room temperature. Different colors represent various phases of CH_4: the blue line is the Raman spectra of the fluid phase, the orange lines are the Raman spectra of phase I, the olive lines are the Raman spectra of phase A, the pink line is the Raman spectra of phase B. The phase B spectrum were obtained when phase A to B transition was fully completed after the pressure reached 10.2 GPa.

After gas loading at 0.2 GPa, fluid sample was optical transparent under viewed under the microscope. Only one Raman mode of ν_1 at around 2912 cm^{-1} can be observed, the ν_3 mode has intensity orders of magnitude lower than the ν_1, hence it was inadequate to fit at pressure lower than 1.8 GPa (Figure 4.2).

The liquid-solid transition under room temperature was observed at 1.8 GPa and marked by the vertical gray dashed line in Figure 4.7 (b) and 4.7 (c). Previous Raman and IR spectra do not show the obvious splitting of the major ν_1 and ν_3 of C-H stretching mode. Thus Raman spectra of phase I has never been reported before. In the results obtained here, through a careful Raman spectroscopy study, we observed changes in both Raman frequency and width of ν_3 in addition to the change in the texture during phase transition. The transition from fluid to phase I is presented in Figure 4.7 (c) and (d), where we observed the width of the ν_1 mode decrease from 12 cm^{-1} to 8 cm^{-1} upon crystallization. Our fluid-solid phase transition pressure shows very good agreement with previous single-x-ray diffraction data [75]. The reduction in the width of C-H vibrational mode could be attributed to the rearrangement of molecules when they form a crystalline lattice.

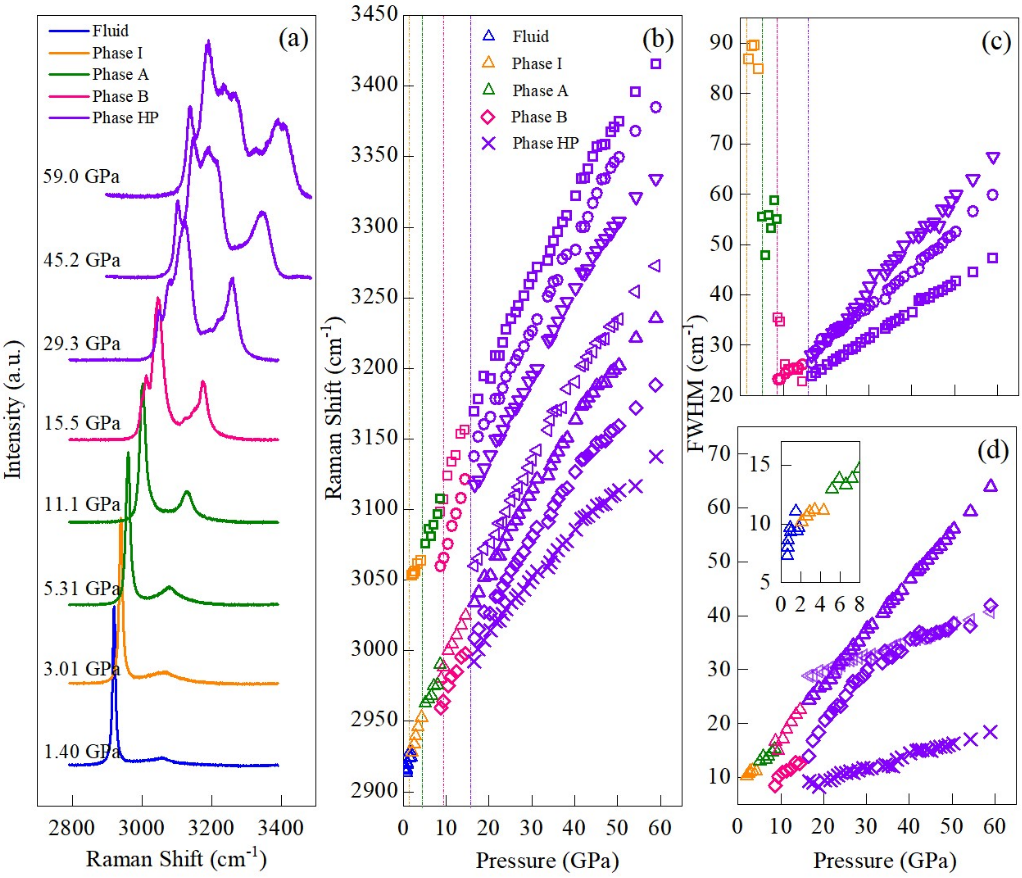

Figure 4.7 *(a). Raman spectrum of CH_4 phase transitions up to 59 GPa at room temperature on slow compression; the blue line is the Raman spectra of CH_4 fluid phase, the orange line is the Raman spectra of CH_4 phase I, the olive lines are the Raman spectra of CH_4 phase A, the pink line is the Raman spectra of CH_4 phase B and the purple lines are the Raman spectra of CH_4 phase HP; (b). Raman frequency as a function of pressure for different phases; colors distinguish different phases while data point shapes distinguish center positions of individual peak with the Lorentzian fitting contributes to observed Raman signal. Different colors of dashed lines represents phase boundaries: orange dashed line is boundary of phase I and phase A, olive dashed line is boundary of phase A to phase B and purple dashed line shows boundary of phase B and phase HP. (c). FWHM as a function of pressure for ν_3 modes. (d). FWHM of ν_1 modes as a function of pressure, inset is the FWHM as a function of pressure below 8 GPa.*

At pressure above 5.2 GPa, we observe a significant increase in the intensity of ν_3 Raman peaks which are adequate to fit. We interpreted this change as phase I to phase A transition and fitted three components to all spectra collected from 1.8 GPa to 5.2 GPa (see Figure 4.4). When the pressure is slowly increased to 8.7 GPa, a shoulder peak appears on the low-frequency side of ν_1 and a splitting of the ν_3 Raman peak into two separate components which indicates the phase transition from phase A to phase B. It was proposed that phase A to phase B transition is highly affected by hysteresis which occurs at 12 GPa during compression and at 6.6 GPa during expansion [148]. Unlike previous Raman and IR spectroscopy results, in our own hysteresis study, we observed the phase transition from phase A to phase B at 8.8 GPa in compression and phase B change back to phase A on decompression at 7.9 GPa. The narrow pressure difference from compression and decompression indicates that the transition from phase A to phase B is very likely to be a first order transition. This assumption is supported by previous x-ray diffraction results which they observe a sudden change on the volume during the phase transition from phase A to phase B [150].

At pressure above 16.6 GPa the intensities of the shoulders become higher and two more peaks appear on the lower sides of both ν_1 and ν_3 marking a new phase transition from phase B to phase HP. Raman frequency increases with pressure, however, no obvious discontinuities in frequency to pressure or changes in the peak number occur between 16 and 39 GPa. Further increases pressure, we noted that at around 40 GPa, the intensity of the third and the forth peak of ν_1 weakened, instead the second peak of ν_1 became stronger. Our result is similar to that of phase HP2 reported by Hirai.*et al.* in which they claimed two more high pressure phases, HP2 and HP3 at 35 GPa and 62 GPa respectively [78].

The Raman frequencies of ν_1 and ν_3 on slow compression have been measured in the range 0-59 GPa and plotted as a function of pressure in Figure 4.7 (b). Raman spectra revealed that liquid CH_4 solidified at 1.7 GPa [69, 70]. Changes in the peak numbers and slope of the Raman frequency shift with pressure were distinguished for different phase transitions at 5.2 GPa, 8.7 GPa and 16.6 GPa, as shown in color dashed lines in Figure 4.7 (b).

Previous Raman spectroscopy demonstrated large hysteresis under decompression for CH_4 phases [69–71, 78]. Interestingly, our results show that all the transitions observed on compression reverted in decreasing pressure with little hysteresis (table 4.1). The phase transition from phase HP to phase B at the room-temperature isotherm was found at 14.5 GPa and marked by the vertical dashed line in 4.7 (b) and 4.7 (c). In a previous study this phase transition was characterized by significant downshifts in the Raman frequency upon decompressing, with a transition pressure typically ranging from 24 GPa to 38 GPa with hysteresis larger than 10 GPa [4, 70, 71, 78]. However, in the results obtained here, this phase transition pressure was found to be as low as 16.6 GPa with only small hysteresis (less than 2.1 GPa) under decompression. Phase transition from phase B to phase A at room temperature indicated only 0.1 GPa hysteresis during decompression. The solid-liquid transition along the room-temperature isotherm was found at 1.8 GPa with 0.1 GPa of hysteresis under decompression. The reason for the discrepancy on hysteresis between different research groups can be attributed to molecular rearrangement in different phases, and some phase transition (such as phase A - B) may be kinetically limited and depends on waiting for longer times between each pressure increment.

Table 4.1 is a brief summary of structures, stabilities and hysteresis of 4 solid phases of CH_4 on slow compression at room temperature from both previous research and this work.

Table 4.1 *Summary of structures and stabilities of solid* CH_4 *at room temperature*

CH_4 Phase	Structure	Stability (GPa)/ Ref.	This work	Hysteresis
I	*fcc*	1.7-5.2 [72]	1.8-5.1	1.8-5.1
A	Rhomb	5.2-12 [72]	5.2-8.6	5.1-7.4
B	Simple cubic	12-25 [73]	8.7-14.5	7.9-15.3
HP	Distorted cubic	25-202 [74]	16.6-59	15.5-59

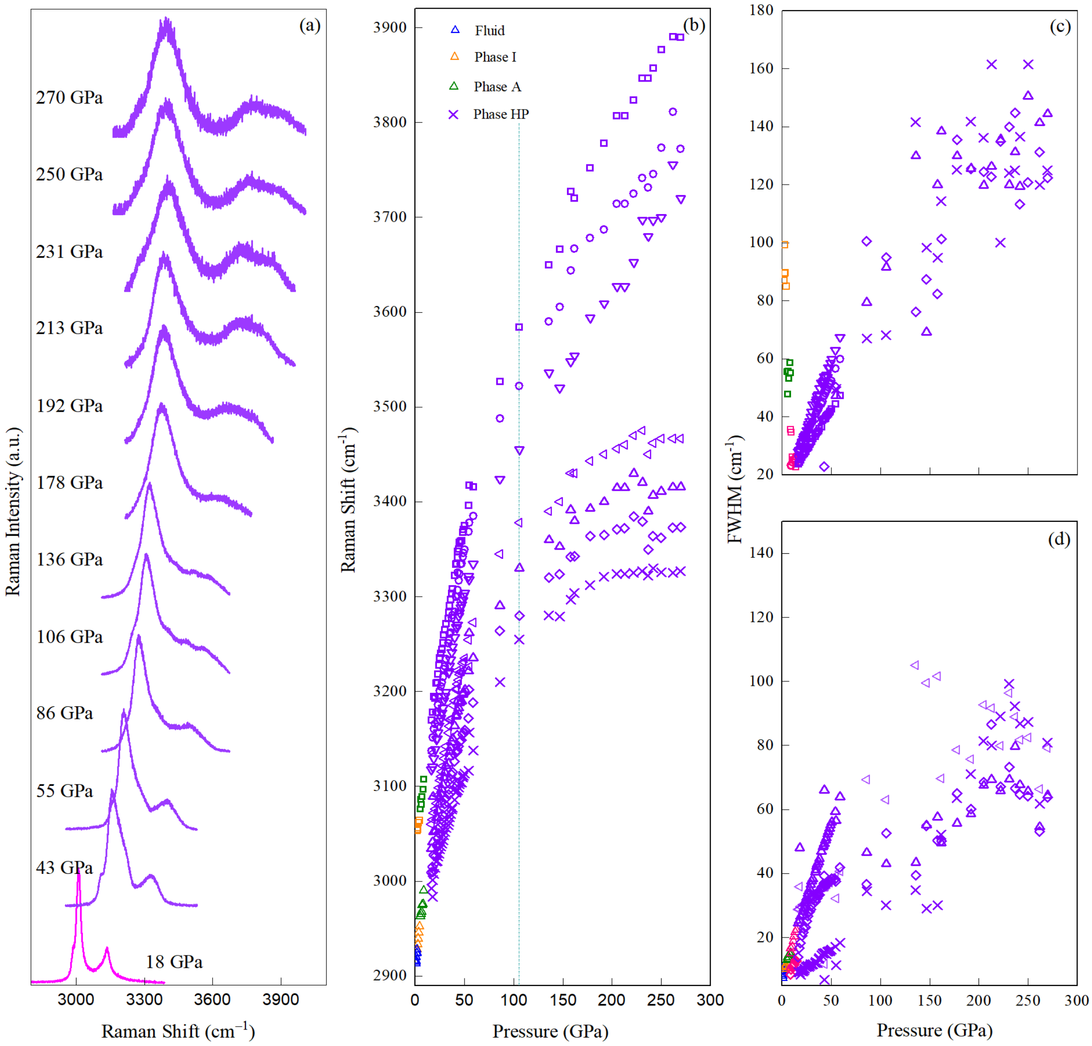

Figure 4.8 *(a). Raman spectrum of CH_4 phase transitions up to 270 GPa at room temperature on slow compression; the pink line is the Raman spectrum of CH_4 phase B after loading at 18 GPa and the purple lines are the Raman spectra of CH_4 phase HP; (b). Raman frequency as a function of pressure for different phases; colors distinguish different phases while data point shapes distinguish center positions of individual peak with the Lorentzian fitting contributes to observed Raman signal. Dark cyan dashed line represents phase transition at 105 GPa. (c). FWHM as a function of pressure for ν_3 modes. (d). FWHM of ν_1 modes as a function of pressure.*

Into the megbar pressure regime, CH_4 has been found to undergo an insulator-semiconductor transition to phase X at pressure up to 288 GPa by reflectivity and transmission measurements [152]. However, the crystal structure of phase X remains unknown. Raman spectroscopy data indicates one intermediate metastable phase and two high pressure phase transitions (HP2 and HP3) at 35 GPa and 62 GPa respectively [78]. There are two multimegabars Raman spectroscopy studies on phase A of CH_4 to 165 GPa and 208 GPa at room temperature [79, 153]. However, there is no experimental Raman spectroscopy of CH_4 reported above 86 GPa with both phase B and phase HP under slow compression at room temperature.

In this work, we studied the phase transition and stability of CH_4 up to 270 GPa using Raman spectroscopy which marks a new high pressure achievement on slow compression of CH_4 at room temperature. Apart from the 5 phase transitions mentioned above, we have observed a discontinuous change in the Raman spectra at approximately 105 GPa (Figure 4.8 (b)), corresponding to the phase transition from the simple cubic to c-HP phase previously reported by X-ray diffraction experiments [150]. However, we did not observe the expected decomposition of CH_4 into diamond and hydrogen up to the highest pressure reached in our study, 270 GPa [88].

Figure 4.8 (a) shows the Raman spectra of CH_4 up to 270 GPa and 300 K. At pressure below 178 GPa, one can clearly see the HP phase, we fitted them with 7 Lorentzian components as we did for room temperature phase HP (Figure 4.6). Above this pressure, ν_1 and ν_3 modes become increasingly broad and their intensities decrease, leading to significant overlap and making them challenging to resolve for all the components at higher pressure. Figure 4.8 (b) is the Raman frequency as a function of pressure to 270 GPa. Up to 60 GPa, our data is in agreement with previous Raman studies (Figure 4.7), observing the evolution from crystallization up to HP phase, characterized by the vibrational modes of ν_1 and ν_3. Above this pressure, the observed Raman modes shift to higher frequency with increasing pressure as expected from 60 GPa to 100 GPa. No obvious changes have been observed from 60 GPa to 100 GPa, which may suggest that there is no phase transition during this pressure range. Our results show disagreement with previous Raman spectroscopy study on slow compression in which they claim another phase transitions from HP2 to HP3 at around 62 GPa [78].

Above 100 GPa the vibrational mode's response to pressure is very unusual and does not follow the previously discussed criteria observed at lower pressures any more. In the compressing run above 100 GPa, we clearly observe changes in Raman intensity and frequency of ν_1: Raman intensity is decreasing with pressure and Raman frequency is flattening with increasing pressure. Plotting the Raman frequency as a function of pressure, all the 3 ν_3 modes above 3450 cm^{-1} are observed to increase linearly with pressure, whilst the frequency of the 4 ν_1 modes above 3250 cm^{-1} flatten and do not follow the linear relation with increasing pressure any more. This unusual behavior suggests the possibility of another phase transition occurring above 100 GPa. We attribute this new transition to the phase transition from the simple cubic to c-HP phase, corresponding to the one previously observed with X-ray diffraction from 94 GPa up to 288 GPa [150]. However, it is important to stress the limitations of Raman spectroscopy as a method to detect phase transition under extreme pressure. The unusual flattening of the ν_1 modes could also result from the poorly constrained curve fitting, owing to the unavoidable poor signal-to-noise ratio at such extreme pressures.

4.2 High Pressure High Temperature Phase Diagram

Using the high pressure high temperature techniques discussed in chapter 3, we have succeeded in melting CH_4 at elevated temperatures in excess of 1200 K to collect Raman spectra and to accurately track the parameter evolution, position and FWHM of the characteristic ν_1 and ν_3 C-H stretching modes in fluid, phase I, phase A, phase B and phase HP. All these phase transformations are characterized by noticeable modifications of the Raman spectra with temperature, such as significant upshift/downshift of characteristic vibrational modes, dramatic changes in width and disappearance of the librational modes. The data presented further extend the current understanding of the CH_4 phase diagram up to 1200 K and 60 GPa. Our Raman experiment results will consequently require a significant revision of the CH_4 phase diagram under high temperature and high pressure.

It is of great importance to accurately identify melting in resistive heating experiments in diamond anvil cell. Previous laser heating experiments using several criteria to recognize melting, such as the convection motion of small particles (coupler) embedded in the sample chamber or the phase boundary by different refractive indices of fluid and solid phases. In the contributing work, by collecting high quality Raman spectra, tracking the evolution of the Raman ν_1 and ν_3 C-H stretching modes in phases HP, B, A, phase I and fluid (see chapter 4.3.1), we succeed in identifying melting in CH_4 at elevated temperatures. The monitoring of the phase transformations and melting used in this work is more elaborate than the one reported: we not only study the appearance/disappearance and the Raman frequency changes of the vibrational modes of ν_1 and ν_3 but also their full-width at half-maximum (FWHM).

4.2.1 Melting at Low Pressure

CH_4 melting curves were reliably reported by two individual group by resistive heating technique in diamond anvil cell to 4.8 GPa and 6.8 GPa, respectively [1, 2]. Our melting curve at low pressure region shows good agreement with their results.

Inverse behaviour to what was observed upon solidification under room temperature has also been observed upon melting as shown in Fig 4.9. In the heating run that started at 6.4 GPa, we observed two phase transitions from phase A phase I at 370 K (6.6 GPa) and phase I to fluid at 550 K (7.5 GPa), respectively. Raman shifts and FWHM of ν_1 change discontinuously above 6.6 GPa, 370 K. The width of ν_3 increased dramatically at the same conditions (by 58 cm^{-1}). We interpreted these changes as phase transition from phase A to phase I. Further increase temperature we observed the change in both Raman frequency and width for ν_1 together with the disappearance of ν_3 which could be interpreted as melting at around 7.3 GPa and 560 K. The melting at around 7.3 GPa is similar to what was observed at lower pressures, whilst the vibrational mode of ν_1 undergo a upshift by 12 cm^{-1} due to pressure increase. Care needs to be taken to accurately track the melting because the subtle changes in the ν_1 and ν_3 frequency and width during melting can be obscured by pressure and temperature fluctuations during resistive heating experiment using lever arms.

Our melting curve measured below 10 GPa shows very good agreement with previously reported melting curve of CH_4 under 500 K [1–3].

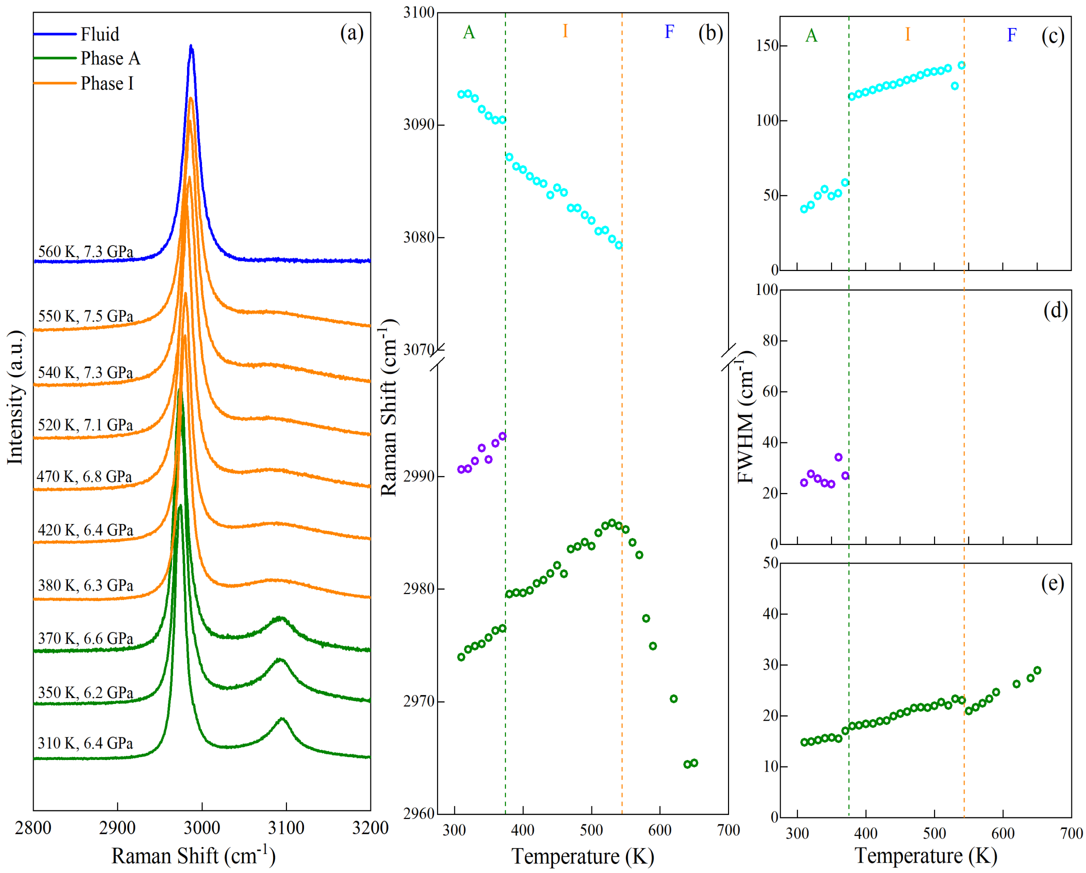

Figure 4.9 *(a). Representative Raman spectra of CH_4 phase A, phase I and fluid at around 7 GPa during heating experiment: the blue line is the Raman spectra of CH_4 fluid phase, the orange lines are the Raman spectra of CH_4 phase I, the olive lines are the Raman spectra of CH_4 phase A; Melting is indicated by a change in colour from orange to blue at around 375 K and 560 K. (b), (c), (d) and (e) (f) and (g) give the vibrational frequency and FWHM of the vibrational modes at 6.3 GPa and 7.3 GPa, from 300 K to 650 K. The phase transition temperature from phase A to phase I is represented by an olive dashed line, while the melting temperature at 7.3 GPa, is indicated by an orange dashed line.*

4.2.2 Melting at High Pressure and Temperatures

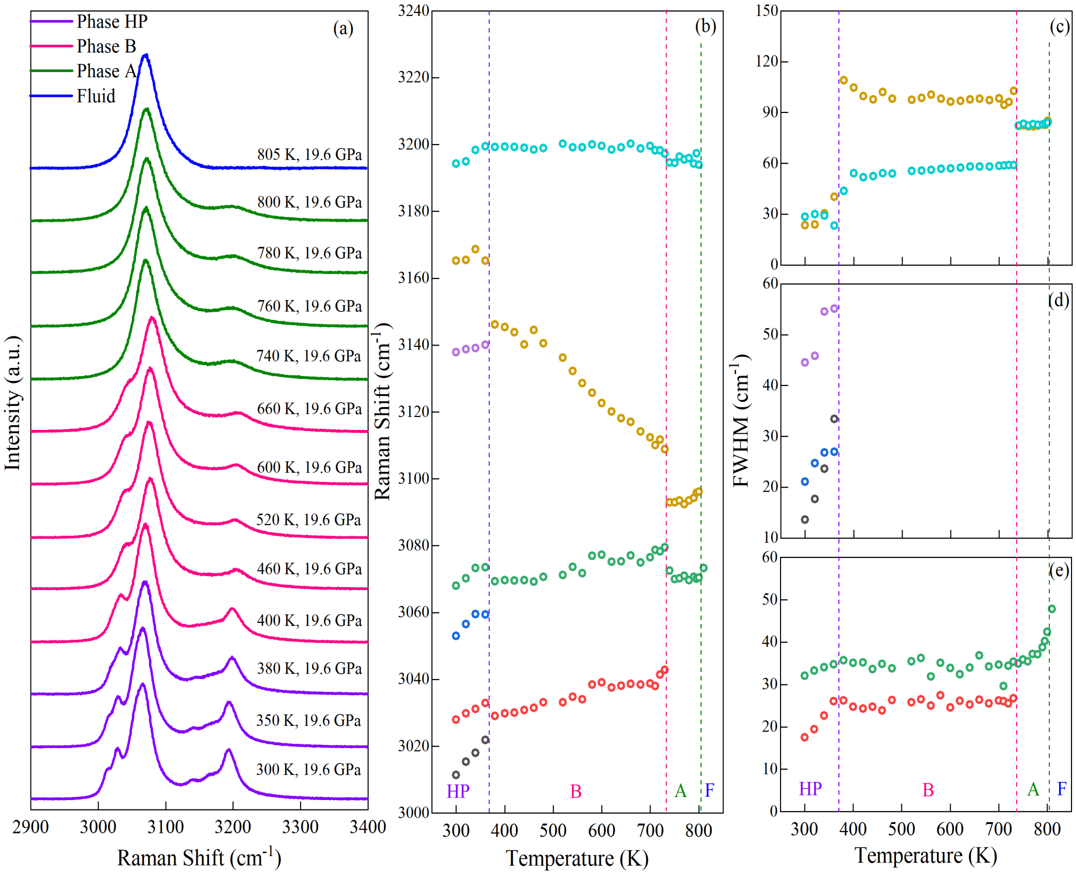

Figure 4.10 *(a). Representative Raman spectra of CH_4 phase HP, phase B, phase A and fluid at around 19.6 GPa during heating experiment: the blue line is the Raman spectra of CH_4 fluid phase, the olive lines are the Raman spectra of CH_4 phase A, the pink line is the Raman spectra of CH_4 phase B and the purple lines are the Raman spectra of CH_4 phase HP; Melting is indicated by a change in colour from olive to blue at around 805 K. (b), (c), (d) and (e) give the vibrational frequency and FWHM of the vibrational mode at 19.6 GPa, from 300 K to 805 K. Phase transitions and melting temperatures are shown by dashed lines from b to e.*

There are only two previous experimental work reporting the melting curve of CH_4 through laser heating experiments in diamond anvil cell [3, 82]. Hirai *et al.* suggest an unusually low-gradient melting curve for solid methane: CH_4 does not melt and retains in high pressure phase ranging from 10.4 GPa to 81.4 GPa below 1100 K; above 1100 K, solid CH_4 starts to melt and polymerization process begin to produce ethane (C_2H_4), and the amount of C_2H_4 increase with temperature; fot temperature higher than 2200 K, longer polymers or heavier hydrocarbon form and above 3000 K, diamond forms [82].

In contrast, Lobanov *et al.* indicate a less steep melting line for CH_4, shifting from 700 K at 20 GPa to below 1000 K at 80 GPa [3]. They have combined both resistive heating and laser heating techniques in the study. This would imply that the CH_4 melting line up to 80 GPa would be below or similar to that of hydrogen whose maximum melting temperature is around 900 K at 75 GPa [5, 80].

Interestingly, theoretical works predicted the melting curve of CH_4 to be considerably steeper and higher in temperature than the previous laser heating experimental results, going from approximately 1000 K at 10 GPa to 1250 K at 80 GPa [81].

The discrepancy between the results obtained by the two groups using laser heating may arise from inaccurately estimating the temperature during laser heating experiments as well as from kinetic, and analytical reasons. The uncertainties in their laser heating temperature measurements are larger than 200 K, especially at low pressure where the melting temperature is also low, and therefore the thermal emission used to determine temperature is weak. Instead of the melting curve, they predicted a rough band of melting. We also noticed that the largest uncertainty lies at 10 GPa, which is the onset of their laser heating pressure, it is also around the phase transition pressure from phase A to phase B. The P-T conditions of CH_4 system is of great importance to planetary sciences, as CH_4 makes up a significant amount in both the atmosphere and middle layer of icy giant planets as well as in the deep Earth. To better describe the internal structure and evolution in the icy giant planets and in the deep Earth, a more accuracy and detailed phase diagram of CH_4 is needed.

By using a combination of two internal heaters and one external heat with three thermocouples in diamond anvil cell (see Chapter 3 for details), we have succeed in obtaining and measuring temperatures accurately in excess of 1100 K over a broad pressure range from 0 to 45 GPa. The aforementioned phase transition in chapter 4.3.2 demonstrated that above 8.6 GPa at room temperature CH_4 is found to transform from a rhombohedral phase A into the simple cubic phase B. The transformation from phase A to phase B above 8.6 GPa is extremely sluggish and phase B could easily be missed on fast compression. Taking this sluggish transition into consideration, we always perform heating experiments from the most stable phase under room temperature, namely: phase I below 1.6 GPa; phase A below 5.2 GPa; phase B below 14.5 and phase HP above 16.6 GPa. Especially for the phase A to phase B transition, a long reaction times are needed to finish the transition completely. This obvious phase transition was characterised by appearance of a new shoulder peak on low frequency side of ν_1 and a splitting of ν_3. Here, for the first time, we report a triple point of fluid, phase I, phase A and a slope change in the melting curve of CH_4 above room temperature.

Figure 4.10 depicts one of the heating runs from phase HP at an initial pressure of 19.6 GPa. Upon heating, we clearly observed three phase transitions from phase HP to fluid at 390 K, 740 K and 805 K respectively. At a temperature as low as 390 K, two shoulder peaks of phase HP on low frequency side of ν_1 disappeared and a dramatic decrease on the intensity of ν_3 at temperature above 390 K which we interpreted as a first phase transition at 19.6 GPa from phase HP to phase B. Above 740 K, characteristic shoulder peak of phase B on low frequency side of ν_1 disappeared and a significant decrease on the intensity of ν_3 upon further heating occurs which could be interpreted as second phase transition from phase B to phase A at the same pressure. Raman shifts and FWHM, of ν_1 change discontinuously above 740 K, 19.6 GPa. The width of ν_3 increased dramatically at the same temperature. We interpreted these changes as phase transition from phase A to phase I. Further increasing temperature we observed the change in both Raman frequency and width for ν_1 and the disappearance of ν_3 which could be interpreted as melting at around 19.6 GPa and 805 K. The melting at around 19.6 GPa is different from what was observed at 7.5 GPa during previous heating run, seen in Fig 4.9.

Through out the high temperature experiment mentioned above, we realized that the behaviour of CH_4 at elevated temperatures and pressures above certain pressure is very unusual. In the heating run about 19.6 GPa (from phase HP) we clearly observe the melting of CH_4 directly from phase A to fluid instead of from phase I.

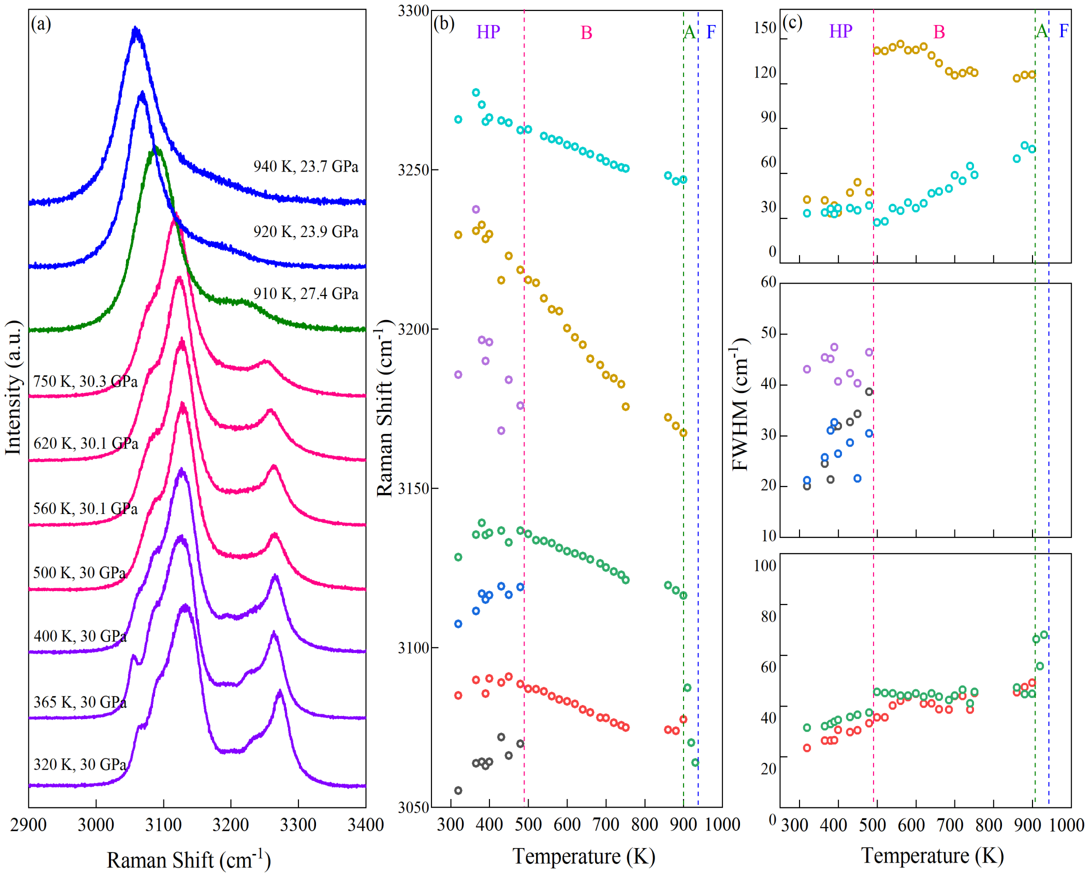

Figure 4.11 *(a). Representative Raman spectra of CH_4 phase HP, phase B, phase A and fluid at 30 GPa during heating experiment: the blue lines are the Raman spectra of CH_4 fluid phase, the olive line is the Raman spectra of CH_4 phase A, the pink lines are the Raman spectra of CH_4 phase B and the purple lines are the Raman spectra of CH_4 phase HP; Melting is indicated by a change in colour from olive to blue at 920 K. (b), (c), (d) and (e) give the vibrational frequency and FWHM of the vibrational modes at 30 GPa, from 300 K to 940 K. Phase transition temperatures from phase HP to fluid are represented by colorful dashed lines, and the melting temperature is indicated by a blue dashed line in (b) and (c).*

In order to detect phase transitions under higher temperature and pressure, as well as to construct boundaries between individual phases in the phase diagram. A large number of resistive heating experiments have been performed. Further details can be found in Appendix A sample list table.

At higher pressure, Figure 4.11 shows another experiment heating from high pressure phase at pressure of 30 GPa. Three phase transitions are clearly detectable when CH_4 is heated up to 940 K at 30 GPa. HP phase to phase B, phase B to phase A and phase A to fluid at 500 K, 900 K and 920 K respectively. Firstly, characteristic Raman modes of phase HP can be observed with four components of ν_1 and three components ν_3 at 30 GPa under room temperature. Heating up at 30 GPa, we observed the first phase transition at 500 K with the disappearance of two ν_1 modes and one ν_3 mode. Further heating phase B, we did not observe any obvious changes except for the decrease on the intensity of ν_3 up to 900 K. The phase transition at around 900 K is similar to what was observed at around 19.6 GPa during a previous heating run, seen in Fig 4.10, whilst the width of ν_3 undergoes a significant upshift by 12 cm^{-1} due to the increase in pressure. Further increasing temperature we observed the change in both the Raman frequency and width for ν_1 and the disappearance of ν_3 which we interpreted as melting at 30 GPa and 920 K. The melting at around 27.4 GPa is similar to what was observed at 19.6 GPa, seen in Fig 4.10, We also noticed the melting at 27.4 GPa from phase A directly instead of from phase I. At the highest temperatures measured during this experiment, ν_1 shows a drop in frequency due to a decrease in pressure to 23.7 GPa.

Apart from all the high temperature experiments at different pressures, we also conducted more than 8 isotherm decompression experiments in the P-T range studied. Inverse behaviour to what was observed during heating is seen upon decompressing as expected and is represented in Figure 4.12. We observed a sequence of phase transitions from phase B to fluid from 26.5 GPa to 4.6 GPa at 460 K. The first phase transition from phase B to phase A was found at around 16.9 GPa with the disappearance of the characteristic shoulder peak of ν_1 mode in phase B; the second phase transition was observed at 10.2 GPa with the broadening of ν_3 mode in phase A; the solid-to-liquid transition along 460 K isotherm was found at around 4.6 GPa and is indicated by color change from orange (Phase I) to blue (fluid) as marked by dashed line in Figure 4.12 (b) and (c).

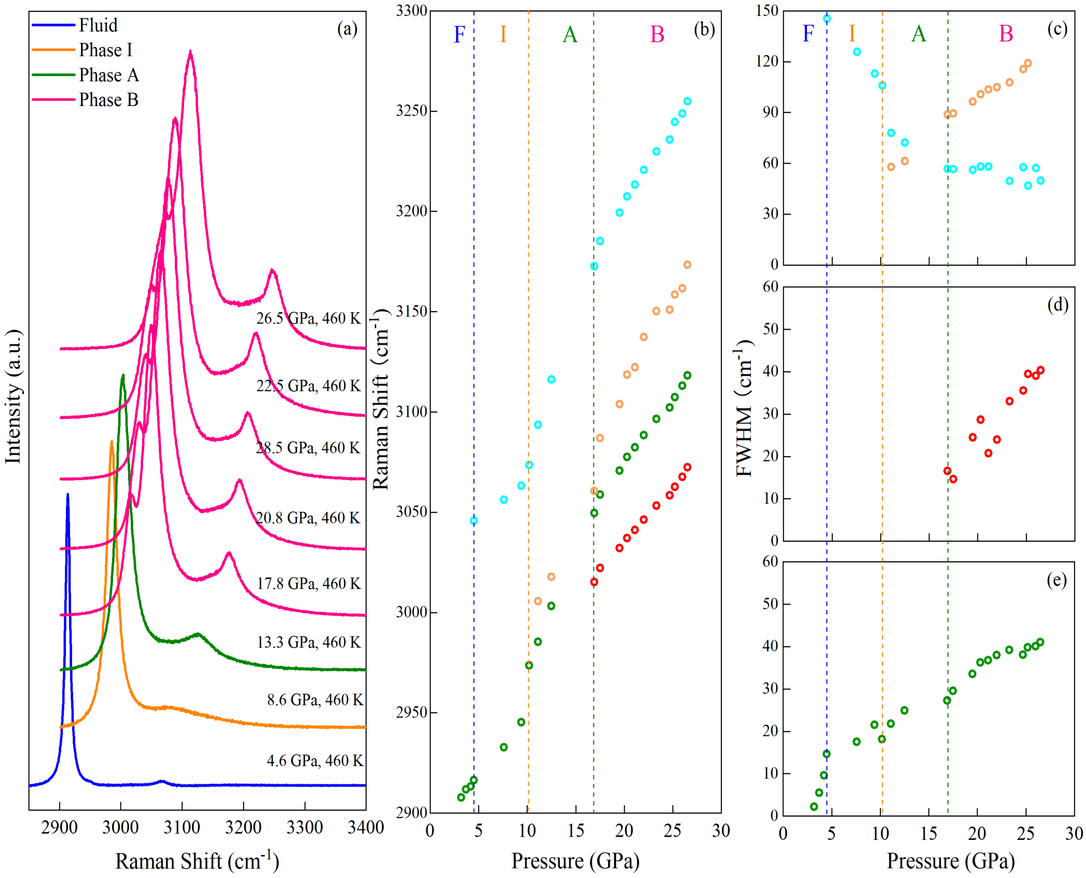

Figure 4.12 *(a). Representative Raman spectra of CH_4 phase B, phase A, phase I and fluid at 460 K during decompression: the blue line is the Raman spectra of CH_4 fluid phase, the orange line is the Raman spectra of CH_4 phase I, the olive line is the Raman spectra of CH_4 phase A, the pink lines are the Raman spectra of methane phase B; melting is indicated by a change in colour from orange to blue at around 4.6 GPa. (b), (c), (d) and (e) give the vibrational frequency and FWHM of the vibrational modes at 460 K, from 26.5 GPa to 4.6 GPa. Transition from phase B to phase A is indicated by olive dashed line at around 16.9 GPa; phase A to phase I transition is shown in orange dashed line at 10.2 GPa; melting at 4.6 GPa is indicated by an olive dashed line.*

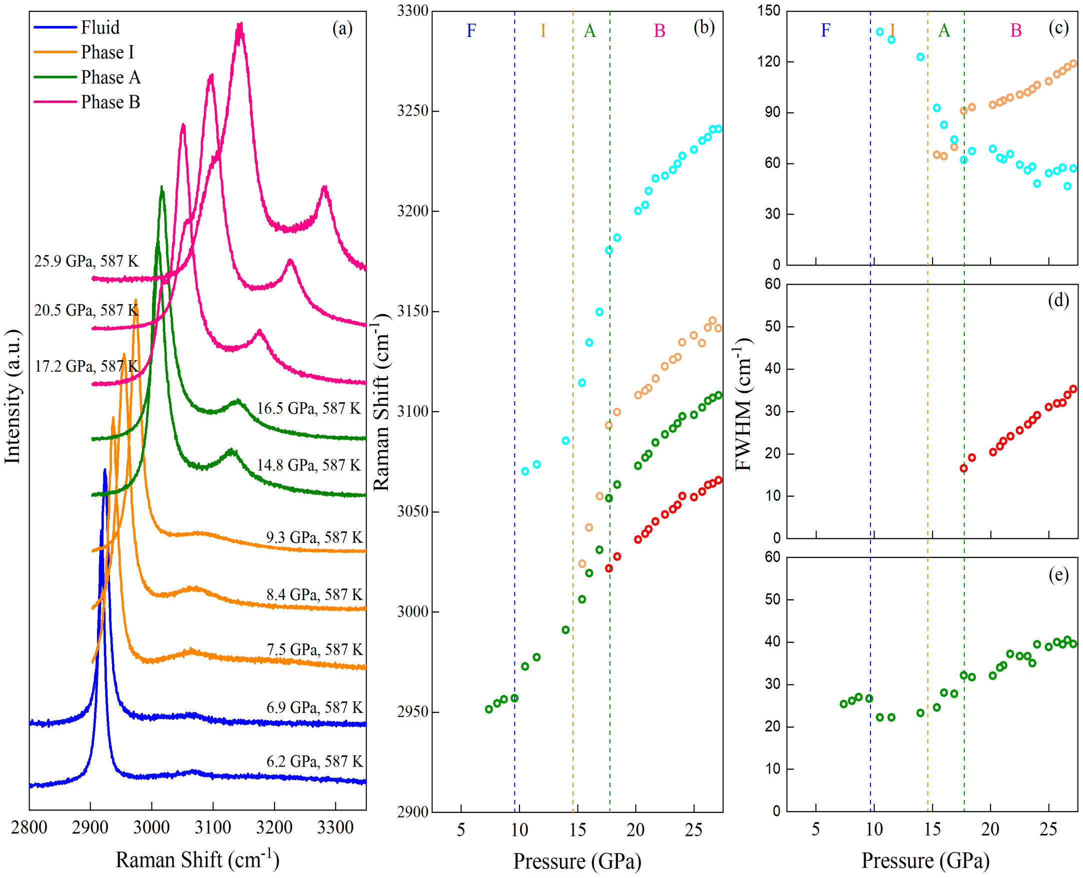

Figure 4.13 *(a). Representative Raman spectra of CH_4 phase B, phase A, phase I and fluid at 587 K during decompression: the blue lines are the Raman spectra of CH_4 fluid phase, the orange lines are the Raman spectra of CH_4 phase I, the olive lines are the Raman spectra of CH_4 phase A, the pink lines are the Raman spectra of CH_4 phase B; melting is indicated by a change in colour from orange to blue at 9.6 GPa. (b), (c), (d) and (e) give the vibrational frequency and FWHM of the vibrational modes at 587 K, from 25.9 GPa to 6.2 GPa. Transition from phase B to phase A is indicated by olive dashed line at around 17.9 GPa; phase A to phase I transition is shown in orange dashed line at 14.5 GPa; melting at 9.6 GPa is indicated by an blue dashed line.*

The melting at 460 K was characterized by the disappearance of the ν_3 mode and a small negative shift in the Raman frequency of the ν_1 modes upon decompression, typically by 16 cm^{-1}.

Figure 4.13 is another isotherm decompression at around 587 K, 25.9 GPa to 6.2 GPa. We also observed a sequence of phase transitions from phase B at 25.9 GPa to melting during decompressing the sample to 6.2 GPa. The first phase transition from phase B to phase A was found at around 17.7 GPa with the disappearance of the characteristic shoulder peak of ν_1 mode in phase B; the second phase transition was observed at 14.5 GPa with the significant broadening of the ν_3 mode in phase A; the solid-to-liquid transition along 587 K isotherm was found at around 9.6 GPa and is indicated by color change from orange (Phase I) to blue (fluid) as marked by dashed line in Figure 4.13 (b) and (c). The melting at 587 K was characterized by the disappearance of ν_3 mode and a small negative shifts in the Raman frequency upon decompression, by 15 cm^{-1}.

Above 17 GPa the vibrational mode's response to melting is quite unusual and does not follow the previously discussed criteria observed at lower pressures and temperatures. Unlike melting through phase I at lower pressures and temperatures, we noticed that CH_4 phase HP transforms to fluid via phase A instead. This unusual phenomena were observed in all heating runs in phase HP above 17 GPa and it becomes more obvious with increasing pressure. This fascinating phenomena show a slope change in the melting curve above 17 GPa, as shown in the phase diagram, will be discussed in the following section.

Through a series of high temperature experiments at pressure above 10 GPa. We find that phase I of CH_4 remains stable in a limited range of pressure and temperature (T $<$ 750 K, P $<$ 18 GPa) and then is superseded by phase A in the phase diagram above 18 GPa.

We also find that Phase A seems to be stable in a surprisingly narrow range of pressure above ambient and is superseded by phase B, which occupies a significant portion of the phase diagram up to and above 40 GPa. We traced the melting line to 45.5 GPa and 1200 K, where it intersects the extrapolated melting curve forming two triple points, at 17.9 GPa, 740 K and 41.5 GPa, 1104 K, respectively.

4.2.3 Phase Diagram of CH_4 to 45 GPa and 1400 K

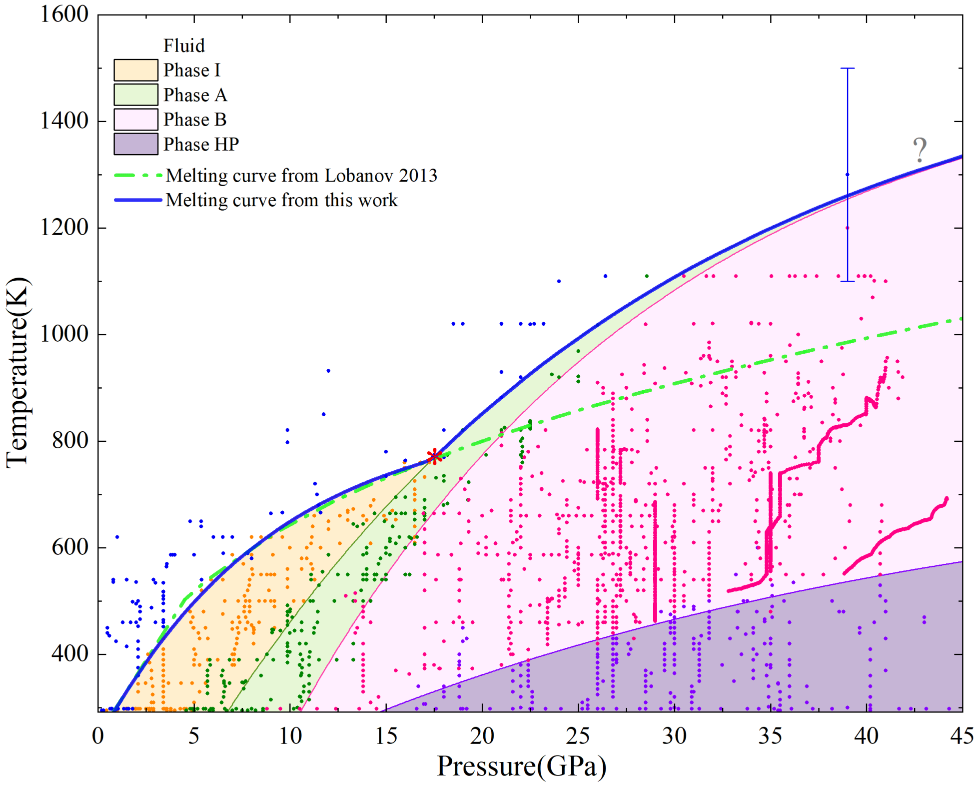

Figure 4.14 *Proposed CH_4 phase diagram up to 45 GPa. The colored, solid circles in the figure represent different Raman spectra from various phases observed during heating/isothermal decompression experiments. The solid blue line indicates the proposed melting curve of CH_4, while the colored lines denote phase boundaries, all accompanied by an error bar of approximately ± 2 GPa and ± 10 K. Phase boundary lines guides to the eye. The melting point at 40 GPa is obtained from a laser heating experiment. The asterisk represents the first triple point along the melting line at 16.7 GPa, 710 K. The solid line ending with the question mark indicates another potential triple point. The dashed green line corresponds to the melt line given by Lobanov et al. [3].*

Figure 4.14 shows the proposed phase diagram of CH_4 up to 45 GPa and 1400 K which also acts as a summary of all the P-T points investigated in the contributing work.

The data points in the phase diagram present the regions explored during heating experiments at different pressures or decompressing at isothermal temperatures. We use the same color for the same phase: blue points are the spectra in fluid, orange points stands for spectra of phase I, olive points are spectra of phase A, pink points represents spectra of phase B and purple points for phase HP. Some of the area in the phase diagram have different symbols which means this are has been affected by hysteresis.

Phase I and phase A are found to be stable in a narrow P-T range, which is in contrast to phase B that exists in an extensive stability field. Below 5 GPa, we observed CH_4 melting via phase I directly and the melting temperature increase with pressure. Upon heating, from 5 GPa to 8 GPa, CH_4 first undergo a phase transition from phase A to phase I and then melt through phase I to fluid at elevated temperatures.

Our resistive heating experiments show that at the highest temperature, 710 K, where phase I was found, it is superseded by phase A at pressures above 16.7 GPa. From this pressure, upon heating, phase B of CH_4 first transforms to phase A before melting to fluid at higher temperatures. After more than 60 heating/decompressing experiments at various pressures and temperatures, we found phase A only exists in a long and narrow stability field, shown in Figure 4.14 as the light green area. The phase transition line from phase A to phase I is found to continue at a constant gradient until it reaches the melt curve at 16.7 GPa, 710 K, suggesting a new triple point (Phase A - I - Liquid). This is the first triple point under high pressures and temperatures, possibly having implications for the continuation of the melting line.

By combining resistive heating and laser heating at higher pressure and temperatures, we observed that phase A is found to be superseded by phase B at pressure above 40 GPa and temperature above 1110 K. Above this P-T point, no phase A could be observed upon heating: phase HP of CH_4 first undergo a phase transition to phase B which finally found to melt directly from the same phase at higher temperatures. The phase transition line from phase B to phase A is found to continue at a constant gradient until it reaches the melt curve at around 42 GPa, 1110 K, indicating another possible triple point (Phase B - A - Liquid). This could be the second triple point under high pressures and temperatures. However, we were unable to obtain an accurate pressure and temperature conditions of this possible triple point due to the accuracy limitation of our high pressure measurements at high pressures.

Our heating experiments at 40 GPa proves that phase B is the dominate phase in the studied P-T range of phase diagram (see in Figure 4.14 pink area), which shows very good agreement with the phase diagram at low temperatures by Raman spectroscopy and Brillouin scattering[70, 148]. In the low pressure Raman study of Bini. *et.al.*, phase B of CH_4 was found to be stable up to 25 GPa which occupies a substantial partial in the phase diagram at low P-T region [69].

Our high P-T study suggest a positive slope change in the melting curve above the first triple point at 16.7 GPa and 710 K. In fact, the only experimental work regarding the melting line of CH_4, which reported a melting band instead of melting curve due to the large uncertainties, the estimated upper melting curve is found to be in reasonable agreement with what we have observed in our experiments [3].

4.3 CH_4 Phase A to 176 GPa at Room Temperature

4.3.1 Room Temperature Compression of Phase A to 176 GPa

It is well know that the transition from phase A-CH_4 to phase B-CH_4 at around 8 GPa is extremely sluggish and phase B can be easily missed if fast compressed at around 8 GPa. However, little research has been conducted to phase A of CH_4 under pressures higher than this pressure.

The Raman spectra from fluid to phase A upon fast compression and slow compression below 8.7 GPa are identical (see Figure 4.7). Liquid CH_4 crystallizes to solid phase I of CH_4 at 1.7 GPa. A transformation from phase I to phase A was observed at 5.2 GPa. However, further increasing pressure without waiting for the fully transition will yield phase A of CH_4 to 67.7 GPa, as showed in Fig 4.15 (a). From Figure 4.15 we did not observe obvious changes in the Raman shift as a function of pressure but the width of both ν_1 and ν_3 modes changed a lot with pressure at around 19 GPa.

In the contributing work, we performed Raman experiments on phase A of CH_4 to 176 GPa under room temperature upon fast compression. Representative Raman spectrum of CH_4 phase transitions and Raman frequency as a function of pressures up to 176 GPa at room temperature on fast compression are given in Fig. 4.16 (a). Different colors represent various phases of CH_4: the blue line is the Raman spectra of fluid phase after loading and the olive lines are the Raman spectra of phase A. Except for the width changes at around 19 GPa mentioned above, we have observed a discontinuous change in the width and height of C-H modes at 100 - 110 GPa.

Figure 4.16 (a) is the Raman spectra of CH_4 up to 176 GPa and 300 K. At a pressure of 32 GPa, one can clearly see a particularly clear Raman spectrum of phase A, we fitted it with 3 Lorentzian components (two components of asymmetric ν_1 and one for ν_3) as we did for lower pressure phase A (Figure 4.6). Above this pressure, ν_1 and ν_3 modes are broadening with pressure and getting significantly overlapped thus hard to deconvolute or even to be resolved at higher pressures for all the 3 components.

The Raman frequencies of ν_1 and ν_3 have been measured in the range 0-176 GPa and plotted as a function of pressure in Figure 4.16 (b). Two characteristic vibrational modes ν_1 and ν_3 can be observed from phase I. At pressure above 19 GPa, we observed a clearly splitting of asymmetric ν_1 mode with two different intensity components. We also noticed that the rate of increase in FWHM changes significantly above this pressure, which does not follow the near linearly relation with increase pressure any more. Above this pressure, Raman shifts to higher frequency with increasing pressure as expected from 20 GPa to 100 GPa. No obvious changes have been observed from 20 GPa to 100 GPa, which may suggest that there is no phase transition during this pressure range. Up to 165 GPa our result is in good agreement with previous Raman studies [79].

In the fast compressing run above 100 GPa, we observed the softening of both components of ν_1: Raman intensity is decreasing with pressure and Raman frequency is flattening with increasing pressure. Plotting the Raman frequency as a function of pressure, all the visible ν_1 vibrational modes are observed to flatten and do not follow the nearly linear relation with increasing pressure below 100 GPa. Such behaviour is similar to what we have observed in the mega-bar experiments on slow compression of high pressure phase of CH_4 up to 270 GPa which we attribute the transition to the phase transition from the simple cubic to c-HP phase, corresponding to the one previously observed with x-ray diffraction from 94 GPa up to 288 GPa [150].

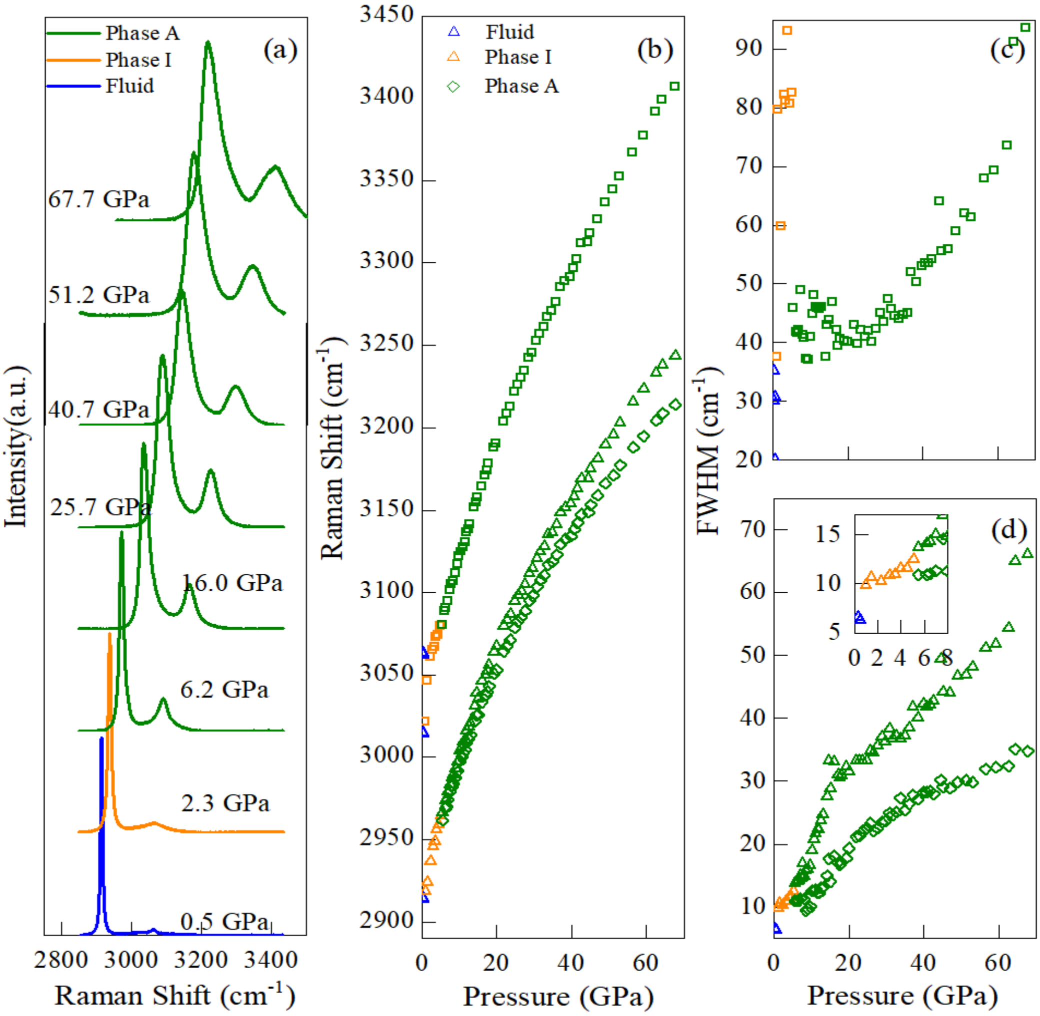

Figure 4.15 *(a). Raman spectrum of CH_4 phase transitions up to 67.7 GPa at room temperature on fast compression; the blue line is the Raman spectra of CH_4 fluid phase, the orange line is the Raman spectra of CH_4 phase I, the olive lines are the Raman spectra of CH_4 phase A. (b). Raman frequency as a function of pressure for different phases. (c). FWHM of ν_3 modes as a function of pressure. (d). FWHM of ν_1 mode as a function of pressure.*

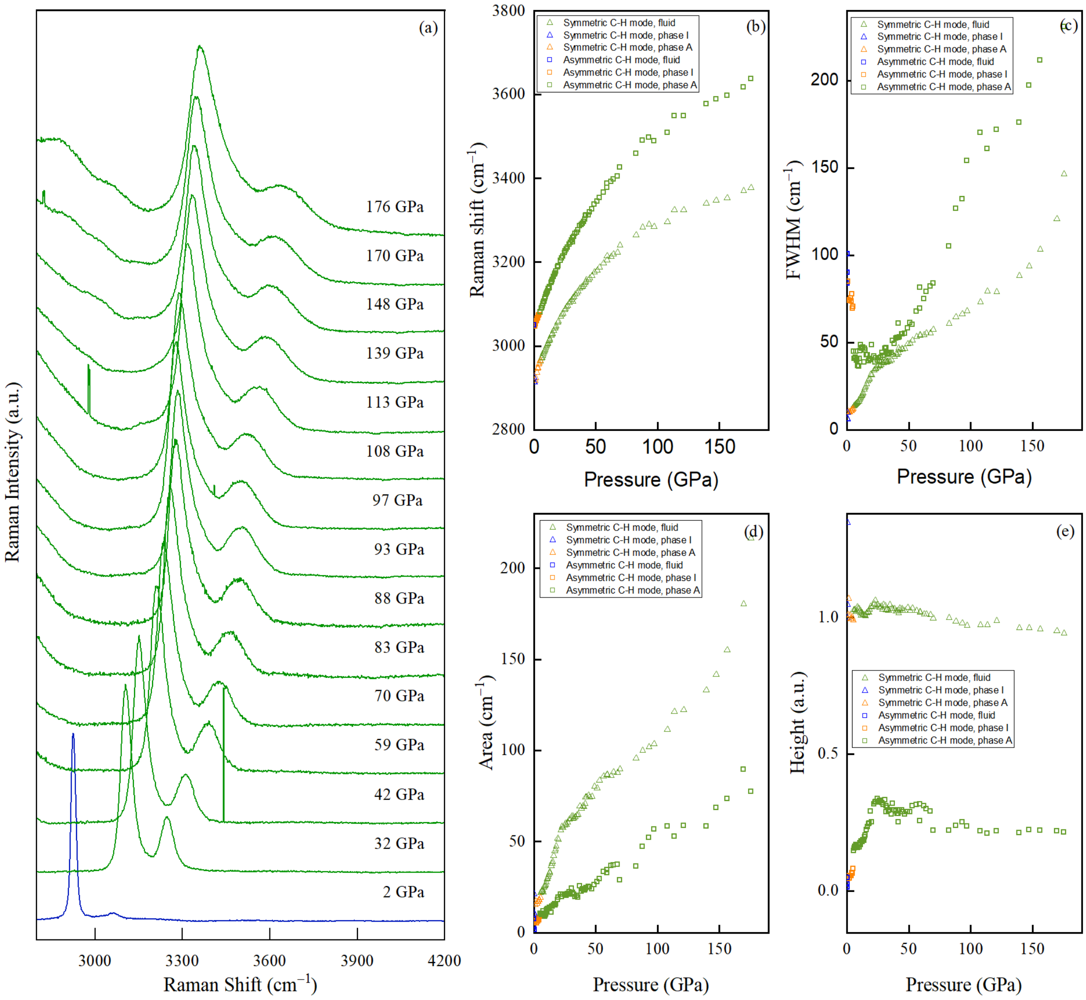

Figure 4.16 *(a). Raman spectrum of* CH_4 *phase transitions up to 176 GPa at room temperature on fast compression; the blue line is the Raman spectra of* CH_4 *fluid phase and the olive lines are the Raman spectra of* CH_4 *phase A. (b). Raman shift as a function of pressure for different phases. (c). FWHM of* ν_3 *modes as a function of pressure. (d). Area of* ν_1 *and* ν_3 *modes as a function of pressure. (e). Height of* ν_1 *and* ν_3 *modes as a function of pressure.*

4.3.2 Kinetic Control of CH_4 Phase A

As mentioned above, very little previous research has focused on the sluggish transition from phase A to phase B and the mechanism behind this transition remains unclear. Through both room temperature and high temperature studies in this work, we identified that several factors, such as reaction time, temperatures and pressure can lead to different pathways thus produce different phases of CH_4 (phase A or phase B).

The first factor we need to take into consideration is the reaction time. Previous results have suggested that phase B is the thermodynamically stable phase at pressures above 8 GPa at room temperature [70, 71]. However, in all the experiments conducted within the stability field of phase B at pressures above 8 GPa, it was observed that a significant reaction time is required for the complete transition from phase A, which is the stable phase at lower pressures. Figure 4.17 (a) and 4.17 (b) is the representative Raman spectra of solid CH_4 from phase A to phase B/phase HP at 12 GPa, 15 GPa and room temperature as a function of time. At 12 GPa, we see the formation of phase B with its characteristic shoulder peak on the low frequency side of ν_1 clearly within 180 minutes after loading; at 15 GPa, we observed the onset of phase B after 60 minutes and then the formation of phase HP within two hours of loading. Interestingly, similar phenomenon has been observed and reported by Bini *et al* [69]. They studied the kinetics of phase A to phase B transition by measuring the intensity changes of ω_1 and ω_3 in IR spectroscopy which they found the average chemical reaction rate constant k_{AB} from A to B transition to be 0.23 h^{-1} at 13.8 GPa and 0.02 h^{-1} at 10 GPa. They claim the phase transition is affected by hystersis which occurs at different pressures during compression and decompression.

We have also conducted synchrotron x-ray diffraction on both phase A and phase B under room temperature up to 50 GPa. Figure 4.18 is the volume per CH_4 molecule as a function of pressure up to 50 GPa. Olive data points are volumes of phase A at different pressure while pink circles are volumes of phase B at various pressures. As we can see from the figure, volume of phase A is slightly bigger than that of phase B at any given pressures. The volume change at the rhombohedral (phase A) to simple cubic (phase B) is found to be $\triangle V/V = -4\%$. Previous angle dispersive x-ray diffraction reported the coexist of phase A and phase B ranging from 19 GPa to 27 GPa. The reported values on the volume change at transition points of $\triangle V/V = -5\%$ are in a good agreement with our present values [150]. The coexistance of phase A and phase B, the volume differences at same pressure together the aforementioned narrow hysteresis on compression and decompression suggest that the transition from phase A to phase B is a first order transition.

In addition to reaction time, temperature plays an important role in the transformation from phase A to phase B. In Figure 4.19 (a), we show the phase transition temperature from phase A to phase B as a function of pressure. Without giving enough reaction time for the fully transformation, at pressure above 5.8 GPa, we see the formation of phase A which persists to the highest pressure under room temperature. Upon heating phase A at around 16 GPa, 20.3 GPa, 24 GPa, 25 GPa and 28 GPa, we observed the transformation to phase B at 370 K, 440 K, 467 K, 483 K and 495 K respectively. The whole transformation process from phase A to phase B during the heating experiments complete within several minutes, significantly faster than occurs under room temperature. The required transformation temperatures increase with pressure. From Figure 4.19 (a) we got a rough transformation curve which marks in dashed gray line, by heating to temperature above this curve, one can get phase B in a much faster way.

We also tried to avoid the formation of phase B by changing the pathway, see Figure 4.19 (b). Firstly, we heated the sample from phase A at around 5 GPa slowly and then increase pressure to 13 GPa, heated again before increasing to 29 GPa. During heating from 520 K at 29 GPa, we see the same transformation from phase A to phase B at 710 K. This result proves that phase B is inevitable under high temperatures at pressure above 8.6 GPa.

Above experiments result show clearly evident that phase A, favored under kinetic control, while phase B is the stable product, preferred under thermodynamic control at pressures exceeding 8 GPa.

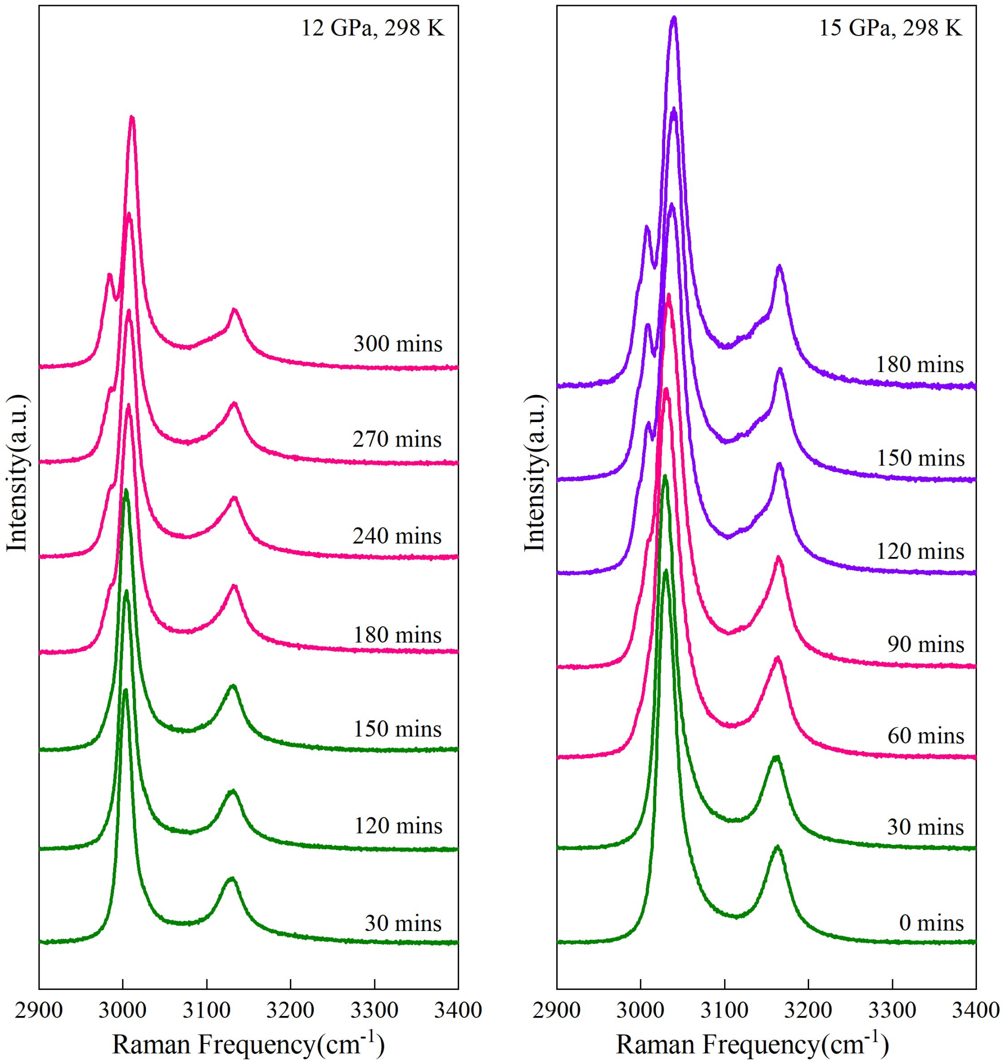

Figure 4.17 *(a). Representative Raman spectra of* CH_4 *phase A transform to phase B at around 12 GPa, 298 K with time. (b). Representative Raman spectra of* CH_4 *phase A to phase B, phase B to phase HP at 15 GPa, 298 K with time: olive are the spectra of phase A, pink lines stands for spectra of phase B while purple lines represents spectra of phase HP.*

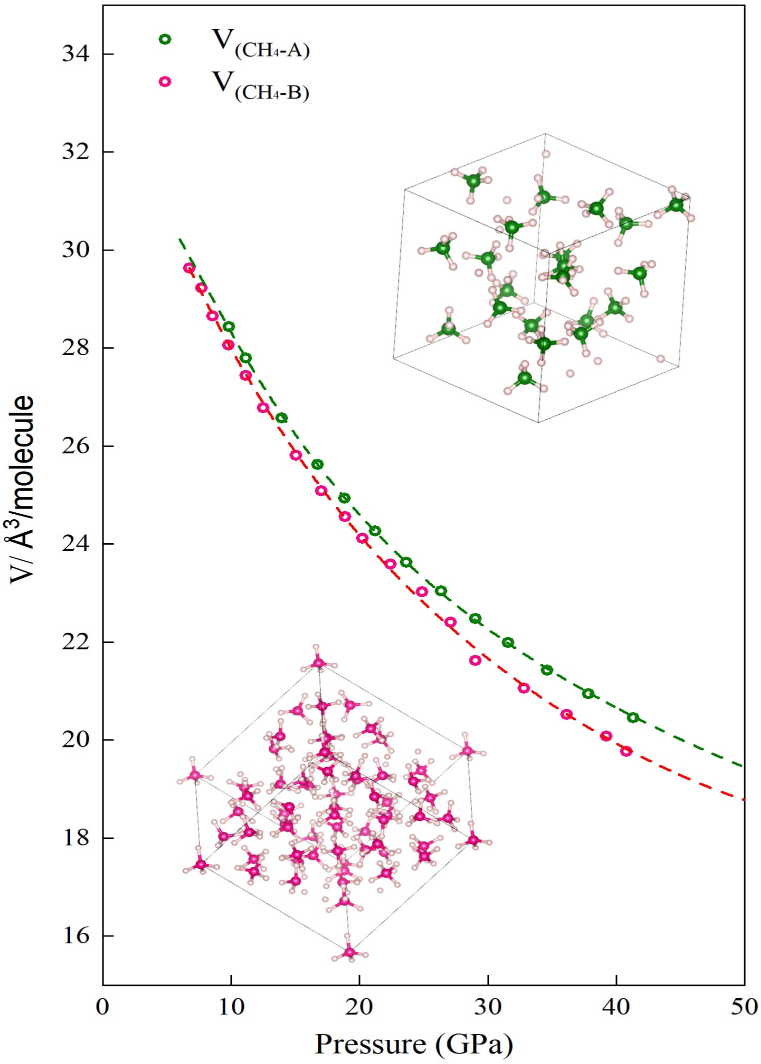

Figure 4.18 *Equation of state for phase A and phase B up to 50 GPa: olive points are volume of phase A while pink points are volume of phase B. Top right is the crystal structure of phase A and bottom left is the crystal structure of phase B.*

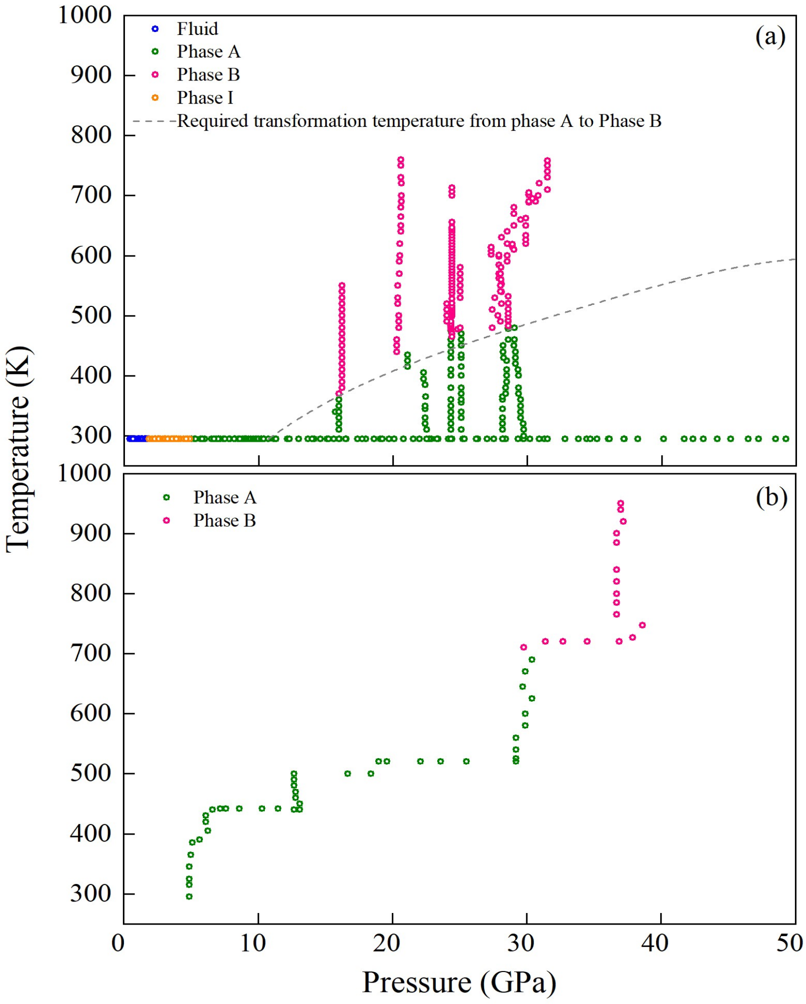

Figure 4.19 *(a). Phase transition temperature as a function of pressure for phase A to phase B. Colorful points represent different phases we observed during heating experiments: blue points are the spectra in fluid, orange points stands for spectra of phase I, olive points are spectra of phase A, pink points represents spectra of phase B; Gray dashed curve is phase transformation temperatures guide to the eye through our heating experiment points. (b). Alternative pathway to complete phase A to phase B transition within minutes.*

Chapter 5

Rare Gas Solids and Their Mixtures

The binary Xe-Ar system has been studied in a series of high pressure diamond anvil cell experiments up to 60 GPa at 300 K [1]. *In-situ* x-ray powder diffraction and Raman spectroscopy indicate the formation of a van der Waals compound, $XeAr_2$, at above 3.5 GPa. Powder x-ray diffraction analysis demonstrates that $XeAr_2$ adopts a Laves $MgZn_2$-type structure with space group $P6_3/mmc$ and cell parameters a = 6.569 Å c = 10.644 Å at 4 GPa. Density functional theory calculations support the structure determination, with agreement between experimental and calculated Raman spectra. The combined data suggests that $XeAr_2$ would remain stable without any structural transformation or decomposition into elemental Xe and Ar up to at least 80 GPa.

5.1 Synchrotron X-ray Diffraction

At room temperature, argon solidifies at 1.3 GPa [37], adopting the *fcc* configuration, while Xe crystallizes at 0.42 GPa with the same structure [47]. Xenon and argon are miscible in the fluid phase at 300 K. Their mixture solidifies at a pressure of 3.5 GPa, which is higher than the solidification pressure of both constituent elements. X-ray diffraction analysis reveals the formation of a new Xe-Ar van der Waals compound, $XeAr_2$. In all samples, $XeAr_2$ was phase separated

---

[1] Mengnan Wang prepared DACs, carried out Raman experiments up to 60 GPa at room temperature, collected and analysed synchrotron X-ray diffraction data with the help of Dr. Mikhail Kuzovnikov. Dr. Ross Howie conceived and designed the project. Prof. Andreas Hermann carried out DFT calculations.

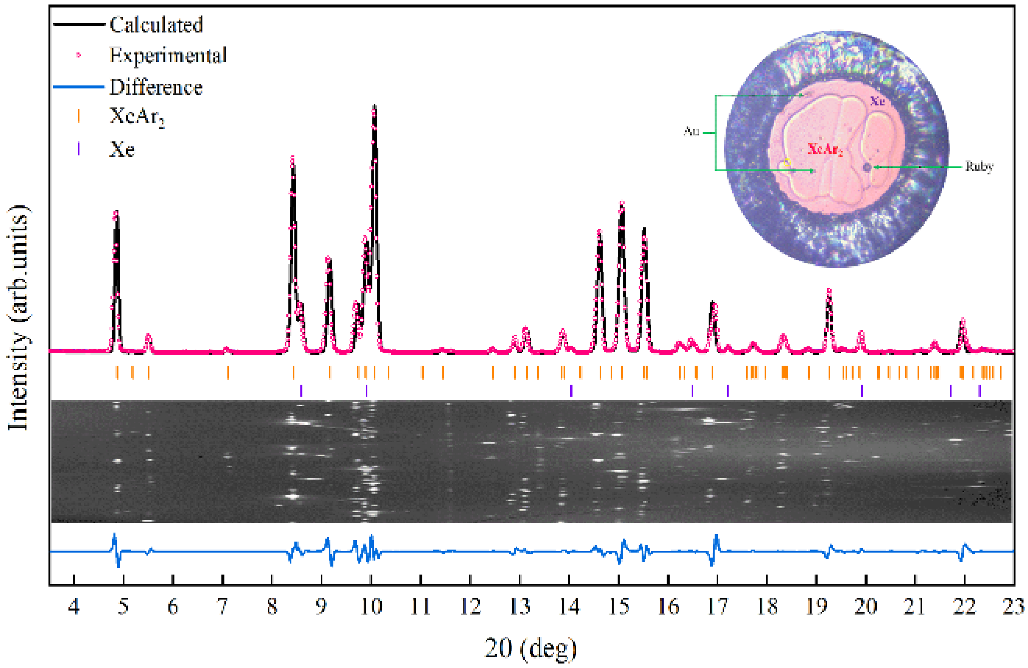

Figure 5.1 *X-ray diffraction pattern (λ = 0.4828 Å) of XeAr$_2$ obtained from an Xe-Ar mixture at 4 GPa with its Le Bail refinement. Two solid phases (XeAr$_2$ and fcc-Xe) are observed in the system. XeAr$_2$ adopts a hexagonal (P6$_3$/mmc) unit cell with a = 6.569 Å, c = 10.644 Å and fcc-Xe (Fm-3m) with a = 5.607 Å. Top left inset: photomicrograph of the XeAr2 crystals embedded in Xe at 4 GPa; arrows indicate the pressure marker Au (for x-ray diffraction measurements) and ruby sphere (for Raman measurements). Bottom inset: a cake representation of the diffraction pattern.*

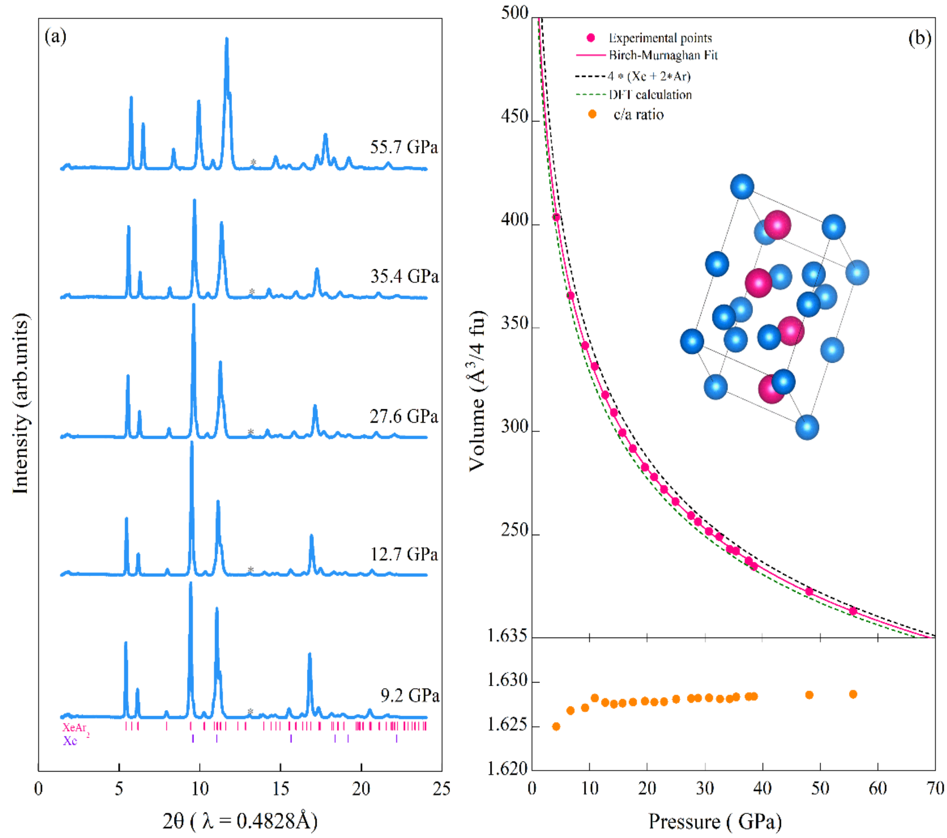

Figure 5.2 *(a): High-pressure x-ray diffraction patterns ($\lambda = 0.4828$ Å) of XeAr$_2$ to 55.7 GPa on compression at room temperature. Asterisks correspond to Re gaskets. The pressures were determined from the equation of state of Au. The pink and purple ticks indicate the calculated peak positions for hexagonal XeAr$_2$ and fcc-Xe, respectively. (b): volume per four formula units as a function of pressure. Pink circles are the experimental data for XeAr$_2$ (the error bars are smaller than the symbol size). The pink curve represents the fit of the V (P) data for XeAr$_2$ by the third-order Birch–Murnaghan equation of state with the parameters listed in the Table 5.1. The green dashed line represents the volume as a function of pressure derived from our DFT calculations, and the black dashed lines are the volumes of ideal mixtures of $8 \times$ Ar + $4 \times$ Xe using the previously determined equations of state of pure Xe and Ar. Top inset: crystal-structure of the Laves phase XeAr$_2$, where the Xe atoms (pink spheres) and the Ar (blue spheres) occupy the Mg (4f) and Zn (2a+6h) sites, respectively. Bottom inset: the experimental c/a ratio of XeAr$_2$ as a function of pressure.*

from excess Xe (see right inset to Fig. 1). The Le Bail refinement of $XeAr_2$ (Fig. 1) indicates that it has hexagonal symmetry, with a = 6.569 Å, c = 10.644 Å at 4 GPa. Its indexing by charge-flipping suggests the space group $P6_3/mmc$ and accounts for all observed Bragg peaks. The hexagonal structure of $XeAr_2$ with 12 atoms in the unit cell can be assigned to the $MgZn_2$-type where the Xe atoms and the Ar occupy the Mg (4f) and Zn (2a+6h) sites, respectively (Fig 5.2 inset).

We find $XeAr_2$ remains stable with no phase transition in the studied pressure range. The unit cell volume and cell parameters of $XeAr_2$ shift smoothly with increasing pressure, as shown in Fig. 5.2 (a), suggesting no change of stoichiometry nor phase transition up to 56 GPa. The volume of the cell, 331.238 $Å^3$ is only 0.14 % lower than the volume of 8 × Ar + 4 × Xe at the same pressure, 10.9 GPa, indicating no chemical interaction between xenon and argon. There is good agreement between the experimental and theoretically derived volumes (green dashed line in Fig. 5.2 (b)). In addition, the c/a ratio is close to the ideal value of $\sqrt{8/3}$. The volume per 4 formula as a function of pressure of $XeAr_2$ from experiment, $XeAr_2$ from DFT calculation, and a literature value of 4 × (Xe + 2* Ar) are fitted with the third-order Birch–Murnaghan P–V equation of states (see Fig. 5. 2(b)) with the fit parameters shown in Table 5.1. Estimated from the equation of state of xenon and argon, the radius ratio varies from 1.15 to 1.2 between 6 and 100 GPa [37, 47]. The bulk moduli of $XeAr_2$ are slightly smaller than pure Xe but bigger than pure Ar.

Our DFT calculations support the structural assignment, as the $MgZn_2$ structure type is the energetically most favoured Laves type structure for $XeAr_2$ at all pressures (Figure 5.4 and Figure 5.5). Its calculated pressure-volume relation is close to, but systematically below, the experimental data, see Fig. 5.2. While there is a thermal expansion discrepancy between the DFT data (calculated in the ground state) and the XRD (measured at room temperature), this can not account alone for this difference, as the role of thermal effects should decrease with increasing pressure. Since there is no chemical bonding in this compound, its compressibility is determined solely by Pauli repulsion, and therefore depends on how accurately the DFT functional describes the closed shell electron distribution of both Xe and Ar. We conjecture that the PBE functional produces atoms that are slightly “ smaller ” and “ softer ” than they should be, therefore artificially increasing the density and compressibility of $XeAr_2$.

Table 5.1 *Third-order Birch-Murnaghan EoS fittings for XeAr$_2$.*

Substance	V_0 ($\AA^3$/4.fu)	B_0 (GPa)	B_0'	Source
XeAr$_2$-Exp	613 ± 55	3.7 ± 1.3	4.9 ± 0.3	This work
XeAr$_2$-DFT	600 ± 43	1.6 ± 1.7	5.7 ± 0.7	This work
4*Xe + 8*Ar	672 ± 66	2.8 ± 1.7	5.0 ± 0.4	[49], [154]

5.2 Raman Spectroscopy

We have performed Raman spectroscopy experiments on both pure xenon and pure argon to 50 GPa at room temperature to provide a comparison with their mixture. There are no Raman-active modes for *fcc* xenon and argon, however upon the transformation to the *hcp* phase, the transverse optic E$_{2g}$ phonon mode could be observed (see Fig. 5.3). The onset of E$_{2g}$ phonon mode of *hcp* -Xe appears at 7.9 GPa with frequency of 50 cm^{-1}, reaching 97 cm^{-1} at 52.7 GPa. Whilst, the argon E$_{2g}$ phonon mode appears at 20.1 GPa with a frequency of 111cm^{-1}, and its Raman frequency increases with pressure to 169 cm^{-1} at 51.5 GPa. The Raman intensity of the E$_{2g}$ increase with pressure for both xenon and argon, which results from a gradual increase of the relative fraction of the hcp phase in a two-phase *fcc* + *hcp* mixture. This is in very good agreement with previous experimental and theoretical work [155, 156].

The Raman modes of XeAr$_2$ appear upon solidification of the mixture. The Raman spectrum consists of four resolvable modes as shown in Fig 5.3 (c). At 3.5 GPa, the lowest-frequency mode (predicted to be at a frequency of 40 cm^{-1}) overlaps with that of pure Xe at the same conditions, however this becomes resolvable at higher pressure.

5.3 DFT Calculation

Our calculations yield a total of 7 Raman active modes of XeAr$_2$, with 4 of these observed in experiments. The remaining calculated modes have intensities an order of magnitude lower than the others, hence they were not observed in the experiments. Fig. 5.6 shows the experimental Raman spectra (lower) and re-normalized fitted peak intensities compared with theoretical DFT intensities (top) at 30 GPa. The pressure dependencies of the frequencies obtained in the experiments and theoretical DFT calculation are in very good agreement with one

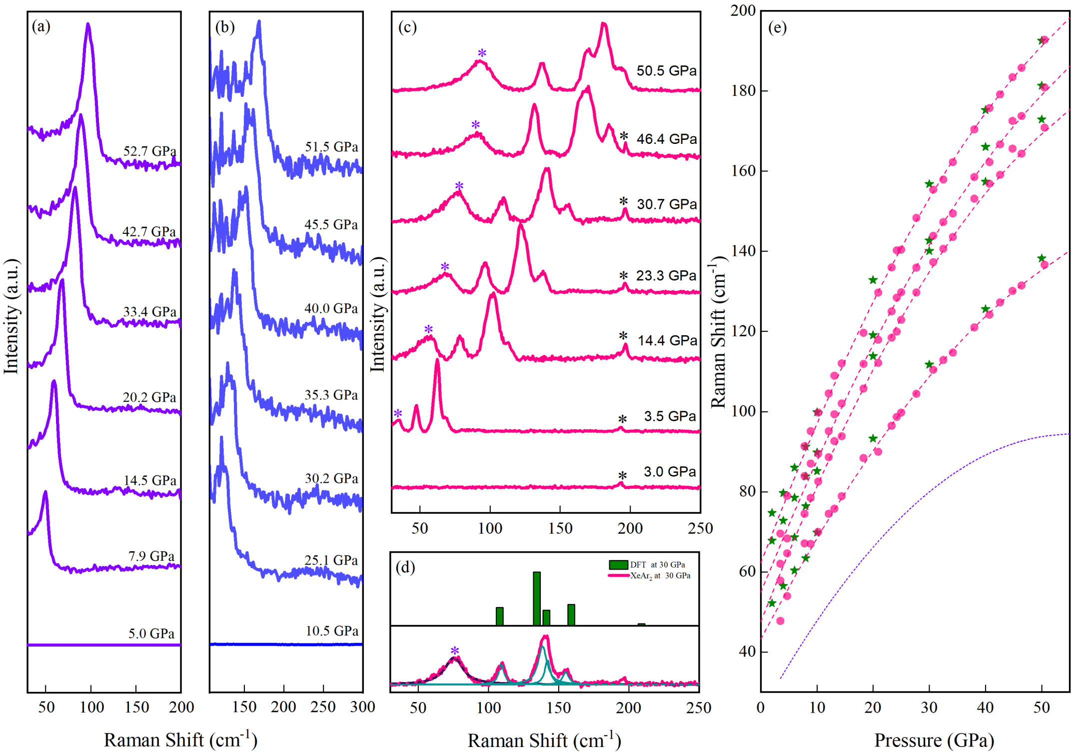

Figure 5.3 *Representative Raman spectra of pure Xe, Ar and their mixture. (a) Raman spectra of pure xenon as a function of pressure. (b) Raman spectra of pure argon as a function of pressure. (c) Raman spectra of* $XeAr_2$*: purple asterisks indicate the mode corresponding to excess Xe in the sample chamber, while the gray asterisks indicate a peak that does not emanate from the sample. (d) Comparison between the experimental Raman spectra (lower) and the Raman spectra obtained from DFT calculations (top) at 30 GPa. The fitted peak intensities of the experimental Raman spectra have been renormalized to make a direct comparison. (e) Vibrational frequencies of* $XeAr_2$ *as a function of pressure. Pink solid circles correspond to the 4 experimentally measured Raman modes of* $XeAr_2$*, green stars are the Raman frequencies derived from DFT calculations. The purple dash dotted curve is the Raman frequency of excess Xe. Pink dashed thin lines are the fittings to the experimental data.*

other. The frequencies of all the Raman modes harden with pressure, however interestingly, the lowest E_{2g} is predicted to monotonically decrease with pressure above 50 GPa. At 2 GPa, the maximum frequency is about 4.2 THz, which increases to 11.5 THz at 30 GPa, and around 14 THz at 50 GPa (Fig. 5.7). These results suggest $XeAr_2$ is dynamically stable.

In binary systems, the mixtures whose ratios of atomic radii r_A/r_B are close to 1.2:1 (this value could varies from 1.05 to 1.7 under extreme condition) are usually considered to be the substitutional AB_2 compounds, referred as the Laves phases [57–59]. For geometric reasons, Laves phase compounds have close packed structures with maximum packing fraction. Three different poly-types of the Laves phase structure are generally observed: cubic $MgCu_2$-type, the hexagonal $MgZn_2$-type, and the hexagonal $MgNi_2$-type. Although a great variety of Laves phase compounds have been synthesized, it is impossible to predict which type of Laves phase one compound belongs to. It is well known that the geometric and electronic factors such as the atomic size ratio, electronegativity and valence electron numbers can affect the structure type of a Laves phase.

In order to provide additional insight and to enable a more systematic understanding of weakly-bonded RGS-RGS binary systems under pressure, we compare $XeAr_2$ with other known RGS-RGS compounds, $NeHe_2$ and $ArNe_2$ [60, 62]. $NeHe_2$ was the first Laves phase reported in the RGS-RGS binary system. At 12.8 GPa, neon and helium form a homogeneous solid mixture, $NeHe_2$. This compound has a hexagonal structure with 12 atoms per unit cell (space group $P6_3/mmc$), with helium occupying 6h (He) sites and neon 4f (Ne) sites. This structure is known as an $MgZn_2$- type Laves phase ($r_{Ne}/r_{He} = 1.19$ at 15 GPa), where neon atoms form a hexagonal diamond sublattice and helium atoms are in the sublattice and form triangular bi-pyramidal chains. $NeHe_2$ has a large bulk modulus and remains stable up to 90 GPa [60]. Another Laves phase stoichiometric compound $ArNe_2$, was recently synthesized and studied up to 60 GPa. $ArNe_2$ adopts a hexagonal structure with 12 atoms in the unit cell (space group $P6_3/mmc$), the structure also belongs to the $MgZn_2$-type Laves phase ($r_{Ar}/r_{Ne} = 1.228$ at 6 GPa) [62]. It is not surprising that Xe and Ar form the identical phase having the hexagonal structure with 12 atoms in the unit cell. $XeAr_2$ belongs to $MgZn_2$-type Laves phase where the Xe atoms and the Ar occupy the Mg (4f) and Zn (2a+6h) sites, respectively. Estimated from equation of state of xenon and argon, radius ratio varies from 1.15 to 1.2 between 6 GPa and 100 GPa [37, 49].

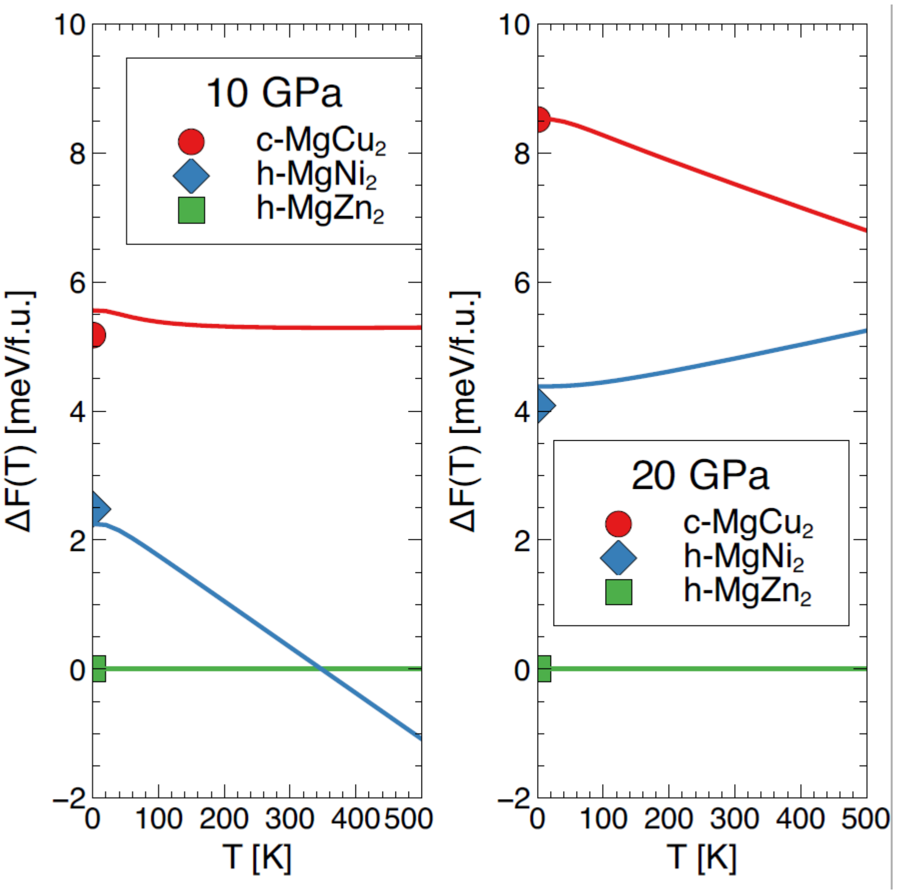

Figure 5.4 *Relative harmonic vibrational free energies for three structure types of* $XeAr_2$*, plotted against temperature at* P *= 10 GPa (left) and 20 GPa (right). Big symbols at* T *= 0 K correspond to relative ground state enthalpies, while lines include zero-point energy (ZPE) and vibrational entropy contributions.*

In the hard sphere model, Laves phases are expected to be stable in a limited pressure range and to decompose into pure end-members with increasing pressure [157]. Previous DFT calculations predicted that for RGS-RGS binary system, the $MgZn_2$ structure is the dominate structure at high temperatures, while $MgCu_2$-type structure is favored at high pressure (density) [61]. These three molecular Laves phases observed experimentally suggest that pressure can stabilize molecular compounds in rare gas solids binary systems. The Laves phases formed within that systems have a $MgZn_2$-type structure at room temperature, showing some disagreement with previous DFT calculations [61, 63]. Moreover, our structure searching results suggest $XeAr_2$ is the only thermodynamically stable configuration whose stability will increase with pressure and it will not decompose into elemental Xe and Ar over a broad pressure range (from 0 GPa to 80 GPa).

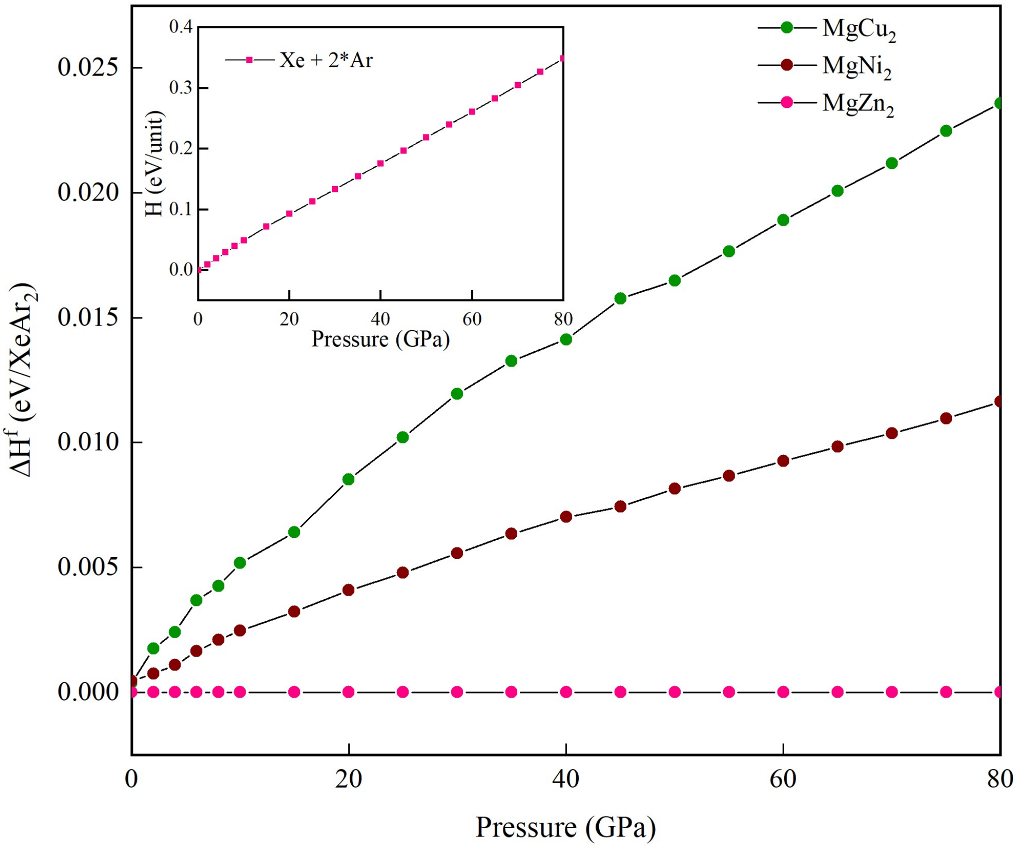

Figure 5.5 *Ground state formation enthalpies of different* $XeAr_2$ *structures, relative to the h-*$MgZn_2$ *structure type, as function of pressure, from DFT-PBE calculations. Note the strongly positive relative enthalpy of the constituents Xe + 2*Ar.*

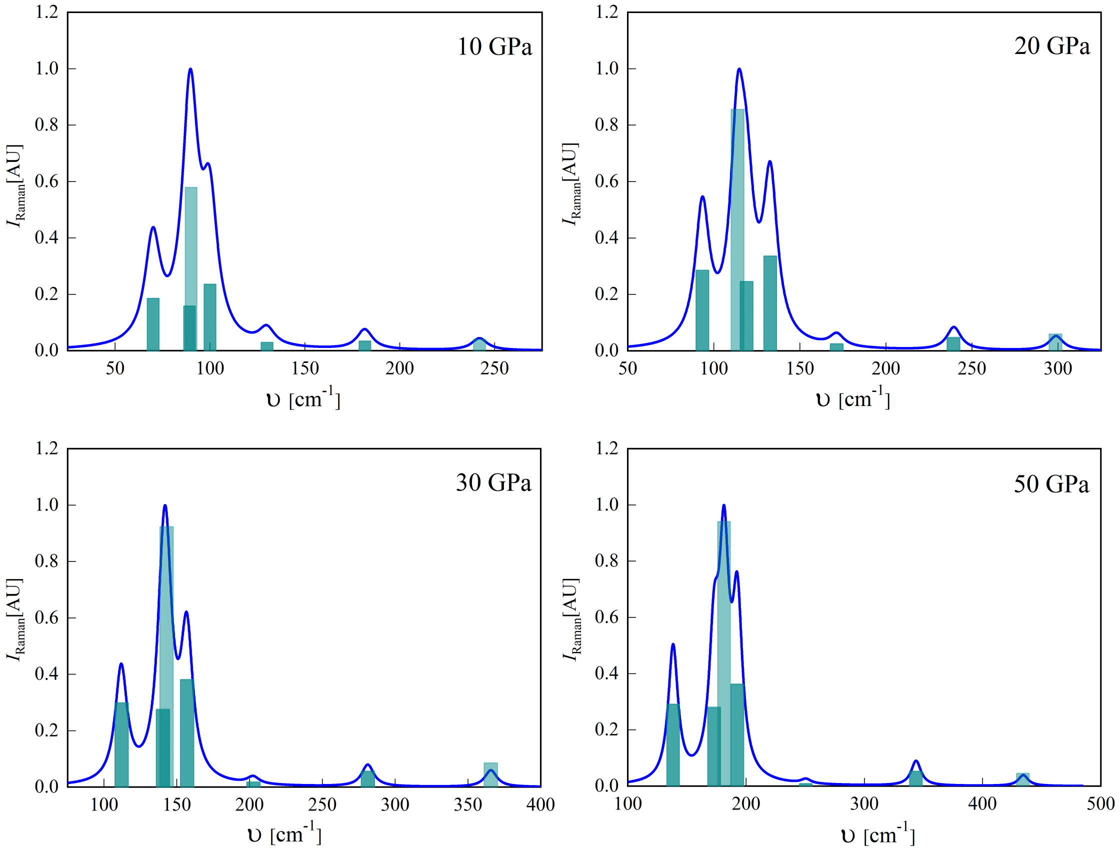

Figure 5.6 *Simulated Raman spectra of* $XeAr_2$ *at 10 GPa, 20 GPa, 30 GPa and 50 GPa, respectively, in the h-*$MgZn_2$ *structure type. We have used a fixed FWHM of 10* cm^{-1} *for all modes.*

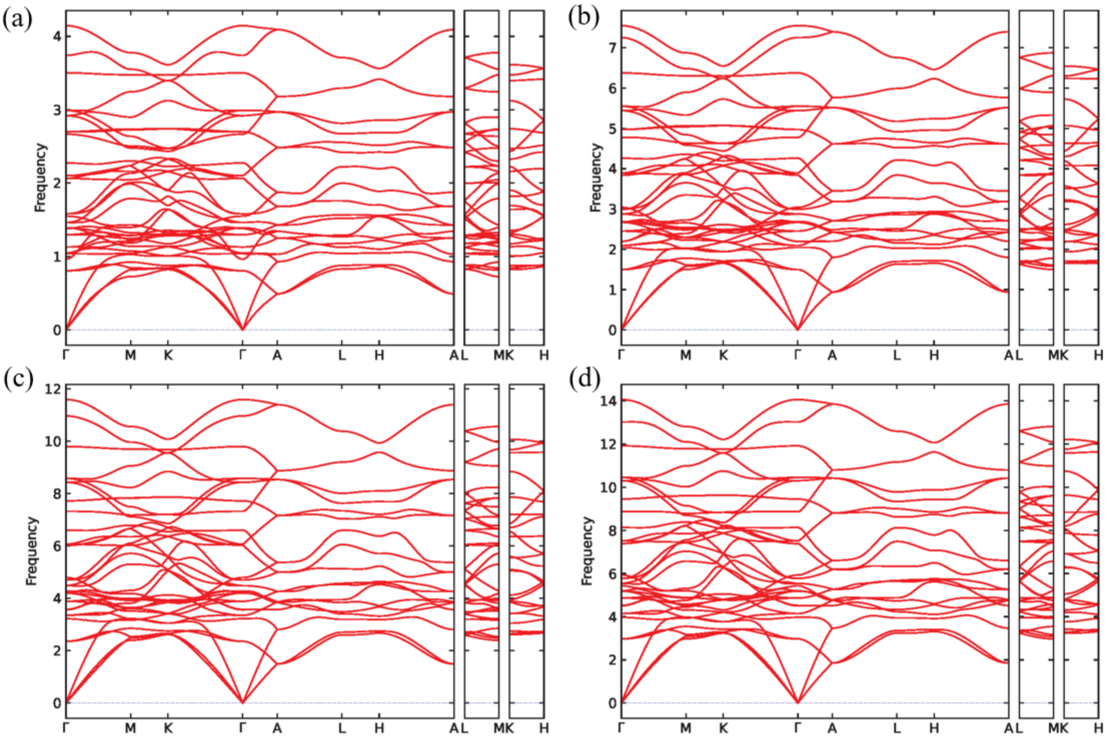

Figure 5.7 *DFT-PBE phonon dispersions of* $XeAr_2$ *at 10 GPa, 20 GPa, 30 GPa and 50 GPa, respectively.*

Chapter 6

Structure and Properties of Nitrogen-trifluoride under Extreme Conditions

Through a series of high-pressure Raman spectroscopy and synchrotron x-ray diffraction experiments combined with DFT calculations, we explored the pressure-temperature phase diagram of nitrogen-trifluoride (NF_3) up to 120 GPa and between 77 and 300 K [1]. Contrary to the previous reports, we observed only one solid-solid phase transition of NF_3 within the studied P-T range. At 300 K nitrogen trifluoride solidifies at 3.3 GPa in a plastic phase I. Further increasing pressure we observed a solid-solid phase transition from plastic phase I to phase HP. Phase HP has a orthorhombic structure ($Pnma$) with the lattice parameters a = 5.771 Å, b = 6.581 Å, c = 4.073 Å at 9 GPa which persists to the highest pressure reached in this work, 120 GPa. Our measurements together with DFT calculations demonstrate that phase HP is stable up to at least 150 GPa at room temperature.

---

[1] Mengnan Wang prepared DACs, carried out Raman experiments up to 120 GPa at room temperature, collected and analysed synchrotron X-ray diffraction data with the help of Dr. Mikhail Kuzovnikov. Low temperature experiments performed by Mengnan with the help of Dr. Xiaodi Liu. Dr. Ross Howie conceived and designed the project. Dr. Bin Li carried out DFT calculations.

6.1 Results and Discussion

6.1.1 Synchrotron X-ray Diffraction

After cryogenic loading, fluid NF_3 confined in DAC sample chamber was warmed up to room temperature. Liquid NF_3 is homogeneously transparent when optically viewed under the microscope. Four characteristic Raman modes can be observed from 0.8 GPa up to 3.5 GPa. Further compressing beyond 3.5 GPa leads to the crystallization of NF_3 into plastic phase I, accompanied by the texture change in the sample chamber.

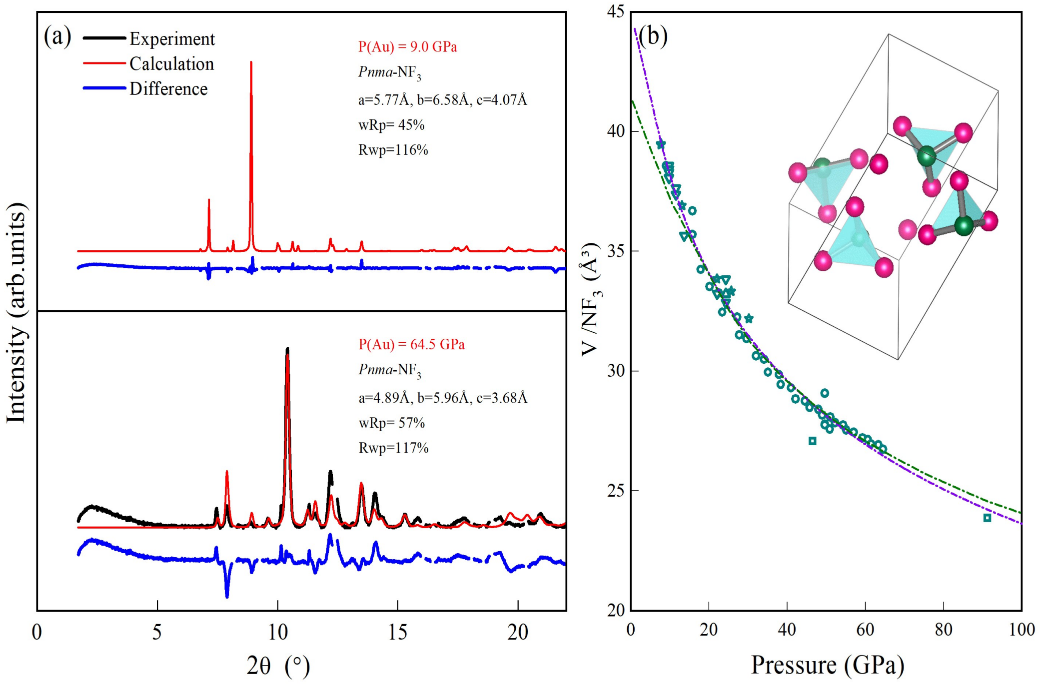

Figure 6.1 *(a): Integrated diffraction data of NF_3 with Rietveld refinement at 9 GPa and 64.5 GPa respectively;* $\lambda = 0.4101$ *Å (b): Equation of state for NF_3 up to 91 GPa. Different symbols refer to different experimental runs, purple dash line is the Vinet EoS, olive solid line is the EoS from calculation. Inset is the crystal structure of NF_3.*

Phase I has been very well studied by neutron diffraction with space group symmetry *P42/mnm*, and cell parameter a = 15.334 Å, c = 7.820 Å under ambient conditions [158]. Phase I remains stable up to 7.5 GPa at room temperature. An obvious change was observed from x-ray pattern when phase I was compressed to 7.5 GPa which we interpreted this as solid-solid phase transition from phase I to phase HP. Through our synchrotron powder x-ray diffraction, phase HP was observed to have a orthorhombic crystal scructure with space group symmetry *Pnma* and unit-cell parameter a = 5.771 A, b = 6.581 A, c = 4.073 A at 9.0 GPa. Phase HP was found to be stable to at least 91 GPa and adopts the same structure throughout the pressure range, even after laser heating at 48 GPa. Figure 6.1 (a) shows the integrated diffraction data of NF_3 with the Rietveld refinement at 9 GPa and 64.5 GPa respectively. Figure 6.1 (b) inset is the crystal structure of NF_3 at 30 GPa. Our interpretation of NF_3 crystal structure shows good agreement with previous DFT calculation [102].

Previous research demonstrated the polymerization into dimer under moderate pressure and decomposition into elemental components at higher pressure on PH_3 and NH_3 [103, 104]. However, unlike PH_3 and NH_3, NF_3 was found to be chemically stable and remains in the molecular form at high pressures. Figure 6.1 (b) is the equation of state for NF_3 compound. Volumes of NF_3 were observed to shift smoothly with increasing pressure and closely follow the calculation values, suggesting no polymerization or decomposition up to 100 GPa. The large electronegativity of fluorine atoms and the lack of hydrogen bond in NF_3 could be the reason of this significant difference.

Under low temperature, NF_3 has been reported to have a orthorhombic structure (space group *Pnma*) with lattice parameters a = 6.71457(13) Å, b = 7.30913(14) Å, c = 4.55189(8) Å at 6 K by neutron diffraction [107]. Our synchrotron x-ray diffraction at high pressure suggests, Phase HP, has the same space group symmetry *Pnma*, with unit-cell parameter a = 5.77 Å, b = 6.58 Å, c = 4.07 Å at 9.0 GPa. Our result and the previous x-ray result indicate the same structure between the low temperature α-phase and the high pressure phase HP. This result could be used to explore the molecular rotations and to construct the phase diagram of NF_3 which will be discussed in the following section.

6.1.2 Raman Spectroscopy

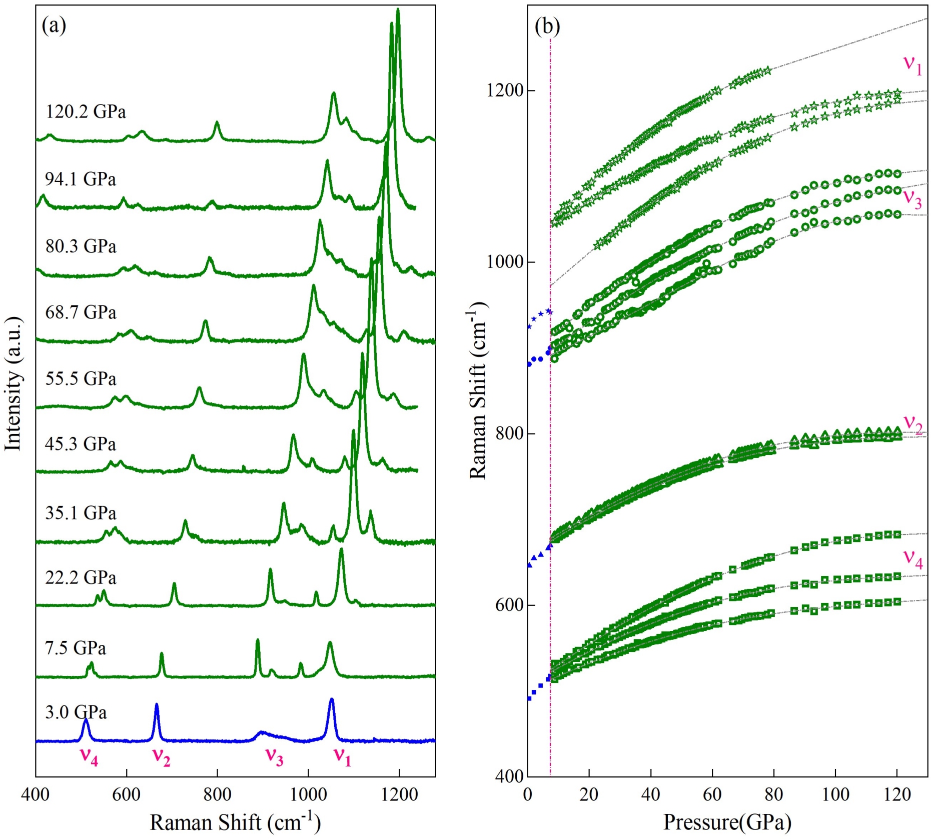

Figure 6.2 *(a): NF_3 Raman spectra to 120 GPa at 300 K. Blue is fluid phase and olive spectra presents solid phase I; (b): Frequency as a function of pressure at room temperature. Different colors refer to different Raman modes. Orange dash dot line presents the crystallized pressure at 7.5 GPa.*

Figure 6.2 (a) shows the Raman spectra of NF_3 up to 120 GPa on compression at room temperature. Characteristic fundamental Raman modes (ν_1-ν_4) can be observed after cryogenic loading at 0.8 GPa. The characteristic fundamental Raman modes of the fluid phase are symmetric stretching mode ν_1 at 1051 cm^{-1}, symmetric bending mode ν_2 at 666 cm^{-1}, asymmetric stretching mode ν_3 at 898 cm^{-1} and asymmetric bending mode ν_4 at 511 cm^{-1} at 3 GPa. Further increasing pressure leads to the crystallization of liquid NF_3 at 3.5 GPa. Raman spectra do not clearly distinguish between the fluid phase and the plastic phase I of NF_3. However, the sample texture resulting from visual observation under a microscope could be used to provide useful information. Above 7.5 GPa we observed obvious splittings of ν_1 to ν_4 Raman modes which we interpreted as phase I to phase HP transition under room temperature.

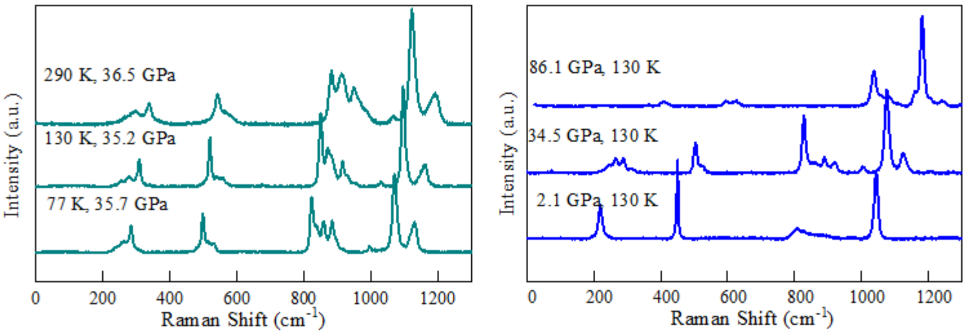

Figure 6.3 *(a): Raman spectra of NF_3 at around 35 GPa. (b): Raman spectra of NF_3 at 130 K.*

In phase HP, the highly polarized ν_1 splits into three modes, ν_1 at 1074 cm^{-1} and two shoulder peaks at 1018 cm^{-1} and 1107 cm^{-1} which can be assigned to the hot band ν_1+ν_4-ν_4 comparing with previous Infrared spectra [159]. The ν_3 mode is less polarized than ν_1 and splits into three peaks whose intensity increase with pressure dramatically. The behavior of ν_1 and ν_3 results from a large transition dipole-transition dipole interaction (TD-TD interaction) [160]. ν_2 centered at 670 cm^{-1} is less polarized than ν_1 in fluid Phase, its intensity decreases with pressure. The depolarized ν_4 splits into three peaks. ν_4 modes has a temperature-sensitive symmetric spectra in the liquid which shows no significant changes in both fluid phase and plastic phase I.

Figure 6.2 (b) shows the Raman frequency of NF_3 as a function of pressure up to 120 GPa. More peaks were detected by Raman spectra, and Raman frequencies of ν_2, ν_3 and ν_4 dramatically decreased and started to red shift at 7.5 GPa which suggest the formation of phase HP. Further increase pressure no drastic changes on ν_1 to ν_4 Raman frequency can be observed. Above phase HP, the frequencies of all Raman modes increase almost linearly up to the highest pressure of the experiment which indicates NF_3 is stable up to at least 120 GPa. Raman frequency of ν_1 - ν_4 modes were found to increase continuously with pressure up to 120 GPa. Previous Raman study on NF_3 claimed three solid-solid transitions at 9, 18, and 39.5 GPa, respectively [102]. However, except for the only plastic phase I to phase HP transition at 7.5 GPa, we did not observe any discontinuously changes in both Raman frequency and width of ν_1 - ν_4 modes. Our results indicate phase HP is the only stable phase in pressure range from 7.5 GPa to 120 GPa at room temperature. This conclusion is supported by our synchrotron x-ray diffraction result.

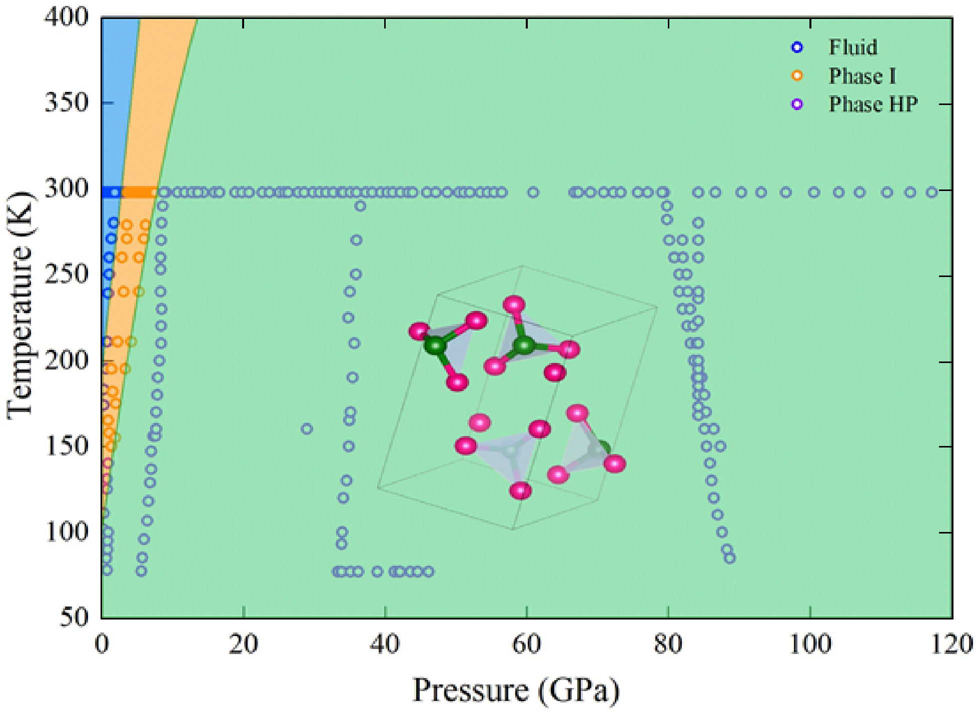

Figure 6.4 *Proposed phase diagram of NF_3 up to 120 GPa. Data points represent different experimental runs. Different colors represent different phases: light blue is the fluid phase; oranges region is plastic Phase I and green area is high pressure phase. Phase boundary lines guides to the eye. Inset is the crystal structure of high pressure phase of NF_3 at 7.5 GPa.*

The phase transition from plastic phase I to phase HP has been studied as a function of pressure and temperature. Our low temperature experiments recorded the phase transition of NF_3 from liquid to solid phase HP at 0.8 GPa, 90 K. Figure 6.3 (a) and (b) plotted Raman spectra at different temperatures around 35 GPa and isothermal decompression at 130 K. Raman spectra suggest the low temperature phase and high pressure phase HP are identical. Only one solid-solid phase transition (phase I to phase HP) has been observed over a broad temperature range from 77 K to 298 K which shows good agreement with both x-ray diffraction and Raman results at room temperature.

Based on the low temperature and room temperature experiment results, we proposed the phase diagram to 120 GPa from 77 K to 300 K (Figure 6.4). The blue area represents the fluid phase of NF_3, orange region in indicates the proposed stability field of the plastic phase I and the light green region is the high pressure phase of NF_3.

The phase diagram of NF_3 displays two solid phases in the studied P-T range. At low temperatures (T) and ambient pressure (P), NF_3 crystallizes in the plastic phase I. By compressing the liquid above 200 K, a rotationally disordered (plastic) phase I with tetragonal structure is obtained. Compression above 112 K gives another solid phase, phase HP, with orthorhombic structure.

Plastic phase I is found to be stable in a narrow P-T region, ranging from 112 K to 200 K (pressure from 3.5 GP a to 7.5 GPa at room temperature). However, phase HP is found to be the dominate phase that exists in an extensive stability field (light green area). The phase diagram of NF_3 is found to be very similar to that of NH_3, both of which crystallize in plastic phase I and undergo a transformation to the orthorhombic phase HP within the same pressure-temperature (P-T) range. The main difference between NH_3 and NF_3, in terms of intermoecular interactions, is the absence of hydrogen bonds in NF_3, the similitude between NH_3 and NF_3 indicates that the hydrogen bonds have little influence on the melting properties of NF_3 in the P-T range covered by our experiments.

Previous studies show that NH_3 and PH_3 are chemically unstable at high pressures, partially dissociating into its elemental components [103, 104]. However, unlike the hydrogen-bond trigonal pyramidal compounds, NF_3 is found to be very stable under room teperature (Figure A.3). We also performed laser heating experiment on NF_3 at 94 GPa and no drastic changes of the Raman spectra can be observed even pressure went up to 120 GPa.

6.1.3 DFT Calculation

To better understand the stability and structural characteristic of the high-pressure transitions in NF_3 we performed first principles DFT calculations up to 100 GPa. The relative enthalpy of the most stable structures of NF_3 is found to be orthorhombic $Pnma$-NF_3. Only one phase transition was observed up to 100 GPa. Figure 6.5 shows the Raman and IR spectrum of NF_3 at 40 GPa from DFT calculation which shows good agreement with our Raman results and previous IR result under the same pressure [102].

The phonon spectra of *Pnma* (No.62) phase for NF_3 from 0 GPa to 100 GPa are shown in figure 6.6. Owing to the crystal symmetry, the spectra curves are shown along the high symmetry direction Γ - X - S - Y - Γ - Z - U - R - T - Z | X - U | Y - T | S - R of the Brillouin zone. There are no imaginary frequency for all cases, which demonstrate dynamic stable for all pressures we studied. The vibration frequencies show phonon hardening as the pressure increases. At 0 GPa, the maximum frequency is about 1000 cm^{-1} (30 THz), which increases to 1100 cm^{-1} (33 THz) at 50 GPa, and around 1200 cm^{-1} (35 THz) at 100 GPa. The point group of Pnma-NF$_3$ is $D_{2\mathrm{h}}$ (mmm). The irreducible representation $\Gamma = 7A_{\mathrm{g}} \oplus 5A_{\mathrm{u}} \oplus 5B_{1\mathrm{g}} \oplus 7B_{1\mathrm{u}} \oplus 7B_{2\mathrm{g}} \oplus 5B_{2\mathrm{u}} \oplus 5B_{3\mathrm{g}} \oplus 7B_{3\mathrm{u}}$, with Raman active modes: $7A_{\mathrm{g}} \oplus 5B_{1\mathrm{g}} \oplus 7B_{2\mathrm{g}} \oplus 5B_{3\mathrm{g}}$, and infrared active modes: $6B_{1\mathrm{u}} \oplus 4B_{2\mathrm{u}} \oplus 6B_{3\mathrm{u}}$.

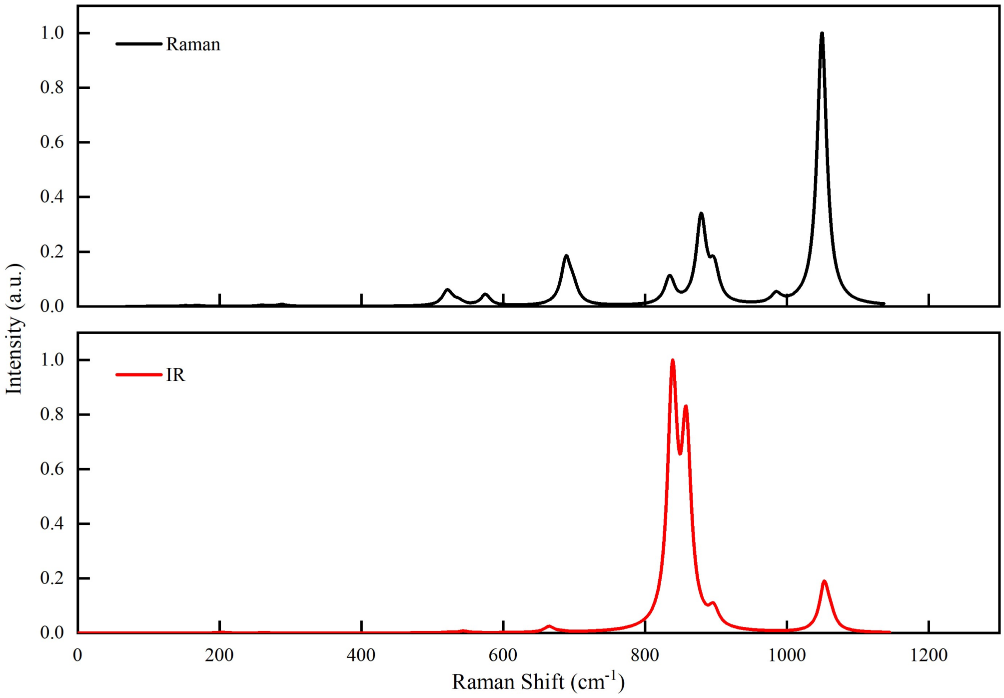

Figure 6.5 *Raman and IR spectrum of NF$_3$ from DFT calculation at 40 GPa.*

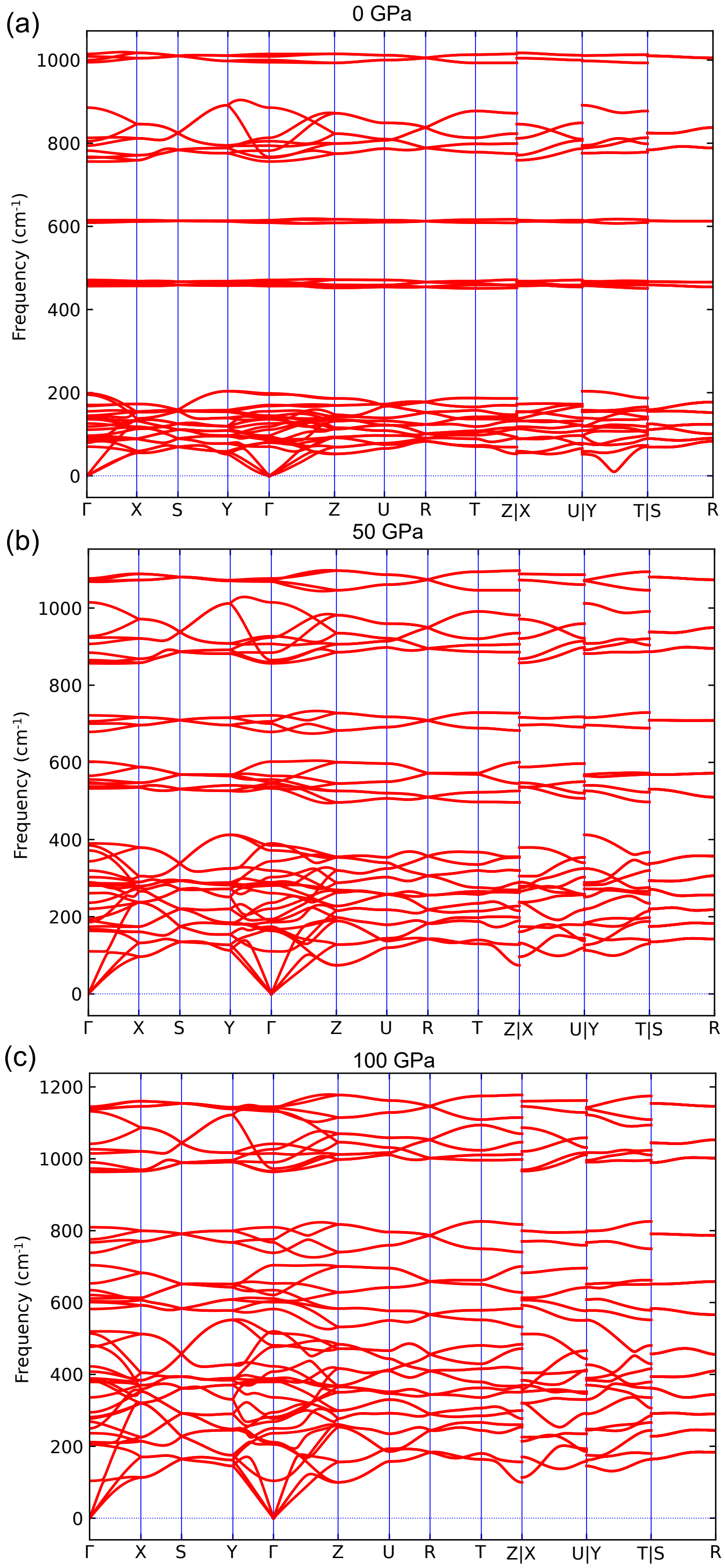

Figure 6.6 *Phonon dispersion spectrum of* NF_3 *at 0 GPa, 50 GPa and 100 GPa, respectively.*

Chapter 7

Conclusions and Future Work

The purpose of this thesis was to investigate structures and properties of three simple gases under extreme conditions. Due to the high compressibility, simple gases under high pressure usually exhibit exotic properties and rich chemistry. This chapter provides a summary of the main findings from the study of three gas/gas mixture systems, with a particular emphasis on CH_4, and outlines potential directions for future research.

As the simplest hydrocarbon, CH_4 exhibits a rich variety of crystal structures due to differences in orientational ordering of molecules. In contrast to the abundance of experimental and theoretical work at low temperatures, phase relations in the C–H system under high temperatures were poorly understood, even at relatively low pressures. In this work, by combining Raman spectroscopy and *in-situ* high-pressure, high-temperature resistive heating and laser heating techniques, we demonstrated the complexity of the phase diagram of CH_4 up to 45 GPa and 1400 K.

First we performed high pressure studies on the well-documented phases and phase transitions of CH_4 at room temperature, to explore their respective stability fields. By using Raman spectroscopy, we observed all the reported phases and identified five phase transitions from fluid to phase HP of CH_4. The monitoring of the phase transformations used in this work was more elaborate than the ones reported: we not only studied the appearance/disappearance and the Raman frequency changes of the vibrational modes of ν_1 and ν_3 but also examined their full-width at half-maximum (FWHM).

Furthermore, we investigated the phase transitions and stabilities of CH_4 up to 270 GPa using Raman spectroscopy, marking a significant high-pressure achievement on slow compression of CH_4 at room temperature. In addition to the previously mentioned five phase transitions, we observed a discontinuous change in the Raman spectra at approximately 105 GPa, corresponding to the phase transition from the simple cubic to *c*-HP phase as previously reported by X-ray diffraction experiments [150]. However, we did not observe the expected decomposition of CH_4 into diamond and hydrogen, even at the highest pressure reached in our study, 270 GPa. [88].

Our high temperature study started with the known phase diagram of CH_4, to study its melting curve at moderate pressure. The melting curve of CH_4 through resistive heating technique showed good agreement with previous reported results below 10 GPa [1, 2]. Conducting a series of high-pressure, high-temperature experiments allowed us to detect all phase transitions and construct a comprehensive phase diagram of CH_4. The phase behaviour of CH_4 were found to be more complicated than previous thought.

Below 5 GPa, we observed CH_4 melting directly via phase I, with the melting temperature increasing with pressure. Upon heating, from 5 GPa to 8 GPa, CH_4 underwent a phase transition from phase A to phase I and then melted through phase I to fluid at elevated temperatures. Above 8 GPa, we observed that phase B of CH_4 first transformed to phase A before melting to fluid at higher temperatures. By combining resistive heating and laser heating at higher pressure and temperatures, we observed that at pressure above 16.6 Pa, phase HP of CH_4 changed to phase B ultimately melting directly from the same phase at higher temperatures. Our results suggested that Phase I and phase A remain stable in a very narrow P-T range, in contrast to phase B, which exists in an extensive stability field.

We traced the phase I-phase A boundary of phase I and phase A up to 16.7 GPa and 710 K, where it intersects the extrapolated melting curve, forming a triple point (Phase A - I - Liquid). This marks the first triple point observed under high pressures and temperatures along the melting curve. Our high P-T study results suggested a positive slope change above this triple point. The phase transition line from phase B to phase A is found to continue at a constant gradient until it reaches the melt curve at around 42 GPa, 1110 K, indicating another possible triple point (Phase B - A - Liquid). This could be the second triple point under high pressures and temperatures. However, we were unable to obtain accurate pressure and temperature conditions for this potential triple point due to the accuracy limitations of our high temperature measurements under high pressure.

Furthermore, the previously reported sluggish transitions from phase A to phase B and phase HP were found to be controlled by kinetics. In this study, we observed that various factors, such as reaction time, temperatures, and pressure, can lead to different pathways, thus producing different phases of CH_4 (phase A or phase B).

The second system studied in this work was rare gas binary system. The simple closed-shell electronic configurations make rare gases and their mixtures an ideal case to compare experiment and theory. The structures and properties of rare gases and rare gas mixtures are of significant importance for chemistry, physics, and planetary science as they have been considered to help understanding van der Waals (vdW) interactions. Furthermore, heavier rare gases such as Kr and Xe play crucial roles in chemical synthesis processes.

As a consequence of their simplicity and inert chemical behaviour, rare gases are not known to react with one another, but can form van der Waals compounds under extreme pressure conditions. In this work, we explored the Xe-Ar system up to pressures of 60 GPa using combined Raman spectroscopy, x-ray diffraction, and first-principle DFT calculations. A novel van der Waals compound $XeAr_2$ was observed at 3.5 GPa. Powder x-ray diffraction analysis demonstrated that $XeAr_2$ adopted a Laves $MgZn_2$-type structure with space group $P6_3/mmc$ and cell parameters a = 6.569 Å c = 10.644 Å at 4 GPa. We found that pressure stabilized the formation of a stoichiometric, solid van der Waals compound of composition $XeAr_2$. Our Raman spectroscopy suggested that $XeAr_2$ remained stable up to 60 GPa. Our DFT calculation on formation enthalpy indicated $XeAr_2$ was the only stable van der Waals compound in the Xe-Ar system, and it remained stable without any phase transition or decomposition up to at least 80 GPa.

The third simple gas studied in this work was nitrogen-trifluoride. Through a series of high-pressure Raman spectroscopy and synchrotron x-ray diffraction experiments combined with DFT calculations, we explored the pressure-temperature phase diagram of nitrogen-trifluoride (NF_3) up to 120 GPa and between 77 and 300 K. Contrary to the previous reports, we observed only one solid-solid phase transition of NF_3 within the studied P-T range. At 300 K nitrogen trifluoride solidified at 3.3 GPa in a plastic phase I. Further increasing pressure, we observed a solid-solid phase transition from plastic phase I to phase HP. Our powder synchrotron x-ray diffraction result suggested that phase HP had a orthorhombic structure (*Pnma*) with the lattice parameters a = 5.771 Å, b = 6.581 Å, c = 4.073 Å at 9 GPa which persisted to the highest pressure reached in this work, 120 GPa. Our measurements together with DFT calculations demonstrated that phase HP was stable up to at least 150 GPa at room temperature.

This work suggests three clear directions for possible future studies:

(1). In this work, we investigated the phase transition and constructed the phase diagram of CH_4 up to 45 GPa and 1400 K. We precisely identified a triple point at 16.7 GPa and 710 K and proposed the existence of another potential triple point along the melting curve at pressures exceeding 42 GPa. More resistive heating experiments are needed to construct the phase diagram of CH_4 to higher pressure and temperatures.

(2). It is almost certain that polymerization of CH_4 and diamond formation would occur, as indicated by this work and previous research. However, a comprehensive study of carbon-hydrogen reactions at higher pressure and temperatures would be of great significance for understanding the properties and revolutions of the Earth and some giant icy planets.

(3). A novel compound $XeAr_2$ has been successfully synthesized in Xe-Ar binary system. However, the mechanism explaining the coexistence of *fcc* and *hcp* phases over a broad pressure range for heavier rare gases remains unclear. Meanwhile, despite the capability of DFT calculations to predict the formation of intermediate compounds in rare gas systems, they currently lack the ability to differentiate between the three Laves-type phases mentioned in chapter 5. A more systematic study in rare gas binary systems would be highly beneficial.

Bibliography

[1] Takehiko Yagi and Hiroto Suzuki. Melting curve of methane to 4.8 GPa determined by the ruby pressure-temperature marker. *Proceedings of the Japan Academy, Series B*, 66(9):167–172, 1990.

[2] Evan H Abramson. Melting curves of argon and methane. *High Pressure Research*, 31(4):549–554, 2011.

[3] Sergey S Lobanov, Pei-Nan Chen, Xiao-Jia Chen, Chang-Sheng Zha, Konstantin D Litasov, Ho-Kwang Mao, and Alexander F Goncharov. Carbon precipitation from heavy hydrocarbon fluid in deep planetary interiors. *Nature Communications*, 4(1):1–8, 2013.

[4] Maxim Bykov, Elena Bykova, Chris J Pickard, Miguel Martinez-Canales, Konstantin Glazyrin, Jesse S Smith, and Alexander F Goncharov. Structural and vibrational properties of methane up to 71 GPa. *Physical Review B*, 104(18):184105, 2021.

[5] Ross T Howie, Philip Dalladay-Simpson, and Eugene Gregoryanz. Raman spectroscopy of hot hydrogen above 200 GPa. *Nature materials*, 14(5):495–499, 2015.

[6] P W Bridgman. Explorations toward the limit of utilizable pressures. *Journal of Applied Physics*, 12(6):461–469, 1941.

[7] CE Weir, ER Lippincott, A Van Valkenburg, and EN Bunting. Infrared studies in the 1-to-15-micron region to 30,000 atmospheres. *Journal of research of the National Bureau of Standards. Section A, Physics and chemistry*, 63(1):55, 1959.

[8] John C Jamieson, AW Lawson, and ND Nachtrieb. New device for obtaining x-ray diffraction patterns from substances exposed to high pressure. *Review of Scientific instruments*, 30(11):1016–1019, 1959.

[9] Ho-Kwong Mao and Peter M Bell. High-pressure physics: the 1-megabar mark on the ruby R_1 static pressure scale. *Science*, 191(4229):851–852, 1976.

[10] Richard A Forman, Gasper J Piermarini, J Dean Barnett, and Stanley Block. Pressure measurement made by the utilization of ruby sharp-line luminescence. *Science*, 176(4032):284–285, 1972.

[11] Henry Cavendish. Xiii. experiments on air. *Philosophical Transactions of the Royal Society of London*, 74:119–153, 1784.

[12] Lord Rayleigh and William Ramsay. Argon, a new constituent of the atmosphere. *Philosophical Transactions of the Royal Society of London. A*, 186:187–241, 1895.

[13] William Crookes. The spectrum of helium. *The Astrophysical Journal*, 2:227, 1895.

[14] William Ramsay and Morris William Travers. On a new constituent of atmospheric air. *Proceedings of the Royal Society of London*, 63(389-400):405–408, 1898.

[15] Irving Langmuir. The arrangement of electrons in atoms and molecules. *Journal of the American Chemical Society*, 41(6):868–934, 1919.

[16] Howard H Claassen, Henry Selig, and John G Malm. Xenon tetrafluoride. *Journal of the American Chemical Society*, 84(18):3593–3593, 1962.

[17] Henry Selig, Howard H Claassen, Cedric L Chernick, John G Malm, and John L Huston. Xenon tetroxide: preparation and some properties. *Science*, 143(3612):1322–1323, 1964.

[18] Agnès Dewaele, Nicholas Worth, Chris J Pickard, Richard J Needs, Sakura Pascarelli, Olivier Mathon, Mohamed Mezouar, and Tetsuo Irifune. Synthesis and stability of xenon oxides Xe_2O_5 and Xe_3O_2 under pressure. *Nature chemistry*, 8(8):784–790, 2016.

[19] Jules Janssen. Indications de quelques-uns des résultats obténusa guntoor, pendant l'éclipse du mois d'août dernier. *Comptes Rendus*, 67:838–39, 1868.

[20] David J Stevenson. Metallic helium in massive planets. *Proceedings of the National Academy of Sciences*, 105(32):11035–11036, 2008.

[21] Tristan Guillot. The interiors of giant planets: Models and outstanding questions. *Annu. Rev. Earth Planet. Sci.*, 33:493–530, 2005.

[22] Lars Stixrude and Raymond Jeanloz. Fluid helium at conditions of giant planetary interiors. *Proceedings of the National Academy of Sciences*, 105(32):11071–11075, 2008.

[23] George H Watson Jr and William B Daniels. Raman scattering from solid helium at high pressure. *Physical Review B*, 31(7):4705, 1985.

[24] HK Mao, RJ Hemley, Y Wu, AP Jephcoat, LW Finger, CS Zha, and WA Bassett. High-pressure phase diagram and equation of state of solid helium from single-crystal x-ray diffraction to 23.3 GPa. *Physical review letters*, 60(25):2649, 1988.

[25] P Loubeyre, R LeToullec, JP Pinceaux, HK Mao, J Hu, and RJ Hemley. Equation of state and phase diagram of solid he from single-crystal x-ray diffraction over a large p-t domain. *Physical review letters*, 71(14):2272, 1993.

[26] Chang-Sheng Zha, Ho-Kwang Mao, and Russell J Hemley. Elasticity of dense helium. *Physical Review B*, 70(17):174107, 2004.

[27] WJ Nellis, NC Holmes, AC Mitchell, RJ Trainor, GK Governo, M Ross, and DA Young. Shock compression of liquid helium to 56 GPa (560 kbar). *Physical Review Letters*, 53(13):1248, 1984.

[28] LW Finger, RM Hazen, G Zou, HK Mao, and PM Bell. Structure and compression of crystalline argon and neon at high pressure and room temperature. *Applied Physics Letters*, 39(11):892–894, 1981.

[29] WL Vos, JA Schouten, DA Young, and M Ross. The melting curve of neon at high pressure. *The Journal of chemical physics*, 94(5):3835–3838, 1991.

[30] Hiroyasu Shimizu, Hiroki Imaeda, Tetsuji Kume, and Shigeo Sasaki. High-pressure elastic properties of liquid and solid neon to 7 gpa. *Physical Review B*, 71(1):014108, 2005.

[31] RJ Hemley, CS Zha, AP Jephcoat, HK Mao, LW Finger, and DE Cox. X-ray diffraction and equation of state of solid neon to 110 gpa. *Physical Review B*, 39(16):11820, 1989.

[32] Anatoly B Belonoshko, Rajeev Ahuja, and Börje Johansson. Molecular dynamics study of melting and fcc-bcc transitions in xe. *Physical Review Letters*, 87(16):165505, 2001.

[33] K Takemura, T Watanuki, K Ohwada, A Machida, A Ohmura, and K Aoki. Powder x-ray diffraction study of ne up to 240 gpa. In *Journal of Physics: Conference Series*, volume 215, page 012017. IOP Publishing, 2010.

[34] Agnes Dewaele, Frédéric Datchi, Paul Loubeyre, and Mohamed Mezouar. High pressure–high temperature equations of state of neon and diamond. *Physical Review B*, 77(9):094106, 2008.

[35] Frédéric Datchi, Paul Loubeyre, and René LeToullec. Extended and accurate determination of the melting curves of argon, helium, ice (h 2 o), and hydrogen (h 2). *Physical Review B*, 61(10):6535, 2000.

[36] Hiroyasu Shimizu, Hideyuki Tashiro, Tetsuji Kume, and Shigeo Sasaki. High-pressure elastic properties of solid argon to 70 GPa. *Physical review letters*, 86(20):4568, 2001.

[37] D Errandonea, R Boehler, S Japel, M Mezouar, and LR Benedetti. Structural transformation of compressed solid ar: An x-ray diffraction study to 114 GPa. *Physical Review B*, 73(9):092106, 2006.

[38] I Kwon, LA Collins, JD Kress, and N Troullier. First-principles study of solid ar and kr under high compression. *Physical Review B*, 52(21):15165, 1995.

[39] Yu A Freiman, Alexander F Goncharov, SM Tretyak, A Grechnev, S Tse John, D Errandonea, Ho-kwang Mao, and Russell J Hemley. Raman scattering in hcp rare gas solids under pressure. *Physical Review B*, 78(1):014301, 2008.

[40] RK Crawford. Ch. 11 of rare gas solids. eds. ml klein and ja venables, 1976.

[41] Daniel Errandonea, Beate Schwager, Reinhard Boehler, and Marvin Ross. Phase behavior of krypton and xenon to 50 GPa. *Physical Review B*, 65(21):214110, 2002.

[42] H Shimizu, N Saitoh, and S Sasaki. High-pressure elastic properties of liquid and solid krypton to 8 gpa. *Physical Review B*, 57(1):230, 1998.

[43] Hiroyasu Shimizu, Masashi Kawajiri, Tetsuji Kume, Shigeo Sasaki, Yuri A Freiman, and Sergey M Tretyak. High-pressure fcc-to-hcp phase transition in solid krypton studied by raman spectroscopy. *Physical Review B*, 79(13):132101, 2009.

[44] David A Nelson Jr and Arthur L Ruoff. Metallic xenon at static pressures. *Physical Review Letters*, 42(6):383, 1979.

[45] M Ross and AK McMahan. Condensed xenon at high pressure. *Physical Review B*, 21(4):1658, 1980.

[46] Kenneth A Goettel, Jon H Eggert, Isaac F Silvera, and William C Moss. Optical evidence for the metallization of xenon at 132(5) GPa. *Physical review letters*, 62(6):665, 1989.

[47] Wendel A Caldwell, Jeffrey H Nguyen, Bernd G Pfrommer, Francesco Mauri, Steven G Louie, and Raymond Jeanloz. Structure, bonding, and geochemistry of xenon at high pressures. *Science*, 277(5328):930–933, 1997.

[48] AP Jephcoat, H-k Mao, LW Finger, D E Cox, R J Hemley, and C-S Zha. Pressure-induced structural phase transitions in solid xenon. *Physical review letters*, 59(23):2670, 1987.

[49] H Cynn, CS Yoo, B Baer, V Iota-Herbei, AK McMahan, M Nicol, and S Carlson. Martensitic fcc-to-hcp transformation observed in xenon at high pressure. *Physical review letters*, 86(20):4552, 2001.

[50] Maddury Somayazulu, Przemyslaw Dera, Alexander F Goncharov, Stephen A Gramsch, Peter Liermann, Wenge Yang, Zhenxian Liu, Ho-kwang Mao, and Russell J Hemley. Pressure-induced bonding and compound formation in xenon–hydrogen solids. *Nature chemistry*, 2(1):50–53, 2010.

[51] D Laniel, G Weck, and P Loubeyre. $Xe(N_2)_2$ compound to 150 gpa: Reluctance to the formation of a xenon nitride. *Physical Review B*, 94(17):174109, 2016.

[52] Cheng Ji, Alexander F Goncharov, Vivekanand Shukla, Naresh K Jena, Dmitry Popov, Bing Li, Junyue Wang, Yue Meng, Vitali B Prakapenka, Jesse S Smith, et al. Stability of $Ar(H_2)_2$ to 358 gpa. *Proceedings of the National Academy of Sciences*, 114(14):3596–3600, 2017.

[53] Annette K Kleppe, Mónica Amboage, and Andrew P Jephcoat. New high-pressure van der waals compound $Kr(H_2)_4$ discovered in the krypton-hydrogen binary system. *Scientific reports*, 4(1):1–6, 2014.

[54] Ross T Howie, Robin Turnbull, Jack Binns, Mungo Frost, Philip Dalladay-Simpson, and Eugene Gregoryanz. Formation of xenon-nitrogen compounds at high pressure. *Scientific Reports*, 6(1):1–6, 2016.

[55] C Kittel. Introduction to solid state physics, 6th edn., translated by y. *Uno, N. Tsuya, A. Morita and J. Yamashita,(Maruzen, Tokyo, 1986) pp*, pages 124–129, 1986.

[56] W L Vos, L W Finger, R J Hemley, J Z Hu, H K Mao, and J A Schouten. A high-pressure van der waals compound in solid nitrogen-helium mixtures. *Nature*, 358(6381):46–48, 1992.

[57] F Laves. Theory of alloy phases (american society for metals symposium). *Cleveland, Ohio*, 124, 1956.

[58] A Sari and G Merad. Ab initio study of structural stability and electronic properties of $Ti_{1\text{-}x}Mg_xCr_2$ and $TiMg_xCr_{2\text{-}x}$ laves phase. In *AIP Conference Proceedings*, volume 1653, page 020094. AIP Publishing LLC, 2015.

[59] Frank Stein, Martin Palm, and Gerhard Sauthoff. Structure and stability of laves phases. part i. critical assessment of factors controlling laves phase stability. *Intermetallics*, 12(7-9):713–720, 2004.

[60] Paul Loubeyre, Michel Jean-Louis, René LeToullec, and Lydie Charon-Gérard. High pressure measurements of the He−Ne binary phase diagram at 296 K: Evidence for the stability of a stoichiometric $NeHe_2$ solid. *Phys. Rev. Lett.*, 70:178–181, Jan 1993.

[61] C Cazorla, D Errandonea, and E Sola. High-pressure phases, vibrational properties, and electronic structure of $NeHe_2$ and $ArHe_2$: A first-principles study. *Physical Review B*, 80(6):064105, 2009.

[62] Agnès Dewaele, Angelika D. Rosa, and Nicolas Guignot. Argon-neon binary diagram and $ArNe_2$ laves phase. *The Journal of Chemical Physics*, 151(12):124708, 2019.

[63] Geng. Hua Y. Yan. Xiao Z, Chen. Yang M. Prediction of the reactivity of argon with xenon under high pressures. *ACS Omega*, 4:13640–13644, 2019.

[64] W B Hubbard, W J Nellis, A C Mitchell, N C Holmes, S S Limaye, and P C McCandless. Interior Structure of Neptune: Comparison with Uranus. *Science*, 253:648 – 651, 1991.

[65] Bradford A Smith, Laurence A Soderblom, D Banfield, AT Basilevsky, RF Beebe, K Bollinger, JM Boyce, A Brahic, GA Briggs, RH Brown, et al. Voyager 2 at neptune: Imaging science results. *Science*, 246(4936):1422–1449, 1989.

[66] Gunnar F Lindal, JR Lyons, DN Sweetnam, VR Eshleman, DP Hinson, and GL Tyler. The atmosphere of uranus: Results of radio occultation measurements with voyager 2. *Journal of Geophysical Research: Space Physics*, 92(A13):14987–15001, 1987.

[67] H Hirai, K Konagai, T Kawamura, Y Yamamoto, and T Yagi. Polymerization and diamond formation from melting methane and their implications in ice layer of giant planets. *Physics of the Earth and Planetary Interiors*, 174(1-4):242–246, 2009.

[68] L R Benedetti, J H Nguyen, W A Caldwell, H Liu, M Kruger, and R Jeanloz. Dissociation of CH_4 at High Pressures and Temperatures: Diamond Formation in Giant Planet Interiors? *Science*, 286:100 – 102, 1999.

[69] Roberto Bini, Lorenzo Ulivi, Hans J Jodl, and Pier R Salvi. High pressure crystal phases of solid CH_4 probed by fourier transform infrared spectroscopy. *The Journal of chemical physics*, 103(4):1353–1360, 1995.

[70] Roberto Bini and Gabriele Pratesi. High-pressure infrared study of solid methane: Phase diagram up to 30 gpa. *Physical Review B*, 55(22):14800, 1997.

[71] Pei-Nan Chen, Chang-Sheng Zha, Xiao-Jia Chen, Jinfu Shu, Russell J Hemley, and Ho-kwang Mao. Raman study of phase transitions in compressed methane using moissanite anvil cells. *Physical Review B*, 84(10):104110, 2011.

[72] William M Haynes. *CRC handbook of chemistry and physics*. CRC press, 2016.

[73] AI Prokhvatilov and AP Isakina. Lattice parameters, thermal expansion coefficients, and vacancy density in solid CD_4. *physica status solidi (a)*, 78(1):147–155, 1983.

[74] JH Colwell, EK Gill, and JA Morrison. Thermodynamic properties of CH_4 and CD_4. interpretation of the properties of the solids. *The Journal of Chemical Physics*, 39(3):635–653, 1963.

[75] RM Hazen, HK Mao, LW Finger, and PM Bell. Structure and compression of crystalline methane at high pressure and room temperature. *Applied Physics Letters*, 37(3):288–289, 1980.

[76] HE Maynard-Casely, CL Bull, M Guthrie, I Loa, MI McMahon, E Gregoryanz, RJ Nelmes, and JS Loveday. The distorted close-packed crystal structure of methane a. *The Journal of chemical physics*, 133(6):064504, 2010.

[77] HE Maynard-Casely, LF Lundegaard, I Loa, MI McMahon, E Gregoryanz, RJ Nelmes, and JS Loveday. The crystal structure of methane b at 8 gpa—an α-mn arrangement of molecules. *The Journal of Chemical Physics*, 141(23):234313, 2014.

[78] Hirai. H, K. Konagai, T. Kawamura, Y. Yamamoto, and T. Yagi. Phase changes of solid methane under high pressure up to 86 GPa at room temperature. *Chemical Physics Letters*, 454(4-6):212–217, 2008.

[79] J E Proctor, H E Maynard-Casely, M A Hakeem, and D Cantiah. Raman spectroscopy of methane (CH_4) to 165 GPa: Effect of structural changes on raman spectra. *Journal of Raman Spectroscopy*, 48(12):1777–1782, 2017.

[80] Eugene Gregoryanz, Alexander F Goncharov, Kiyoto Matsuishi, Ho-kwang Mao, and Russell J Hemley. Raman spectroscopy of hot dense hydrogen. *Physical Review Letters*, 90(17):175701, 2003.

[81] Lewis J Conway and Andreas Hermann. High pressure hydrocarbons revisited: from van der waals compounds to diamond. *Geosciences*, 9(5):227, 2019.

[82] Anastasia S Naumova, Sergey V Lepeshkin, and Artem R Oganov. Hydrocarbons under pressure: Phase diagrams and surprising new compounds in the c–h system. *The Journal of Physical Chemistry C*, 123(33):20497–20501, 2019.

[83] Anton Kolesnikov, Vladimir G Kutcherov, and Alexander F Goncharov. Methane-derived hydrocarbons produced under upper-mantle conditions. *Nature Geoscience*, 2(8):566–570, 2009.

[84] A Zerr, George Serghiou, R Boehler, and M Ross. Decomposition of alkanes at high pressures and temperatures. *High Pressure Research*, 26(1):23–32, 2006.

[85] W J Nellis, D C Hamilton, and A C Mitchell. Electrical conductivities of methane, benzene, and polybutene shock compressed to 60 GPa (600 kbar). *The Journal of Chemical Physics*, 115(2):1015–1019, 2001.

[86] Dominik Kraus, J Vorberger, A Pak, NJ Hartley, LB Fletcher, S Frydrych, E Galtier, EJ Gamboa, DO Gericke, SH Glenzer, et al. Formation of diamonds in laser-compressed hydrocarbons at planetary interior conditions. *Nature Astronomy*, 1(9):606–611, 2017.

[87] Chi Zhang and Zhenhao Duan. A model for c–o–h fluid in the earth's mantle. *Geochimica et Cosmochimica Acta*, 73(7):2089–2102, 2009.

[88] Guoying Gao, Artem R Oganov, Yanming Ma, Hui Wang, Peifang Li, Yinwei Li, Toshiaki Iitaka, and Guangtian Zou. Dissociation of methane under high pressure. *The Journal of Chemical Physics*, 133(14):144508, 2010.

[89] JF Kenney, Vladimir A Kutcherov, Nikolai A Bendeliani, and Vladimir A Alekseev. The evolution of multicomponent systems at high pressures: Vi. the thermodynamic stability of the hydrogen–carbon system: The genesis of hydrocarbons and the origin of petroleum. *Proceedings of the National Academy of Sciences*, 99(17):10976–10981, 2002.

[90] F Ancilotto, Guido L Chiarotti, S Scandolo, and E Tosatti. Dissociation of methane into hydrocarbons at extreme (planetary) pressure and temperature. *Science*, 275(5304):1288–1290, 1997.

[91] Marvin Ross. The ice layer in uranus and neptune—diamonds in the sky? *Nature*, 292(5822):435–436, 1981.

[92] Randall Scheele, Bruce McNamara, Andrew M Casella, and Anne Kozelisky. On the use of thermal NF_3 as the fluorination and oxidation agent in treatment of used nuclear fuels. *Journal of nuclear materials*, 424(1-3):224–236, 2012.

[93] Igor'Appolinarievich Fedorov. Efficiency of using nitrogen trifluoride as an oxidiser in a supersonic continuous-wave chemical HF laser. *Quantum Electronics*, 50(2):157, 2020.

[94] Mingfu He, Yuanda Li, Rui Guo, and Betar M Gallant. Electrochemical conversion of nitrogen trifluoride as a gas-to-solid cathode in li batteries. *The journal of physical chemistry letters*, 9(16):4700–4706, 2018.

[95] Bing Ji, James H. Yang, Peter R. Badowski, and Eugene J. Karwacki. Optimization and analysis of NF_3 *in-situ* chamber cleaning plasmas. *Journal of Applied Physics*, 95(8):4452–4462, 2004.

[96] Yongsheng Niu, Lixin Sun, Congwei Hu, Jinhao Zhou, Qiang Dou, and Qingnuan Li. Study on the fluorination reaction of uranium tetrafluoride by nitrogen trifluoride. *Journal of Fluorine Chemistry*, 230:109436, 2020.

[97] Tim Arnold, Christina M Harth, Jens Mühle, Alistair J Manning, Peter K Salameh, Jooil Kim, Diane J Ivy, L Paul Steele, Vasilii V Petrenko, Jeffrey P Severinghaus, et al. Nitrogen trifluoride global emissions estimated from

updated atmospheric measurements. *Proceedings of the National Academy of Sciences*, 110(6):2029–2034, 2013.

[98] Ray F Weiss, Jens Mühle, Peter K Salameh, and Christina M Harth. Nitrogen trifluoride in the global atmosphere. *Geophysical Research Letters*, 35(20), 2008.

[99] Thomas M Klapötke. Nitrogen–fluorine compounds. *Journal of fluorine chemistry*, 127(6):679–687, 2006.

[100] Richard D Harcourt and Thomas M Klapötke. Valence bond and molecular orbital studies of the a–f bond lengths in some AFn type molecules and their fluorinated cations. *Journal of fluorine chemistry*, 123(2):273–278, 2003.

[101] Michael J Prather and Juno Hsu. NF_3, the greenhouse gas missing from kyoto. *Geophysical Research Letters*, 35(12), 2008.

[102] D Kurzydłowski, H B Wang, I A Troyan, and M I Eremets. Lone-pair interactions and photodissociation of compressed nitrogen trifluoride. *The Journal of Chemical Physics*, 141(6):064706, 2014.

[103] JGO Ojwang, R Stewart McWilliams, Xuezhi Ke, and Alexander F Goncharov. Melting and dissociation of ammonia at high pressure and high temperature. *The Journal of Chemical Physics*, 137(6):064507, 2012.

[104] Ye Yuan, Yinwei Li, Guoyong Fang, Guangtao Liu, Cuiying Pei, Xin Li, Haiyan Zheng, Ke Yang, and Lin Wang. Stoichiometric evolutions of ph3 under high pressure: implication for high-t c superconducting hydrides. *National Science Review*, 6(3):524–531, 2019.

[105] Fernando Blanco, Ibon Alkorta, Isabel Rozas, Mohammad Solimannejad, and José Elguero. A theoretical study of the interactions of NF_3 with neutral ambidentate electron donor and acceptor molecules. *Physical Chemistry Chemical Physics*, 13(2):674–683, 2011.

[106] Verner Schomaker and Chia-Si Lu. An electron-diffraction investigation of nitrogen trifluoride. *Journal of the American Chemical Society*, 72(3):1182–1185, 1950.

[107] Karl O. Christe, Richard D. Wilson, and Ira B. Goldberg. Formation and decomposition mechanism of tetrafluoronitrogen (1+) salts. *Inorganic Chemistry*, 18(9):2572–2577, 1979.

[108] Adolf Smekal. Zur quantentheorie der dispersion. *Naturwissenschaften*, 11(43):873–875, 1923.

[109] Gr Landsberg and L Mandelstam. Über die lichtzerstreuung in kristallen. *Zeitschrift für Physik*, 50(11):769–780, 1928.

[110] C. V. Raman and K. S. Krishnan. The optical analogue of the compton effect. *Nature*, 121(3053):711–711, 1928.

[111] Chandrasekhara Venkata Raman and Kariamanikkam Srinivasa Krishnan. A new type of secondary radiation. *Nature*, 121(3048):501–502, 1928.

[112] L Andrew Lyon, Christine D Keating, Audrey P Fox, Bonnie E Baker, Lin He, Sheila R Nicewarner, Shawn P Mulvaney, and Michael J Natan. Raman spectroscopy. *Analytical Chemistry*, 70(12):341–362, 1998.

[113] Peter W Atkins and Ronald S Friedman. *Molecular quantum mechanics*. Oxford university press, 2011.

[114] Miriam Peña-Alvarez, Veronika Afonina, Philip Dalladay-Simpson, Xiao-Di Liu, Ross T Howie, Peter IC Cooke, Ioan B Magdau, Graeme J Ackland, and Eugene Gregoryanz. Quantitative rotational to librational transition in dense H_2 and D_2. *The Journal of Physical Chemistry Letters*, 11(16):6626–6631, 2020.

[115] M Wojdyr. *Fityk*: a general-purpose peak fitting program. *Journal of Applied Crystallography*, 43:1126–1128, 2010.

[116] Walter Friedrich, Paul Knipping, and Max Laue. Interferenzerscheinungen bei roentgenstrahlen. *Annalen der Physik*, 346(10):971–988, 1913.

[117] William Henry Bragg and William Lawrence Bragg. The reflection of x-rays by crystals. *Proceedings of the Royal Society of London. Series A, Containing Papers of a Mathematical and Physical Character*, 88(605):428–438, 1913.

[118] William Lawrence Bragg. The structure of some crystals as indicated by their diffraction of x-rays. *Proceedings of the Royal Society of London. Series A, Containing papers of a mathematical and physical character*, 89(610):248–277, 1913.

[119] Clemens Prescher and Vitali B. Prakapenka. Dioptas: a program for reduction of two-dimensional x-ray diffraction data and data exploration. *High Pressure Research*, 35(3):223–230, 2015.

[120] Werner Kraus and Gert Nolze. POWDER CELL–a program for the representation and manipulation of crystal structures and calculation of the resulting x-ray powder patterns. *Journal of applied Crystallography*, 29(3):301–303, 1996.

[121] H-P Liermann, Z Konôpková, W Morgenroth, K Glazyrin, J Bednarčik, EE McBride, S Petitgirard, JT Delitz, M Wendt, Y Bican, et al. The extreme conditions beamline p02. 2 and the extreme conditions science infrastructure at petra iii. *Journal of synchrotron radiation*, 22(4):908–924, 2015.

[122] Susannah M Dorfman, Vitali B Prakapenka, Yuanku Meng, and Thomas S Duffy. Intercomparison of pressure standards (au, pt, mo, MgO, NaCl and ne) to 2.5 mbar. *Journal of Geophysical Research: Solid Earth*, 117(B8), 2012.

[123] HK Mao, J-A Xu, and PM Bell. Calibration of the ruby pressure gauge to 800 kbar under quasi-hydrostatic conditions. *Journal of Geophysical Research: Solid Earth*, 91(B5):4673–4676, 1986.

[124] Javier Gonzalez-Platas, Matteo Alvaro, Fabrizio Nestola, and Ross Angel. *EosFit7-GUI*: a new graphical user interface for equation of state calculations, analyses and teaching. *Journal of Applied Crystallography*, 49(4):1377–1382, Aug 2016.

[125] Thomas Scheler, Olga Degtyareva, and Eugene Gregoryanz. On the effects of high temperature and high pressure on the hydrogen solubility in rhenium. *The Journal of chemical physics*, 135(21):214501, 2011.

[126] Thomas Scheler, Feng Peng, Christophe L Guillaume, Ross T Howie, Yanming Ma, and Eugene Gregoryanz. Nanocrystalline tungsten hydrides at high pressures. *Physical Review B*, 87(18):184117, 2013.

[127] Mikhail A Kuzovnikov, Vasily S Minkov, Stella Chariton, Vitali B Prakapenka, and Mikhail I Eremets. Synthesis of osmium hydride under high hydrogen pressure. *Physical Review B*, 102(21):214109, 2020.

[128] DJ Dunstan. Theory of the gasket in diamond anvil high-pressure cells. *Review of scientific instruments*, 60(12):3789–3795, 1989.

[129] R L Mills, D H Liebenberg, J C Bronson, and L C Schmidt. Procedure for loading diamond cells with high-pressure gas. *Review of Scientific Instruments*, 51(7):891–895, 1980.

[130] Alexander F Goncharov and Jonathan C Crowhurst. Pulsed laser raman spectroscopy in the laser-heated diamond anvil cell. *Review of Scientific Instruments*, 76(6):063905, 2005.

[131] Chang-Sheng Zha and William A Bassett. Internal resistive heating in diamond anvil cell for *in-situ* x-ray diffraction and raman scattering. *Review of scientific instruments*, 74(3):1255–1262, 2003.

[132] Philip Dalladay-Simpson. *Raman Studies on Hot Dense Hydrogen.* PhD thesis, University of Edinburgh, 2016.

[133] Zhong-Hua Shen and Shu-Yi Zhang. Laser heating of thin plate with time-dependent absorptance. *Microwave and optical technology letters*, 28(5):364–367, 2001.

[134] Ge J Piermarini, S Block, JD Barnett, and RA Forman. Calibration of the pressure dependence of the R_1 ruby fluorescence line to 195 kbar. *Journal of Applied Physics*, 46(6):2774–2780, 1975.

[135] M Hanfland, K Syassen, S Fahy, Steven G Louie, and Marvin L Cohen. Pressure dependence of the first-order raman mode in diamond. *Physical Review B*, 31(10):6896, 1985.

[136] Yuichi Akahama and Haruki Kawamura. High-pressure raman spectroscopy of diamond anvils to 250 gpa: Method for pressure determination in the multimegabar pressure range. *Journal of Applied Physics*, 96(7):3748–3751, 2004.

[137] Y. Akahama and H. Kawamura. Pressure calibration of diamond anvil raman gauge to 310 gpa. *Journal of Applied Physics*, 100(4):043516, 2006.

[138] Ming S Liu, Les A Bursill, S Prawer, and R Beserman. Temperature dependence of the first-order raman phonon line of diamond. *Physical Review B*, 61(5):3391, 2000.

[139] Philip Dalladay-Simpson, Ross T Howie, and Eugene Gregoryanz. Evidence for a new phase of dense hydrogen above 325 gigapascals. *Nature*, 529(7584):63–67, 2016.

[140] Dion L Heinz and Raymond Jeanloz. The equation of state of the gold calibration standard. *Journal of applied physics*, 55(4):885–893, 1984.

[141] Brian H. Toby and Robert B. Von Dreele. *GSAS-II*: the genesis of a modern open-source all purpose crystallography software package. *Journal of Applied Crystallography*, 46(2):544–549, Apr 2013.

[142] G. Kresse and J. Furthmüller. Efficient Iterative Schemes for ab initio Total-energy Calculations Using a Plane-wave Basis Set. *Phys. Rev. B*, 54(16):11169–11186, oct 1996.

[143] John P. Perdew, Kieron Burke, and Matthias Ernzerhof. Generalized Gradient Approximation Made Simple. *Phys. Rev. Lett.*, 77(18):3865–3868, 1996.

[144] Atsushi Togo and Isao Tanaka. First principles phonon calculations in materials science. *Scripta Materialia*, 108:1–5, 2015.

[145] Jonathan M. Skelton, Lee A. Burton, Adam J. Jackson, Fumiyasu Oba, Stephen C. Parker, and Aron Walsh. Lattice dynamics of the tin sulphides SnS_2, SnS and Sn_2S_3: Vibrational spectra and thermal transport. *Phys. Chem. Chem. Phys.*, 19(19):12452–12465, 2017.

[146] Václav Petříček, Michal Dušek, and Lukáš Palatinus. Crystallographic computing system jana2006: general features. *Zeitschrift für Kristallographie-Crystalline Materials*, 229(5):345–352, 2014.

[147] Karlheinz Schwarz, Peter Blaha, and Georg KH Madsen. Electronic structure calculations of solids using the wien2k package for material sciences. *Computer physics communications*, 147(1-2):71–76, 2002.

[148] P Hebert, A Polian, P Loubeyre, and R Le Toullec. Optical studies of methane under high pressure. *Physical Review B*, 36(17):9196, 1987.

[149] FD Medina and WB Daniels. Raman spectrum of phase iii of solid CH_4 in the lattice and intramolecular regions. *The Journal of Chemical Physics*, 70(6):2688–2694, 1979.

[150] Liling Sun, Wei Yi, Lin Wang, Jinfu Shu, Stas Sinogeikin, Yue Meng, Guoyin Shen, Ligang Bai, Yanchuan Li, Jing Liu, et al. X-ray diffraction studies and equation of state of methane at 202 GPa. *Chemical Physics Letters*, 473(1-3):72–74, 2009.

[151] S Umemoto, T Yoshii, Y Akahama, and H Kawamura. X-ray diffraction measurements for solid methane at high pressures. *Journal of Physics: Condensed Matter*, 14(44):10675, 2002.

[152] L Sun, A L Ruoff, C-S Zha, and G Stupian. Optical properties of methane to 288 GPa at 300 K. *Journal of Physics and Chemistry of Solids*, 67(12):2603 – 2608, 2006.

[153] Liling Sun, Zhongxian Zhao, Arthur L Ruoff, Chang-Sheng Zha, and Gary Stupian. Raman studies on solid CH_4 at room temperature to 208 gpa. *Journal of Physics: Condensed Matter*, 19(42):425206, 2007.

[154] M Ross, HK Mao, PM Bell, and JA Xu. The equation of state of dense argon: A comparison of shock and static studies. *The Journal of chemical physics*, 85(2):1028–1033, 1986.

[155] Yu. A. Freiman, Alexander F. Goncharov, S. M. Tretyak, A. Grechnev, John S. Tse, D. Errandonea, Ho-kwang Mao, and Russell J. Hemley. Raman scattering in *hcp* rare gas solids under pressure. *Phys. Rev. B*, 78:014301, Jul 2008.

[156] Hiroyasu Shimizu, Naoyuki Wada, Tetsuji Kume, Shigeo Sasaki, Yansun Yao, and John S. Tse. Pressure-induced structural transformation in solid xenon studied by raman spectroscopy. *Phys. Rev. B*, 77:052101, Feb 2008.

[157] A-P Hynninen, L Filion, and M Dijkstra. Stability of LS and LS_2 crystal structures in binary mixtures of hard and charged spheres. *The Journal of chemical physics*, 131(6):064902, 2009.

[158] Sergei I Ivlev, Matthias Conrad, Markus Hoelzel, Antti J Karttunen, and Florian Kraus. Crystal structures of α-and β-nitrogen trifluoride. *Inorganic chemistry*, 58(9):6422–6430, 2019.

[159] M Kent Wilson and Santiago R Polo. The infrared spectra of NF_3 and PF_3. *The Journal of Chemical Physics*, 20(11):1716–1719, 1952.

[160] M Gilbert, P Nectoux, and M Drifford. The raman spectrum of NF_3: Coriolis coupling and transition dipole interaction in the liquid. *The Journal of Chemical Physics*, 68(2):679–691, 1978.

Publications

[1] Wang, M.; Howie, R.T.; Gregoryanz, E. and Alvarez, M.P. Revised Phase Diagram of Methane. *Submitted.*

[2] Wang, M.; Kuzovnikov, M.A.; Binns, J.; Li, X.; Alvarez, M.P. Hermann, A.; Gregoryanz, E. and Howie, R.T. Synthesis and Characterization of $XeAr_2$ under High Pressure. *accepted.*

[3] Wang, M.; Li, B.; Kuzovnikov, M.A.; Binns, J.; Liu, X-D; Alvarez, M.P.; Gregoryanz, E. and Howie, R.T. Structure and Phase Diagram of Nitrogen-trifluoride at Extreme Conditions. *under review.*

[4] Wang, M.; Binns, J.; Donnelly, M-E.; Dalladay-Simpson, P. and Howie, R.T.; High pressure synthesis and stability of cobalt hydrides. *J. Chem. Phys* 148, 144310 (2018).

[5] Ranieri, U.; Conway, L. J.; Donnelly, M-E.; Hu, H.; Wang, M.; Dalladay-Simpson, P.; Alvarez, M.P.; Gregoryanz, E.; Hermann, A.; and Howie, R.T.; Formation and Stability of Dense Methane-Hydrogen Compounds. *Phys. Rev. Lett.* 128, 215702 (2022).

[6] Alvarez, M. P.; Brovarone, A. V.; Donnelly, M-E.; Wang, M.; Dalladay-Simpson, P.; Howie, R.T.; and Gregoryanz, E.; *In-situ* abiogenic methane synthesis from diamond and graphite under geologically relevant conditions. *Nat Commun.* 12, 6387 (2021).

[7] Binns, J.; Hermann, A.; Alvarez, M.P.; Donnelly, M-E.; Wang, M.; Kawaguchi, S.I.; Gregoryanz, E.; Howie, R.T.; and Dalladay-Simpson, P.; Superionicity, disorder, and bandgap closure in dense hydrogen chloride. *Science Advances.* 7, 36 (2021).

[8] Binns, J.; He, Y.; Donnelly, M-E.; Alvarez, M.P.; Wang, M.; Kim, D.Y.; Gregoryanz, E.; Dalladay-Simpson, P.; and Howie, R.T.; Complex Hydrogen Substructure in Semimetallic RuH_4. *J. Phys. Chem. Lett.* 11, 9, 3390–3395 (2020).

[9] Binns, J.; Donnelly, M.E.; Wang, M.; Dalladay-Simpson, P.; Hermann, A.; Gregoryanz, E.; and Howie, R.T.; “Synthesis of Ni_2H_3 at High Temperature and Pressure”, *Phys. Rev. B,* 98, 140101 (2018).

[10] Turnbull, R.; Donnelly, M.E.; Wang, M.; Alvarez, M.P.; Cheng, J.; Dalladay-Simpson, P.; Mao, H.-K.; Gregoryanz, E.; Howie, R.T.; “Reactivity of Hydrogen-Helium and Hydrogen-Nitrogen Mixtures at High Pressures”, *Phys. Rev. Lett,* 121, 195702 (2018).

[11] Dalladay-Simpson, P.; Binns, J.; Wang, M.; Alvarez, M.P.; Pace, E. J.; Gregoryanz, E. Chen, X. J.; and Howie, R.T.; “Structure of Lithium-Zinc Compounds at High Pressure”, *J. Chem. Phys,* 149, 024306 (2018).

[12] Binns, J.; Dalladay-Simpson,P.; Wang, M.; Gregoryanz, E.; and Howie, R.T.; “Enhanced Reactivity of Lithium and Copper at High Pressure”, *J. Phys. Chem. Lett.* 9, 11, 3149-3153 (2018).

[13] Binns, J.; Dalladay-Simpson, P.; Wang, M.; Ackland, G.J.; Gregoryanz, E.; and Howie, R.T. “Formation of H_2-rich Iodine-Hydrogen Compounds at High Pressure”, *Phys. Rev. B,* 97, 024111 (2018).

Supplementary Material for CH_4

Supplementary Table 1. List of high temperature high pressure experiments for CH_4.

No.	Dates	Experimental details	Initial phase	Phase transitions
1	10 - Aug 2021	P-C cell, Re gasket, Mo heater, 20 µm, ruby	Phase A	Phase A - phase I at 6.5 GPa, 370 K; Phase I - fluid at 7.1 GPa, 560 K.
2	17 - Aug 2021	P-C cell, Re gasket, Mo heater, 19 µm, ruby	Phase A	Phase A - phase I at 7.7 GPa, 430 K; Phase I - fluid at 6.7 GPa, 545 K; Fluid - phase A at 17.2 GPa, 683 K.
3	24 - Aug 2021	P-C cell, Re gasket, Mo heater, 19 µm, ruby	Phase I	Phase I - fluid at 1.4 GPa, 415 K.
4	25 - Aug 2021	P-C cell, Re gasket, Mo heater,17 µm, ruby	Phase I	Phase I - fluid at 3.2 GPa, 426 K + reacted.
5	01 - Sept 2021	P-C cell, Re gasket, Mo heater, 20 µm, ruby	Fluid (room T)	Phase I - phase A at 5.1 GPa, 298 K; Phase A - phase B at 7.9 GPa, 298 K; Phase B - phase HP at 23.5 GPa, 298 K.
6	24 - Sept 2021	P-C cell, Re gasket, Mo heaters, 20 µm, ruby	Fluid	Fluid - phase I at 17.2 GPa, 683 K; Phase I - phase A at 4.5 GPa, 298 K; Phase A - phase I at 4.7 GPa, 410 K; Phase I - fluid at 4.7 GPa, 430 K; Fluid - phase I at 4.3 GPa, 476 K; Phase I - phase A at 10.2 GPa, 492 K;

				Phase A - Phase B at 19.3 GPa, 492 K; Phase B - phase A at 12.7 GPa, 562 K, Phase A - phase I at 13.3GPa, 600 K; Phase I - fluid at 11.8 GPa, 760 K.
7	29-Sept 2021	P-C cell, Re gasket, Mo heater, 18 µm, ruby	Phase B	Phase B - phase A at 12 GPa, 400 K.
8	01-Oct 2021	P-C cell, Re gasket, Mo heaters, 15 µm, ruby	Fluid (room T)	Fluid - phase I at 1.6 GPa, 298 K; Phase I - phase A at 5.3 GPa, 298 K; Phase A - phase B at 16.5 GPa, 298 K; Phase B - phase HP at 22.8 GPa, 298 K.
9	11- Oct 2021	P-C cell, Re gasket, Mo heater, 15 µm, ruby	Phase A	Phase A - phase I at 9 GPa 430 K; Phase I - fluid at 8.7 GPa, 515 K.
10	19- Oct 2021	P-C cell, Re gasket, Mo heaters, 32 µm, ruby	Phase A	Phase A - phase I at 7.7 GPa 365 K; Phase I - fluid at 6.6 GPa, 435 K.
11	7- Mar 2022	P-C cell, Re gasket, Mo heater, 18 µm, ruby	Phase A	Phase A - phase B at 18 GPa, 411 K.
12	8- Mar 2022	P-C cell, Re gasket, Mo heaters, 15 µm, DE	Phase A	Phase A - phase B at 20.3 GPa, 418 K.
13	14- Mar 2022	P-C cell, Os gasket, Mo heaters, 18 µm, DE	Phase A	Phase A - phase B at 24 GPa, 477 K; Phase B - fluid at 24 GPa, 810 K.

14	21-Apr 2022	P-C cell, Os gasket, Mo heater, 18 µm, DE	Phase A	Phase A - phase B at 28.9 GPa, 480 K.
15	18- May 2022	GG cell, Os gasket, Pt heater, 18 µm, ruby	Fluid (room T)	Fluid - phase I at 1.9 GPa, 298 K; Phase I - phase A at 5.7 GPa, 298 K; Phase A - phase B at 10.2 GPa after 10 days.
16	03- Jun 2022	P-C cell, Os gasket, Pt heater, 18 µm, DE	Phase A	Phase A - phase B at 16.2 GPa, 360 K.
17	09- Jun 2022	GG cell, Os gasket, Pt heater, 18 µm, DE	Phase B	Phase B - phase A at 18.5 GPa, 560 K; Phase A - fluid at 14.7 GPa, 680 K; Cooling down: phase A.
18	09- Jun 2022	GG cell, Os gasket, Mo heater, 15 µm, DE	Phase A	Phase A stays from 300 K to 685 K at 21.6 GPa; Phase B never show up.
19	10- Jun 2022	P-C cell, Os gasket, Pt heater, 17 µm, ruby	Phase A	Phase A to phase B at 42.7 GPa, 470 K; Cooling down: Phase HP from 700 K to 298 K.
20	14- Jun 2022	P-C cell, Os gasket, Pt heater, 17 µm, ruby	Phase A	Phase A - phase I at 6.2 GPa, 380 K; Phase I - fluid at 6.7 GPa, 460 K. Cooling down: Fluid – phase I at 10 GPa, 600 K; Phase I to phase A at 10 GPa, 380 K.

21	18- Aug 2022	P-C cell, Os gasket, KA1 heater, 15 µm, DE	Phase B	Phase B - phase A at 11.5 GPa, 375 K, Phase A - fluid at 14.7 GPa, 680 K.
22	23- Aug 2022	P-C cell, Os gasket, Pt heater, 16 µm, DE	Phase A	Phase B – phase A at 16.7 GPa, 535 K; Phase A – phase I at 15.8GPa, 560 K; Phase I – fluid at 16.8 GPa, 660 K; Cooling down: Phase A from 610 K to 300 K at 14.5 GPa.
23	31- Aug 2022	P-C cell, Os gasket, Pt heater, 17 µm, DE and ruby	Phase A	Phase A never melt from 298 K to 760 K at 30.7 GPa.
24	05- Sept 2022	P-C cell, Os gasket, Pt heater, 14 µm, DE	Phase A	Phase A – phase B at 24 GPa, 480 K.
25	09- Sept 2022	P-C cell, Os gasket, Pt heater, 13 µm, DE	Phase HP	Phase HP – phase B at 45.6 GPa, 575 K;
26	20- Sept 2022	P-C cell, Os gasket, Pt heater, 13 µm, DE		
27	22- Sept 2022	P-C cell, Os gasket, Pt heater, 14 µm, DE	Phase HP	Phase HP – phase B at 26.7 GPa, 430 K; Phase B – phase A at 20.7 GPa, 710 K; Phase A – fluid at 19.9 GPa, 710 K; Cooling down: Phase A from 710 K to 300 K at 19.3 GPa.
28	23- Sept 2022	P-C cell, Re gasket, 17 µm, DE	Fluid (room T)	Fluid – Phase I at 1.7 GPa, 298 K; Phase I to phase A at 5.5 GPa, 298 K; Phase B never show up to 67.7 GPa, 298 K (without giving enough reaction time).

29	27- Sept 2022	P-C cell, Re gasket, Pt heate , 15 µm, DE	Phase HP	Phase HP – phase B at 23.4 GPa, 410 K; Phase B – phase A at 24.1 GPa, 735 K + Reacted.
30	13- Oct 2022	P-C cell, Re gasket, Pt heater, 15 µm, DE	Phase HP	Phase HP – phase B at 26.7 GPa, 440 K; Phase B – phase A at 20.3 GPa, 660 K; Phase A – Phase I at 17.3 GPa, 660 K; Phase I – fluid at 14.7 GPa, 660 K; Cooling down: Phase I from 660 K to 300 K at 10.2 GPa.
31	02- Nov 2022	P-C cell, Re gasket, Pt heater, 15 µm, DE	Phase HP	Phase HP – phase B at 31.8 GPa, 490 K; Phase B – phase A at 16.3 GPa, 550 K; Phase A – Phase I at 9.9 GPa, 550 K; Phase I – fluid at 7.6 GPa, 550 K; Cooling down: Phase A from 550 K to 300 K at 13.6 GPa
32	08- Nov 2022	P-C cell, Re gasket, Mo heater, 15.5 µm, DE	Phase HP	Phase HP – phase B at 28.5 GPa, 486 K;
33	21- Nov 2022	P-C cell, Re gasket, Mo heater, 17 µm, DE	Phase HP	Phase HP – phase B at 29.3 GPa, 492 K; Phase B – phase A at 13.3 GPa, 454 K; Phase A – Phase I at 8.8 GPa, 454 K; Phase I – fluid at 4.6 GPa, 454 K.
34	22- Nov 2022	P-C cell, Os gasket, Pt heaters, 16 µm, DE	Phase HP	Phase B – phase A at 13.1 GPa, 530 K; Phase A – Phase I at 12.5 GPa, 560 K; Phase I – fluid at 18.9 GPa, 720 K + Reacted; Cooling down: phase A from 720 K to 300 K at 20 GPa.

35	23- Nov 2022	GG cell, Os gasket, Pt heaters, 19 µm, DE	Phase A (room T)	Phase B – Phase A at 7.9 GPa, 298 K.
36	29- Nov 2022	PC cell, Os gasket, Pt heaters, 15 µm, DE	Phase HP	Phase HP – phase B at 28.2 GPa, 500 K; Phase B – phase A at 27.7 GPa, 910 K; Phase A – fluid at 22.2 GPa, 920 K + Reacted.
37	2- Dec 2022	PC cell, Os gasket, Pt heaters, 15 µm, DE	Phase HP	Phase HP – phase B at 24.2 GPa, 440 K; Phase B – phase A at 19.8 GPa, 608 K; Phase A – Phase I at 14.9 GPa, 610 K; Phase B – phase A at 17.7 GPa, 587 K; Phase A – Phase I at 15.4 GPa, 587 K; Phase I – fluid at 9.6 GPa, 587 K; Cooling down: phase A from 587 K to 300 K at 21 GPa.
38	6- Dec 2022	PC cell, Os gasket, Pt heaters, 16 µm, DE	Phase HP	Phase HP – phase B at 19.6 GPa, 390 K; Phase B – phase A at 22.0 GPa, 780 K; Phase A – fluid at 9.0 GPa, 810 K; Cooling down: phase A from 810 K to 300 K at 22 GPa.
39	9- Dec 2022	PC cell, Os gasket, Pt heaters, 15 µm, DE	Phase HP	Phase HP – phase B at 21.0 GPa, 400 K; Phase A – fluid at 23 GPa, 810 K + Reacted.
40	19- Dec 2022	PC cell, Os gasket, Pt heaters, 13 µm, DE	Phase HP	Phase HP – phase B at 17.7 GPa, 340 K; Phase B – phase A at 18.0 GPa, 673 K; Phase A – fluid at 18.9 GPa, 735 K + Reacted.

41	4- Jan 2023	GG cell, Os gasket, Pt heater, 15 µm, DE	Phase A (room T)	Phase A – Phase B at 12 GPa, 298 K + 150 minutes; Phase A – Phase B at 14.9 GPa, 298 K + 60 minutes; Phase A – Phase B at 9.9 GPa, 550 K + 360 minutes.
42	5- Jan 2023	PC cell, Os gasket, Pt heaters, 15 µm, DE	Phase HP	Phase HP – phase B at 35 GPa, 530 K; Phase B – fluid at 12.8 GPa, 635 K ; Phase A – Phase I at 13.6 GPa, 600 K; Phase I – Phase A at 14.6 GPa, 550 K; Phase A – Phase I at 10.2 GPa, 500 K; Phase I – Phase A at 13.8 GPa, 450 K; Phase A – Phase I at 7.2 GPa, 390 K; Phase I – Phase A at 13.1 GPa, 346 K; Phase A – Phase I at 6.7 GPa, 298 K; Phase I – fluid at 3.2 GPa, 298 K.
43	11- Jan 2023	PC cell, Os gasket, Pt heaters, 15 µm, DE	Phase HP	Phase HP – phase B at 36.2 GPa, 545 K; Phase B – phase A at 24.2 GPa, 823 K; Phase A – fluid at 20.7 GPa, 823 K + Reacted.
44	20- Jan 2023	PC cell, Os gasket, Pt heater, 17 µm, DE	Phase HP	Phase HP – phase B at 40.7 GPa, 569 K.
45	20- Jan 2023	GG cell, Os gasket, Pt heaters, 18µm, DE	Phase HP (room T)	Phase HP – phase B at 15.3 GPa, 298 K; Phase B – phase A at 7.5 GPa, 298 K; Phase A – fluid at 1.7 GPa, 298 K.

46	20- Jan 2023	PC cell, Os gasket, Pt heaters, 15 µm, DE	Phase A	Phase A – Phase B at 29.8 GPa, 710 K; Phase B – phase A at 17.5 GPa, 709 K;
47	27- Jan 2023	PC cell, Os gasket, 16 µm, DE	Phase HP	Phase HP – phase B at 35.1 GPa, 540 K; Phase B – fluid at 22.3 GPa, 930 K + Reacted.
48	03- Apr 2023	PC cell, Os gasket, 16 µm, DE	Phase HP	Phase HP-phase B at 17 GPa 374 K, Phase B to phase A at 20 GPa 675 K, Phase A to fluid between 18 GPa and 695 K and 13 GPa 665, Fluid to phase I 14 GPa 645 K, Phase I to Phase A 17 GPa 665 K, Phase A to fluid between 25 GPa and 21 GPa at 750 K.
49	29- Apr 2023	PC cell	Phase A	Phase A to phase I at 18 GPa and 600K Decompression at 620 K. phase I to fluid 15.5 and 17.8 GPa reacts at 16 GPa
50	12- Jun 2023	PC cell, Os gasket, 13 µm, DE	Phase A and phase HP, both in the same chamber different locations	Phase A to phase B at 540 K 27 GPa, Phase HP to phase B at 475 K, Phase B to phase A at 825 K and 27 GPa, Not sure if phase A to melt 834 K, then reacted.
51	14- Jun 2023	PC cell, Os gasket, Pt heater, DE	Phase A	Phase A – phase HP at 40.8 GPa, 440 K; Phase HP – phase B at 38.8 GPa, 552 K; Phase B – Phase A at 26.7 GPa, 925 K; Phase A – fluid at 23.7 GPa, 925 K + Reacted.

52	15- Jun 2023	PC cell, Os gasket, Pt heater, DE	Phase HP	Phase HP – phase B at 34.1 GPa, 530 K; Phase B – phase A at 30.4 GPa, 1020 K; Phase B – fluid at 23.7 GPa, 1020 K + Reacted.
53	16- Jun 2023	PC cell, Os gasket, Pt heater, DE	Phase A	Phase A – phase HP at 33.2 GPa, 435 K; Phase HP – phase B at 31. GPa, 527 K; Phase B – Phase A at 30.2 GPa, 1113 K; Phase A – fluid at 27.3 GPa, 1113 K + Reacted.
54	28- Dec 2022	GG cell, Os gasket, DE	Phase A	**H_2** at 1.8 GPa, 298 K after laser heating.
55	28- Dec 2022	PC cell, Os gasket, Pt heater, DE	Phase A	**H_2** at 1.0 GPa, 370 K after resistive heating.
56	29- May 2023	GG cell, Os gasket, Pt coupler laser heating, DE	Phase HP	Phase HP to phase A at 40 GPa, 560 K; Phase A to fluid at 40 GPa, 1295 K.
57	12- Jul 2021	GG cell, Re gasket, DE	Phase B	Phase B to phase HP at 43 GPa, 298 K; Phase HP to c-HP at 100 GPa, 298 K.
58	21- Dec 2021	GG cell, Re gasket, DE	Fluid	Fluid to phase A at 32 GPa, 298 K; Phase HP to c-HP at 100 GPa, 298 K.

*The different colours correspond to the different known phases of CH_4: liquid (blue), phase I (orange), phase A (olive), phase B (pink), phase HP (purple) and phase c-HP (light grey).

PHYSICAL REVIEW LETTERS **128,** 215702 (2022)

Editors' Suggestion **Featured in Physics**

Formation and Stability of Dense Methane-Hydrogen Compounds

Umbertoluca Ranieri,[1,2] Lewis J. Conway,[3] Mary-Ellen Donnelly,[1] Huixin Hu,[1] Mengnan Wang,[1]
Philip Dalladay-Simpson,[1] Miriam Peña-Alvarez,[3] Eugene Gregoryanz,[1,3,4] Andreas Hermann,[3] and Ross T. Howie[1,3,*]
[1]*Center for High Pressure Science and Technology Advanced Research, 1690 Cailun Road, Shanghai, 201203, China*
[2]*Dipartimento di Fisica, Università di Roma La Sapienza, Piazzale Aldo Moro 5, 00185 Rome, Italy*
[3]*Centre for Science at Extreme Conditions and The School of Physics and Astronomy, The University of Edinburgh,*
Peter Guthrie Tait Road, Edinburgh, United Kingdom
[4]*Key Laboratory of Materials Physics, Institute of Solid State Physics, CAS, Hefei, China*

(Received 25 November 2021; revised 2 February 2022; accepted 20 April 2022; published 27 May 2022)

Through a series of x-ray diffraction, optical spectroscopy diamond anvil cell experiments, combined with density functional theory calculations, we explore the dense CH_4-H_2 system. We find that pressures as low as 4.8 GPa can stabilize $CH_4(H_2)_2$ and $(CH_4)_2H_2$, with the latter exhibiting extreme hardening of the intramolecular vibrational mode of H_2 units within the structure. On further compression, a unique structural composition, $(CH_4)_3(H_2)_{25}$, emerges. This novel structure holds a vast amount of molecular hydrogen and represents the first compound to surpass 50 wt % H_2. These compounds, stabilized by nuclear quantum effects, persist over a broad pressure regime, exceeding 160 GPa.

DOI: 10.1103/PhysRevLett.128.215702

Hydrogen and methane are, besides water, the most prevalent small molecules in the outer Solar System. Their interplay under extreme conditions is of key interest to understanding the evolution and interior dynamics of Neptune and Uranus, as well as of Earth and exoplanets [1–4]. The simplest molecule, H_2, has been shown to exhibit rich physical phenomena, including quantum rotational phases and pressure-induced steps toward an atomic metallic solid, while methane (CH_4), the simplest hydrocarbon, has been proposed to polymerize during compression to form long-chain hydrocarbons and at further extremes decompose into diamond plus H_2 [5–19].

Hydrogen reacts with a number of materials at high pressures and temperatures but also has a propensity to form van der Waals compounds that can be stable far beyond 100 GPa [20–32]. Methane and hydrogen were first reported to crystallize into inclusion (host-guest) compounds over 25 years ago at pressures between 5 and 7 GPa. A range of compositions were claimed: $(CH_4)_2H_2$, CH_4H_2, $CH_4(H_2)_2$, and $CH_4(H_2)_4$ [21]. However, the experimental evidence for these compounds was limited, with only the shift of the hydrogen intramolecular vibrational mode ν_1-H_2 (vibron) relative to that of pure hydrogen being reported together with the lattice parameters of potential structures. Assuming that these structural compositions were correct, a later experimental study explored the recoverability of $CH_4(H_2)_4$ at low temperature to investigate its potential as a hydrogen storage media [33,34].

In contrast to experimental work, the CH_4-H_2 system has recently had a surge of theoretical investigations, predicting a variety of extremely hydrogen-rich compositions to emerge such as triclinic $(CH_4)_2(H_2)_3$, trigonal $(CH_4)_2(H_2)_7$, and hexagonal $CH_4(H_2)_9$, as well as several CH_4H_2 structures [18,35–37]. Furthermore, it was suggested that CH_4-H_2 structures could be the most stable form of carbon and hydrogen at pressures up to 200 GPa [18].

Surprisingly, given these predictions and the advent of technological advances over the past 25 years, no further experimental exploration has been conducted despite undetermined CH_4-H_2 compound signatures emerging as a by-product in many prolific studies of hydrocarbons at planetary conditions [3,19,38–41]. Moreover, the doping of carbon (or methane) could even enhance the properties of materials at extreme pressures, with the unprecedented claim of room temperature superconductivity in the carbonaceous sulfur hydride system [42–44]. The lack of knowledge regarding CH_4-H_2 compound formation inhibits our understanding of these more complex ternary systems and how doping could induce novel properties. As such, it is of fundamental interest to know which methane-hydrogen compounds are actually formed and test their pressure stability limits.

In this Letter, we have conducted a series of high-pressure synchrotron powder x-ray diffraction and Raman spectroscopy experiments in diamond anvil cells combined with density functional theory (DFT) calculations and structural searching to explore the formation and properties of CH_4-H_2 compounds from mixtures of methane and hydrogen. In H_2-rich mixtures, we observe the formation of hexagonal $CH_4(H_2)_2$ above 5 GPa, before partially transforming into monoclinic $(CH_4)_3(H_2)_{25}$. $(CH_4)_3(H_2)_{25}$ represents a unique composition and contains an unprecedented 51.1 wt % H_2, which is the highest hydrogen content of any currently known

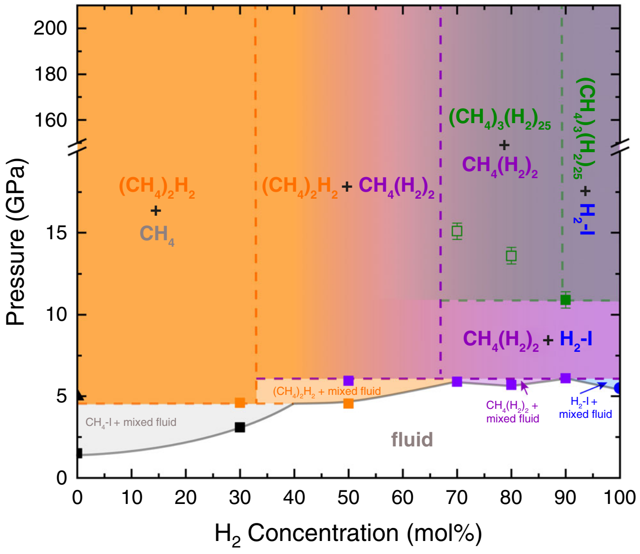

FIG. 1. Pressure-composition phase diagram of the CH_4-H_2 binary system. Filled square symbols indicate the formation pressures of each compound: $(CH_4)_2H_2$ (orange), $CH_4(H_2)_2$ (purple), and $(CH_4)_3(H_2)_{25}$ (green). The green open squares represent the pressures at which $(CH_4)_3(H_2)_{25}$ is first observed. The black squares, black triangle, and blue circle represent the formation pressure of CH_4-I, CH_4-A, and H_2-I, respectively. The gray line represents the liquidus curve and is adapted from Ref. [21]. Below 7 GPa, the error in pressure is ±0.2 GPa and smaller than the size of the symbol. Initial gas mixtures have a tolerance of 1%.

stoichiometric compound. In CH_4-rich mixtures, tetragonal $(CH_4)_2H_2$ forms, which undergoes extreme hardening of the H_2 intramolecular vibrational mode with pressure. All three compounds exhibit remarkable stability, exceeding pressures of 160 GPa.

At pressures below 1.5 GPa, all mixture concentrations (30, 50, 70, 80, and 90 mol % H_2) are homogeneous well-mixed fluids and display the Raman signatures of both constituent species (see Fig. 1 for the pressure-composition phase diagram, Supplemental Material [45] for experimental methods, and Figs. S1–S9 [45] for Raman spectra of all mixtures). On compression of hydrogen-rich CH_4-H_2 mixtures (70–90 mol % H_2) above 5 GPa, the fluid mixture crystallizes into a solid which we identify as $CH_4(H_2)_2$. X-ray diffraction measurements reveal that this compound adopts a hexagonal $MgZn_2$ Laves phase structure (space group $P6_3/mmc$), where the CH_4 molecules occupy the Mg sites and the H_2 molecules occupy the Zn sites (see Fig. 2), the lattice parameters of which are $a = 4.981$ Å and $c = 8.125$ Å at 16.6 GPa. This structure and composition was suggested previously but attributed to a compound forming in a narrow pressure regime (between approximately 6 and 7 GPa) and between 35 and 65 mol % H_2 mixture concentrations [21]. Here, we find that $CH_4(H_2)_2$ is the dominant phase across all H_2-rich mixtures and persistent over a large pressure regime. Raman spectroscopy reveals two distinct H_2 vibrons, ν_{1H} and ν_{2H}, the latter of which is approximately 50 times lower in intensity. The two most intense CH_4 stretching modes, ν_{1M} and ν_{2M}, are shifted to higher frequency compared to pure CH_4, while the wagging mode is shifted to lower frequency (see Figs. 3 and 4).

On further compression, we observe another compound emerge evidenced by visual changes in the sample morphology and the appearance of three distinct H_2 vibrational modes (the lowest in frequency being the most intense by 2 orders of magnitude) and CH_4 stretching bands that can be isolated from $CH_4(H_2)_2$ (see Figs. 3 and 4 and Supplemental Material [45]). The most intense H_2 vibron is lower in frequency than that of $CH_4(H_2)_2$, suggestive that the compound has a higher H_2 content. X-ray diffraction measurements indicate the compound is weakly scattering; however, this could be in part due to only partial transformation of the sample. The patterns could be indexed to a hexagonal cell, with $a = 7.804$ Å and $c = 11.199$ Å at 17.3 GPa (see Fig. 2). Systematic absences, unit cell volume, and c/a ratio suggest this compound has a close resemblance with the previously reported $R\bar{3}m$ structure of $Xe(H_2)_8$ [23,26] and an initial composition estimate of $CH_4(H_2)_8$. This seemed plausible given CH_4 and Xe have similar van der Waals diameters (3.78 and 4.32 Å, respectively).

We subsequently performed DFT calculations to help identify this phase. We constructed a series of structures of variable composition, starting by populating the hexagonal cell with randomly oriented CH_4 molecules on the Xe sites of $Xe(H_2)_8$, before adding H_2 molecules on hexagonal close packed (hcp) arrangements commensurate with the cell, using up to $3 \times 3 \times 4$ repeats of the hcp lattice and a random offset against the CH_4 sublattice. H_2 molecules too close to CH_4 were removed before fully optimizing the remaining atoms and all lattice parameters. Several thousand of these structures were generated with stoichiometries ranging from $CH_4(H_2)_7$ to $CH_4(H_2)_{11}$. Of these, $CH_4(H_2)_{8.33}$ [or $(CH_4)_3(H_2)_{25}$] emerged as the most energetically competitive and was found to be dynamically stable at and above 20 GPa (see Figs. S20 and S21 [45]). It is also the only computationally obtained structure which reproduces the positions and intensities of the experimental diffraction peaks across the studied pressure range (see Fig. S14 [45]), which is meaningful given that no symmetry restrictions were applied in the structures' construction and subsequent optimization. While we find both $CH_4(H_2)_2$ and $(CH_4)_2H_2$ stable or close to stability within the CH_4-H_2 phase diagram across a wide pressure range, once zero point energies and vibrational entropies are accounted for, $(CH_4)_3(H_2)_{25}$ remains metastable throughout (see Supplemental Material [45]).

Considering methane and hydrogen molecules to be spherical, the structure of $(CH_4)_3(H_2)_{25}$ is monoclinic with space group $C2/m$ (coordinates are given in Supplemental

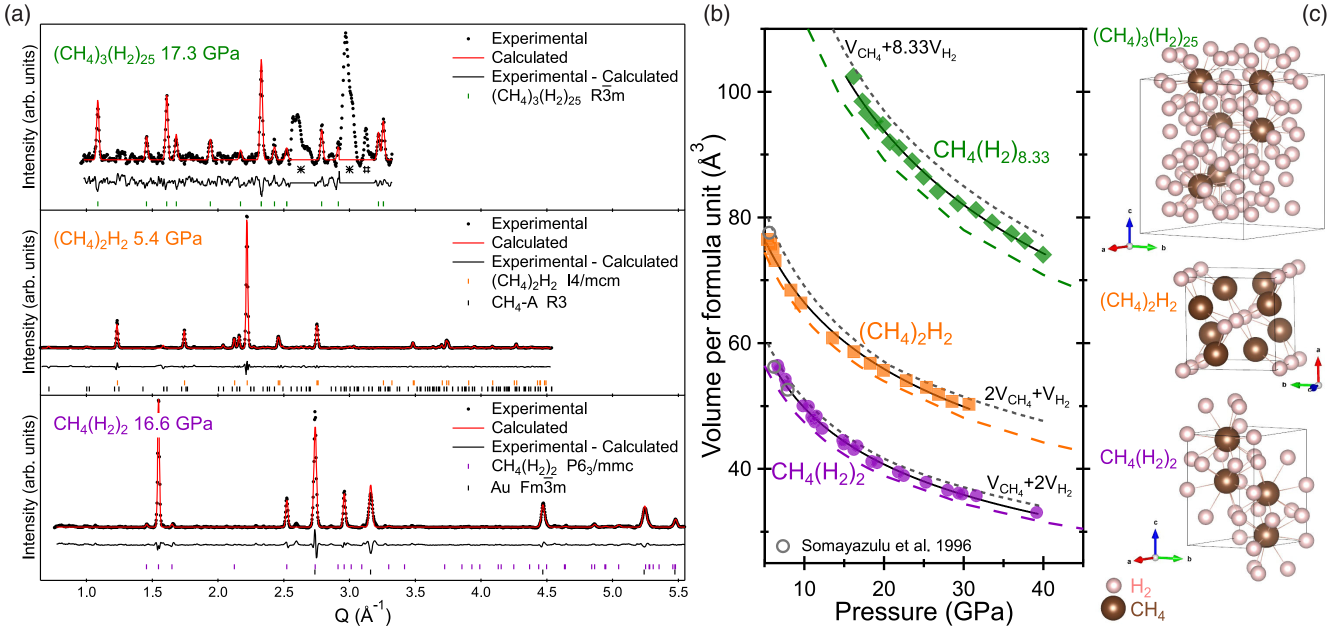

FIG. 2. (a) Representative x-ray diffraction patterns of the three compounds plotted as a function of exchanged wave vector and their Le Bail refinements. Refinements include $(CH_4)_3(H_2)_{25}$-$R\bar{3}m$ ($a = 7.804$ Å and $c = 11.199$ Å), $(CH_4)_2H_2$-$I4/mcm$ ($a = 7.195$ Å and $c = 5.909$ Å), CH_4-A-$R3$ ($a = 12.306$ Å and $c = 15.520$ Å), $CH_4(H_2)_2$-$P6_3/mmc$ ($a = 4.981$ Å and $c = 8.125$ Å), and Au-$Fm\bar{3}m$ ($a = 3.976$ Å). Excluded regions in the pattern of $(CH_4)_3(H_2)_{25}$ correspond to rhenium (gasket material) and rhenium hydride (*) and excess H_2 (#). (b) Volumes per formula unit as a function of pressure. Symbols represent experimental data (the error bars are smaller than the symbol size), and black full lines represent their best second-order Birch-Murnaghan fits: $CH_4(H_2)_{8.33}$, $V_0 = 246 \pm 17$ Å^3 and $K = 3.0 \pm 0.6$ GPa; $(CH_4)_2H_2$, $V_0 = 101 \pm 2$ Å^3 and $K = 10.2 \pm 0.8$ GPa; $CH_4(H_2)_2$, $V_0 = 90 \pm 3$ Å^3 and $K = 5.0 \pm 0.4$ GPa. Dashed lines represent volumes derived from our DFT calculations, and gray dotted lines represent the volumes of ideal mixtures of CH_4-A/CH_4-B and H_2-I using the previously determined equations of state [14,17,69]. The experimental volumes given in Ref. [21] are represented by gray circles. (c) Structural models of the three compounds, where CH_4 and H_2 are represented by brown and white spheres, respectively, and lines indicate CH_4-H_2 nearest neighbors.

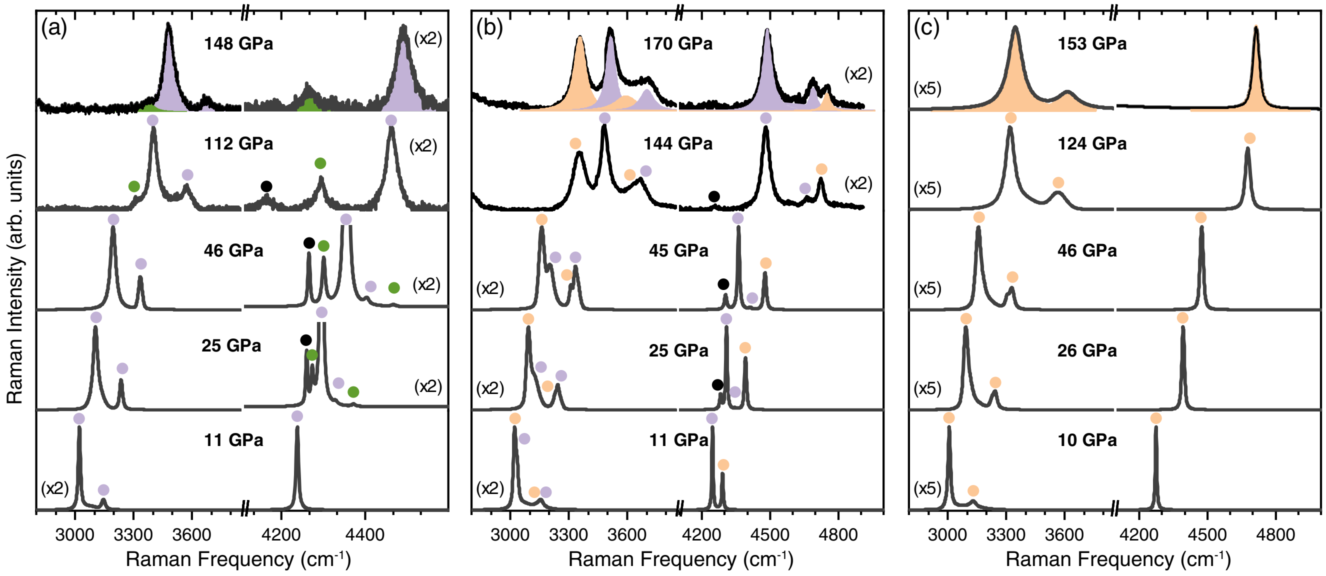

FIG. 3. Representative vibrational Raman spectra of (a) 70% H_2, (b) 50% H_2, and (c) 30% H_2 mixtures. Colors indicate the modes assigned to $CH_4(H_2)_2$ (purple), $(CH_4)_3(H_2)_{25}$ (green), $(CH_4)_2H_2$ (orange), and excess H_2 (black).

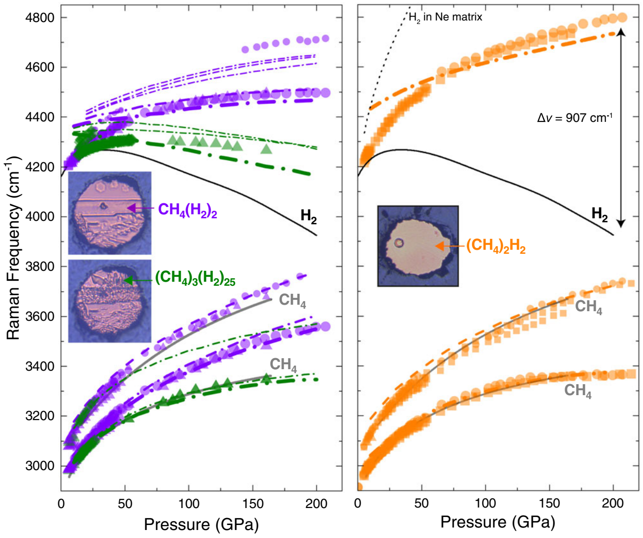

FIG. 4. Raman shift as a function of pressure of the H_2 vibrational modes and C-H stretching modes of $CH_4(H_2)_2$ and $(CH_4)_3(H_2)_{25}$ (left panel, purple and green symbols, respectively), and $(CH_4)_2H_2$ (right panel, orange symbols). Frequencies are collated from 30% (squares), 50% (circles), 70% (triangles), 80% (diamonds), and 90% (hexagons) H_2 mixtures, with the most intense modes represented by larger symbols. Raman frequencies of individual mixtures are given in Supplemental Material [45]. The dot-dashed lines represent the calculated frequencies of the H_2 modes and C-H stretching bands of each compound, with the thickest line representing the most intense modes. Black and gray solid lines represent pure H_2 [6] and CH_4 [15], respectively. The black dotted line represents the frequency of H_2 in a Ne matrix [70]. The error in pressure ranges from ±0.2 GPa below 50 GPa, ±1 GPa below 150 GPa, and ±5 GPa above. The error bars in frequency are smaller than the symbol size. Photomicrographs show examples of morphology of synthesised samples within the DAC sample chamber.

Material [45]). Le Bail refinements of the experimental diffraction patterns were performed using the trigonal space group $R\overline{3}m$, which is obtained considering the carbon atoms only, and the hexagonal setting, which resulted in good fits to the data. The obtained volume per methane molecule is close to $V_{CH_4} + 8.33V_{H_2}$ (see Fig. 2), the volume of an ideal mixture of CH_4 and H_2 with the same composition. A comparison between the experimental and computational vibrational Raman modes of $CH_4(H_2)_2$-$P6_3/mmc$ and $(CH_4)_3(H_2)_{25}$-$C2/m$ is given in Fig. 4, where we see qualitatively good agreement between the number of modes, relative intensity, and frequency for both compounds.

In methane-rich concentrations of 30 mol % H_2, we observe a body-centered tetragonal Al_2Cu-type structure (space group $I4/mcm$) to form above 4.6 GPa (with $a = 7.195$ Å and $c = 5.909$ Å at 5.4 GPa), which is consistent with the previously reported composition of $(CH_4)_2H_2$ [21] (see Fig. 1). Raman spectroscopy measurements show that the CH_4 stretching bands of $(CH_4)_2H_2$ are close to the frequencies of pure solid CH_4, while two wagging modes are observed. The number of modes and frequencies are in good agreement with our calculated values (see Fig. 4). The ν_{1H} mode, corresponding to H_2 units within the structure, exhibits the most extreme hardening of any stoichiometric molecular compound [25,28]. At a pressure of 207 GPa, $(CH_4)_2H_2$-ν_{1H} has a frequency of 4798 cm^{-1}, over 900 cm^{-1} higher than H_2-ν_1 (see Fig. 4). Remarkably, the frequencies we observe reach similar values to an impurity H_2 molecule isolated in a noble gas matrix, albeit at higher pressure [70]. Up to pressures of 207 GPa, we do not observe a turnover of ν_{1H} (and 500 GPa in our calculations), unlike in pure H_2, which exhibits a maximum frequency at approximately 38 GPa [5].

These results highlight the enormous impact that the local environment around a H_2 molecule can have on its vibron frequency. In Supplemental Material [45], we present a simple molecular model demonstrating that the vibron frequency of a H_2 surrounded by two CH_4 (respectively, H_2) will continuously increase (respectively, decrease) if the surrounding molecules are pushed closer. A molecular orbital analysis reveals that, in H_2-dominated environments, intermolecular interactions lead to occupancy of antibonding H-H σ^* states, which does not happen in CH_4-dominated environments. In $(CH_4)_2H_2$, every H_2 has two nearest H_2 neighbors and eight nearest CH_4 neighbors; as a result, the vibron exhibits extreme hardening [see Fig. 2(c) and Supplemental Material [45] for graphical representations of the unit cells and intermolecular distances]. This local environment is reversed in $(CH_4)_3(H_2)_{25}$ with an average of 9.8 H_2 neighbors but only 2.24 CH_4 neighbors per H_2 molecule; still, it remains very different from H_2-*I*, having a coordination number of 12 and considerably shorter H_2-H_2 distances [28]. For $(CH_4)_3(H_2)_{25}$, the ν_{1H} mode has a maximum at about 70 GPa, and the vibron frequencies tend toward the values found for pure H_2. In $CH_4(H_2)_2$, where each H_2 has six nearest H_2 neighbors and six nearest CH_4 neighbors, the vibron frequencies are interpolated between $(CH_4)_3(H_2)_{25}$ and $(CH_4)_2H_2$.

We find that the pressure-composition phase diagram is simpler than previously reported [21], with only three stable CH_4-H_2 compositions. In 50 mol % H_2 mixtures, we observe the coexistence of both $(CH_4)_2H_2$ and $CH_4(H_2)_2$, together with some excess H_2, indicative that equilibrium has not been reached. Furthermore, we observe trace amounts of $(CH_4)_3(H_2)_{25}$, which can be attributed to macroscopic inhomogeneity within the sample chamber. In 70 mol % and 80 mol % H_2 mixtures, we first observe the Raman signatures of $(CH_4)_3(H_2)_{25}$ at 14.5 GPa and at 13.6 GPa (shown as open symbols in Fig. 1), respectively, while in 90 mol % mixtures, we observe $(CH_4)_3(H_2)_{25}$ at 10.9 GPa. It is possible that, in 70 mol % and 80 mol % H_2 mixtures, formation occurs at lower pressure but is below the detection limit in the Raman spectra. We find that even in 90 mol % mixtures the transformation from $CH_4(H_2)_2$

and H_2 to $(CH_4)_3(H_2)_{25}$ is never complete, suggestive that the transformation is kinetically sluggish and due to hindered diffusion of H_2 in the solid state. Although our liquidus curve is in good agreement with that reported previously, we do not observe either CH_4H_2 and $CH_4(H_2)_4$ and attribute this to a misinterpretation of $CH_4(H_2)_2$ [21]. The experimental volume given for hexagonal wurtzite CH_4H_2 is identical to our experimental volume for $CH_4(H_2)_2$ at the same given pressure. Furthermore, after extensive structure searches, with randomly orientated molecules in the reported wurtzite center-of-mass positions, we do not find any version of the hexagonal wurtzite structure to be dynamically stable. The evidence for $CH_4(H_2)_4$ was predominantly based on Raman spectroscopy, and we find to be a misinterpretation of the coexistence between the CH_4-H_2 mixed fluid and solid $CH_4(H_2)_2$ (see Fig. S8 [45]).

$(CH_4)_3(H_2)_{25}$ possesses 51.1 wt % molecular hydrogen (63.4 wt % if the hydrogen of methane is included), which is the highest hydrogen content of any currently known stoichiometric compound. Notwithstanding the good agreement between the experimental and calculated data, $(CH_4)_3(H_2)_{25}$ represents an unusual and unique composition. All three compounds exhibit remarkable stability, with the Raman signatures of $(CH_4)_2H_2$ and $CH_4(H_2)_2$ detectable to at least 215 GPa and $(CH_4)_3(H_2)_{25}$ up to 165 GPa. We estimate the melting temperatures T_m of $(CH_4)_2H_2$ and $CH_4(H_2)_2$ using Lindemann's equation based on calculated Debye temperatures and found T_m significantly higher than molecular hydrogen at all pressures (see Supplemental Material [45]). This would imply that hydrogen mixed with methane would potentially not possess the melting line turnover that is observed in pure hydrogen [7]. Taken together in a planetary context, this could influence critical properties of planetary matter such as thermal conductivities and viscosities. In a materials science context, high Debye temperatures coupled with extremely large vibron frequencies ν_H are promising ingredients for high-T_c superconductivity—provided a reasonable density of states $N(E_F)$ at the Fermi energy. The molecular compounds described here are insulators (all remain transparent in the visible up to the highest pressures reached), but the presence of an electron or hole dopant would metallize the system, with partially charged entities $H_2^{\pm\delta}$ present. This motif, at least in calculations, can lead to T_c close to 200 K [71].

Parts of this research were carried out at P02.2 at DESY, a member of the Helmholtz Association (HGF), and we thank H.-P. Liermann and K. Glazyrin for assistance. We also acknowledge the European Synchrotron Radiation Facility for provision of synchrotron radiation facilities at the ID15B beam line and assistance from M. Hanfland and D. Comboni. R. T. H. acknowledges that the project has received funding from the European Research Council (ERC) under the European Union's Horizon 2020 research and innovation program (Grant Agreement No. 948895 "MetElOne"). M. P.-A. acknowledges the support of the UKRI Future leaders fellowship Mrc-Mr/T043733/1. L. J. C. was supported by the Engineering and Physical Sciences Research Council through the Condensed Matter Center for Doctoral Training (EP/L015110/1). Computational resources provided by the United Kingdom's National Supercomputer Service through the United Kingdom Car-Parrinello consortium (EP/P022561/1) and Project ID No. d56 "Planetary Interiors" and by the United Kingdom Materials and Molecular Modelling Hub (EP/P020194) are gratefully acknowledged. The authors thank J. Binns and F. A. Gorelli for useful discussions.

[1] W. B. Hubbard, W. J. Nellis, A. C. Mitchell, N. C. Holmes, S. S. Limaye, and P. C. McCandless, Science **253**, 648 (1991).
[2] R. Chau, S. Hamel, and W. J. Nellis, Nat. Commun. **2**, 203 (2011).
[3] S. S. Lobanov, P.-N. Chen, X.-J. Chen, C.-S. Zha, K. D. Litasov, H.-K. Mao, and A. F. Goncharov, Nat. Commun. **4**, 2446 (2013).
[4] R. Helled and J. J. Fortney, Phil. Trans. R. Soc. A **378**, 20190474 (2020).
[5] H.-k. Mao and R. J. Hemley, Rev. Mod. Phys. **66**, 671 (1994).
[6] R. T. Howie, C. L. Guillaume, T. Scheler, A. F. Goncharov, and E. Gregoryanz, Phys. Rev. Lett. **108**, 125501 (2012).
[7] R. T. Howie, P. Dalladay-Simpson, and E. Gregoryanz, Nat. Mater. **14**, 495 (2015).
[8] P. Dalladay-Simpson, R. T. Howie, and E. Gregoryanz, Nature (London) **529**, 63 (2016).
[9] E. Gregoryanz, C. Ji, P. Dalladay-Simpson, B. Li, R. T. Howie, and H.-K. Mao, Matter Radiat. Extremes **5**, 038101 (2020).
[10] P. Loubeyre, F. Occelli, and P. Dumas, Nature (London) **577**, 631 (2020).
[11] R. M. Hazen, H.-K. Mao, L. W. Finger, and P. M. Bell, Appl. Phys. Lett. **37**, 288 (1980).
[12] H. Hirai, K. Konagai, T. Kawamura, Y. Yamamoto, and T. Yagi, Phys. Earth Planet. Inter. **174**, 242 (2009).
[13] L. Sun, A. L. Ruoff, C.-S. Zha, and G. Stupian, J. Phys. Chem. Solids **67**, 2603 (2006).
[14] L. Sun, W. Yi, L. Wang, J. Shu, S. Sinogeikin, Y. Meng, G. Shen, L. Bai, Y. Li, J. Liu, H.-K. Mao, and W. L. Mao, Chem. Phys. Lett. **473**, 72 (2009).
[15] J. E. Proctor, H. E. Maynard-Casely, M. A. Hakeem, and D. Cantiah, J. Raman Spectrosc. **48**, 1777 (2017).
[16] H. E. Maynard-Casely, C. L. Bull, M. Guthrie, I. Loa, M. I. McMahon, E. Gregoryanz, R. J. Nelmes, and J. S. Loveday, J. Chem. Phys. **133**, 064504 (2010).
[17] H. E. Maynard-Casely, L. F. Lundegaard, I. Loa, M. I. McMahon, E. Gregoryanz, R. J. Nelmes, and J. S. Loveday, J. Chem. Phys. **141**, 234313 (2014).
[18] L. J. Conway and A. Hermann, Geosciences **9**, 227 (2019).
[19] M. Peña-Alvarez, A. V. Brovarone, M.-E. Donnelly, M. Wang, P. Dalladay-Simpson, R. Howie, and E. Gregoryanz, Nat. Commun. **12**, 6387 (2021).

[20] P. Loubeyre, R. Letoullec, and J.-P. Pinceaux, Phys. Rev. Lett. **72**, 1360 (1994).

[21] M. S. Somayazulu, L. W. Finger, R. J. Hemley, and H. K. Mao, Science **271**, 1400 (1996).

[22] T. A. Strobel, P. Ganesh, M. Somayazulu, P. R. C. Kent, and R. J. Hemley, Phys. Rev. Lett. **107**, 255503 (2011).

[23] M. Somayazulu, P. Dera, A. F. Goncharov, S. A. Gramsch, P. Liermann, W. Yang, Z. Liu, H.-K. Mao, and R. J. Hemley, Nat. Chem. **2**, 50 (2010).

[24] D. K. Spaulding, G. Weck, P. Loubeyre, F. Datchi, P. Dumas, and M. Hanfland, Nat. Commun. **5**, 5739 (2014).

[25] A. K. Kleppe, M. Amboage, and A. P. Jephcoat, Sci. Rep. **4**, 4989 (2014).

[26] M. Somayazulu, P. Dera, J. Smith, and R. J. Hemley, J. Chem. Phys. **142**, 104503 (2015).

[27] E. J. Pace, J. Binns, M. Peña Alvarez, P. Dalladay-Simpson, E. Gregoryanz, and R. T. Howie, J. Chem. Phys. **147**, 184303 (2017).

[28] C. Ji, A. F. Goncharov, V. Shukla, N. K. Jena, D. Popov, B. Li, J. Wang, Y. Meng, V. B. Prakapenka, J. S. Smith, R. Ahuja, W. Yang, and H.-k. Mao, Proc. Natl. Acad. Sci. U.S.A. **114**, 3596 (2017).

[29] D. Laniel, V. Svitlyk, G. Weck, and P. Loubeyre, Phys. Chem. Chem. Phys. **20**, 4050 (2018).

[30] R. Turnbull, M.-E. Donnelly, M. Wang, M. Peña-Alvarez, C. Ji, P. Dalladay-Simpson, H.-k. Mao, E. Gregoryanz, and R. T. Howie, Phys. Rev. Lett. **121**, 195702 (2018).

[31] J. Binns, P. Dalladay-Simpson, M. Wang, G. J. Ackland, E. Gregoryanz, and R. T. Howie, Phys. Rev. B **97**, 024111 (2018).

[32] M. Ceppatelli, D. Scelta, M. Serrano-Ruiz, K. Dziubek, G. Garbarino, J. Jacobs, M. Mezouar, R. Bini, and M. Peruzzini, Nat. Commun. **11**, 6125 (2020).

[33] W. L. Mao and H. K. Mao, Proc. Natl. Acad. Sci. U.S.A. **101**, 708 (2004).

[34] W. L. Mao, V. V. Struzhkin, H. K. Mao, and R. J. Hemley, Chem. Phys. Lett. **402**, 66 (2005).

[35] Y. Liu, D. Duan, F. Tian, X. Huang, D. Li, Z. Zhao, X. Sha, B. Chu, H. Zhang, B. Liu, and T. Cui, RSC Adv. **4**, 37569 (2014).

[36] G. Saleh and A. R. Oganov, Sci. Rep. **6**, 32486 (2016).

[37] A. S. Naumova, S. V. Lepeshkin, and A. R. Oganov, J. Phys. Chem. C **123**, 20497 (2019).

[38] A. Zerr, G. Serghiou, R. Boehler, and M. Ross, High Press. Res. **26**, 23 (2006).

[39] H. Kadobayashi, S. Ohnishi, H. Ohfuji, Y. Yamamoto, M. Muraoka, S. Yoshida, N. Hirao, S. Kawaguchi-Imada, and H. Hirai, Sci. Rep. **11**, 8165 (2021).

[40] A. Kolesnikov, V. G. Kutcherov, and A. F. Goncharov, Nat. Geosci. **2**, 566 (2009).

[41] D. A. Kudryavtsev, T. M. Fedotenko, E. G. Koemets, S. E. Khandarkhaeva, V. G. Kutcherov, and L. S. Dubrovinsky, Sci. Rep. **10**, 1483 (2020).

[42] E. Snider, N. Dasenbrock-Gammon, R. McBride, M. Debessai, H. Vindana, K. Vencatasamy, K. V. Lawler, A. Salamat, and R. P. Dias, Nature (London) **586**, 373 (2020).

[43] W. Cui, T. Bi, J. Shi, Y. Li, H. Liu, E. Zurek, and R. J. Hemley, Phys. Rev. B **101**, 134504 (2020).

[44] A. F. Goncharov, E. Bykova, M. Bykov, X. Zhang, Y. Wang, S. Chariton, and V. B. Prakapenka, J. Appl. Phys. **131**, 025902 (2022).

[45] See Supplemental Material at http://link.aps.org/supplemental/10.1103/PhysRevLett.128.215702 for further methodological details and additional experimental and computational figures, which includes Refs. [46–68].

[46] E. Aprà *et al.*, J. Chem. Phys. **152**, 184102 (2020).

[47] S. B. Ramsey, M. Pena-Alvarez, and G. J. Ackland, Phys. Rev. B **101**, 214306 (2020).

[48] V. Labet, R. Hoffmann, and N. W. Ashcroft, J. Chem. Phys. **136**, 074502 (2012).

[49] V. Labet, R. Hoffmann, and N. W. Ashcroft, J. Chem. Phys. **136**, 074503 (2012).

[50] H.-K. Mao, J. Xu, and P. M. Bell, J. Geophys. Res. **91**, 4673 (1986).

[51] Y. Akahama and H. Kawamura, J. Appl. Phys. **100**, 043516 (2006).

[52] Y. Grin, F. R. Wagner, M. Armbrüster, M. Kohout, A. Leithe-Jasper, U. Schwarz, U. Wedig, and H. G. von Schnering, J. Solid State Chem. **179**, 1707 (2006).

[53] S. Schaack, U. Ranieri, P. Depondt, R. Gaal, W. F. Kuhs, P. Gillet, F. Finocchi, and L. E. Bove, Proc. Natl. Acad. Sci. U.S.A. **116**, 16204 (2019).

[54] H. T. Stokes, D. M. Hatch, and B. J. Campbell, FINDSYM, ISOTROPY Software Suite (iso.byu.edu).

[55] H. T. Stokes and D. M. Hatch, J. Appl. Crystallogr. **38**, 237 (2005).

[56] T. Ohba, Y. Kitano, and Y. Komura, Acta Cryst. C **40**, 1 (1984).

[57] K. Ishizaki, P. Bolsaitis, and I. Spain, Solid State Commun. **15**, 1591 (1974).

[58] J. J. Gilvarry, Phys. Rev. **102**, 308 (1956).

[59] F. A. Lindemann, Phys. Z. **11**, 609 (1910).

[60] K. Refson, P. R. Tulip, and S. J. Clark, Phys. Rev. B **73**, 155114 (2006).

[61] A. Tkatchenko and M. Scheffler, Phys. Rev. Lett. **102**, 073005 (2009).

[62] G. Gao, A. R. Oganov, Y. Ma, H. Wang, P. Li, Y. Li, T. Iitaka, and G. Zou, J. Chem. Phys. **133**, 144508 (2010).

[63] S. J. Clark, M. D. Segall, C. J. Pickard, P. J. Hasnip, M. I. J. Probert, K. Refson, and M. C. Payne, Z. Kristallogr. **220**, 567 (2005).

[64] K. Momma and F. Izumi, J. Appl. Crystallogr. **44**, 1272 (2011).

[65] J. Gonzalez-Platas, M. Alvaro, F. Nestola, and R. Angel, J. Appl. Crystallogr. **49**, 1377 (2016).

[66] J. Rodríguez-Carvajal, Physica (Amsterdam) **192B**, 55 (1993).

[67] Y. Fei, A. Ricolleau, M. Frank, K. Mibe, G. Shen, and V. Prakapenka, Proc. Natl. Acad. Sci. U.S.A. **104**, 9182 (2007).

[68] C. Prescher and V. B. Prakapenka, High Press. Res. **35**, 223 (2015).

[69] P. Loubeyre, R. LeToullec, D. Hausermann, M. Hanfland, R. J. Hemley, H. K. Mao, and L. W. Finger, Nature (London) **383**, 702 (1996).

[70] P. Loubeyre, R. Letoullec, and J. P. Pinceaux, Phys. Rev. Lett. **67**, 3271 (1991).

[71] B. Chen, L. J. Conway, W. Sun, X. Kuang, C. Lu, and A. Hermann, Phys. Rev. B **103**, 035131 (2021).

nature COMMUNICATIONS

ARTICLE

https://doi.org/10.1038/s41467-021-26664-3 OPEN

In-situ abiogenic methane synthesis from diamond and graphite under geologically relevant conditions

Miriam Peña-Alvarez[1], Alberto Vitale Brovarone[2,3], Mary-Ellen Donnelly[4], Mengnan Wang[1],
Philip Dalladay-Simpson[4], Ross Howie[4] & Eugene Gregoryanz[1,4,5]✉

Diamond and graphite are fundamental sources of carbon in the upper mantle, and their reactivity with H_2-rich fluids present at these depths may represent the key to unravelling deep abiotic hydrocarbon formation. We demonstrate an unexpected high reactivity between carbons' most common allotropes, diamond and graphite, with hydrogen at conditions comparable with those in the Earth's upper mantle along subduction zone thermal gradients. Between 0.5-3 GPa and at temperatures as low as 300 °C, carbon reacts readily with H_2 yielding methane (CH_4), whilst at higher temperatures (500 °C and above), additional light hydrocarbons such as ethane (C_2H_6) emerge. These results suggest that the interaction between deep H_2-rich fluids and reduced carbon minerals may be an efficient mechanism for producing abiotic hydrocarbons at the upper mantle.

---

[1] Centre for Science at Extreme Conditions and School of Physics and Astronomy, University of Edinburgh, Edinburgh, UK. [2] Dipartimento di Scienze Biologiche, Geologiche e Ambientali (BiGeA), Alma Mater Studiorum Università di Bologna, Piazza di Porta San Donato 1, 40126 Bologna, Italy. [3] Sorbonne Université, Muséum National d'Histoire Naturelle, UMR CNRS 7590, IRD, Institut de Mináralogie, de Physique des Matáriaux et de Cosmochimie, IMPMC, 75005 Paris, France. [4] Center for High Pressure Science and Technology Advanced Research (HPSTAR), Shanghai, China. [5] Key Laboratory of Materials Physics, Institute of Solid State Physics, Chinese Academy of Sciences, Hefei, China. ✉email:

The process of abiotic hydrocarbon formation in the deep Earth is still contested, despite being central in geobiological processes and potential natural energy sources[1,2]. Light hydrocarbons of abiotic origin have been identified in an increasing number of geological fluids in the Earth's lithosphere[3–6]. Methane has also been detected within deep diamonds, suggesting the presence of abiotic hydrocarbons at mantle depths[7–9]. However, their formation mechanisms and distribution, as well as their possibility to degas towards the crust and the atmosphere, remain largely unconstrained. The abiotic formation of stable light hydrocarbons, such as methane (CH_4), was mainly considered to occur through reduction paths and, generally, in the presence of oxygen carrying species such as carbon monoxide (CO) or carbon dioxide (CO_2) through the so-called Fischer–Tropsch Type reactions[10–14].

In the Earth's interior, diamond and graphite are the major carbon reservoirs[14], whereas hydrogen (H_2) is among the most volatile fluid elements. Graphite and other forms of carbonaceous materials are dominant at depths between 50 and 140 km (2–4 GPa)[14–16], whereas deeper than 140 km depth (4 GPa) diamond becomes stable[17]. In Fig. 1, we summarize the relationship between pressure, in deep in the Earth's mantle, and the evolution of the distribution of graphite and diamond, together with hydrogen and methane clusters.

Methane may be a fundamental component of upper mantle fluids[14]. It reacts under high pressure, forming long-chain hydrocarbons, and then it is predicted to eventually dissociate into diamond, graphitic carbon and hydrogen[18–21]. Methane at depths could co-exist with molecular hydrogen (H_2) and small amounts of light hydrocarbons and different carbon allotropes[10,13,14]. However, the origin of methane in the upper mantle remains largely unconstrained[2].

Reactions between H_2-rich fluids and carbon-bearing parent minerals may be effective to produce methane and other hydrocarbons abiotically. At upper mantle conditions, H_2 may be present and immiscible in aqueous fluids, and react with condensed carbon minerals[22–26]. Water–rock interactions at subduction zone conditions may also be effective in generating H_2-rich fluids[6,27–31], also in the presence of graphite[25,32,33]. Molecular hydrogen may also be present in minerals at upper mantle conditions[34]. Recent analysis of fluid inclusions in super-deep diamonds indicates that H_2 may represent a significant component of upper mantle fluids in the presence of diamond[7,8]. Yet, reactivity between diamond and H_2 at upper mantle conditions has not been contemplated as a source of abiogenic hydrocarbons.

Here we investigate abiotic methane production from the precursors of pure H_2 and condensed carbon minerals such as diamond and graphite. We conduct in situ experiments using a resistively heated diamond anvil cell (DAC) at pressure and temperature conditions in the range of 0.5–5 GPa and 300–730 °C, and use Raman spectroscopy as the diagnostic tool. Most of the investigated conditions are consistent with Earth's upper mantle and subduction zone *P*–*T* (pressure and temperature) gradients[35]. We find that at these mild *P*–*T* conditions, diamond and graphite react readily with H_2 to form methane and other light hydrocarbons, such as ethane (C_2H_6). This demonstrates that the reaction between condensed carbon phases and H_2 could be an important source of abiotic hydrocarbons, which should be considered in the deep Earth's carbon cycle.

Results

Diamond and hydrogen. At room temperature and at pressures between 2 and 3 GPa, Raman measurements show only the characteristic spectrum of the H_2 sample, and that of the diamond anvils (Fig. 2). Heating hydrogen in a DAC at 2 GPa (which corresponds to Earth depths of about 70 km[36], see Fig. 1) to temperatures of 500 °C, we observe a new Raman band appearing at ~2900 cm^{-1} within ~20 min (see Fig. 2). This new band can be detected uniformly across the sample chamber. Repeating measurements at 3 GPa (below or around 70 km depth, see Fig. 1) and holding the sample at lower temperatures of 300 °C for a period of 2 h, the same results are observed; a new band at 2900 cm^{-1} appears and its intensity grows with time. This new mode coincides with the most intense C-H vibrational

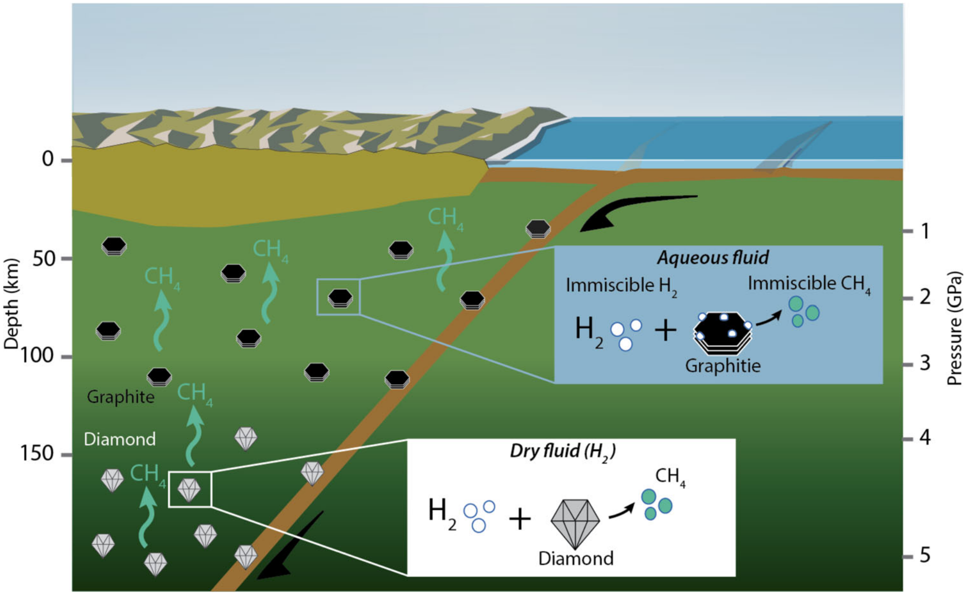

Fig. 1 Sketch modified after Fig. 1 in Li et al.[52] summarizing the implications of this study on the genesis of abiotic CH_4 in the upper mantle. Below about 140 km depth (4 GPa), the immiscibility of H_2 in aqueous fluids[22] can promote interactions between H_2 gas and graphitic carbon, leading to the formation of CH_4 (Fig. 3). This condition is plausible in reducing settings with low oxygen concentrations within the upper mantle[17] or where reducing conditions are generated in subduction zones[25]. At greater depths in the diamond stability field, the oxygen fugacity is predicted to be lower[14] and dry H_2 fluids are more common[7, 8] and interact with diamond to form abiotic CH_4 (Fig. 1).

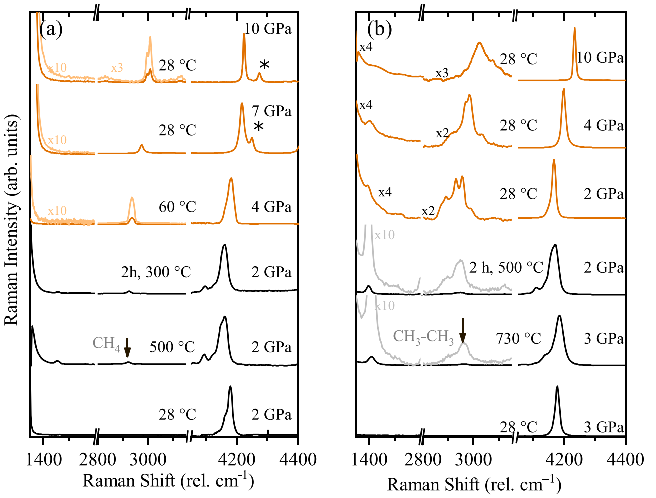

Fig. 2 Raman spectra of resistive heating of hydrogen in a diamond anvil cell at selected pressures and temperatures. a Up to a maximum temperature of 500 °C and held at 300 °C for 2 h and after cooling down. Orange spectra correspond to the cooled down sample. **b** Up to a maximum temperature of 730 °C and held at 500 °C for 2 h and after cooling down. Orange spectra correspond to cooled down sample. The CH stretching modes of CH_4 (**a**) and C_2H_6 (**b**) appear between 2900 and 3000 cm^{-1}. In the cooled down sample of experiment **b**, the CH wagging mode is seen at around 1480 cm^{-1}. The band at around 4200 cm^{-1} corresponds to the vibrational mode of H_2 (Q_1[50], this is accompanied by the rotational + vibrational band ($Q_1 + S_0$) visible in liquid hydrogen. At high temperatures, there is another band at lower frequency, which corresponds to the thermally populated second vibrational state of hydrogen[51]. Asterisks mark the vibrational mode from the CH_4-H_2 van der Waals compounds[41].

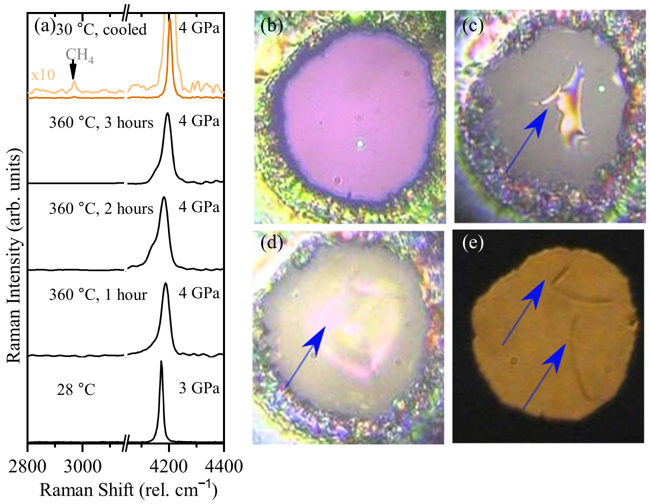

Fig. 3 Hydrogen sample resistively heated during heating and cooling process at 3 GPa, using a diamond anvil cell whose culets and gasket hole had been coated with 300 nm Al_2O_3 with chemical vapour deposition. a Representative Raman spectra during heating and cooling (orange spectrum). **b** Image taken in transmitted and reflected light, while being heated at 360 °C for 1 h. **c** Image of the sample at 360 °C for 3 h, the image has been taken in reflected light so the region of the chamber where coating is becoming damaged is seen. **d** Image of the sample after cooling in transmitted light. **e** Image of the sample after cooling down only in transmitted light. Blue arrows are used to point the regions of the damaged Al_2O_3 layer; green spots are due to the laser beam.

stretching mode of methane, indicating abiotic methane production from the only elements present in the experimental chamber: hydrogen and diamond.

High-temperature studies of dense methane have yielded other light hydrocarbons such as ethane (C_2H_6), propane (C_3H_8), butane (C_4H_{10}) and isobutane (C_4H_{10})[19]. In our experiments, increasing temperature to 730 °C at 3 GPa leads to the growth of more complex vibrational excitations, centred around ~2950 cm^{-1} (Fig. 2b). The intensity of these modes increases with time if the sample is held at above 500 °C for 2 h. By comparing the obtained spectrum with spectra reported for hydrocarbons in the literature[37–39], we can identify the additional product as ethane (C_2H_6). Upon temperature quenching, samples were subsequently compressed up to 30 GPa at room temperature. The evolution of the vibrational spectra and their frequencies vs. pressure are in good agreement with those of methane and ethane (Supplementary Fig. 2)[37,40,41]. We also note that at above 5 GPa, we observe an additional vibrational mode, which is present neither in pure methane nor in hydrogen (see mode indicated by asterisks in Fig. 2a). This new mode has previously been interpreted as being a feature of a CH_4-H_2 van der Waals compounds[41]. Experiments were repeated using deuterium as a precursor instead of hydrogen, in which we observed the formation of CD_4 (Supplementary Fig. 1). The presence of CD_4 after heating is evidence that the reaction is between the D_2 sample and diamond, and not from residuals and/or a contaminant from the preparation process.

We performed three control experiments to eliminate the possibility of carbon contaminants in the sample chamber, whereby the gasket and diamonds were insulated from the hydrogen sample with aluminium oxide (Al_2O_3) (see Fig. 3). Al_2O_3 has been shown to provide a protective layer that slows down hydrogen diffusion into diamond at high pressures and temperatures[42]. Therefore, it could preclude the formation of CH_4 from the diamond anvil and hydrogen. Inspection of the optical images of the sample chamber after 1 h at 360 °C and 4 GPa reveals that the coating was still pristine (Fig. 3b) and no methane was observed spectroscopically. However, after 3 h at this temperature, part of the coating began breaking up and detaching from the diamond (Fig. 3c), becoming more visible during the cooling of the sample (Fig. 3d–e). This deterioration of the coating with temperature and time enabled hydrogen to reach the diamonds, forming methane on contact. We also considered that the transition metals from which the gaskets are made, could catalyse the reactions[43]. We conducted several heating runs with different gasket materials such as rhenium (Re) and tungsten (W), and gasket liners, e.g., gold (Au) and Al_2O_3 (see Supplementary Table 1 for a list of the materials used). We observed that, regardless of the gasket and gasket insert materials, if the diamonds are not protected by Al_2O_3, CH_4 and/or C_2H_6 are always produced.

Graphite, glass-like carbon and hydrogen. As graphite may be an important component of subducted sedimentary rocks[44–46], we repeated our experiments by adding graphite into the sample chamber. These experimental runs yielded identical results producing larger amounts of methane on a shorter timescale than with the diamond precursor. We also explored the reactivity of disordered carbonaceous materials using a glass-like form of carbon (for which thermodynamic data are available[46]), which may be common below 500–600 °C in subduction zones[15]. Figure 4 shows the Raman spectra between 1.0 and 1.5 GPa during heating cycles of (a) H_2-graphite and (b) H_2-glassy-like carbon. In both cases, there is a rapid growth of the C-H stretching mode of methane with time. Similar to the methane production from diamond, CH_4 forms compounds with H_2 on compression of the quenched sample[41].

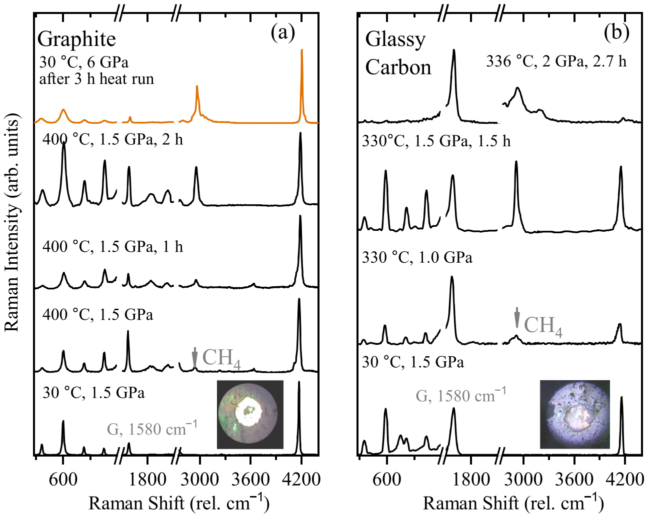

Fig. 4 Resistive heating of hydrogen in a diamond anvil cell. a Graphite loaded together with H_2, spectra at selected temperatures and pressure. Spectra have been normalized to the H_2 stretching mode, around 4200 cm^{-1}. Orange spectrum correspond to the quenched sample. **b** Glassy-like carbon loaded together with H_2, spectra are normalized to the G band characteristic of carbonaceous materials at around 1580 cm^{-1}. Inserted images correspond to the sample within the diamond anvil cell chamber during the experiment.

Discussion

In each of the graphite and glassy carbon experiments, similar amounts of samples were used. Comparing the intensities of methane produced by different carbonaceous samples, one can conclude that glassy-like carbon and graphite are naturally more reactive to H_2 than diamond (see Supplementary Fig. 4 to compare the relative intensities of methane peaks generated from the different starting materials). Of course, this statement is tentative and approximate, as the graphite and glassy-like carbon measurements also contain a contribution from the methane formed from the diamond anvils and there are other factors such as background and hydrogen accessibility to the carbonaceous sample that influence the experiment. Nevertheless, this suggests that graphitic carbon materials can act as an efficient reactant for abiotic CH_4 formation in upper mantle and crustal environments.

Condensed carbon reservoirs and their mobilization in deep fluids may represent a key to unravelling deep carbon recycling. We have shown that under dry conditions, and in the absence of oxygen or a catalyst, methane is formed from diamond, graphite or glassy carbon and hydrogen, at conditions comparable to the outer layers of the Earth's mantle (depths of 18–160 km, pressures of 0.5–5 GPa and temperatures between 300 °C and 730 °C). Fluids rich in H_2 may be common in the upper mantle and generated by fluid-rock or melt-rock reactions[6,6,47], or dissolved in minerals[34]. Moreover, immiscibility of H_2 or H_2-CH_4 in aqueous fluids in the graphite or diamond stability field[22–25] could extend the effectiveness of our results to local fluid–mineral interactions in oxygen-bearing systems. Fig. 1 summarizes the main results of this work, in which we propose that hydrogen and different reduced carbon species found in the Earth's mantle could be an important source of abiogenic hydrocarbons. Our results provide a possible explanation for geological findings of the detection of methane and hydrogen in diamonds extracted from the lower mantle[7,8]. Thus, the different species might contribute to the cycling of deep carbon in the Earth's upper mantle via methane production and act as sources of deep energy for shallower reservoirs[1,6,48].

Methods

Ultra-low fluorescent diamond anvils, with culet diameters ranging between 200 and 300 μm, were used. Re-foil or W-foil gaskets were used to contain the samples. No differences were found when using Re or W, or Au-lined Re gaskets. Research-grade (99.9999%) hydrogen and deuterium samples were gas loaded into DACs at a pressure of 0.2 GPa. Prior to gas loading, the diamond surfaces were thoroughly cleaned with several washes, first with acetone and then with of doubly distilled deionized water and the use of organic solvents was avoided. The gasket was first cleaned in water in an ultrasonic bath and then placed on the diamond surface for immediate loading. After loading, samples were mapped with Raman spectroscopy to rule out any possible contamination. High-purity graphite (99.8%, 43078 Alfa Aesar) and glass-like spherical powder by Alpha Aesar were loaded into the DAC, and research-grade hydrogen (99.9999%) was subsequently gas loaded at a pressure of 0.2 GPa. Al_2O_3 coatings were done via chemical vapour deposition. High-quality Raman spectra were acquired using a custom-built micro-focused Raman system, using a 514 nm laser as the excitation line. High-temperature experiments were conducted using modified high-temperature Mao–Bell DACs equipped with a primary and a secondary heater, and thermocouples. A type-K thermocouple was partially clamped between the gasket and the diamond anvil. Good mechanical contact ensures a more accurate temperature measurement, while ensuring optimum proximity to the sample chamber. Heating was done in two stages: (i) the primary, external to the cell assembly heating to 500 °C; and (ii) a secondary internal heater, situated around the diamond anvils, heating to 730 °C. The secondary heater made of a Mo-coil heating element was driven by a DC power supply on a feedback loop with a high sampling rate controller[49–51].

Data availability

The data that support the findings of this study are available from the corresponding author upon request.

Received: 24 May 2021; Accepted: 8 October 2021;

References

1. Gold, T. The deep, hot biosphere. *Proc. Natl Acad. Sci. USA* **89**, 6045–6049 (1992).
2. Sephton, M. A. & Hazen, R. M. On the origins of deep hydrocarbons. *Rev. Mineral. Geochem.* **75**, 449–465 (2013).
3. Charlou, J., Donval, J., Fouquet, Y., Jean-Baptiste, P. & Holm, N. Geochemistry of high h_2 and ch_4 vent fluids issuing from ultramafic rocks at the rainbow hydrothermal field. *Chem. Geo.* **191**, 345–359 (2002).
4. Etiope, G. & Sherwood Lollar, B. Abiotic methane on earth. *Rev. Geophys.* **51**, 276–299 (2013).
5. Young, E. et al. The relative abundances of resolved $^{12}CH_2D_2$ and $^{13}CH_3D$ and mechanisms controlling isotopic bond ordering in abiotic and biotic methane gases. *Geochim. Cosmochim. Acta* **203**, 235–264 (2017).
6. Vitale-Brovarone, A. et al. Subduction hides high-pressure sources of energy that may feed the deep subsurface biosphere. *Nat. Commun.* **11**, 1–11 (2020).
7. Smith, E. M. et al. Large gem diamonds from metallic liquid in Earth's deep mantle. *Science* **354**, 1403–1405 (2016).
8. Smith, E. M. et al. Blue boron-bearing diamonds from Earth's lower mantle. *Nature* **560**, 84–87 (2018).
9. Smit, K. V., Shirey, S. B., Stern, R. A., Steele, A. & Wang, W. Diamond growth from C–H–N–O recycled fluids in the lithosphere: evidence from CH_4 micro-inclusions and $\delta^{13}C$–$\delta^{15}N$-N content in marange mixed-habit diamonds. *Lithos* **265**, 68–81 (2016).
10. Anderson, R. B., Kölbel, H. & Ralek, M. *The Fischer-Tropsch Synthesis* Vol. 16 (Academic, 1984).
11. McCollom, T. M. Laboratory simulations of abiotic hydrocarbon formation in Earth's deep subsurface. *Rev. Mineral. Geochem.* **75**, 467–494 (2013).
12. McCollom, T. M. Abiotic methane formation during experimental serpentinization of olivine. *Proc. Natl Acad. Sci. USA* **113**, 13965–13970 (2016).
13. Spanu, L., Donadio, D., Hohl, D., Schwegler, E. & Galli, G. Stability of hydrocarbons at deep earth pressures and temperatures. *Proc. Natl Acad. Sci. USA* **108**, 6843–6846 (2011).
14. Frost, D. J. & McCammon, C. A. The redox state of Earth's mantle. *Annu. Rev. Earth Planet. Sci.* **36**, 389–420 (2008).
15. Buseck, P. R. & Huang, B.-J. Conversion of carbonaceous material to graphite during metamorphism. *Geochim. Cosmochim. Acta* **49**, 2003–2016 (1985).
16. Zhang, C. & Duan, Z. A model for C–O–H fluid in the Earth's mantle. *Geochim. Cosmochim. Acta* **73**, 2089–2102 (2009).
17. Day, H. W. A revised diamond-graphite transition curve. *Am. Mineral.* **97**, 52–62 (2012).

18. Benedetti, L. R. et al. Dissociation of CH_4 at high pressures and temperatures: diamond formation in Giant planet interiors?. *Science* **286**, 100–102 (1999).
19. Kolesnikov, A., Kutcherov, V. G. & Goncharov, A. F. Methane-derived hydrocarbons produced under upper-mantle conditions. *Nat. Geosci.* **2**, 566 (2009).
20. Hirai, H., Konagai, K., Kawamura, T., Yamamoto, Y. & Yagi, T. Polymerization and diamond formation from melting methane and their implications in ice layer of giant planets. *Phys. Earth Planet. Inter.* **174**, 242–246 (2009). ***Advances in high pressure mineral physics: from deep mantle to the core***.
21. Hazen, R., Mao, H., Finger, L. & Bell, P. Structure and compression of crystalline methane at high pressure and room temperature. *Appl. Phys. Lett.* **37**, 288–289 (1980).
22. Bali, E., Audétat, A. & Keppler, H. Water and hydrogen are immiscible in Earth's mantle. *Nature* **495**, 220–222 (2013).
23. Huang, F., Daniel, I., Cardon, H., Montagnac, G. & Sverjensky, D. A. Immiscible hydrocarbon fluids in the deep carbon cycle. *Nat. Commun.* **8**, 1–8 (2017).
24. Li, Y. Immiscible CHO fluids formed at subduction zone conditions. *Geochem. Perspect. Lett.* **3**, 12–21 (2017).
25. Vitale-Brovarone, A. et al. Massive production of abiotic methane during subduction evidenced in metamorphosed ophicarbonates from the Italian Alps. *Nat. Commun.* **8**, 1–13 (2017).
26. Griffin, W. L. et al. Super-reducing conditions in ancient and modern volcanic systems: sources and behaviour of carbon-rich fluids in the lithospheric mantle. *Mineral. Petrol.* **112**, 101–114 (2018).
27. Ferrando, S., Frezzotti, M. L., Orione, P., Conte, R. C. & Compagnoni, R. Late-alpine rodingitization in the bellecombe meta-ophiolites (Aosta Valley, Italian Western Alps): evidence from mineral assemblages and serpentinization-derived H_2-bearing brine. *Int. Geol. Rev.* **52**, 1220–1243 (2010).
28. Boutier, A., Vitale-Brovarone, A., Martinez, I., Sissmann, O. & Mana, S. High-pressure serpentinization and abiotic methane formation in metaperidotite from the Appalachian Subduction, Northern Vermont. *Lithos* **396**, 106190 (2021).
29. Peng, W. et al. Abiotic methane generation through reduction of serpentinite-hosted dolomite: implications for carbon mobility in subduction zones. *Geochim. Cosmochim. Acta* **311**, 119–140 (2021).
30. Mao, H. K. et al. When water meets iron at Earth's core–mantle boundary. *Natl Sci. Rev.* **4**, 870–878 (2017).
31. Mao, H.-K. & Mao, W. L. Key problems of the four-dimensional Earth system. *Matter Radiat. Extremes* **5**, 038102 (2020).
32. Malvoisin, B., Chopin, C., Brunet, F. & Galvez, M. E. Low-temperature wollastonite formed by carbonate reduction: a marker of serpentinite redox conditions. *J. Petrol.* **53**, 159–176 (2012).
33. Galvez, M. E. et al. Graphite formation by carbonate reduction during subduction. *Nat. Geosci.* **6**, 473–477 (2013).
34. Moine, B. et al. Molecular hydrogen in minerals as a clue to interpret ∂D variations in the mantle. *Nat. Commun.* **11**, 1–10 (2020).
35. Penniston-Dorland, S. C., Kohn, M. J. & Manning, C. E. The global range of subduction zone thermal structures from exhumed blueschists and eclogites: rocks are hotter than models. *Earth Planet. Sci. Lett.* **428**, 243–254 (2015).
36. Dziewonski, A. M. & Anderson, D. L. Preliminary reference earth model. *Phys. Earth Planet. Inter.* **25**, 297–356 (1981).
37. Shimizu, H., Shimazaki, I. & Sasaki, S. High-pressure Raman study of liquid and molecular crystal ethane up to 8 GPa. *Jpn J. Appl. Phys.* **28**, 1632 (1989).
38. Kudryavtsev, D. et al. Raman and IR spectroscopy studies on propane at pressures of up to 40 GPa. *J. Phys. Chem. A* **121**, 6004–6011 (2017).
39. Kudryavtsev, D. A., Kutcherov, V. G. & Dubrovinsky, L. S. Raman high-pressure study of butane isomers up to 40 GPa. *AIP Adv.* **8**, 115104 (2018).
40. Wu, Y., Sasaki, S. & Shimizu, H. High-pressure Raman study of dense methane: CH_4 and CD_4. *J. Raman Spectrosc.* **26**, 963–967 (1995).
41. Somayazulu, M. S., Finger, L. W., Hemley, R. J. & Mao, H. K. High-pressure compounds in methane-hydrogen mixtures. *Science* **271**, 1400–1402 (1996).
42. Subramanian, N., Goncharov, A. F., Struzhkin, V. V., Somayazulu, M. & Hemley, R. J. Bonding changes in hot fluid hydrogen at megabar pressures. *Proc. Natl Acad. Sci. USA* **108**, 6014–6019 (2011).
43. Chou, I.-M. & Anderson, A. J. Diamond dissolution and the production of methane and other carbon-bearing species in hydrothermal diamond-anvil cells. *Geochim. Cosmochim. Acta* **73**, 6360–6366 (2009).
44. Beyssac, O., Goffé, B., Chopin, C. & Rouzaud, J. Raman spectra of carbonaceous material in metasediments: a new geothermometer. *J. Metamorph. Geol.* **20**, 859–871 (2002).
45. Hayes, J. M. & Waldbauer, J. R. The carbon cycle and associated redox processes through time. *Philos. Trans. R. Soc. Lond. B Biol. Sci.* **361**, 931–950 (2006).
46. Tumiati, S. et al. Dissolution susceptibility of glass-like carbon versus crystalline graphite in high-pressure aqueous fluids and implications for the behavior of organic matter in subduction zones. *Geochim. Cosmochim. Acta* **273**, 383–402 (2020).
47. Tollan, P., Gurenko, A. & Hermann, J. Elucidating the processes affecting highly primitive lavas of the Borgarhraun flow (Northern Iceland) using trace elements in olivine. *Geochim. Cosmochim. Acta* **286**, 441–460 (2020).
48. Mukhina, E., Kolesnikov, A. & Kutcherov, V. The lower *PT* limit of deep hydrocarbon synthesis by $CaCO_3$ aqueous reduction. *Sci. Rep.* **7**, 1–5 (2017).
49. Gregoryanz, E., Goncharov, A. F., Matsuishi, K., Mao, H. K. & Hemley, R. J. Raman spectroscopy of hot dense hydrogen. *Phys. Rev. Lett.* **90**, 4 (2003).
50. Howie, R. T., Dalladay-Simpson, P. & Gregoryanz, E. Raman spectroscopy of hot hydrogen above 200 GPa. *Nat. Mater.* **14**, 495–499 (2015).
51. Peña-Alvarez, M. et al. Intensity of Raman modes as a temperature gauge in fluid hydrogen and deuterium. *J. Appl. Phys.* **125**, 025901 (2019).
52. Li, J., Redfern, S. A. T. & Giovannelli, D. Introduction: deep carbon cycle though five reactions. *Am. Mineral.* **104**, 465–467 (2019).

Acknowledgements

M.P.A. acknowledges the support of the UKRI Future leaders fellowship Mrc-Mr/T043733/1. M.P.A. and E.G. acknowledge the support of the European Research Council (ERC) Grant 'Hecate' Reference number 695527 held by Professor Graeme Ackland. A.V.B acknowledges the support from the European Research Council (ERC) under the European Union's Horizon 2020research and innovation programme (Grant agreement No. 864045, ERC CoG DeepSeep) and from the Richard Lounsbery foundation. R.T.H. acknowledges the support of the National Science Foundation of China (Grant number 11974034) and ERC Grant 'MetElOne' Reference number 948895. The authors thank Josh Wood for the help with the Fig. 1.

Author contributions

M.P.A., A.V.-B. and E.G. planned the research. P.D.-S., E.G. and R.T.H. contributed materials/diagnostic tools. M.P.A., M.-E.D., M.W., P.D.-S. and R.T.H. carried out the experiments. M.P.A. analysed and interpreted the data. M.P.A., A.V.-B. and E.G. wrote the paper.

Competing interests

The authors declare no competing interests.

Additional information

Supplementary information The online version contains supplementary material available at https://doi.org/10.1038/s41467-021-26664-3.

Correspondence and requests for materials should be addressed to Eugene Gregoryanz.

Peer review information *Nature Communications* thanks Dimitri Sverjensky and the other, anonymous, reviewer(s) for their contribution to the peer review of this work.

Reprints and permission information is available at http://www.nature.com/reprints

Publisher's note Springer Nature remains neutral with regard to jurisdictional claims in published maps and institutional affiliations.

CONDENSED MATTER PHYSICS

Superionicity, disorder, and bandgap closure in dense hydrogen chloride

Jack Binns[1†], Andreas Hermann[2*], Miriam Peña-Alvarez[2], Mary-Ellen Donnelly[1], Mengnan Wang[1], Saori Imada Kawaguchi[3], Eugene Gregoryanz[1,4,2], Ross T. Howie[1], Philip Dalladay-Simpson[1*]

Hydrogen bond networks play a crucial role in biomolecules and molecular materials such as ices. How these networks react to pressure directs their properties at extreme conditions. We have studied one of the simplest hydrogen bond formers, hydrogen chloride, from crystallization to metallization, covering a pressure range of more than 2.5 million atmospheres. Following hydrogen bond symmetrization, we identify a previously unknown phase by the appearance of new Raman modes and changes to x-ray diffraction patterns that contradict previous predictions. On further compression, a broad Raman band supersedes the well-defined excitations of phase V, despite retaining a crystalline chlorine substructure. We propose that this mode has its origin in proton (H^+) mobility and disorder. Above 100 GPa, the optical bandgap closes linearly with extrapolated metallization at 240(10) GPa. Our findings suggest that proton dynamics can drive changes in these networks even at very high densities.

INTRODUCTION

Hydrogen bond networks are defined by the interactions between donor and acceptor atoms, epitomized in the ice rules governing the structure of water ice. The responses of these interactions to changes in temperature or pressure are critical to understand the physical properties of molecular crystals (*1*–*5*). Hydrogen bonds have been observed to rearrange, amorphize, and symmetrize under compression, leading to the extensive polymorphism defining the phase diagrams of simple molecules such as H_2O, H_2S, and NH_3 (*6*–*16*). The behavior of hydrogen bond networks at very high densities, beyond symmetrization, is not well explored except in computational predictions and is difficult to generalize. Water ice is suggested to transform to an orthorhombic structure that retains symmetric hydrogen bonds (*17*) before further transitions, including metallization, are predicted to lower the network symmetry in the terapascal pressure regime (*18*–*20*). The extensive icy mantles of Neptune, Uranus, and their exoplanet analogs experience pressures above the known symmetrization pressure of pure H_2O ($P \approx 90$ GPa), making this the dominant hydrogen-bonding regime beyond Earth (*21*–*24*).

Due to their comparatively weak hydrogen bonding, the hydrogen halides (HX, X = F, Cl, Br, and I) form solid phases characterized by disorder of the hydrogen atoms. In their lowest-density forms, hydrogen atoms are free to rotate about the halide centers of mass. When cooled and/or compressed, HX molecules form zigzagging chains with the underlying face-centered cubic (fcc) packing of the halide atom positions remaining essentially unchanged (*25*–*28*). The heavier hydrogen halides HBr and HI decompose under increasing pressure into their constituent elements at 39 and 11 GPa, respectively (*29*, *30*). However, previous studies of hydrogen chloride (HCl) indicate that decomposition should occur at much higher pressures (*31*, *32*), making it ideal for the study of a weakly constrained hydrogen-bonded system in the regime beyond symmetrization.

Prior work on compressed HCl has been limited to Raman and Brillouin spectroscopy measurements to 60 and 4.5 GPa, respectively (*32*, *33*); no diffraction studies at high pressure have been carried out to date. The structure of low-temperature/high-pressure phase III was determined by neutron diffraction (space group $Cmc2_1$) (*25*). Raman spectroscopy indicates that at room temperature, HCl phase I transforms to phase III at 19 GPa (*31*) before a further change to a phase IV with symmetrized hydrogen bonds at 51 GPa. The onset of symmetrization was inferred from the weakening and eventual disappearance of H—Cl stretching modes, implying that H atoms occupy positions in the center of Cl—H—Cl bonds. In doing so, the space group symmetry of the crystal is transformed to *Cmcm* (*29*, *31*). Density functional theory (DFT) calculations have been applied to predict the behavior of HCl at high densities. Structure-searching methods suggest a sequence of low-symmetry phases dominated by zigzag chains of symmetric hydrogen bonds: a triclinic $P\bar{1}$ structure above 108 GPa (*34*), a monoclinic $P2_1/m$ phase more stable than phase IV above 233 GPa (*35*), and another monoclinic $C2/m$ phase more stable than $P\bar{1}$ above 250 GPa (*36*).

Here, we combine experimental measurements and first-principles calculations to study HCl up to 256(10) GPa, more than four times the pressure limit of previous experiments. Our Raman spectroscopy measurements extend to 205(10) GPa above which the signal decays. X-ray diffraction patterns were collected up to 190(10) GPa. Visual and near-infrared (IR) optical transmission measurements could be performed up to 207(10) GPa at which point no transmission was measurable. Visual observation and microphotography demonstrate increased reflectivity suggestive of metallic behavior starting from ca. 220(10) GPa to 256(10) GPa, the highest pressure reached in this study. Our measurements confirm the structural transitions coinciding with hydrogen bond order (I to III) and inferred symmetrization (III and IV) reported previously (*31*, *32*). Phase IV is found to be stable up to 80(10) GPa. Above this pressure, phase V is identified by the appearance of new Raman modes accompanying subtle changes in diffraction patterns. Calculations indicate that

---

[1] Center for High Pressure Science & Technology Advanced Research, 1690 Cailun Rd, Pudong, Shanghai 201203, China. [2] School of Physics and Centre for Science at Extreme Conditions, University of Edinburgh, Edinburgh EH9 3JZ, UK. [3] Japan Synchrotron Radiation Research Institute (JASRI), Sayo, Hyogo 679-5198, Japan. [4] Key Laboratory of Materials Physics, Institute of Solid State Physics, Chinese Academy of Sciences, Hefei, China.
[redacted]hor. Email: [redacted] (P.D.-S.); [redacted] (A.H.)
†Present address: School of Science, RMIT University, Melbourne, Victoria 3000, Australia.

this transition reintroduces dynamic disorder as protons become mobile, hopping to new lattice sites. Upon further compression, a broad low-frequency feature emerges above 90(10) GPa, which, from our calculations, is found to be correlated to the gradual inhibition of the proton mobility. At 170(10) GPa, despite no substantial changes in the diffraction, the pressure-dependent behavior of this excitation changes, and HCl exhibits a closing bandgap, increased reflectivity, and intraband absorption, suggesting the presence of free charge carriers.

RESULTS AND DISCUSSION

HCl appears as a transparent liquid at room temperature, from which crystals of phase I nucleate after pressure was increased above 0.7 GPa. Phase I is characterized by Cl atoms forming an fcc lattice. Hydrogen atoms are free to rotate unhindered about the Cl atoms, and this isotropic state gives rise to a characteristic single Raman vibrational mode (vibron) (Fig. 1A) (*32*). This rotator phase was stable up to 18.1 GPa above which transition to phase III occurred, marked by the appearance of eight additional Raman modes. The relatively large stability range of phase I is a testament to the weak hydrogen bonding present in HCl. By comparison, the rotator phase of NH_3 orders at 3 to 4 GPa (*37*) and is absent in H_2O. X-ray diffraction patterns of phase III (Fig. 2) could be indexed to a *C*-centered orthorhombic unit cell $a = 4.5433(5)$, $b = 4.2822(5)$, and $c = 4.4404(5)$ Å at 19.3 GPa, space group $Cmc2_1$. The structure of phase III is characterized by zigzagging chains of HCl molecules with ordered hydrogen atoms in asymmetric Cl⋯H—Cl hydrogen bonds (*25*).

With increasing pressure, the hydrogen bonds in phase III shorten, eventually leading to an equalization of interatomic distances between the H atom and the neighboring donor and acceptor Cl atoms (Cl⋯H⋯Cl) (fig. S1). This change is detected in Raman spectroscopy measurements that show the softening and eventual loss of the HCl stretching mode at pressures above 51 GPa (Fig. 1). This continuous transition results in the symmetric hydrogen bond network that distinguishes phase IV and increases the space group symmetry to *Cmcm* (*31*, *32*). X-ray diffraction measurements cannot directly corroborate the phase III to IV transition due to the low scattering power of hydrogen. However, no changes were observed in diffraction patterns before or after this transition, confirming that the phase transformation is due to changes in hydrogen atom positions only. A secondary indication is provided by a distinct change in the linear compressibilities with pressure, which decreases due to the symmetrization (fig. S2). Our own calculations confirm the hydrogen bond symmetrization transition at 50(3) GPa (fig. S1), and unit cell dimensions derived from DFT calculations show excellent

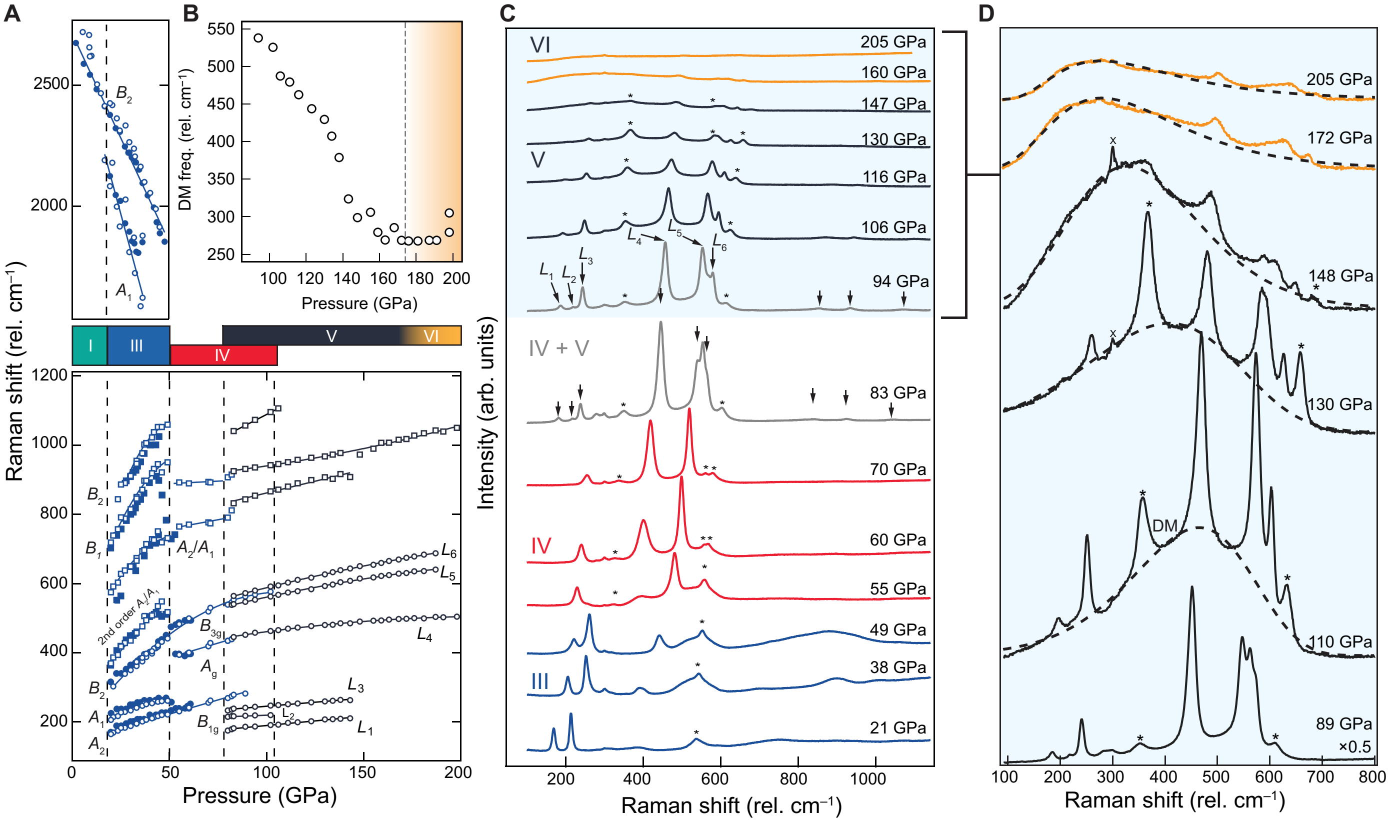

Fig. 1. Raman spectroscopy of HCl. (**A**) Raman frequencies of HCl up to 200 GPa, and the top indicates the symmetric and antisymmetric H—Cl stretch, with their disappearance associated with the symmetrization of the hydrogen bond network. Square markers denote the HCl excitations that are found to be in an energy regime typical of librational movement (*31*). The filled symbols correspond to previous studies (*31*, *32*). (**B**) Pressure dependence of the frequency of the broad disordered mode (DM) highlighted in (D), and dashed line indicates the approximate point of inflection. (**C**) Raman spectra of HCl phases III, IV, and V/VI up to 205 GPa. Stars indicate the excitations due to trace Cl_2 impurities (*47*). (**D**) Selected Raman spectra above 89(10) GPa show that a broad band emerges, which increases in intensity while red shifting with pressure. The dashed black line represents a log-normal excitation profile frequently used in the characterization of the boson peak in disordered systems (*64*).

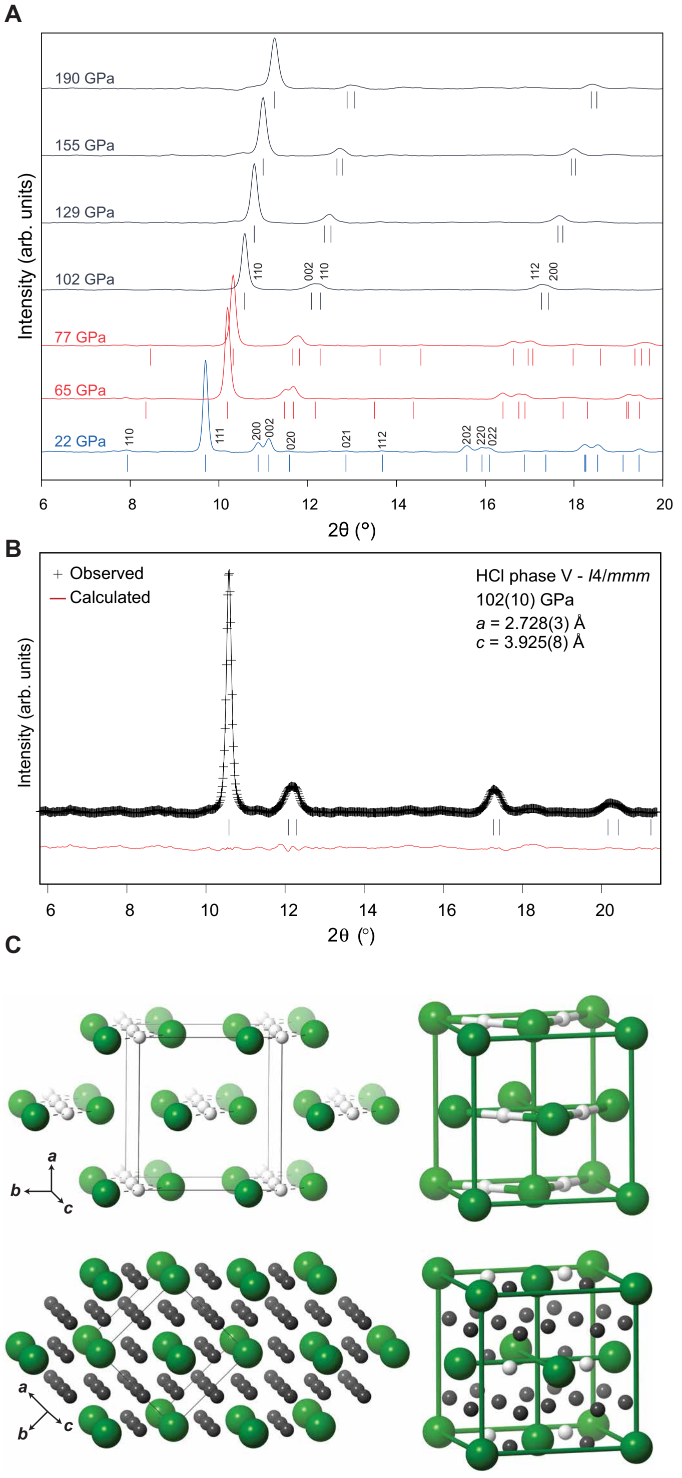

Fig. 2. X-ray diffraction patterns of HCl under pressure. (**A**) Powder diffraction patterns of HCl with increasing pressure ($\lambda = 0.4131$ Å). Tick marks show the calculated peak positions, and indices are given for major reflections. Line colors denote phases II, IV, and V following Fig. 1. (**B**) Representative Le Bail refinement of HCl at 102(10) GPa. Experimental data are indicated with points, calculated profile is shown in black, and difference is shown as the lower red trace. Refined unit cell dimensions are $a = 2.728(3)$ and $c = 3.925(8)$ Å. (**C**) Crystal structures of phase IV (top) and phase V (bottom); new disordered H positions are shown in gray. Thin black lines outline unit cells, and thick green lines indicate the approximate fcc unit cell of the chlorine lattice.

agreement with those determined experimentally (fig. S2). In addition, the frequencies generated in a previous numerical study (*35*) show excellent consistency with our measurements for phase III/IV (Fig. 1A).

The transition to the postsymmetrized phase, phase V, occurs in the region 80(10) to 100(10) GPa, where nine additional Raman modes (indicated with arrows in Fig. 1C) emerge and are found to coexist with excitations inherent to phase IV. In the low-frequency region, we assign the Raman modes that are below 650 cm^{-1} as optical lattice modes (L_1 to L_6). Above 800 cm^{-1}, we also observe enhanced Raman activity in a frequency region formerly occupied by librational excitations of the presymmetrized phase III (*32*). Changes in the x-ray diffraction patterns are observed above 90 GPa and are more subtle: The (020) reflection is lost, and the (200) and (002) reflections merge to form one broad peak at ca. $2\theta = 12°$ (Fig. 2A).

Structure searching and molecular dynamics (MD) calculations have suggested two possible phase V structures in space groups $P2_1/m$ (*35*) and $P\bar{1}$ (*34*). However, there is poor agreement between the calculated x-ray diffraction patterns of these predicted structures and our experimental data (fig. S3). Instead, we find the structure of phase V to be tetragonal with unit cell dimensions $a = 2.728(3)$ and $c = 3.925(8)$ Å at 102 GPa. This unit cell is derived by direct distortion of phase IV and provides an excellent fit to the observed data (Fig. 2). The equation of state of HCl is presented in fig. S4; the refined equation of state parameters are as follows: $V_0 = 42.8(10)$ Å^3, $K_0 = 5.9(8)$ GPa, and $K_\text{p} = 3.91(7)$.

To gain insight into the underlying physics driving the IV-to-V transition, we investigated the behavior of HCl, and in particular the hydrogen atoms, using DFT MD calculations at 95 GPa and ran at temperatures up to 1000 K. Simulations used supercells of both the experimentally determined phase V lattice parameters and those of the calculated phase IV at 95 GPa. Results are very similar for both sets of structures. We find that, under all temperature conditions, Cl atoms retain a solid lattice, in agreement with our x-ray diffraction measurements, that can be understood as an approximately fcc structure. In contrast, the protons' behavior changes qualitatively with temperature: At 625 K and less, protons do not leave the bonds of phase IV, while at 750 K and above, they become mobile. The protons do not move freely through the crystal but hop into the midpoints of all 12 nearest-neighbor Cl─Cl connections, occupying them roughly equally (Fig. 3A). Despite the localized nature of the proton sites [also seen in superionic water (*38*) and water-ammonia mixtures (*39*)], the hopping mechanism leads to macroscopic proton diffusion. The ionic conductivity at 750 K, the onset of hydrogen diffusion, is estimated from the Nernst-Einstein relation to be 9.8 S cm^{-1}, well above the accepted threshold of 1 S cm^{-1} for superionic materials (*40*). The resulting proton disorder, as we discuss below, explains both our x-ray and Raman measurements. Note that we find proton mobility at temperatures much higher than the experimental conditions. However, our calculations did not include nuclear quantum effects, defects, or interfaces and used supercells (108 to 256 molecules) that likely experience superheating; all of which are expected to artificially stabilize the solid against any diffusive state. It is not unlikely that mobile hydrogen can already be present at room temperature in our experiments. For comparison, analogous diffusive hydrogen sublattices simulated in H_2O and NH_3 at similar pressures require higher temperatures of 1700 and 1000 K, respectively, in the simulations but have been detected at temperatures 700 and 300 K lower (*13*, *41*, *42*).

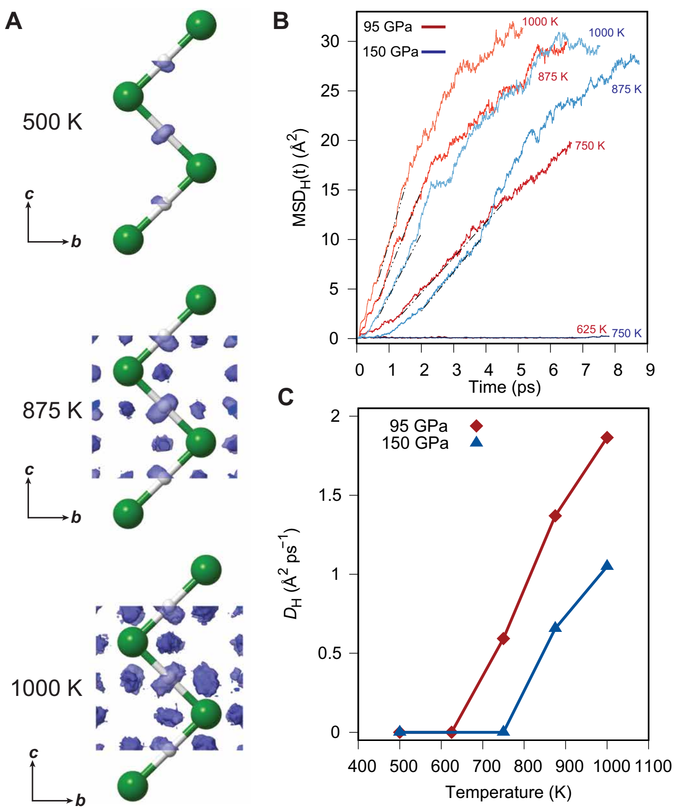

Fig. 3. MD and proton mobility. (**A**) Average proton positions (blue) for phase V at 150 GPa and different temperatures compared to initial geometries (balls and sticks) from DFT MD simulations. From 750 K (at 95 GPa) and above, protons migrate to additional sites lying on Cl···Cl interatomic contacts. (**B**) Proton mean squared displacement MSD$_H$(*t*) at 95 GPa (red) and 150 GPa (blue) and different temperatures (500 to 1000 K). Linear fits are indicated with black dashed lines. (**C**) Derived proton diffusion coefficients D_H for HCl with increasing temperature.

The relationship between the ordered (IV) and disordered (V) hydrogen positions can be seen if the underlying Cl sublattice is indeed approximated as an fcc structure (Fig. 2C). In this approximated phase IV, hydrogen atoms occupy 4 of the 24 equivalent 24d Wyckoff sites, giving rise to the zigzagging chains of symmetric hydrogen bonds. In the observed tetragonal structure, the equivalent H atom positions are (1/2, 0, 0, 4*c*) and (1/4, 1/4, 1/4, 8*f*). We propose that transitioning to phase V leads to hydrogen atoms partially occupying all the 24*d* sites with equal probability. Critically, through the occupancy of new hydrogen lattice sites, the local bonding environment of each Cl atom is altered. A notably similar phenomenon was observed in water ice VII above ca. 26 GPa using neutron diffraction (*43*). In this phase, compression leads to increasing partial occupancy of "interstitial void" sites that lie outside the assumed hydrogen bond between oxygen atoms. The appearance of H atoms outside the expected covalent bond was postulated to be due to a relative weakening of the covalent O—H interaction versus hydrogen bond strength. This effect can be seen even more clearly in HCl phase V, as hydrogen bond strength that increases the energetic difference between the covalent "ordered" (white) and "disordered" 24*d* sites (gray) is lowered to the point at which proton migration occurs.

Further support for the emergence of a disordered hydrogen sublattice can be found by comparing the enthalpies of predicted phases. Transitioning to the predicted structures in (*34*, *35*) requires significant distortions in the Cl sublattice that lead to increased packing efficiency as compared to the disordered phase V, as measured by *PV* terms in computed enthalpies. While this might seem to imply that phase V is metastable, DFT inherently fails to capture the contribution of configurational entropy due to proton disorder. A conservative estimate of the entropic contribution, assuming that each Cl atom is bonded to two H atoms, equates to 38 meV per HCl molecule at 300 K. This contribution stabilizes phase V against the predicted structures up to at least 230 GPa, when the $P\bar{1}$ structure (*34*) is more stable than phase IV by 40 meV per HCl. In the absence of this disorder, our own calculations indicate that, in the ground state, phase IV is the thermodynamically most stable phase up to 120 GPa above which the predicted $P\bar{1}$ phase has the lowest enthalpy in agreement with (*34*).

Above 90 GPa, in contrast with the subtle changes observed in x-ray diffraction patterns, the Raman spectra of phase V are seen to undergo profound changes, as seen in Fig. 1C, comparing spectra at 94 and 147 GPa. Intriguingly, these changes are observed primarily to be a consequence of an emergent broad low-frequency excitation (full width at half maximum of ~300 cm^{-1}), illustrated by the black dashed line in Fig. 1D. Typically, broad features in the frequency range of the lattice modes are indicative of structural disorder, hence our designation of "disorder mode(s)" (DM) in Fig. 1D. For example, broad excitations are a defining characteristic in amorphous materials (*44*), where the overall Raman spectrum is found to resemble the vibrational density of states as symmetry restraints are relaxed and optical phonons spanning the Brillouin zone are active. Intuitively, the emergence of this mode in HCl would initially appear to be in contradiction with our diffraction observations, which demonstrate the persistence of a crystalline powder. Upon further compression, this band is found to shift to lower frequencies while increasing in intensity, eventually superseding the well-defined Raman excitations above 148 GPa. Above ca. 175 GPa, the frequency of this excitation plateaus and gradually weakens, becoming difficult to detect above 200 GPa as seen in Fig. 1D.

Correlated to the spectral changes discussed previously, HCl is also found to change in appearance, as seen in the sequential photomicrographs in Fig. 4A. These changes are typical of a pressure-induced optical bandgap closure (*45*–*47*), whereby the absorption edge passes through the visible wavelengths (Fig. 4 and fig. S6). With increasing pressure, it is found that the optical bandgap of HCl (estimated from the absorption edge; fig. S6) reduces with a linear pressure dependence and is extrapolated to close at ca. 240(10) GPa. Above 210 GPa, the sample becomes sufficiently optically dense that no transmission could be detected down to 0.7 eV as seen in Fig. 4B. Curiously, a significant change is found between pressures of 164(10) and 180(10) GPa, where an abrupt drop in the transmission above 1200 nm, seen in fig. S6B, results in a steep rise in the absorbance, reaching our detection limit (~2 optical density), and shifts to higher energies as a function of pressure (Fig. 4A). The energy range of this feature (0.8 to 1 eV) is characteristic of intraband excitations and therefore could be explained as an absorption due to free charge carriers populating the conduction band. Additional techniques such as in situ four-probe electrical measurements or optical reflectivity would greatly enhance our understanding of the conductive properties of HCl (*48*–*50*); however, this compound poses significant technical

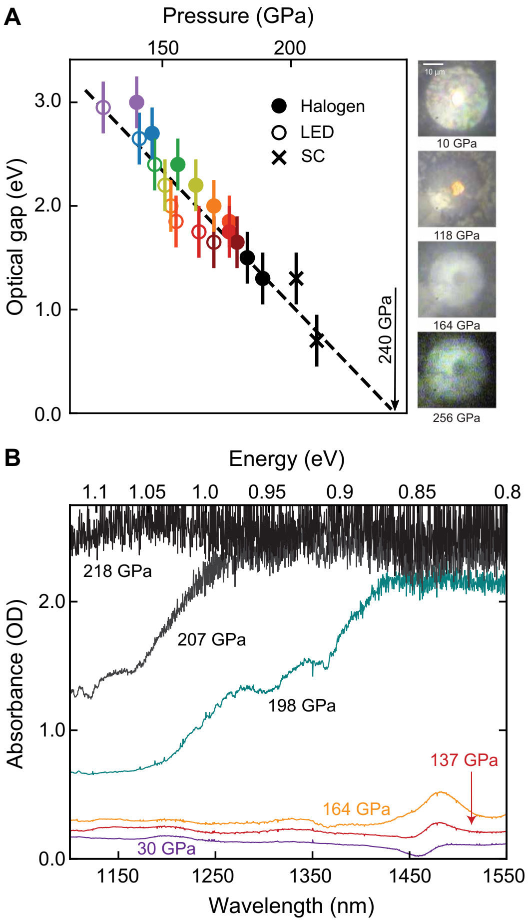

Fig. 4. Optical absorption under pressure. (**A**) Left: Optical bandgap measurements, estimated from the absorption edge (see fig. S7), using various broadband light sources as a function of pressure. The dashed black line is a linear fit that indicates that the optical bandgap will close at around 240(10) GPa. Right: Sequential microphotographs of the HCl sample chamber from 10 to 256 GPa; the sample appears darker and redder with pressure as shorter wavelength light becomes attenuated. SC, supercontinuum. (**B**) Absorbance spectrum over the shortwave IR range. A large increase in absorbance is found between 164 and 198 GPa below 1.1 eV, indicative of free-charge carriers populating the conduction band. No detectable transmission was observed above 210 GPa down to 1700 nm, suggesting that the bandgap is less than 0.7 eV. OD, optical density; LED, light-emitting diode.

challenges because of the cryogenic loading technique and its highly reactive and corrosive nature. Therefore, although HCl has not become fully metallic above 160 GPa, it may exhibit a degree of conductivity before it fully metallizes at 240(10) GPa.

At approximately 170 GPa, we define the complete transformation to phase VI, which was found to sluggishly transform over an 80-GPa interval. We characterize this phase as a high-pressure modification of phase V and having the following observable characteristics: a crystalline chlorine sublattice and disordered vibrational properties. As mentioned previously, initially, it would appear that these characteristics are incompatible; however, it is important to note that the x-ray diffraction is sensitive only to the chlorine positions, having a negligible contribution from hydrogen. Therefore, to explain the inherent disorder captured in our Raman measurements, we again turn to our first-principles calculations to elucidate the role of hydrogen in phase VI. Further simulations were carried out at 150 GPa following the same methodology; the resulting proton mean squared displacement and derived diffusion coefficients at both 95 and 150 GPa are shown in Fig. 3 (B and C). It is seen that the simulations at 150 GPa require significantly higher temperatures, in excess of 850 K, to induce comparable proton diffusion, indicating that proton mobility becomes increasingly inhibited upon compression above 100 GPa. Similar behavior in population exchanges of mobile/immobile hydrogen has been recently reported in an analogous system, high-pressure water ice, using proton nuclear magnetic resonance (*51*). In addition, in this study, it was also found that the nuclear quantum effects lead to far greater mobility of hydrogen-bonded protons than indicated by calculations, a result supported by recent DFT calculations (*52*).

In summary, we find that HCl resists decomposition up to pressures in excess of 250 GPa and find no evidence for the previously predicted candidate structures. Instead, we identify a new phase, phase V (space group *I*4/*mmm*), characterized by the reintroduction of configurational disorder as protons become mobilized, via a hopping mechanism, to new lattice sites. Upon further compression, we observe the gradual transformation to phase VI, distinguishable from phase V by exhibiting disordered vibrational characteristics and a strong absorption in the near IR, likely due to the presence of free charge carriers. Through MD calculations, this transition is found to be correlated and therefore suggested to be motivated by the reduction of proton mobility with pressure. Ultimately, we find that, even at densities far surpassing hydrogen bond symmetrization, phases are still found to be characterized by the physics of the hydrogen atoms. These findings raise intriguing questions about the nature of hydrogen bonding and superionicity in materials at ultrahigh pressures. Current theoretical approaches struggle to describe disordered systems, and it may be that quantum nuclear effects play a far greater role in hydrogen-bonded systems at high densities than previously thought, having implications for hydrogen-rich matter under conditions of extreme temperature and pressures, such as planetary mantles.

MATERIALS AND METHODS

Experimental procedures

We have studied the behavior of pure HCl up to pressures of 260 GPa in diamond anvil cells (DACs) by x-ray diffraction and Raman spectroscopy. Flat culet diamonds (200 μm) were used for x-ray diffraction experiments under 60 GPa, while 30-μm culets were used for higher-pressure Raman spectroscopy experiments. Rhenium foil is inert to HCl and was used as the gasket material in all experiments (*32*). Solid HCl (99.9% purity) was cryogenically loaded into a DAC under a dry nitrogen atmosphere. Successful loading was confirmed by Raman spectroscopy.

Excitation wavelengths of 532 and 660 nm were used for Raman spectroscopy measurements using a custom-built confocal microfocused Raman system. Pressure was determined through both ruby fluorescence ($P < 100$ GPa) and the Raman edge of stressed diamond correlated to the equation of state of a tungsten pressure marker (*53*).

Absorbance was estimated through transmission spectroscopy in the visible range using a black-body spectrum broadband halogen and light-emitting diode light sources (between ~400 and 1000 nm) with a charge-coupled device (CCD) sensitive to the visible. Absorbance in the IR range (between ~800 and 1800 nm) was measured using a supercontinuum laser using the appropriate InGaAs CCD detector, which is sensitive in the IR regime.

Angle-dispersive x-ray diffraction patterns were recorded on a fast image plate detector with synchrotron radiation ($\lambda = 0.4141$ Å, 30 keV) at beamline BL10XU, SPring-8, Japan (*54*). Two-dimensional image plate data were integrated with DIOPTAS (*55*) to yield intensity versus 2θ plots. Le Bail (*56*) profile refinements were carried out in Jana2006 (*57*). Volume and linear equation of state parameters were determined using EoSFit 7 (*58*).

Ab initio calculations

DFT calculations were performed with the Vienna Ab initio Simulation Package (VASP) using plane wave basis sets (cutoff energy $E_c = 800$ eV) in conjunction with projector augmented wave (PAW) datasets (cutoff radii $r_{c,O} = 1.5a_B$, $r_{c,H} = 0.8a_B$) (*59*, *60*). Structural optimizations and MD simulations used the dispersion-corrected optB88-vdW exchange-correlation functional (*61*, *62*); the lattice constants of phases III and IV were very similar when using the semilocal Perdew-Burke-Ernzerhof (PBE) functional. Brillouin zone linear sampling rates were $2\pi \times 0.025$ Å^{-1} for optimizations ($2\pi \times 0.05$ Å^{-1} for MD). MD simulations used 108-molecule supercells starting from both phase IV (calculated) and phase V (experimental) lattice parameters at 95 and 150 GPa. Tests with 256-molecule supercells showed no discernible difference in diffusion behavior (fig. S8). Simulations used a 0.5-fs time step and a Nosé thermostat (*63*), were equilibrated for 0.5 ps, and ran for up to 8.5 ps.

SUPPLEMENTARY MATERIALS

Supplementary material for this article is available at https://science.org/doi/10.1126/sciadv.abi9507

REFERENCES AND NOTES

1. A. Janotti, C. G. Van De Walle, Hydrogen multicentre bonds. *Nat. Mater.* **6**, 44–47 (2007).
2. C. J. Sahle, C. Sternemann, C. Schmidt, S. Lehtola, S. Jahn, L. Simonelli, S. Huotari, M. Hakala, T. Pylkkänen, A. Nyrow, K. Mende, M. Tolan, K. Hämäläinen, M. Wilke, Microscopic structure of water at elevated pressures and temperatures. *Proc. Natl. Acad. Sci. U.S.A.* **110**, 6301–6306 (2013).
3. B. Santra, J. Klimes, D. Alfe, A. Tkatchenko, B. Slater, A. Michaelides, R. Car, M. Scheffler, Hydrogen bonds and van der Waals forces in ice at ambient and high pressures. *Phys. Rev. Lett.* **107**, 185701 (2011).
4. E. Schwegler, G. Galli, F. Gygi, Water under pressure. *Phys. Rev. Lett.* **84**, 2429–2432 (2000).
5. V. Naden Robinson, Y. Wang, Y. Ma, A. Hermann, Stabilization of ammonia-rich hydrate inside icy planets. *Proc. Natl. Acad. Sci. U.S.A.* **114**, 9003–9008 (2017).
6. A. F. Goncharov, V. V. Struzhkin, M. S. Somayazulu, R. J. Hemley, H. K. Mao, Compression of ice to 210 gigapascals: Infrared evidence for a symmetric hydrogen-bonded phase. *Science* **273**, 218–220 (1996).
7. P. Loubeyre, R. LeToullec, E. Wolanin, M. Hanfland, D. Hausermann, Modulated phases and proton centring in ice observed by x-ray diffraction up to 170 GPa. *Nature* **397**, 503–506 (1999).
8. O. Mishima, L. D. Calvert, E. Whalley, An apparently first-order transition between two amorphous phases of ice induced by pressure. *Nature* **314**, 76–78 (1985).
9. Y. Q. Cai, H.-K. Mao, P. C. Chow, J. S. Tse, Y. Ma, S. Patchkovskii, J. F. Shu, V. Struzhkin, R. J. Hemley, H. Ishii, C. C. Chen, I. Jarrige, C. T. Chen, S. R. Shieh, E. P. Huang, C. C. Kao, Ordering of hydrogen bonds in high-pressure low-temperature H_2O. *Phys. Rev. Lett.* **94**, 025502 (2005).
10. I. Errea, M. Calandra, C. J. Pickard, J. R. Nelson, R. J. Needs, Y. Li, H. Liu, Y. Zhang, Y. Ma, F. Mauri, Quantum hydrogen-bond symmetrization in the superconducting hydrogen sulfide system. *Nature* **532**, 81–84 (2016).
11. X. Huang, X. Wang, D. Duan, B. Sundqvist, X. Li, Y. Huang, H. Yu, F. Li, Q. Zhou, B. Liu, T. Cui, High-temperature superconductivity in sulfur hydride evidenced by alternating-current magnetic susceptibility. *Natl. Sci. Rev.* **6**, 713–718 (2019).
12. E. J. Pace, X.-D. Liu, P. Dalladay-Simpson, J. Binns, M. Peña-Alvarez, J. P. Attfield, R. T. Howie, E. Gregoryanz, Properties and phase diagram of $(H_2S)_2H_2$. *Phys. Rev. B* **101**, 174511 (2020).
13. C. Cavazzoni, G. L. Chiarotti, S. Scandolo, E. Tosatti, M. Bernasconi, M. Parrinello, Superionic and metallic states of water and ammonia at giant planet conditions. *Science* **238**, 44–46 (1999).
14. M. Gauthier, P. Pruzan, J. C. Chervin, J. M. Besson, Raman scattering study of ammonia up to 75 GPa: Evidence for bond symmetrization at 60 GPa. *Phys. Rev. B* **37**, 2102–2115 (1988).
15. J. L. Finney, D. T. Bowron, A. K. Soper, T. Loerting, E. Mayer, A. Hallbrucker, Structure of a New dense amorphous ice. *Phys. Rev. Lett.* **89**, 205503 (2002).
16. C. J. Pickard, R. J. Needs, Highly compressed ammonia forms an ionic crystal. *Nat. Mater.* **7**, 775–779 (2008).
17. M. Benoit, M. Bernasconi, P. Focher, M. Parrinello, New high-pressure phase of ice. *Phys. Rev. Lett.* **76**, 2934–2936 (1996).
18. Y. Wang, H. Liu, J. Lv, L. Zhu, H. Wang, Y. Ma, High pressure partially ionic phase of water ice. *Nat. Commun.* **2**, 563–565 (2011).
19. A. Hermann, N. W. Ashcroft, R. Hoffmann, High pressure ices. *Proc. Natl. Acad. Sci.* **109**, 745–750 (2011).
20. B. Militzer, H. F. Wilson, New phases of water ice predicted at megabar pressures. *Phys. Rev. Lett.* **105**, 195701 (2010).
21. M. Guthrie, R. Boehler, J. J. Molaison, B. Haberl, A. M. Dos Santos, C. Tulk, Structure and disorder in ice VII on the approach to hydrogen-bond symmetrization. *Phys. Rev. B* **99**, 184112 (2019).
22. N. Nettelmann, R. Helled, J. J. Fortney, R. Redmer, New indication for a dichotomy in the interior structure of Uranus and Neptune from the application of modified shape and rotation data. *Planet. Space Sci.* **77**, 143–151 (2013).
23. J. J. Lissauer, D. C. Fabrycky, E. B. Ford, W. J. Borucki, F. Fressin, G. W. Marcy, J. A. Orosz, J. F. Rowe, G. Torres, W. F. Welsh, N. M. Batalha, S. T. Bryson, L. A. Buchhave, D. A. Caldwell, J. A. Carter, D. Charbonneau, J. L. Christiansen, W. D. Cochran, J.-M. Desert, E. W. Dunham, M. N. Fanelli, J. J. Fortney, T. N. Gautier III, J. C. Geary, R. L. Gilliland, M. R. Haas, J. R. Hall, M. J. Holman, D. G. Koch, D. W. Latham, E. Lopez, S. McCauliff, N. Miller, R. C. Morehead, E. V. Quintana, D. Ragozzine, D. Sasselov, D. R. Short, J. H. Steffen, A closely packed system of low-mass, low-density planets transiting Kepler-11. *Nature* **470**, 53–58 (2011).
24. A. S. J. Méndez, F. Trybel, R. J. Husband, G. Steinle-Neumann, H. P. Liermann, H. Marquardt, Bulk modulus of H_2O across the ice VII-ice X transition measured by time-resolved x-ray diffraction in dynamic diamond anvil cell experiments. *Phys. Rev. B* **103**, 064104 (2021).
25. E. Sándor, R. F. C. Farrow, Crystal structure of solid hydrogen chloride and deuterium chloride. *Nature* **213**, 171–172 (1967).
26. E. Sándor, M. W. Johnson, Crystal structure and the lower phase transition in solid deuterium bromide. *Nature* **217**, 541–543 (1968).
27. M. W. Johnson, E. Sándor, E. Arzi, The crystal structure of deuterium fluoride. *Acta Crystallogr. Sect. B* **31**, 1998–2003 (1975).
28. A. Ikram, B. H. Torrie, B. M. Powell, Structures of solid deuterium bromide and deuterium iodide. *Mol. Phys.* **79**, 1037–1049 (1993).
29. E. Katoh, H. Yamawaki, H. Fujihisa, M. Sakashita, K. Aoki, Raman and infrared study of phase transitions in solid HBr under pressure. *Phys. Rev. B* **59**, 11244–11250 (1999).
30. J. Binns, X.-D. Liu, P. Dalladay-Simpson, V. Afonina, E. Gregoryanz, R. T. Howie, Synthesis and stability of hydrogen iodide at high pressures. *Phys. Rev. B.* **96**, 144105 (2017).
31. K. Aoki, E. Katoh, H. Yamawaki, M. Sakashita, H. Fujihisa, Hydrogen-bond symmetrization and molecular dissociation in hydrogen halids. *Phys. B Condens. Matter.* **265**, 83–86 (1999).
32. E. Katoh, H. Yamawaki, H. Fujihasa, M. Sakashita, K. Aoki, Raman study of phase transition and hydrogen bond symmetrization in solid DCl at high pressure. *Phys. Rev. B.* **61**, 119–124 (2000).
33. H. Shimizu, K. Kamabuchi, T. Kume, S. Sasaki, High-pressure elastic properties of the orientationally disordered and hydrogen-bonded phase of solid HCl. *Phys. Rev. B* **59**, 11727–11732 (1999).
34. L. Zhang, Y. Wang, X. Zhang, Y. Ma, High-pressure phase transitions of solid HF, HCl, and HBr: An ab initio evolutionary study. *Phys. Rev. B* **82**, 014108 (2010).
35. D. Duan, F. Tian, Z. He, X. Meng, L. Wang, C. Chen, X. Zhao, B. Liu, T. Cui, Hydrogen bond symmetrization and superconducting phase of HBr and HCl under high pressure: An ab initio study. *J. Chem. Phys.* **133**, 074509 (2010).
36. C. Chen, Y. Xu, X. Sun, S. Wang, Novel superconducting phases of HCl and HBr under high pressure: An Ab initio study. *J. Phys. Chem. C* **119**, 17039–17043 (2015).
37. F. Datchi, S. Ninet, M. Gauthier, A. M. Saitta, B. Canny, F. Decremps, Solid ammonia at high pressure: A single-crystal x-ray diffraction study to 123 GPa. *Phys. Rev. B Condens. Matter Mater. Phys.* **73**, 1741115 (2006).
38. J.-A. Hernandez, R. Caracas, Superionic-superionic phase transitions in body-centered cubic H_2O ice. *Phys. Rev. Lett.* **117**, 135503 (2016).

39. V. Naden Robinson, A. Hermann, Plastic and superionic phases in ammonia–water mixtures at high pressures and temperatures. *J. Phys. Condens. Matter* **32**, 184004 (2020).
40. J. B. Boyce, B. A. Huberman, Superionic conductors: Transitions, structures, dynamics. *Phys. Rep.* **51**, 189–265 (1979).
41. A. F. Goncharov, N. Goldman, L. E. Fried, J. C. Crowhurst, I.-F. W. Kuo, C. J. Mundy, J. M. Zaug, Dynamic ionization of water under extreme conditions. *Phys. Rev. Lett.* **94**, 125508 (2005).
42. S. Ninet, F. Datchi, A. M. Saitta, Proton disorder and superionicity in hot dense ammonia ice. *Phys. Rev. Lett.* **108**, 165702 (2012).
43. M. Guthrie, R. Boehler, C. A. Tulk, J. J. Molaison, A. M. dos Santos, K. Li, R. J. Hemley, Neutron diffraction observations of interstitial protons in dense ice. *Proc. Natl. Acad. Sci. U.S.A.* **110**, 10552–10556 (2013).
44. R. J. Hemley, H. K. Mao, P. M. Bell, B. O. Mysen, Raman spectroscopy of SiO_2 glass at high pressure. *Phys. Rev. Lett.* **57**, 747–750 (1986).
45. S. Desgreniers, Y. K. Vohra, A. L. Ruoff, Optical response of very high density solid oxygen to 132 GPa. *J. Phys. Chem.* **94**, 1117–1122 (1990).
46. M. I. Eremets, R. J. Hemley, H. K. Mao, E. Gregoryanz, Semiconducting non-molecular nitrogen up to 240 GPa and its low-pressure stability. *Nature* **411**, 170–174 (2001).
47. P. Dalladay-Simpson, J. Binns, M. Peña-Alvarez, M.-E. Donnelly, E. Greenberg, V. Prakapenka, X.-J. Chen, E. Gregoryanz, R. T. Howie, Band gap closure, incommensurability and molecular dissociation of dense chlorine. *Nat. Commun.* **10**, 1134 (2019).
48. M. Hou, Y. He, B. G. Jang, S. Sun, Y. Zhuang, L. Deng, R. Tang, J. Chen, F. Ke, Y. Meng, V. B. Prakapenka, B. Chen, J. H. Shim, J. Liu, D. Y. Kim, Q. Hu, C. J. Pickard, R. J. Needs, H. K. Mao, Superionic iron oxide–hydroxide in Earth's deep mantle. *Nat. Geosci.* **14**, 174–178 (2021).
49. M. I. Eremets, I. A. Troyan, Conductive dense hydrogen. *Nat. Mater.* **10**, 927–931 (2011).
50. G. Rillo, M. A. Morales, D. M. Ceperley, C. Pierleoni, Optical properties of high-pressure fluid hydrogen across molecular dissociation. *Proc. Natl. Acad. Sci. U.S.A.* **116**, 9770–9774 (2019).
51. T. Meier, S. Petitgirard, S. Khandarkhaeva, L. Dubrovinsky, Observation of nuclear quantum effects and hydrogen bond symmetrisation in high pressure ice. *Nat. Commun.* **9**, 2766 (2018).
52. F. Trybel, M. Cosacchi, T. Meier, V. M. Axt, G. Steinle-Neumann, Proton dynamics in high-pressure ice-VII from density functional theory. *Phys. Rev. B* **102**, 184310 (2020).
53. Y. Akahama, H. Kawamura, Pressure calibration of diamond anvil Raman gauge to 410 GPa. *J. Phys. Conf. Ser.* **215**, 12195 (2010).
54. Y. Ohishi, N. Hirao, N. Sata, K. Hirose, M. Takata, Highly intense monochromatic X-ray diffraction facility for high-pressure research at SPring-8. *High Press. Res.* **28**, 163–173 (2008).
55. C. Prescher, V. B. Prakapenka, *DIOPTAS*: A program for reduction of two-dimensional x-ray diffraction data and data exploration. *High Press. Res.* **35**, 223–230 (2015).
56. A. Le Bail, H. Duroy, J. L. Fourquet, Ab-initio structure determination of LiSbWO6 by X-ray powder diffraction. *Mater. Res. Bull.* **23**, 447–452 (1988).
57. V. Petříček, M. Dušek, L. Palatinus, Crystallographic computing system JANA2006: General features. *Zeitschrift für Krist. Mater.* **229**, 345–352 (2014).
58. J. Gonzalez-Platas, M. Alvaro, F. Nestola, R. J. Angel, *EosFit7-GUI*: A new graphical user interface for equation of state calculations, analyses and teaching. *J. Appl. Cryst.* **49**, 1377–1382 (2016).
59. G. Kresse, F. Furthmüller, Efficient iterative schemes for ab initio total-energy calculations using a plane-wave basis set. *Phys. Rev. B* **54**, 11169–11186 (1996).
60. G. Kresse, D. Joubert, From ultrasoft pseudopotentials to the projector augmented-wave method. *Phys. Rev. B* **59**, 1758–1775 (1999).
61. J. Klimeš, D. R. Bowler, A. Michaelides, Chemical accuracy for the van der Waals density functional. *J. Phys. Condens. Matter* **22**, 022201 (2010).
62. J. Klimeš, D. R. Bowler, A. Michaelides, Van der Waals density functionals applied to solids. *Phys. Rev. B* **83**, 195131 (2011).
63. S. Nosé, A unified formulation of the constant temperature molecular dynamics methods. *J. Chem. Phys.* **81**, 511–519 (1984).
64. W. Schirmacher, G. Diezemann, C. Ganter, Harmonic vibrational excitations in disordered solids and the "Boson Peak". *Phys. Rev. Lett.* **81**, 136–139 (1998).

Acknowledgments

Funding: P.D.-S. and R.T.H. acknowledge their respective "1000 Young Talents" awards and the "Top 1000 Talents" award of H.-K. Mao. R.T.H. acknowledges that part of this research was supported by the National Natural Science Foundation of China (NSFC) project no. 11974034. M.P.-A. acknowledges the support of the European Research Council (ERC) Grant Hecate reference no. 695527 secured by G. Ackland and FLF Award - MR/T043733/1. Parts of this research were also conducted at the SPring-8 facility under proposal no. 2017A1401. Computational resources provided by the U.K.'s National Supercomputer Service through the U.K. Car-Parrinello consortium (EPSRC grant no. EP/P022561/1) and by the U.K. Materials and Molecular Modelling Hub (no. EP/P020194) are acknowledged. **Author contributions:** J.B., E.G., R.T.H., and P.D.-S. designed the study and experiments. A.H. carried out simulation work. J.B., M.P.-A., M.-E.D., M.W., S.I.K., E.G., R.T.H., and P.D.-S. performed the experiments. J.B., A.H., and P.D.-S. analyzed experimental and simulation data. J.B., A.H., E.G., R.T.H., and P.D.-S. wrote the manuscript with input from all authors. **Competing interests:** The authors declare that they have no competing interests. **Data and materials availability:** All data needed to evaluate the conclusions in the paper are present in the paper and/or the Supplementary Materials.

Submitted 11 April 2021
Accepted 21 July 2021
Published 1 September 2021
10.1126/sciadv.abi9507

Citation: J. Binns, A. Hermann, M. Peña-Alvarez, M.-E. Donnelly, M. Wang, S. I. Kawaguchi, E. Gregoryanz, R. T. Howie, P. Dalladay-Simpson, Superionicity, disorder, and bandgap closure in dense hydrogen chloride. *Sci. Adv.* **7**, eabi9507 (2021).

Science Advances

Superionicity, disorder, and bandgap closure in dense hydrogen chloride

Jack Binns, Andreas Hermann, Miriam Pea-Alvarez, Mary-Ellen Donnelly, Mengnan Wang, Saori Imada Kawaguchi,
Eugene Gregoryanz, Ross T. Howie, and Philip Dalladay-Simpson

Sci. Adv., **7** (36), eabi9507.
DOI: 10.1126/sciadv.abi9507

Science Advances (ISSN) is published by the American Association for the Advancement of Science. 1200 New York Avenue NW, Washington, DC 20005. The title *Science Advances* is a registered trademark of AAAS.

THE JOURNAL OF PHYSICAL CHEMISTRY Letters

pubs.acs.org/JPCL Letter

Complex Hydrogen Substructure in Semimetallic RuH_4

Jack Binns, Yu He, Mary-Ellen Donnelly, Miriam Peña-Alvarez, Mengnan Wang, Duck Young Kim, Eugene Gregoryanz, Philip Dalladay-Simpson, and Ross T. Howie*

Cite This: *J. Phys. Chem. Lett.* 2020, 11, 3390−3395

Read Online

ACCESS | Metrics & More | Article Recommendations | SI Supporting Information

ABSTRACT: When compressed in a matrix of solid hydrogen, many metals form compounds with increasingly high hydrogen contents. At high density, hydrogenic sublattices can emerge, which may act as low-dimensional analogues of atomic hydrogen. We show that at high pressures and temperatures, ruthenium forms polyhydride species that exhibit intriguing hydrogen substructures with counterintuitive electronic properties. Ru_3H_8 is synthesized from RuH in H_2 at 50 GPa and at temperatures in excess of 1000 K, adopting a cubic structure with short H−H distances. When synthesis pressures are increased above 85 GPa, we observe RuH_4 which crystallizes in a remarkable structure containing corner-sharing H_6 octahedra. Calculations indicate this phase is semimetallic at 100 GPa.

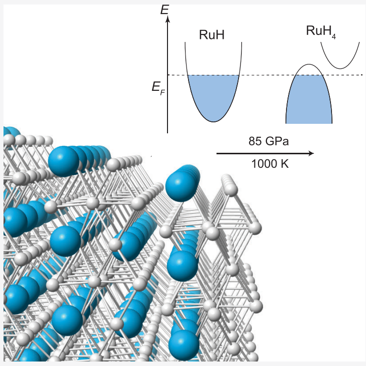

The physical properties of a host metal can be profoundly altered by the presence of hydrogen. Examples include switchable mirrors driven by an electronic transition,[1,2] the disruption of magnetic ordering,[3−6] and the dramatic increases in superconducting transition temperatures (T_c) for metallic hydrides at high pressures ($P > 200$ GPa).[7−10] The solubility of hydrogen in transition metals increases rapidly under compression, with polyhydride species being discovered in a number of first- and second-row members of the group[11−18] and predicted for many others.[19−22] As hydrogen content increases, intriguing substructures emerge, taking the form of H_3^- quasimolecules, clathrate cages, and layers of isolated H atoms.[13,19,23−28] Unique to group 8 metals (Fe, Ru, Os), it has been predicted that increasing hydrogen content should lead to the emergence of a series of nonmetallic hydrides FeH_4,[29] FeH_6,[30] FeH_7,[28] RuH_6,[31] and OsH_6.[24] Despite intensive study of the Fe−H system, none of these materials has been synthesized due to the very high pressures (i.e., >200 GPa) required to stabilize them. Ruthenium polyhydride structures are predicted to emerge at much lower pressures, making it ideal to study the formation and properties of nonmetallic hydrides.

Ruthenium monohydride (RuH) has been shown to form at pressures above 14 GPa at room temperature by reaction of its constituent elements and remains stable to at least 30 GPa.[32] Theoretical structure searches predict the emergence of stable compounds with stoichiometries of RuH_3 and RuH_6, the latter containing molecular H_2 and becoming unstable above 100 GPa.[31]

Here, we report the formation of two new ruthenium polyhydride species synthesized using a combination of high temperatures and pressures. On compression, we observe the formation of the known hydride RuH and confirm its stability up to 100 GPa. After heating RuH in a matrix of solid H_2 at pressures above 50 GPa, new diffraction peaks appear, which we determine to be due to Ru_3H_8, which decomposes below 20 GPa. After heating in H_2 at pressures above 85 GPa, RuH partially transforms to a second novel phase, RuH_4, which remains stable down to 70 GPa. Through a combination of X-ray diffraction and DFT calculations, we characterized the structures and electronic properties of this material. RuH_4 is found to contain atomic hydrogen arranged in corner-sharing octahedra. Our calculations indicate that this material is a semimetal at 100 GPa.

After gas loading at 0.2 GPa, mixtures of Ru and H_2 were compressed to 15 GPa, and in agreement with a previous study, we observe the formation of RuH by compression alone (Figure 1(a)).[32] RuH crystallizes in a face-centered cubic structure (space group $Fm\bar{3}m$, $a = 3.8650(1)$ Å at 33 GPa) isostructural to other transition metal monohydrides (e.g., CoH, RhH, NiH).[14,15,17] In the absence of heating, we find RuH remains stable to pressures of 100 GPa.

In situ laser heating has been shown to be a highly effective route to reaching new transition metal hydrides[11,13−16] and was applied here to explore the formation of predicted ruthenium polyhydrides. Samples of RuH and H_2 were

Received: March 2, 2020
Accepted: April 6, 2020
Published: April 6, 2020

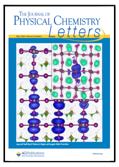

https://dx.doi.org/10.1021/acs.jpclett.0c00688
J. Phys. Chem. Lett. 2020, 11, 3390−3395

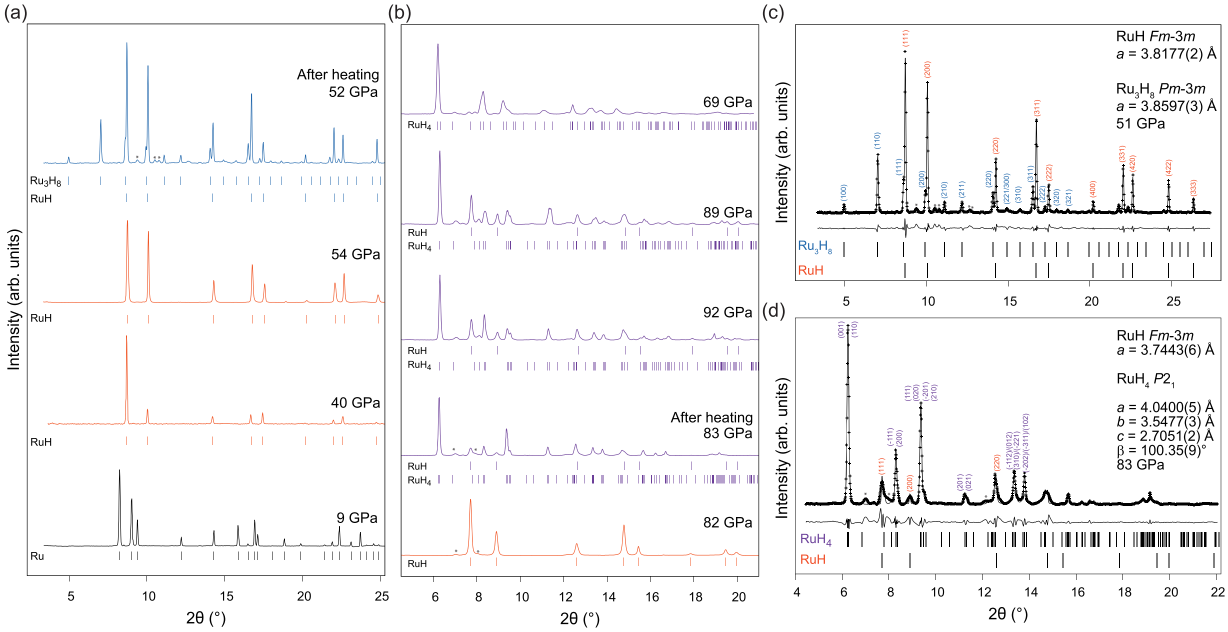

Figure 1. Representative X-ray diffraction patterns of Ru polyhydrides (a) after laser heating at 51 GPa, additional peaks due to Ru_3H_8 can be observed (λ = 0.3344 Å). (b) At higher pressures of 89 GPa, heating RuH + H_2 results in additional peaks indexed to a monoclinic unit cell due to RuH_4 (λ = 0.2897 Å). (c, d) Representative Le Bail refinements of RuH + Ru_3H_8 (λ = 0.3344 Å) and RuH + RuH_4 (λ = 0.2897 Å). Tick marks indicate Bragg peaks for the noted phases. Peaks due to ReH gasket are marked with (*).

compressed and at pressures above 50 GPa laser heated to temperatures over 1500 K, leading to the appearance of new diffraction peaks in addition to those of RuH (Figure 1(a)). All of the new diffraction peaks could be indexed to a primitive cubic unit cell a = 3.8352(3) Å. Structure solution by charge-flipping[33] suggested the presence of a single Ru atom site 3g $\left(\frac{1}{2}, 0{,}0\right)$. Analysis of the volume per Ru atom (Figure 2(a)) suggested a stoichiometry of RuH_3. Samples were subsequently compressed and decompressed to determine the stability range, finding this new phase to be stable up to pressures of at least 71 GPa and down to 17 GPa before decomposing back into RuH + H_2.

Although a RuH_3 phase exhibiting a primitive cubic structure ($Pm\bar{3}m$, a = 2.598 Å at 100 GPa) has been predicted,[31] our experimental diffraction patterns clearly display additional reflections at low angles, which can only be explained with a larger unit cell. To understand this discrepancy, we performed our own structure searching calculations using noninteger values of H/Ru and directed by the experimental lattice constants. These calculations found a stable compound with stoichiometry Ru_3H_8, which shows excellent agreement between calculated and observed unit cell dimensions and volume per Ru atom (Figure 2(a) and S1).

Calculations indicate that our observed Ru_3H_8 structure lies on the convex hull and is 0.446 eV per Ru atom more favorable than RuH_3, as predicted by ref 31, which lies 0.01 eV above at 70 GPa (Figure S2). In Ru_3H_8, each Ru atom is coordinated by eight H atoms with equal Ru−H bonds (1.805 Å at 70 GPa). Remarkably, each unit cell contains a cubic H_8 unit at the center with H−H distances (at 70 GPa) of 1.616 Å along each cube edge. These isolated units result in H−H distances that are significantly shorter than comparable phases such as FeH_3[12] and in fact track closely to those of the molecular hydrides AlH_3 and H_3S.[34,35] Unlike these compounds, the close H−H distances are not part of a continuous network but instead remain discrete units within the crystal structure (Figure 2(b)). Considering the H_8 cluster as a single unit at the unit cell center, the structure of Ru_3H_8 is analogous to the Cu_3Au-type structure. This structure type is a superstructure of the familiar fcc packing, which suggests that Ru atoms and H_8

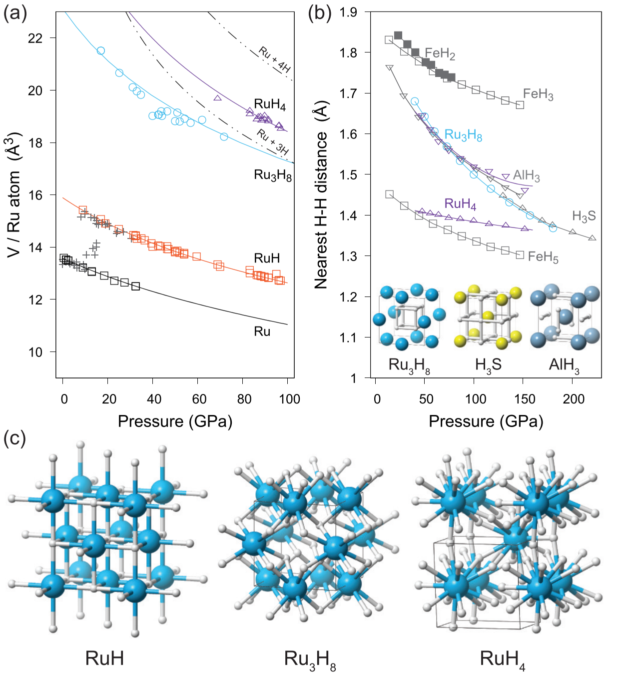

Figure 2. (a) Volume per Ru atom for various Ru−H compounds. Crosses refer to previous study.[32] (b) Nearest H−H interatomic distances in various hydrogen-bearing materials at high pressures.[13,34,35] Inset shows corresponding hydrogen substructures. (c) Crystal structures of Ru−H compounds RuH, Ru_3H_8, and RuH_4. Ru atoms are blue; H atoms are white.

clusters have comparable sizes under these conditions.[36] Calculations show Ru_3H_8 to be metallic and dynamically stable in the observed pressure regime (Figure S3 and S4).

Applying the same heating regime to mixtures of RuH + H_2 at pressures above 82 GPa caused new diffraction peaks to appear, indicating the formation of a second novel high pressure ruthenium polyhydride. All diffraction peaks could be fitted with a *C*-centered monoclinic cell (a = 4.0400(5), b = 3.5477(3), c = 2.7051(2) Å, β = 100.35(9)° at 83 GPa). This unit cell was used to constrain structure-searching calculations which explored stoichiometries with H/Ru > 3 (Figure 2(a)), finding a dynamically stable solution with stoichiometry RuH_4 and space group symmetry $P2_1$ (Figures 2(c) and 3(a)).

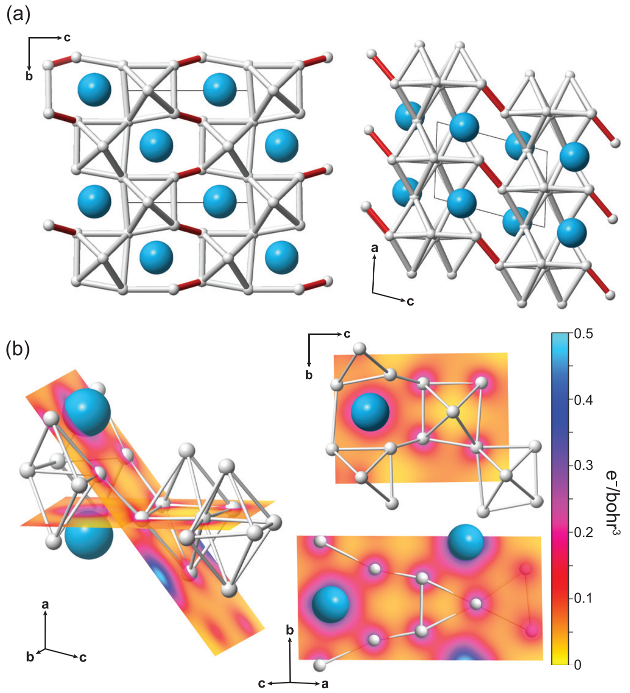

Figure 3. (a) Hydrogen sublattice in RuH_4, white “bonds” are shown between H atoms as a guide to the eye to highlight the structure of octahedral clusters. Short H−H distances between clusters are shown in red. (b) Two representative planes of the electron density distribution in RuH_4 are shown in relation to the crystal structure; (right) electron density maps through key aspects of the H_6 units.

Samples were compressed up to 100 GPa and subsequently decompressed to evaluate the equation of state and stability of this new compound, finding it to be stable down to at least 69 GPa, and changes in unit cell dimensions are in close agreement with calculations (Figure S5 and Table S1). At 70 GPa, RuH_4 is metastable, lying 0.027 eV/f.u. above the convex hull; this deviation is decreased at higher pressures reducing to 0.014 eV/f.u. at 100 GPa (Figure S2). It should be noted that other predicted metastable hydride phases have been synthesized to date, e.g.[37] RuH_4 adopts an entirely new structure type, analogous to the postulated γ-phase of FeH_4, predicted to occur at pressures above 240 GPa but which has remained elusive in experimental studies to date.[29,36]

In RuH_4, each Ru atom is coordinated by 12 H atoms forming highly irregular polyhedra with Ru−H interatomic distances ranging from 1.644 to 1.965 Å (at 100 GPa). However, the remarkable nature of this structure is made clear when we examine the H−H nearest neighbor distances, highlighted with “bonds” to guide the eye in Figure 3(a). Ru atoms are arranged in channels along the a axis with H atoms forming layers of corner-sharing octahedra extending along the b axis. Each layer is two octahedra wide and staggered along a, linked by close H−H distances of 1.385 Å (shown in red Figure 3(a)). The calculated electron density distribution (Figure 3(b)) provides a qualitative indication of the bonding within RuH_4 and in particular the nature of the H_6 octahedra. As expected from other transition metal hydrides, bonding primarily occurs between Ru and H atoms. Examining slices through the H_6 clusters shows the absence of electron density between H atoms, clearly indicating that no H−H bonding is present, either within the H_6 octahedra or along the short H−H links between clusters, confirming the atomic nature of hydrogen in this structure.

Electronic structure calculations were conducted using the HSE hybrid functional which corrects for the known systematic underestimation of band gap energies by standard GGA functionals.[38,39] Calculated electronic band structures indicate that RuH_4 is semimetallic at 100 GPa (Figure 4). To our knowledge, RuH_4 is the first experimentally observed semimetallic transition-metal hydride. It is intriguing to note that although a nonmetallic ruthenium hydride has been predicted, it shares no structural relation to RuH_4 and instead contains molecular H_2 units.[31]

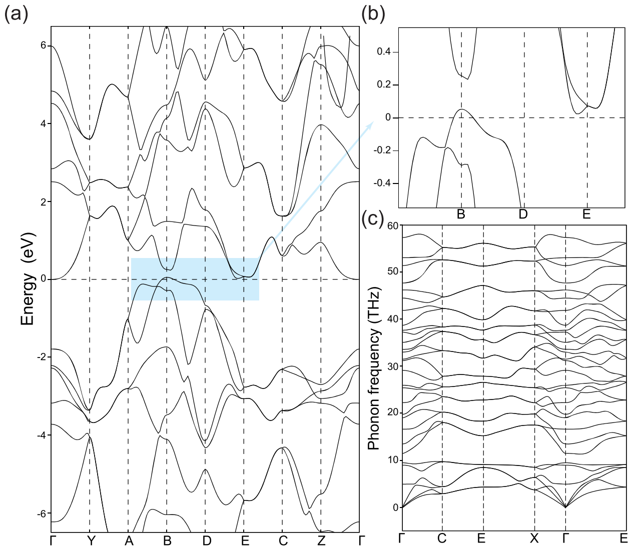

Figure 4. (a) Electronic band structure of RuH_4 at 100 GPa calculated with the HSE06 functional. (b) Region of the Fermi level highlighted. (c) Phonon dispersion curves for RuH_4 at 100 GPa.

Current understanding of the mechanism of high T_c hydrides relies on the coupling of metallic conduction and high hydrogen content.[7] The emergence of complex hydrogen substructures is correlated to a reduction in metallic conduction, strongly suggesting that late transition metals likely provide a poor route to high T_c materials in line with recent critical analyses.[40]

We have demonstrated the formation of a remarkably complex hydrogen sublattice in RuH_4, synthesized at pressures of 85 GPa and temperatures of 1500 K. This structure contains layers of corner-sharing H_6 octahedra surrounding isolated Ru atoms. Electronic structure calculations indicate this phase is semimetallic at 100 GPa. Our findings show that with

https://dx.doi.org/10.1021/acs.jpclett.0c00688
J. Phys. Chem. Lett. 2020, 11, 3390−3395

increasing hydrogen content and pressure, complex emergent atomic hydrogen structures become favorable with counter-intuitive effects on the electronic properties of transition-metal hydrides.

Experimental and Theoretical Methods. High purity ruthenium powder (99.9%, 1−2 μm particle size) from Alfa Aesar was placed into diamond-anvil cells (DACs) together with gold as a pressure marker and subsequently gas loaded with research-grade hydrogen gas (99.9999%) at 0.2 GPa.[41] Loading of hydrogen was confirmed by the observation of the hydrogen vibrational mode using a custom-built microfocused Raman system.[42] Rhenium gaskets were used to form the sample chamber in all experimental runs, diamond anvil culets ranged from 50 to 200 μm.

Ru samples were heated *in situ* from both sides uniaxially by directly coupling to an yttrium−aluminum−garnet (YAG) laser with wavelength λ = 1064 nm. Angle-dispersive X-ray diffraction patterns were recorded on PerkinElmer XRD21 and Mar345 image-plate detectors at the P02.2 ECB (PETRA, Germany) and ID15B (ESRF, France) beamlines with energies in the range 30−42 keV.[43] Two-dimensional image-plate data were integrated with DIOPTAS[44] to yield intensity vs 2θ plots. Patterns were indexed with CONOGRAPH,[45] and Le Bail[46] refinements were carried out in Jana2006.[47] Volume and linear equation of state parameters were determined using EoSFit 7.[48]

The electronic structure calculations were carried out at high pressures within the framework of density function theory (DFT) in conjunction with the projector augment wave method (PAW) as implemented in the VASP code.[49−52] We used Heyd−Scuseria−Ernzerhof (HSE06)[38] functional to determine the electronic properties of Ru−H compounds as the HSE06 functional was shown to predict much better electronic properties than the generalized gradient approximations (GGA). The cutoff energy of the plane wave was set to 800 eV, and Brillouin zone sampling was done on Monkhorst−Pack k-mesh with separations of 0.03 Å^{-1}. The 3p, 4s, and 3d and H 2s and 2p electrons are included in the valence space.

■ ASSOCIATED CONTENT

Supporting Information

The Supporting Information is available free of charge at https://pubs.acs.org/doi/10.1021/acs.jpclett.0c00688.

> Equation of state parameters, electronic and phonon band structures, experimental and calculated unit cell parameters (PDF)

■ AUTHOR INFORMATION

Corresponding Author

Ross T. Howie − *Center for High Pressure Science and Technology Advanced Research (HPSTAR), Shanghai 201203, China*; Email:

Authors

Jack Binns − *Center for High Pressure Science and Technology Advanced Research (HPSTAR), Shanghai 201203, China*; orcid.org/0000-0001-5421-6841

Yu He − *Center for High Pressure Science and Technology Advanced Research (HPSTAR), Shanghai 201203, China; Key Laboratory of High-Temperature and High-Pressure Study of the Earth's Interior, Institute of Geochemistry, Chinese Academy of Sciences, Guiyang, Guizhou 550081, China*

Mary-Ellen Donnelly − *Center for High Pressure Science and Technology Advanced Research (HPSTAR), Shanghai 201203, China*

Miriam Peña-Alvarez − *Centre for Science at Extreme Conditions and The School of Physics & Astronomy, The University of Edinburgh, Edinburgh EH9 3FD, United Kingdom*; orcid.org/0000-0001-7056-7158

Mengnan Wang − *Center for High Pressure Science and Technology Advanced Research (HPSTAR), Shanghai 201203, China*

Duck Young Kim − *Center for High Pressure Science and Technology Advanced Research (HPSTAR), Shanghai 201203, China; Department of Chemistry, Pohang University of Science and Technology (POSTECH), Pohang 37673, Republic of Korea*

Eugene Gregoryanz − *Center for High Pressure Science and Technology Advanced Research (HPSTAR), Shanghai 201203, China; Centre for Science at Extreme Conditions and The School of Physics & Astronomy, The University of Edinburgh, Edinburgh EH9 3FD, United Kingdom*

Philip Dalladay-Simpson − *Center for High Pressure Science and Technology Advanced Research (HPSTAR), Shanghai 201203, China*

Complete contact information is available at: https://pubs.acs.org/10.1021/acs.jpclett.0c00688

Notes

The authors declare no competing financial interest.

■ ACKNOWLEDGMENTS

We acknowledge DESY (Hamburg, Germany), a member of the Helmholtz Association HGF, for the provision of experimental facilities. Parts of this research were carried out at PETRA-III, and we would like to thank H.-P. Liermann and K. Glazyrin for assistance in using beamline P02.2. We acknowledge the European Synchrotron Radiation Facility for provision of synchrotron radiation facilities at the ID15B beamline. MPA acknowledges the support of the European Research Council Grant Hecate Reference No. 695527 held by Graeme Ackland. D.Y.K. acknowledges the support by the NSFC of China (Grant No. 11774015) and the National Research Foundation of Korea (NRF-2020R1A2C1005236). Funding has been provided by the respective Chinese "1000 Talent Award" grants of both P.D.S. and R.T.H.

■ REFERENCES

(1) Huiberts, J. N.; Griessen, R.; Rector, J. H.; Wijngaarden, R. J.; Dekker, J. P.; De Groot, D. G.; Koeman, N. J. Yttrium and lanthanum hydride films with switchable optical properties. *Nature* **1996**, *380*, 231−234.

(2) Den Broeder, F. J.; Van Der Molen, S. J.; Kremers, M.; Huiberts, J. N.; Nagengast, D. G.; Van Gogh, A. T.; Huisman, W. H.; Koeman, N. J.; Dam, B.; Rector, J. H.; et al. Visualization of hydrogen migration in solids using switchable mirrors. *Nature* **1998**, *394*, 656−658.

(3) Chaboy, J.; Piquer, C. Modification of the magnetic properties of the $R_2Fe_{14}B$ series (R = rare earth) driven by hydrogen absorption. *Physical Review B - Condensed Matter and Materials Physics* **2002**, *66*, 1−9.

(4) Fujita, A.; Fujieda, S.; Hasegawa, Y.; Fukamichi, K. Itinerant-electron metamagnetic transition and large magnetocaloric effects in $La(Fe_xSi_{1-x})_{13}$ compounds and their hydrides. *Physical Review B - Condensed Matter and Materials Physics* **2003**, *67*, 12.

(5) San, X.; Ma, Y.; Cui, T.; He, W.; Han, B.; Liu, B.; Zou, G. Pressure-induced magnetic transition in metallic nickel hydrides by ab initio pseudopotential plane-wave calculations. *Phys. Rev. B: Condens. Matter Mater. Phys.* **2006**, *74*, 1−4.

(6) Ying, J.; Zhao, J.; Bi, W.; Alp, E. E.; Xiao, Y.; Chow, P.; Shen, G.; Struzhkin, V. V. Magnetic phase diagram of ϵ'-FeH. *Phys. Rev. B: Condens. Matter Mater. Phys.* **2020**, *101*, 020405.

(7) Peng, F.; Sun, Y.; Pickard, C. J.; Needs, R. J.; Wu, Q.; Ma, Y. Hydrogen Clathrate Structures in Rare Earth Hydrides at High Pressures: Possible Route to Room-Temperature Superconductivity. *Phys. Rev. Lett.* **2017**, *119*, 1−6.

(8) Somayazulu, M.; Ahart, M.; Mishra, A. K.; Geballe, Z. M.; Baldini, M.; Meng, Y.; Struzhkin, V. V.; Hemley, R. J. Evidence for Superconductivity above 260 K in Lanthanum Superhydride at Megabar Pressures. *Phys. Rev. Lett.* **2019**, *122*, 027001.

(9) Drozdov, A.; Kong, P.; Minkov, V.; Besedin, S.; Kuzovnikov, M.; Mozaffari, S.; Balicas, L.; Balakirev, F.; Graf, D.; Prakapenka, V. Superconductivity at 250 K in lanthanum hydride under high pressures. *Nature* **2019**, *569*, 528−531.

(10) Zurek, E.; Bi, T. High-temperature superconductivity in alkaline and rare earth polyhydrides at high pressure: A theoretical perspective. *J. Chem. Phys.* **2019**, *150*, 050901.

(11) Marizy, A.; Geneste, G.; Loubeyre, P.; Guigue, B.; Garbarino, G. Synthesis of bulk chromium hydrides under pressure of up to 120 GPa. *Phys. Rev. B: Condens. Matter Mater. Phys.* **2018**, *97*, 1−7.

(12) Pépin, C. M.; Dewaele, A.; Geneste, G.; Loubeyre, P.; Mezouar, M. New iron hydrides under high pressure. *Phys. Rev. Lett.* **2014**, *113*, 265504.

(13) Pépin, C. M.; Geneste, G.; Dewaele, A.; Mezouar, M.; Loubeyre, P. Synthesis of FeH_5: A layered structure with atomic hydrogen slabs. *Science* **2017**, *357*, 382−385.

(14) Wang, M.; Binns, J.; Donnelly, M.-E.; Peña-Alvarez, M.; Dalladay-Simpson, P.; Howie, R. T. High pressure synthesis and stability of cobalt hydrides. *J. Chem. Phys.* **2018**, *148*, 144310.

(15) Binns, J.; Donnelly, M.-E.; Wang, M.; Hermann, A.; Gregoryanz, E.; Dalladay-Simpson, P.; Howie, R. T. Synthesis of Ni_2H_3 at high temperatures and pressures. *Phys. Rev. B: Condens. Matter Mater. Phys.* **2018**, *98*, 1−4.

(16) Binns, J.; Peña-Alvarez, M.; Donnelly, M.-E.; Gregoryanz, E.; Howie, R. T.; Dalladay-Simpson, P. Structural Studies on the Cu−H System under Compression. *Engineering* **2019**, *5*, 505−509.

(17) Li, B.; Ding, Y.; Kim, D. Y.; Ahuja, R.; Zou, G.; Mao, H.-k. Rhodium dihydride (RhH_2) with high volumetric hydrogen density. *Proc. Natl. Acad. Sci. U. S. A.* **2011**, *108*, 18618−18621.

(18) Bi, T.; Zarifi, N.; Terpstra, T.; Zurek, E. The Search for Superconductivity in High Pressure Hydrides. In *Reference Module in Chemistry*; Molecular Sciences and Chemical Engineering: 2019.

(19) Kvashnin, A. G.; Kruglov, I. A.; Semenok, D. V.; Oganov, A. R. Iron Superhydrides FeH_5 and FeH_6: Stability, Electronic Properties, and Superconductivity. *J. Phys. Chem. C* **2018**, *122*, 4731−4736.

(20) Gao, G.; Wang, H.; Zhu, L.; Ma, Y. Pressure-Induced Formation of Noble Metal Hydrides. *J. Phys. Chem. C* **2012**, *116*, 1995−2000.

(21) Wang, L.; Duan, D.; Yu, H.; Xie, H.; Huang, X.; Tian, F.; Liu, B.; Cui, T. High-Pressure Formation of Cobalt Polyhydrides: A First-Principle Study. *Inorg. Chem.* **2018**, *57*, 181−186.

(22) Zaleski-Ejgierd, P.; Labet, V.; Strobel, T. A.; Hoffmann, R.; Ashcroft, N. W. WH_n under pressure. *J. Phys.: Condens. Matter* **2012**, *24*, 155701.

(23) Wang, H.; Tse, J. S.; Tanaka, K.; Iitaka, T.; Ma, Y. Superconductive sodalite-like clathrate calcium hydride at high pressures. *Proc. Natl. Acad. Sci. U. S. A.* **2012**, *109*, 6463−6466.

(24) Liu, Y.; Duan, D.; Huang, X.; Tian, F.; Li, D.; Sha, X.; Wang, C.; Zhang, H.; Yang, T.; Liu, B.; et al. Structures and Properties of Osmium Hydrides under Pressure from First Principle Calculation. *J. Phys. Chem. C* **2015**, *119*, 15905−15911.

(25) Wang, Z.; Wang, H.; Tse, J. S.; Iitaka, T.; Ma, Y. Stabilization H_3^+ of in the high pressure crystalline structure of H_nCl (n = 2−7). *Chem. Sci.* **2015**, *6*, 522−526.

(26) Struzhkin, V. V.; Kim, D. Y.; Stavrou, E.; Muramatsu, T.; Mao, H.-k.; Pickard, C. J.; Needs, R. J.; Prakapenka, V. B.; Goncharov, A. F. Synthesis of sodium polyhydrides at high pressures. *Nat. Commun.* **2016**, *7*, 12267.

(27) Liu, H.; Naumov, I. I.; Hoffmann, R.; Ashcroft, N. W.; Hemley, R. J. Potential high T_c superconducting lanthanum and yttrium hydrides at high pressure. *Proc. Natl. Acad. Sci. U. S. A.* **2017**, *114*, 6990−6995.

(28) Zarifi, N.; Bi, T.; Liu, H.; Zurek, E. Crystal Structures and Properties of Iron Hydrides at High Pressure. *J. Phys. Chem. C* **2018**, *122*, 24262−24269.

(29) Li, F.; Wang, D.; Du, H.; Zhou, D.; Ma, Y.; Liu, Y. Structural evolution of FeH_4 under high pressure. *RSC Adv.* **2017**, *7*, 12570.

(30) Zhang, S.; Lin, J.; Wang, Y.; Yang, G.; Bergara, A.; Ma, Y. Nonmetallic FeH_6 under High Pressure. *J. Phys. Chem. C* **2018**, *122*, 12022−12028.

(31) Liu, Y.; Duan, D.; Tian, F.; Wang, C.; Ma, Y.; Li, D.; Huang, X.; Liu, B.; Cui, T. Stability and properties of the Ru-H system at high pressure. *Phys. Chem. Chem. Phys.* **2016**, *18*, 1516−1520.

(32) Kuzovnikov, M. A.; Tkacz, M. Synthesis of ruthenium hydride. *Phys. Rev. B: Condens. Matter Mater. Phys.* **2016**, *93*, 064103.

(33) Oszlányi, G.; Süto, A. Ab initio structure solution by charge flipping. *Acta Crystallogr., Sect. A: Found. Crystallogr.* **2004**, *60*, 134−141.

(34) Goncharenko, I.; Eremets, M. I.; Hanfland, M.; Tse, J. S.; Amboage, M.; Yao, Y.; Trojan, I. A. Pressure-Induced Hydrogen-Dominant Metallic State in Aluminum Hydride. *Phys. Rev. Lett.* **2008**, *100*, 045504.

(35) Duan, D.; Liu, Y.; Tian, F.; Li, D.; Huang, X.; Zhao, Z.; Yu, H.; Liu, B.; Tian, W.; Cui, T. Pressure-induced metallization of dense $(H_2S)_2H_2$ with high T_c superconductivity. *Sci. Rep.* **2015**, *4*, 6968.

(36) Bazhanova, Z. G.; Oganov, A. R.; Gianola, O. Fe-C and Fe-H systems at pressures of the Earth's inner core. *Phys.-Usp.* **2012**, *55*, 489−497.

(37) Mishra, A. K.; Muramatsu, T.; Liu, H.; Geballe, Z. M.; Somayazulu, M.; Ahart, M.; Baldini, M.; Meng, Y.; Zurek, E.; Hemley, R. J. New calcium hydrides with mixed atomic and molecular hydrogen. *J. Phys. Chem. C* **2018**, *122*, 19370−19378.

(38) Heyd, J.; Scuseria, G. E.; Ernzerhof, M. Hybrid functionals based on a screened Coulomb potential. *J. Chem. Phys.* **2003**, *118*, 8207−8215.

(39) Heyd, J.; Scuseria, G. E. Efficient hybrid density functional calculations in solids: Assessment of the Heyd−Scuseria−Ernzerhof screened Coulomb hybrid functional. *J. Chem. Phys.* **2004**, *121*, 1187−1192.

(40) Heil, C.; Bachelet, G. B.; Boeri, L. Absence of superconductivity in iron polyhydrides at high pressures. *Phys. Rev. B: Condens. Matter Mater. Phys.* **2018**, *97*, 214510.

(41) Fei, Y.; Ricolleau, A.; Frank, M.; Mibe, K.; Shen, G.; Prakapenka, V. Toward an internally consistent pressure scale. *Proc. Natl. Acad. Sci. U. S. A.* **2007**, *104*, 9182−9186.

(42) Dalladay-Simpson, P.; Howie, R. T.; Gregoryanz, E. Evidence for a new phase of dense hydrogen above 325 gigapascals. *Nature* **2016**, *529*, 63−67.

(43) Liermann, H.-P.; Konôpková, Z.; Morgenroth, W.; Glazyrin, K.; Bednarčik, J.; McBride, E.; Petitgirard, S.; Delitz, J.; Wendt, M.; Bican, Y. The extreme conditions beamline P02. 2 and the extreme conditions science infrastructure at PETRA III. *J. Synchrotron Radiat.* **2015**, *22*, 908−924.

(44) Prescher, C.; Prakapenka, V. B. DIOPTAS: a program for reduction of two-dimensional X-ray diffraction data and data exploration. *High Pressure Res.* **2015**, *35*, 223−230.

(45) Oishi-Tomiyasu, R. Robust powder auto-indexing using many peaks. *J. Appl. Crystallogr.* **2014**, *47*, 593−598.

(46) Le Bail, A.; Duroy, H.; Fourquet, J. Ab-initio structure determination of $LiSbWO_6$ by X-ray powder diffraction. *Mater. Res. Bull.* **1988**, *23*, 447−452.

(47) Petříček, V.; Dušek, M.; Palatinus, L. Crystallographic computing system JANA2006: general features. *Z. Kristallogr. - Cryst. Mater.* **2014**, *229*, 345−352.

(48) Gonzalez-Platas, J.; Alvaro, M.; Nestola, F.; Angel, R. EosFit7-GUI: a new graphical user interface for equation of state calculations, analyses and teaching. *J. Appl. Crystallogr.* **2016**, *49*, 1377.

(49) Kresse, G.; Hafner, J. Ab initio molecular dynamics for liquid metals. *Phys. Rev. B: Condens. Matter Mater. Phys.* **1993**, *47*, 558.

(50) Kresse, G.; Hafner, J. Ab initio molecular-dynamics simulation of the liquid-metal−amorphous-semiconductor transition in germanium. *Phys. Rev. B: Condens. Matter Mater. Phys.* **1994**, *49*, 14251.

(51) Kresse, G.; Furthmüller, J. Efficiency of ab-initio total energy calculations for metals and semiconductors using a plane-wave basis set. *Comput. Mater. Sci.* **1996**, *6*, 15−50.

(52) Blöchl, P. E.; Jepsen, O.; Andersen, O. K. Improved tetrahedron method for Brillouin-zone integrations. *Phys. Rev. B: Condens. Matter Mater. Phys.* **1994**, *49*, 16223.

https://dx.doi.org/10.1021/acs.jpclett.0c00688